

IDAHO TRANSPORTATION DEPARTMENT

# RESEARCH REPORT

## A Precast Pier System for Accelerated Bridge Construction (ABC) in Idaho

RP 281

By

Mustafa Mashal, Arya Ebrahimpour, Mahesh Acharya, Jared Cantrell, Corey  
Marshall, Ali Shokrgozar

Idaho State University

Prepared for

Idaho Transportation Department

[ITD Research Program, Contracting Services](#)

Highways Construction and Operations

August 2021



**YOUR Safety** ●●●▶ **YOUR Mobility** ●●●▶ **YOUR Economic Opportunity**

## Disclaimer

This document is disseminated under the sponsorship of the Idaho Transportation Department and the United States Department of Transportation in the interest of information exchange. The State of Idaho and the United States Government assume no liability of its contents or use thereof.

The contents of this report reflect the view of the authors, who are responsible for the facts and accuracy of the data presented. The contents do not necessarily reflect the official policies of the Idaho Transportation Department or the United States Department of Transportation.

The State of Idaho and the United States Government do not endorse products or manufacturers. Trademarks or manufacturers' names appear only because they are considered essential to the object of this document.

***This report does not constitute a standard, specification, or regulation.***

## Technical Report Documentation Page

1. Report No. FHWA-ID-21-281	2. Government Accession No.	3. Recipient's Catalog No.	
4. Title and Subtitle A Precast Pier System for Accelerated Bridge Construction (ABC) in Idaho		5. Report Date August 2021	
		6. Performing Organization Code	
7. Author(s) Mustafa Mashal ( <a href="https://orcid.org/0000-0003-4654-0531">https://orcid.org/0000-0003-4654-0531</a> ), Arya Ebrahimpour, Mahesh Acharya ( <a href="https://orcid.org/0000-0002-3009-7099">https://orcid.org/0000-0002-3009-7099</a> ), Jared Cantrell, Corey Marshall, and Ali Shokrgozar		8. Performing Organization Report No.	
9. Performing Organization Name and Address Idaho State University Department of Civil and Environmental Engineering 921 S. 8 <sup>th</sup> Ave., Mail Stop 8060 Pocatello, ID 83209-8060		10. Work Unit No. (TRAIS)	
		11. Contract or Grant No. ISU-19-01	
12. Sponsoring Agency Name and Address Idaho Transportation Department (SPR) Highways Construction and Operations, Contracting Services, Research Program PO Box 7129 Boise, ID 83707-7129		13. Type of Report and Period Covered Final Report 01/01/2019 – 06/01/2021	
		14. Sponsoring Agency Code RP-281	
15. Supplementary Notes Project performed in cooperation with the Idaho Transportation Department and Federal Highway Administration.			
16. Abstract Accelerated Bridge Construction (ABC) in seismic regions is currently a research focal point. ABC is bridge construction that uses innovative planning, design, materials, and construction methods in a safe and cost-effective manner to reduce the onsite construction time that occurs when building new bridges or replacing and rehabilitating existing bridges. The research at Idaho State University included large scale experimental and analytical investigation of a new precast pier system for applications in seismic zones. The precast pier system uses hollow structural tubes filled with concrete in plastic hinge locations. Extensive testing on precast cantilever and bent piers was conducted to investigate seismic performance under quasi-static cyclic loads. Results were compared against benchmark cast-in-place specimens. Testing showed superior performance of the precast pier compared to cast-in-place. Limited analytical and some parametric studies are carried out to assist the designer in computational work. Furthermore, flexural analysis, interaction diagrams, design and detailing considerations, construction and assembly technology, limitations, inspection, and some proposed post-earthquake repair methodologies are presented.			
17. Key Words Accelerated Bridge Construction; Pipe connection; Large-scale testing, Pushover, Analytical, Parametric, Seismic		18. Distribution Statement Copies available from the <a href="#">ITD Research Program</a>	
19. Security Classification (of this report) Unclassified	20. Security Classification (of this page) Unclassified	21. No. of Pages 205	22. Price None

## Acknowledgments

The authors are thankful of assistance from Michael Johnson, P.E. (Project Manager) from the Idaho Transportation Department, Ed Miltner, P.E. from the Federal Highway Administration (Idaho Advisor); and Elmar Marx, P.E. (Senior Bridge Engineer) from the Alaska Department of Transportation for peer-reviewing this report.

## Committee

Each research project is overseen by a Technical Advisory Committee (TAC), which is led by an ITD project sponsor and project manager. The TAC is responsible for monitoring project progress, reviewing deliverables, ensuring that study objectives are met, and facilitating implementation of research recommendations. ITD's Research Program Manager appreciates the work of the following TAC members in guiding this research study.

- Matt Farrar, P.E.
- Dan Gorley, P.E.
- Leonard Ruminski, P.E.
- Michael Johnson, P.E.
- Ned Parrish
- Ed Miltner, P.E.
- Craig Wielenga, P.E.

# Table of Contents

Executive Summary.....	16
Summary .....	16
Project Objective .....	16
Project Tasks.....	16
Task 1. Literature review.....	16
Task 2. Experimental Investigation .....	17
Task 3. Numerical Investigation .....	19
Task 4. Parametric Case Studies.....	20
Task 5. Design/Detailing Considerations and Recommendations .....	20
Task 6. Discussions .....	21
Task 7. Final Project Presentation to ITD Bridge Section Staff.....	21
Task 8. Submission of the Final Report to ITD .....	21
Report Overview.....	21
1. Introduction.....	23
Accelerated Bridge Construction.....	23
Concept for a Precast Pier System in Seismic Regions .....	25
2. Literature Review .....	30
Introduction.....	30
Recent Developments .....	30
Conclusion .....	39
3. Experimental Investigation.....	40
Cantilever Column: Cast-In-Place .....	40
Introduction .....	40
Prototype Structure .....	40
Testing Arrangement and Design Considerations.....	41
Construction.....	47
Material Properties .....	49
Test Setup and Instrumentation .....	49
Testing Results .....	51

Summary .....	60
Cantilever Column: Precast .....	61
Introduction .....	61
Overview .....	61
Material Properties .....	62
Design of Precast Specimen .....	62
Construction.....	71
Test Setup and Instrumentation .....	73
Testing Results .....	73
Summary .....	82
Cantilever Columns: Precast vs. Cast-In-Place .....	83
Bent Pier System: Cast-In-Place.....	89
Introduction .....	89
Prototype Structure .....	89
Design of the CIP Specimen .....	92
Construction.....	96
Testing Arrangement .....	101
Instrumentation .....	103
Loading Protocol .....	105
Material Properties .....	108
Testing Results .....	109
Summary .....	120
Bent Pier System: Precast.....	121
Introduction .....	121
Overview .....	121
Precast Bent System Design.....	123
Construction.....	130
Testing Arrangement .....	134
Testing Results .....	135
Summary .....	147
Bent Pier System: Precast vs. Cast-In-Place .....	148

4. Analytical Investigation .....	149
Cantilever Column .....	149
Cast-In-Place Pier .....	149
Precast Pier .....	153
Bent Pier System .....	156
Cast-In-Place Bent .....	156
Precast Bent .....	157
5. Parametric Case Studies .....	158
Description of the Bridge.....	158
Nonlinear Static Analysis .....	159
Nonlinear Dynamic Analysis .....	161
Cast-In-Place Bridge Response.....	165
Precast Bridge Response.....	167
Cast-In-Place Vs. Precast Bridge .....	168
6. Design and Detailing Considerations.....	169
Introduction.....	169
Flexural Analysis .....	169
Interaction Diagrams .....	171
Embedment Length .....	172
Unbonded Length.....	175
Construction Technology and Assembly .....	175
Limitations.....	178
Inspection.....	178
Proposed Repair Methodologies.....	179
Summary.....	183
7. Conclusions.....	184
Future Research Work.....	186
Cited Works.....	188
Appendices.....	190
Appendix A. [Design Calculations of the Column Specimen] .....	191
A.1 Cast-In-Place Column Calculations .....	191

A.2 Precast Column Calculations .....	192
Appendix B. [Design Calculations of the Bent Specimen] .....	193
B.1 Cast-In-Place Bent Calculations .....	193
B.2 Precast Bent Calculations.....	194
Appendix C. [Grout Product Data Sheet].....	195
Appendix D. [Interaction Diagrams and Tables for the Precast Column] .....	199
D.1 HSS Pipe Connection $f'_c = 4$ ksi .....	199
D.2 HSS Pipe Connection $f'_c = 8$ ksi .....	202
D.3 Cast-in-place Moment Capacities with $f'_c = 4$ ksi.....	205

# List of Tables

Table 1. Summary of Performance Factors for the Cast-In-Place and Precast Columns..... 19

Table 2. Summarized Comparison of CIP and Precast Bent..... 19

Table 3. Actual  $f'_c$  values (psi)..... 49

Table 4. Summary of the Cast-In-Place Loading Protocol..... 52

Table 5. Damage Observation from Testing of the CIP Column, Drift % ..... 56

Table 6. Summary of the Performance Points from Testing of the CIP Column..... 56

Table 7. Equivalent Viscous Damping Coefficients for Hysteretic Damping Component..... 59

Table 8. Actual  $f'_c$  Values for the Precast Column (psi)..... 62

Table 9. Summary of Performance Values from Testing of the Precast Column ..... 75

Table 10. Damage Observation from Testing of the Precast Column, Drift (%) ..... 79

Table 11. Summary of the Performance Points from Testing of the Precast Column..... 79

Table 12. CIP Bent Test Day Compressive Strength..... 108

Table 13. CIP Bent Test Day Split Tension..... 108

Table 14. CIP Bent Loading Protocol Summary..... 111

Table 15. Precast Bent Loading Protocol Summary ..... 140

Table 16. Uniform Hazard Spectrum Data Points for Montpelier, Idaho ..... 163

Table 17. Earthquake Records form Different Regions ..... 165

Table 18. Maximum Base Shear and Displacement for CIP Bridge (Absolute Values Shown) ..... 167

Table 19. Maximum Base Shear and Displacement for Precast Bridge (Absolute Values Shown)..... 168

Table 20. Common Corrosion Rates from WSDOT Bridge Design Manual ..... 170

## List of Figures

Figure 1. Column-to-Footing Connection (Not to Scale).....	26
Figure 2. Column-to-Cap Beam Connection and Cap Details (Not to Scale).....	27
Figure 3. Thin-Walled Columns with Varying Thickness a) Uniform Column, b) Graded-Thickness, c) Graded-Thickness Sections (courtesy of Al-Kaseasbeh and Mamaghani 2019) .....	31
Figure 4. a) Column without Grouted Couplers, b) Column with Grouted Couplers, c) Cross Section Designs (courtesy of Qu et al. 2015) .....	32
Figure 5. Details for Bent Cap Pocket Connections (courtesy of Tazarv and Saiidi 2015a) .....	33
Figure 6. Precast Column for Testing Mechanical Bar Splices (courtesy of Tazarv and Saiidi 2015b).....	34
Figure 7. Hollow Precast Concrete Columns (courtesy of Kim et al. 2016) .....	34
Figure 8. Grouted Splice Sleeve Connection Located in the Plastic Hinge of the Column (courtesy of Ameli at el. 2016) .....	35
Figure 9. Column to Footing Connection Alternatives: a) Socket Connection, b) Pocket Connection (courtesy of Galvis and Correal 2017).....	36
Figure 10. CIP and Precast Bent Column Details (courtesy of Mehraein and Saiidi 2016) .....	36
Figure 11. Low-Damage Seismic Design (courtesy of Mashal and Palermo 2019a) .....	37
Figure 12. Precast Bent with Member Socket and Grouted Duct Connections (courtesy of Mashal and Palermo 2019b).....	38
Figure 13. Pipe-Pin Connection Detail (courtesy of Zaghi and Saiidi 2010).....	39
Figure 14. Detail Views of a Typical Bridge in Idaho .....	40
Figure 15. Scaling of a Typical Column, a) Full-Scale Typical Column, b) 0.25 Scale Typical Column .....	41
Figure 16. Testing Arrangement .....	42
Figure 17. ACI Testing Protocol.....	42
Figure 18. Loading Protocol .....	44
Figure 19. Comparison of SAP-2000 and Response-2000.....	45
Figure 20. Cast-In-Place Footing Reinforcing Rebar Layout.....	46
Figure 21. Cast-In-Place Test Specimen .....	47
Figure 22. CIP Construction: a) Completed Rebar Cage, b) Footing Pour, c) Finished Footing, d) Footing Curing, e) Column Formwork Setup, f) Finished Test Specimen.....	48
Figure 23. Column Instrumentation.....	50
Figure 24. Typical Test Setup with Load Cells .....	51
Figure 25. Loading Protocol for the Cast-In-Place Column .....	52
Figure 26. CIP Specimen at a) 0.45% drift, b) 2.67% drift, c) 5.32% drift, d) 8.87% drift, e) 10.64% drift, f) Ruptured Bar.....	53
Figure 27. Force vs. Displacement Plot for the Cast-In-Place Column.....	54
Figure 28. Force vs. Drift Plot for the Cast-In-Place Column .....	55
Figure 29. Backbone Curve for the Cast-In-Place Column .....	55
Figure 30. Cast-In-Place Curvature Distribution .....	57
Figure 31. Dissipated Energy Plot for the CIP Column (1 kJ = 737.56 ft-lb) .....	58
Figure 32. Corrected Area-Based Hysteretic Damping for the CIP Column.....	60

Figure 33. Plastic Stress Distribution .....	64
Figure 34. Embedment Length with Embedded Ring (courtesy of WSDOT) .....	66
Figure 35. Precast Column Detail.....	68
Figure 36. Precast Column to Footing Assembly .....	70
Figure 37. Precast Column Construction: a) Footing Rebar Cage, b) Column Rebar Assembly, c) Finished Footing, d) Finished Column, e) Grout Flowing out of Grout Vent, f) Finished Test Specimen.....	72
Figure 38. Location of Strain Gauges on the HSS Member .....	73
Figure 39. Pipe Failure During the Testing Procedure. ....	74
Figure 40. Loading Protocol for the Precast Column .....	74
Figure 41. Precast Specimen During Testing at: a) 0.45% Drift, b) 2.67% Drift, c) 5.32% Drift, d) 8.87% Drift, e) 13.27% Drift, f) Failed HSS Member .....	76
Figure 42. Force vs. Displacement plot for the Precast Column.....	77
Figure 43. Force vs. Drift Plot for the Precast Column.....	78
Figure 44. Backbone Curve for the Precast Column .....	78
Figure 45. Precast Curvature Distribution .....	80
Figure 46. Dissipated Energy Plot for the Precast Column (1 kJ = 737.56 ft-lb) .....	81
Figure 47. Area-Based Hysteretic Damping for the Precast Column .....	82
Figure 48. Backbone Curve for the Cast-In-Place and Precast Columns.....	84
Figure 49. Cumulative Dissipated Energy for Both Columns (1 kJ = 737.56 ft-lb) .....	85
Figure 50. Dissipated Energy for Each Cycle for Both Columns (1 kJ = 737.56 ft-lb) .....	86
Figure 51. Corrected Area-Based Hysteretic Damping for Both Columns .....	87
Figure 52. Residual Drift for the Cast-In-Place and Precast Columns.....	88
Figure 53. Elevation and Top View of SH-36 Bridge Over Bear River .....	90
Figure 54. Bear River Bent System Elevation View .....	90
Figure 55. CIP Bent Specimen .....	92
Figure 56. CIP Pier Detail.....	93
Figure 57. CIP Pier Cross-Section .....	94
Figure 58. CIP Cap Beam .....	95
Figure 59. CIP Cap Beam Cross-Section .....	95
Figure 60. CIP Footing .....	96
Figure 61. CIP Footing Construction: a) Column Cage, b) Place Column Cage, c) Tying Top Mat, d) Anchor Sleeves, e) Footing Pour.....	97
Figure 62. CIP Footing Placement .....	98
Figure 63. Completed CIP Pier .....	98
Figure 64. Cap False-Work .....	99
Figure 65. CIP Cap Construction: a) Cap Cage, b) Cap Cage Placement, c) Cap Complete False-Work, Cage, and Formwork.....	99
Figure 66. Completed Cap Pour .....	100
Figure 67. CIP Bent Prepared for Instrumentation .....	100
Figure 68. Actuator Cap Anchors .....	101
Figure 69. CIP Bent Testing Arrangement.....	102

Figure 70. CIP Instrumentation Layout: Front Elevation View.....	103
Figure 71. CIP Instrumentation Layout: Top View .....	104
Figure 72. CIP Instrumentation Layout: Rear Elevation View .....	104
Figure 73. ACI Loading Protocol.....	106
Figure 74. Displacement Capacity of a Pier in a Bent with Fixed-Fixed Supports (Caltrans 2013).....	107
Figure 75. CIP Bent Loading Protocol.....	108
Figure 76. CIP Bent Testing: a) Cycle 1: Interface Cracking, b) Cycle 3: Hairline Crack Development, c) Cycle 4: 0.0157 in. (0.4 mm) Crack Development, d) Cycle 8: Spalling and 0.0984 in. (2.5 mm) Cracking, e) Cycle 9: Base Connection Spalling, f) Cycle 13: Spiral Exposure .....	110
Figure 77. CIP Bent Testing: g) Cycle 14: Longitudinal Exposure, h) Cycle 15: Longitudinal Rebar Fracture .....	111
Figure 78. CIP Bent Force-Displacement Hysteresis .....	112
Figure 79. CIP Bent Force-Drift Hysteresis.....	113
Figure 80. CIP Bent Force-Drift Backbone Curve .....	113
Figure 81. South Column: Top (D1-S – D4-S) .....	114
Figure 82. South Column: Bottom (A1-S – A4-S).....	115
Figure 83. North Column: Top (D1-N – D4-N).....	115
Figure 84. North Column: Bottom, (A1-N – A4-N) .....	116
Figure 85. CIP Bent Dissipated Energy per Cycle and Cumulative .....	117
Figure 86. Moment Curvature Curve (Caltrans 2013).....	117
Figure 87. Bilinear Approximation for CIP Bent.....	118
Figure 88. Residual Drift of CIP Bent.....	119
Figure 89. Proposed Connection: Precast Footing Detail .....	121
Figure 90. Proposed Connection: Precast Column Detail .....	122
Figure 91. WSDOT Pipe Embedment Cross-Section.....	126
Figure 92. Precast Bent Cross-Section .....	128
Figure 93. Precast Bent Cap Detail.....	129
Figure 94. Precast Bent Specimen .....	130
Figure 95. Embedded HSS Pipe Prepared for Installation.....	131
Figure 96. Precast Bent Footing Elements .....	131
Figure 97. Precast Bent Column Prepared for Concrete.....	132
Figure 98. Cap Rebar Cage Placement .....	133
Figure 99. Precast Bent Column Erection .....	133
Figure 100. Precast Bent Cap Erection.....	134
Figure 101. Precast Bent Testing: a) Cycle 3: Hairline Cracking, b) Cycle 5: Vertical Hairline Cracking....	135
Figure 102. Precast Bent Testing: c) Cycle 6: Spalling Development, d) Cycle 6: Gap Opening 3/16-inch, e) Cycle 9: Slab Spalling Bottom, f) Cycle 11: Slab Spalling Top, g) Cycle 12: Slab Spalling North, h) Cycle 14: Gap Opening ½ inch .....	136
Figure 103. Precast Bent Failure: a) Cycle 18: HSS Pipe Exposure, b) Cycle 19: Perpendicular Face Cracking, c) Cycle 24: Confinement Failure, d) Cycle 24: Failure .....	137

Figure 104. Precast Bent Top Connection Post Test: a) Bulging HSS Pipe, b) HSS and Grout Separation, c) HSS Bulging, d) HSS Bulging and Separation.....	138
Figure 105. Precast Bent Bottom Connection Post Test: a) South Column, b) North Column.....	139
Figure 106. Cycle 24 Peak State .....	139
Figure 107. Precast Bent Force-Displacement Hysteresis .....	141
Figure 108. Precast Bent Force-Drift Hysteresis .....	142
Figure 109. Precast Bent Force-Drift Backbone Curve.....	142
Figure 110. South Column: Top (D1-S – D4-S) .....	143
Figure 111. South Column: Bottom (A1-S - A4-S) .....	144
Figure 112. North Column: Top (D1-N – D4-N).....	144
Figure 113. North Column: Bottom (A1-N – A4-N) .....	145
Figure 114. Precast Bent Dissipated Energy Per Cycle and Cumulative (1 kJ = 737.56 ft-lb) .....	145
Figure 115. Bilinear Approximation for Precast Bent .....	146
Figure 116. Residual Drift of Precast Bent .....	147
Figure 117. Details of CIP Pier Specimen .....	149
Figure 118. OpenSees Model of the Experimental CIP Column.....	150
Figure 119. Schematic of the Fitted Bi-Linear Curve for the Footing Bond-Slip Moment Rotation .....	151
Figure 120. Combined Strain Vs. Number of Half Cycles to Failure Plot (Based on Brown & Kunnath 2000 and Hawileh, et al. 2009) .....	152
Figure 121. Numerical and Experimental Hysteresis Force-Displacement for CIP Column.....	153
Figure 122. Details of the Precast Pier Specimen .....	154
Figure 123. Detailed Sections of the Model for Precast Column: a) Zone 1, b) Zone 2, and c) Zone 3.....	154
Figure 124. Numerical and Experimental Hysteresis Force-Drift for Precast Column.....	155
Figure 125. Numerical and Experimental Hysteresis Force-Displacement for CIP Bent Pier .....	156
Figure 126. Numerical and Experimental Hysteresis Force-Displacement for Precast Bent Pier.....	157
Figure 127. Plan View of the SH-22 over I-15 Bridge at Dubois (NTS).....	158
Figure 128. Elevation View of the SH-22 over I-15 Bridge at Dubois (NTS) .....	159
Figure 129. Dubois Bridge Nonlinear Model with Node Numbers .....	160
Figure 130. Dubois Bridge Nonlinear Model with Element Numbers .....	160
Figure 131. Base Shear Vs. Displacement for both CIP and Precast Column.....	161
Figure 132. AASHTO Seismic Coefficient Design Spectrum Constructed with the Three-Point Method .	162
Figure 133. Design Spectrum .....	164
Figure 134. Displacement vs. Time for Landers Earthquake .....	166
Figure 135. Pushover vs. Dynamic Response for Landers Earthquake for the Bridge with CIP Columns in Direction 2.....	166
Figure 136. HSS Member Moment Capacity Interaction Diagram .....	172
Figure 137. Embedment Length Determination Flow Chart.....	173
Figure 138. Embedment Length Comparison for HSS Round (in.).....	174
Figure 139. Embedment Length Comparison for Pipe (in.) .....	174
Figure 140. a) Receiving HSS Member, b) Footing Reinforcement, c) Finished Footing, d) Column Reinforcement, and e) Welded Centering Fins.....	177

Figure 141. Repair Methods, a) Embedded Ring Repair, b) Shear Stud Repair, and c) Weld Bead Repair .....	179
Figure 142. Finite Element Model for Repair Methods .....	180
Figure 143. Moment vs. Drift for Repair Methods .....	180
Figure 144. Pedestal Rotation for Repair Methods .....	181
Figure 145. Repair Methods with the Highest Results, a) ER-2x4t, b) SS-x4, c) wb-x3 and wb-x3-1.....	181
Figure 146. Proposed Repair Method for the ITD Precast Pier: a) Embedded Ring, b) Shear Stud, c) Weld Bead .....	182
Figure 147. Mission Bridge, BC, Canada .....	182
Figure 148. Proposed Concrete Jacketing Repair Method for Precast Column Connection .....	183

## List of Abbreviations and Acronyms

AASHTO .....	The American Association of State Highway and Transportation Officials
ABC .....	Accelerated Bridge Construction
ACI .....	American Concrete Institute
ASTM .....	American Society for Testing and Materials
CFST .....	Concrete Filled Steel Tubes
HSS .....	Hollow Structural Section
ITD .....	Idaho Transportation Department
PBES .....	Prefabricated Bridge Elements and Systems
PVC .....	Polyvinyl Chloride
SLAB .....	Structural LAB
SIBC .....	Slide-in Bridge Construction
UHPC .....	Ultra-High Performance Concrete
WSDOT .....	Washington State Department of Transportation

# Executive Summary

## Summary

In this project, a new precast pier with emulative connections is proposed for ABC in seismic regions. The precast pier offers ample tolerance, simple construction, and better seismic performance in addition to other benefits that will be discussed later. It uses structural steel tubes (pipes) filled with concrete in the plastic hinge zones. The pipes are placed at the end of the column during prefabrication. During assembly, the column pipe is inserted inside another pipe with larger diameter that is placed in the cap beam or footing. The gap between the pipes are filled with high-strength grout on-site to complete the connection. In this type of connection, the concrete filled steel pipe provides shear/flexural resistance as well as concrete confinement in the plastic hinge. Results and observations from large-scale testing showed that the proposed precast pier connection outperforms cast-in-place. Based on the results from this research, ITD has incorporated the proposed connection in design of an upcoming bridge in Idaho that is located in a seismic zone.

## Project Objective

The objective of this project is to investigate seismic performance of a proposed pipe connection by ITD and comparison against cast-in-place using the current force-based seismic design philosophy in the United States.

## Project Tasks

### Task 1. Literature review

This task includes a review of the technologies available/implemented for precast pier systems in the context of ABC from ITD and other Departments of Transportation (DOTs) in the United States. This task includes the following sub-tasks:

- a) Literature review on ABC in moderate-to-high seismicity
- b) Available technologies for seismic resistant connections between precast elements
- c) Comparison of past studied connections from the perspectives of transportation, seismic performance, constructability, etc.
- d) Experimental testing techniques for ABC bridge substructure systems
- e) Review of the connections that have been deployed in actual ABC substructure systems in Idaho and elsewhere

A significant amount of research has been conducted to improve and expand the ABC scope and knowledge in seismic regions. The connections discussed include thin-walled steel columns, high strength precast concrete, pocket connections, socket connections, grouted ducts, grouted splice sleeves, mechanical bar splices, hollow precast reinforced concrete, precast shell column, dampers, and pipe-pin connections. Research for ABC in seismic regions continues to be performed to improve and/or simplify the construction of bridges. The research presented in this report aims to present a simple alternative to the current grouted duct, pocket, socket, and pipe-pin connections.

## **Task 2. Experimental Investigation**

This task is the main focus of the project and includes large-scale testing of precast and cast-in-place pier systems (two bents and two cantilever columns) under quasi-static cyclic loading. The columns are octagonal section. This task includes the following sub-tasks:

- a) Design of specimens in accordance with AASHTO/ITD Bridge Design Manuals for experimental testing
- b) Design of test-setup
- c) Construction of the specimens
- d) Materials characterization
- e) Assembly of the specimens in the Structural LAB (SLAB) at Idaho State University
- f) Instrumentation and data acquisition system for experimental testing
- g) Experimental testing of the specimens up to failure point
- h) Disposal/demolition of the tested specimens
- i) Processing of testing results (e.g., force-displacement hysteresis, moment-rotation etc.)

The cast-in-place specimen is intended to be the benchmark for the precast solution. The cast-in-place column is designed following the latest version of the AASHTO LRFD Bridge Design Specifications. The footing and column are constructed using traditional methods and materials. The column is tested under quasi-static loading until failure. The column behaved in a ductile manner. The column achieved its design base shear of 25-kip. The maximum base shear obtained during the testing procedure is 37.8-kip. The maximum displacement achieved is 7.7 in. which corresponded to a ductility of just below 7.5. Damage to the column during the test is within the first 18 in. of the column which is the expected plastic hinge length for a well detailed and confined section. The total energy dissipated during the testing procedure is 456 kJ. A hysteretic damping plot showed that the column had similar values to a Takeda-Thin model up to a displacement ductility of slightly lower than 3.5. Above that, the column had higher values of hysteretic damping compared to a Takeda-Thin model.

The precast specimen is designed to match the capacity and ductility of the cast-in-place benchmark. The precast footing and column are constructed incorporating HSS members. The Concrete Filled Steel Tube (CFST) at the interface of the column and footing provides flexural and shear resistance as well as confinement. The specimen is designed using the CFST equations provided in the WSDOT Bridge Design Manual and the latest version of AASHTO LRFD Bridge Design Specifications. The contribution of the unconfined concrete cover at the interface was ignored for the flexural design of the column. An elastomeric pad is provided at the column and footing interface to prevent cracking during smaller drift ratios and allow rocking of the column. The embedment length of the pipe is selected such to develop the plastic capacity of the column pipe without any premature failure or pullout. An unbonded length of the pipe is provided to distribute inelastic strain during larger drift ratios and to improve the low-cycle fatigue performance of the pipe. The unbonded length region was designed to be the ductile link in the specimen. The footing and other parts of the column are designed to be capacity protected regions. Testing results show good performance of the precast column with enhanced energy dissipation. Damage to the column during the test was observed to be within the first 18 in. of the column which thought to be the plastic hinge region. The loss of the cover concrete occurred during the 4.42% drift ratio. This was later than what was observed in the testing of the cast-in-place benchmark. The failure mechanism for the connection started with an “Elephant-Leg” buckling of the pipe over the unbonded region, followed by the fracture of the pipe on one side. There was a rapid decrease in the lateral capacity of the column when the buckling increased. The maximum force obtained during the testing procedure was 41.2-kip which was approximately 10% higher compared to the cast-in-place benchmark. The maximum displacement achieved was 9.4 in. which is about 20% higher compared to the cast-in-place benchmark. The ultimate displacement ductility is just below 6.5. The lower value of ductility compared to cast-in-place (7.5) was the fact that the precast column had a higher yield point compared to cast-in-place. The total energy dissipated during the testing procedure was 1,025 kJ. This was 2.25 times of the cast-in-place benchmark. The hysteretic damping plot showed that the precast column, overall, had similar values of hysteretic damping of Takeda-Fat and Ramberg-Osgood models. This is thought to be due to enhanced confinement (e.g., Concrete Filled Steel Tube) and detailing considerations. The precast column reached a hysteretic damping of 20% at the failure point. Table 1 presents the summary of performance factors obtained from the experimental investigation of the cast-in-place and precast cantilever columns. Similarly, Table 2 presents the summary of performance factors obtained from the experimental investigation of the cast-in-place and precast bent. The overstrength factor in the table are from experimental studies and can be seen that they are comparable; however, having slightly higher overstrength factor for precast than CIP is because CFST provide better confinement as well as producing more strain hardening. Further research can be carried out to obtain the appropriate overstrength factors for the precast pipe connection when a performance based, or displacement based designed is utilized.

Most importantly, the CIP has slightly higher displacement ductility at failure point because of the smaller yield compared to precast. In reality, precast system is more ductile and provides better ductility. So, the measure should be the energy dissipation (which is 6.21 times higher than CIP) and not the ductility. Overall, the precast system provided great elastic and plastic deformation capacity.

**Table 1. Summary of Performance Factors for the Cast-In-Place and Precast Columns**

Performance Factors	Cast-in-place column	Precast column
Yield Displacement	0.9 in. (1.2% Drift Ratio)	2.6 in. (3.3% Drift Ratio)
Base Shear at Yield	33 kip	37.5 kip
Maximum Curvature at (7.99% Drift Ratio)	0.0038 radian	0.0036 radian
Ultimate Displacement Ductility	7.4	6.3
Ultimate Displacement Capacity	7.7 in. (9.9% Drift Ratio)	9.6 in. (12.3% Drift Ratio)
Ultimate Base Shear	37.8 kip	41.2 kip
Total Energy dissipated	456 kJ	1025 kJ

**Table 2. Summarized Comparison of CIP and Precast Bent**

	CIP	Precast	Precast (% Based)
<b>Max Force</b>	66-kip	71.4-kip	108%
<b>Max Displacement</b>	4.14 in. (4.94%)	7.66 in. (9.15%)	185%
<b>Moment Capacity</b>	460-kip-ft.	498-kip-ft.	108%
<b>Initial Stiffness</b>	56.7-kip/in.	38.7-kip/in.	68%
<b>Initial Yield</b>	0.5% (0.42 in.)	1.13% (0.95 in.)	226%
<b>Global Yield (Bilinear approximation)</b>	0.7% (0.596 in.)	1.49% (1.246 in.)	209%
<b>Correlating Moment Capacity at Global Yield</b>	392-kip-ft.	433-kip-ft.	110%
<b>Energy Dissipation</b>	342 kJ (252,246 ft-lb)	2,125 kJ (1,567,320 ft-lb) *[466 kJ (343,704 ft-lb)]	621% *[136%]
<b>Overstrength Factor</b>	1.76	2.18	124%
<b>Displacement Ductility (Ultimate Base Shear)</b>	3.69	2.03	55%
<b>Displacement Ductility (Failure Point)</b>	7.48	6.02	80%

Note: \*Precast Cumulative Dissipated Energy at Failure of CIP Bent

### Task 3. Numerical Investigation

This task supplements the experimental investigation and includes analytical modeling of the precast and cast-in-place piers in a software package. Appropriate analytical models are developed for the proposed type of connection. This task includes the following sub tasks:

- a) Finite Element Analysis of the proposed connection
- b) Simplified analytical modeling of the proposed connection

- c) Calibration/comparison of analytical models against experimental data
- d) Hysteresis response under cyclic loads

The analytical modeling in this report is aimed to provide a practical tool for bridge engineers when considering new connection details. Analytical models were created for the CIP column and precast column with proposed pipe connection using the Open System for Earthquake Engineering Simulation (OpenSees) software. To predict the experimental results, low-cycle fatigue data were included in the OpenSees model. Results show good agreement between the analytical and experimental data. Similarly, analytical models were created for the CIP bent pier and precast bent pier with proposed pipe connection using OpenSees software. The results showed good agreement between the analytical and experimental data. It was difficult to capture shear deformation and Bauschinger effects for the precast bent pier after 6% drift ratio.

#### **Task 4. Parametric Case Studies**

This task is limited in scope and includes the following sub tasks:

- a) Building analytical models of an actual bridge in Idaho that is located in a high seismic region. The models represent both cast-in-place and the proposed precast connection
- b) Conduct nonlinear static (pushover) and nonlinear dynamic (time-history analysis) on the models and comparing the global seismic response of the bridge (e.g., formation of plastic hinges, force-displacement response etc.)
- c) Comparing capacity versus demand for the proposed precast connection and cast-in-place construction
- d) Summarizing findings from global seismic analysis of the bridge structures

Results from nonlinear static and dynamic analyses showed that the bridge with the precast pier closely emulates the cast-in-place bridge behavior. Both models had similar strength, ductility, and stiffness. Since the location of the Dubois bridge was assumed to be in Montpelier, nonlinear dynamic analysis showed that both cast-in-place and precast bridge models would reach their yield capacity under the four earthquake records. This is to be expected since the design seismic accelerations for Montpelier are larger than those of Dubois. In summary, existing nonlinear analysis techniques for cast-in-place bridges can be used to perform a system level analysis of a bridge with the proposed ITD connection.

#### **Task 5. Design/Detailing Considerations and Recommendations**

This includes the following sub tasks:

- a) Recommendations for design of bridges with the proposed connection type in seismic regions.
- b) Recommendations for precasting and construction on-site

- c) Proposing assembly sequence for precast elements on-site
- d) Limitations on implementation of the proposed connection
- e) To ease the designers in choosing the correct size of the pipe to match cast-in-place strength, a series of interaction curves similar to those shown in Figure C6.12.2.3.3-2 of the AASHTO Specs are developed based on existing information on Concrete-Filled Steel Tubes (CFSTs).
- f) Potential post-earthquake repair methods

The flexural analysis of the pier can be conducted similar to CFSTs. Some design considerations and recommendations for construction/assembly are proposed. A series of interaction diagrams were created using the WSDOT Bridge Design Manual. The interaction diagrams show the moment capacity increasing as the HSS member diameter and wall thickness increase. The interaction diagrams do not account for an axial load but can be used as an effective tool in sizing the HSS/pipe to match a certain cast-in-place capacity. Some limitations of the precast column were presented with respect to the capacity of the connection, precasting technology, and the weight of the precast element. Several potential repair methods using an embedded ring, welded beads, and concrete jacketing were discussed. The proposed repair methods should be experimentally tested to verify their effectiveness in restoring stiffness and strength to the precast pier. Some post-earthquake inspection and indication of damage to the HSS/pipe was also discussed.

## **Task 6. Discussions**

Based on existing literature and results/observations from experimental testing of the proposed connection, some discussions are provided for the following:

- a) Transportation, constructability, and inspection
- b) Post-earthquake inspection methodologies and damage signs
- c) Recommendations for future research work

## **Task 7. Final Project Presentation to ITD Bridge Section Staff**

## **Task 8. Submission of the Final Report to ITD**

## **Report Overview**

This report is divided into seven chapters.

- 1) Chapter 1 presents introduction to ABC and the challenges associated with ABC in seismic regions. This chapter discusses concepts for a precast pier system for ABC in seismic regions.
- 2) Chapter 2 presents literature review on ABC in seismic regions.

- 3) Chapter 3 presents the design, detailing, construction, and results from experimental testing of large-scale precast and cast-in-place specimens.
- 4) Chapter 4 presents the details from the analytical investigation.
- 5) Chapter 5 presents the details from the parametric case studies.
- 6) Chapter 6 describes flexural analysis, design and detailing considerations, construction technology, limitations, inspection, and some proposed post-earthquake repair methods for bridges incorporating the ITD precast pier system.
- 7) Chapter 7 presents conclusions and recommendations for future research work.

# 1. Introduction

## Accelerated Bridge Construction

For the past several years, Accelerated Bridge Construction (ABC) has been gaining popularity in the United States and other parts of the world. The Federal Highway Administration defines ABC as “bridge construction that uses innovative planning, design, materials, and construction methods in a safe and cost-effective manner to reduce the onsite construction time that occurs when building new bridges or replacing and rehabilitating existing bridges” (U.S. Department of Transportation/Federal Highway Administration 2019). While ABC offers great advantages, applications of ABC in seismic regions have been limited due to concerns about the seismic performance of the connection between precast elements. Past earthquakes have shown vulnerability of the connection between precast elements due to limited ductility and strength.

In 2017, ASCE published an infrastructure report card for the nation. The report states that there are 614,387 bridges in the United States. Approximately 4 in 10 of the bridges are 50 years old or older. 56,007 of the nation’s bridges were classified as structurally deficient in the year 2016, with approximately 188 million trips across a structurally deficient bridge each day. A structurally deficient bridge requires a significant amount of maintenance and rehabilitation or needs to be replaced. Overall, the number of structurally deficient bridges is decreasing, but at the same time the average age of the bridges in the nation is rising, 43 years old, and approaching the end of their designed service lives. The ASCE 2017 infrastructure report card states that “The most recent estimate puts the nation’s backlog of bridge rehabilitation needs at \$123 billion” (ASCE 2017).

ASCE also published an infrastructure report for the state of Idaho in 2018. When the report was published, there were 4,492 bridges in Idaho. Out of the total number of bridges, 393 were considered structurally deficient, 45 of which were located on the state highway system, and 280 on local highway systems. 837 of the bridges located along the state highway system had reached or exceeded their designed 50-year life span. According to the ASCE report, the number of bridges on the state highway system that are at or exceeding their designed 50-year life span will increase to 911 in 2021 (ASCE 2018).

To improve the next infrastructure report card, the bridges in the United States need to be either repaired or replaced quickly and efficiently. One of the ways the bridges can be replaced quickly and efficiently is by incorporating ABC methods. Fortunately, the state and highway officials are making a difference, but more techniques need to be developed to hasten the process. In addition, bridges located in seismic zones must be designed using ABC connections that will offer adequate performance during an earthquake.

There are several advantages to using ABC methods, which are evident in most ABC projects. One of the advantages is limiting the duration of disruptions to traffic during construction because of the increased construction speed. Another advantage is improved public perception. The public’s perception is improved because they see the construction progressing faster than usual. Faster project delivery is also

an advantage to ABC. Due to the speed of the construction, the negative economic impact on local businesses is reduced which is counted as another advantage. The use of precast concrete is an advantage because formwork can be reused which reduces costs. Other noteworthy advantages include the following: better quality control of the materials being used, lower machinery and equipment costs, higher durability of the bridge elements, a reduced weight of the bridge structure, increased level of safety, and less environmental impacts to the surrounding area (U.S. Department of Transportation/Federal Highway Administration 2019). The major advantages of ABC are listed below:

1. Limited disruption to traffic during construction, especially in populated areas
2. Fast project delivery
3. Cost savings related to the use of formwork
4. More accuracy in bridge elements due to their prefabrication
5. Better quality control of the materials used in the bridge elements
6. Lower machinery and equipment costs
7. Higher durability of the bridge elements
8. Reduced weight of the bridge structure
9. Higher level of safety
10. Less environmental impacts

There have been plenty of examples for application of ABC in zones of low seismicity, however, application of ABC in regions with moderate-to-high seismicity has been limited. This is due to uncertainty about the seismic performance of the connections between the precast elements. Lessons learned from the past earthquakes have shown specific vulnerability of precast connections in zones of high seismicity.

There are disadvantages associated with using ABC and precast concrete. One of the disadvantages is the difficulty of maintaining tight tolerances. As projects develop with precast concrete, occasionally the precast elements do not fit or align as intended. If the concrete members are not aligning, then a new concrete element will need to be constructed and precious time and money are wasted. Misalignment issues become more common with longer/taller precast elements. Another disadvantage is encountered when the concrete elements have bars extruding from the concrete. In a case where bars are extruding from the concrete, the bars need to be protected from being damaged during transportation and installation. Another disadvantage is the cost of each concrete member. The process involved with precast concrete elements requires a specific skillset to prepare, pour, transport, and install the member, which is not the same as the traditional skillsets required for cast-in-place concrete. One more disadvantage related to the overall cost occurs during the transportation of the precast elements. Concrete is heavy and as a result, the cost associated with the transportation process is high.

When considering the seismic performance of an ABC structure, other challenges arise. Some of the challenges are: inelastic deformations that develop during cyclic behavior, large concentrated forces that develop where key elements join together, and a rapid loss of strength may be evident due to localized buckling (Marsh 2018).

Precast connections are classified in two different ways, emulative and non-emulative. An emulative connection mimics the seismic performance of a traditional cast-in-place connection while a non-emulative connection improves the performance of the connection. The connections that are emulative may incorporate bar couplers, grouted ducts, pocket connections, and member socket connections while the non-emulative connections are segmental post-tensioned rocking piers and hybrid or dissipative controlled rocking connections (Mashal et al. 2016). Emulative connections are usually more desirable than a non-emulative connection because of the confidence with regards to the durability and seismic performance of cast-in-place connections (Marsh et al. 2011).

## **Concept for a Precast Pier System in Seismic Regions**

The Idaho Transportation Department (ITD) has proposed a new precast pier system for ABC in seismic regions. The connection is somewhat similar in appearance to the pipe-pin connection investigated by Zaghi and Saiidi (2009). However, it would be pipe-fixed connection designed to carry full moments expected to develop at the top and bottom of the column. In the type of connection proposed in this research project, the diameter and thickness of the steel pipe protruding from the column into the cap would be selected to resist all design moments and shears at the column-to-cap beam interface. The connection should have similar moment capacity as that provided by the column longitudinal rebars. Figure 1 and Figure 2 presents sketches and details of the proposed connection and precast cap beam.

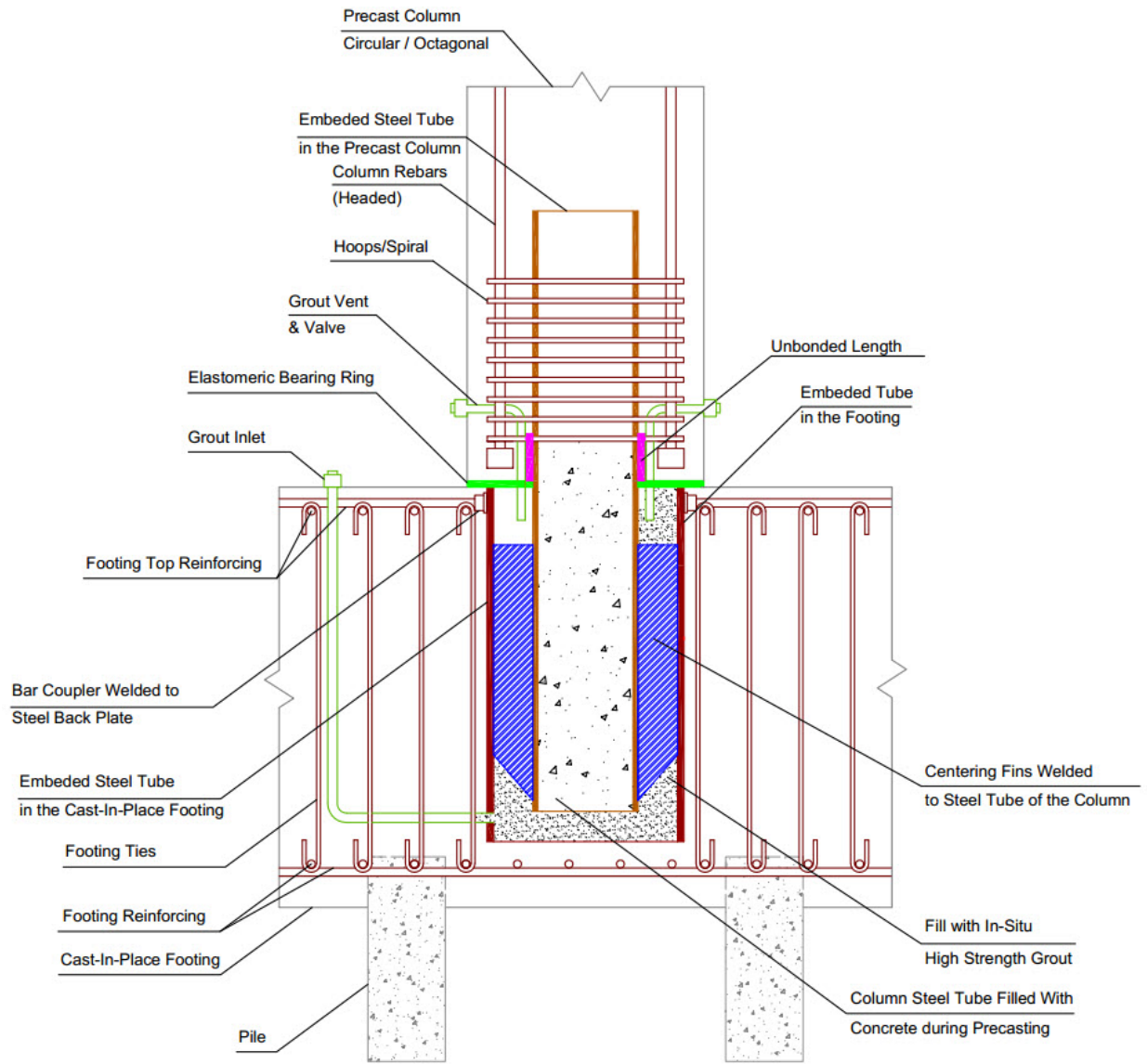


**Figure 1. Column-to-Footing Connection (Not to Scale)**

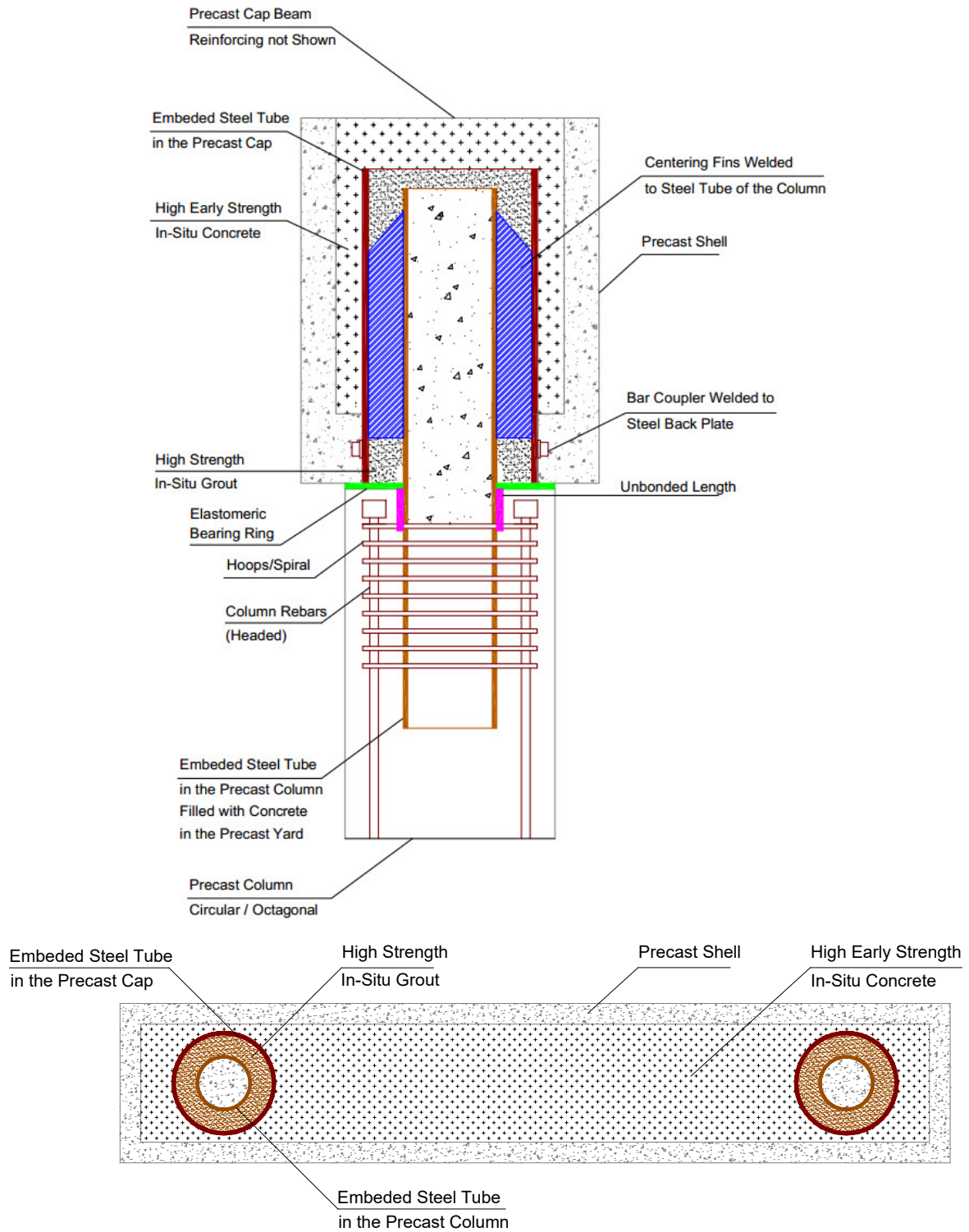


**Figure 2. Column-to-Cap Beam Connection and Cap Details (Not to Scale)**

The proposed connection incorporates hollow structural sections (HSS) made from steel located within the plastic hinge of the column and is referred to as a pipe connection. HSS is installed at the end of the precast column. Approximately half of the HSS is extruding out of the precast column and have centering fins welded to the outside edge of the pipe. In the proposed pier system, the column main reinforcement would be terminated at the top and the bottom with head terminators to improve the rebar development length. In this case, precast column reinforcement would not protrude into the cap, eliminating the risk of its damage during transportation and a cumbersome need of alignment with the grouted ducts or grouted couplers. Instead, the column's steel pipe would be easily "fed" into the larger diameter steel pipe (sleeve) embedded within the precast hollow shell pier cap. Centering fins will be pre-welded to the column pipe at the precast plant and will be sized to provide relatively snug fit inside the footing and the cap pipes, eliminating the need for cumbersome cap alignment and additional external bracing for either column or the cap after their erection. During the assembly on-site, these centering fins would be used to fine-tune the cap final position and to secure the cap on top of column in a similar fashion as a Christmas tree stand without the need of external bracing. The centering fins are not important structurally, but rather are only for inserting the column into the footing or cap beam.

The advantage of the proposed system is that the only fine-tuning required is the correct setting of the top of footing elevation and the correct positioning of the footing pipe. Once this is done, the rest of the components will be automatically aligned in correct positions, like "Lego blocks". Grout will be pumped into the gap between the two pipes to secure the connection after the column is erected. For the column-to-cap beam connection, the next step would be to fill the voids within the hollow cap shell using High-Early Strength (HES) concrete. This would complete the cap installation. It is possible to use expansion joint filler or elastomeric ring placed around the column's pipe in order to isolate the cap and column concrete around its perimeter and to allow for some level of deformations without crushing the concrete. The column steel pipe may also be wrapped with expansion joint filler at the column-to-cap connection in order to avoid stress concentrations and to allow for a small local yielding/gap opening without crushing of concrete. Similar connection detail may also be incorporated in the column-to-footing connection as shown in Figure 2. In this case, the concrete filled steel pipe would protrude from the bottom of column into the pocket within the footing and then the pocket would be filled with HES grout. Similar expansion joint fillers would be used around the pipe in this connection as well, as to allow for certain amount of deformations without crushing of concrete.

The main advantage of the proposed connection lies in its simplicity, ample installation tolerance, ease of erection, use of hollow/partially hollow/solid piers caps (based on project specific preference), and potentially superior performance at reduced costs. The proposed connection does not require any proprietary components and materials, making it more competitive and easier to construct. The pier would be analyzed as if it were built by conventional methods. The size and thickness of concrete filled connecting pipes would then be selected to closely match the column nominal moment resistance. Experimental and analytical investigations need to determine the level of ductility of such concrete filled pipe in comparison with cast-in-place reinforced concrete column and to adjust, as required, assuring the capacity protected design of the cap beam and the footing.

The column-to-cap beam and column-to-footing connection allow some flexibility (gap opening in the connections) during smaller earthquakes, thus reducing the chances of hairline cracking in the column and yielding of the rebar/pipes. Self-centering is provided by gravity loads in this case.

The research project stems from the list of disadvantages associated with some existing ABC connections such as grouted ducts or grouted couplers. Many of the current ABC methods that require couplers or grouted ducts have difficulties connecting the concrete elements due to alignment issues. The proposed connection offers ample tolerance compared to grouted ducts or grouted couplers.

## 2. Literature Review

### Introduction

Several research projects have been devoted to the expansion of ABC methodologies. Some of the institutions that have contributed to ABC research in seismic regions include the University of Nevada-Reno, Texas A&M University, University of Canterbury in New Zealand, Idaho State University, and Washington State University. This chapter will briefly discuss a variety of related literature which includes thin-walled steel columns, high-strength precast concrete, pocket connections, socket connections, grouted ducts, grouted splice sleeves, mechanical bar splices, hollow precast reinforced concrete, precast shell column, dissipative controlled rocking, and pipe-pin connections. Most of these connections are emulative cast-in-place. Emulative cast-in-place connections aim to achieve a similar seismic performance to cast-in-place (e.g., formation of plastic hinges). Non-emulative cast-in-place connections such as dissipative controlled rocking aim for a better and low damage seismic performance compared to traditional cast-in-place (e.g., self-centering after the earthquake, replaceable energy dissipaters etc.). Each type of connection has its advantages and disadvantages. Therefore, it is difficult to identify and select a single ABC connection that works for all projects and types of seismicity.

### Recent Developments

Al-Kaseasbeh and Mamaghani (2019) investigated the hysteretic behavior of circular thin-walled steel columns. The control test column had a continuous wall thickness while the five experimental columns had gradient wall thicknesses with volumes and outside diameters equaling that of the control specimen. The columns are analyzed with a constant axial load and a bidirectional cyclic horizontal loading protocol. The analysis of the members is completed using a finite-element model that allows the material and geometric properties to vary along the length of the pipe, as shown in Figure 3. The gradient columns displayed a significant increase in ultimate strength, ductility, and post-buckling behavior compared to the controlled column with a uniform thickness.

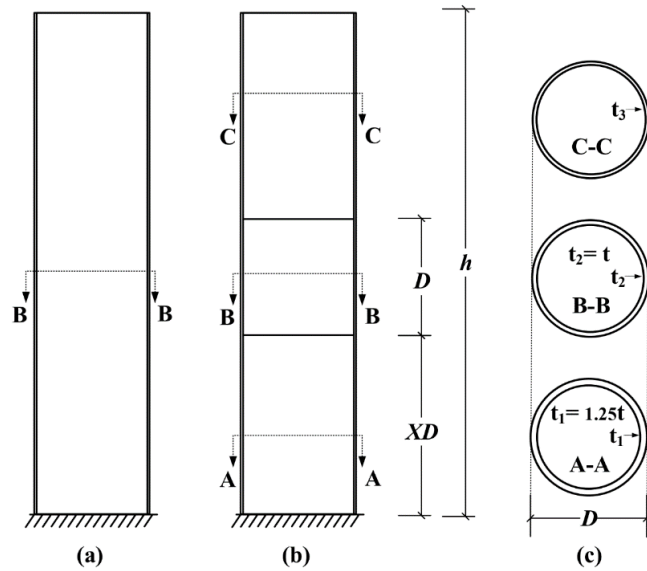


**Figure 3. Thin-Walled Columns with Varying Thickness a) Uniform Column, b) Graded-Thickness, c) Graded-Thickness Sections (courtesy of Al-Kaseasbeh and Mamaghani 2019)**

Ou et al. (2015) performed six cyclic tests on large-scale columns. These large-scale tests are part of Taiwan's new reinforced concrete research effort to develop standards for high strength reinforced concrete structures to incorporate into high-rise building construction projects. The purpose of the research is to investigate the seismic performance of high strength concrete in precast reinforced columns. Each of the six columns is constructed from high-strength concrete, high strength longitudinal bars, and transverse reinforcing bars. Two different construction methodologies are incorporated into the design of the columns. The two methodologies are grouted coupler splices for the longitudinal reinforcement in the plastic hinge zones and butt-welded splices for the transverse reinforcement, shown in Figure 4. The effect of using grouted coupler splices and butt-welded splices in the plastic hinge zone is compared to a cast-in-place column using conventional construction methods. After analyzing the results, it appears that the performance of the precast grouted coupler splices is equivalent to the conventional cast-in-place column. The results also showed the precast columns with butt-welded splices had a lower ultimate drift capacity compared to the conventional hooked transverse reinforcement. The reduction in ultimate drift capacity is a result of the longitudinal reinforcement buckling sooner than the traditional transverse hook methodology.

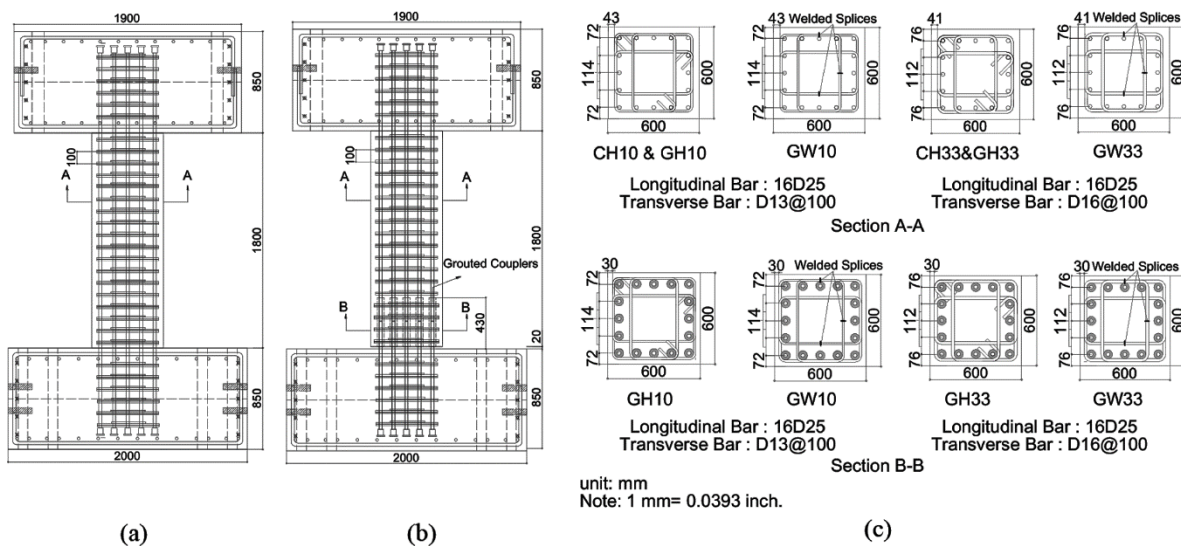
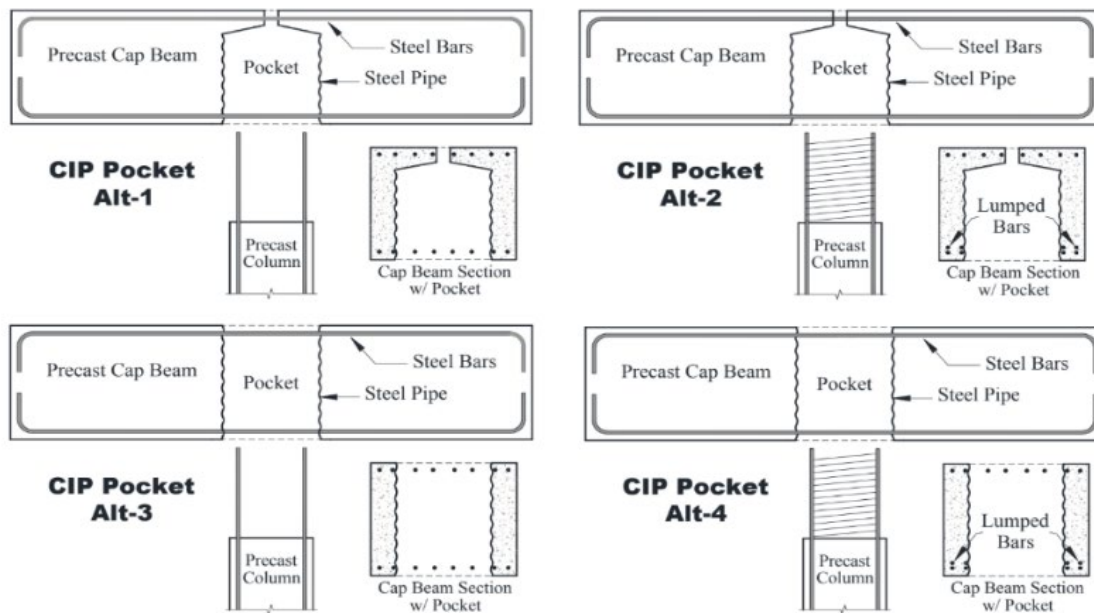
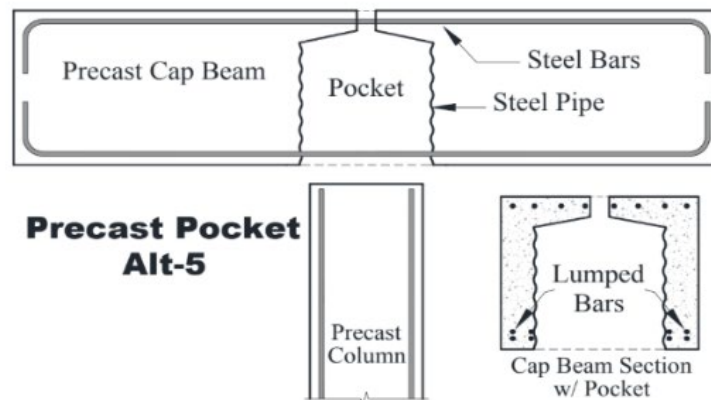


**Figure 4. a) Column without Grouted Couplers, b) Column with Grouted Couplers, c) Cross Section Designs (courtesy of Qu et al. 2015)**

Tazarv and Saiidi (2015a) investigated the use of pocket connections in high seismic regions. Although the AASHTO Scan 11-02 had studies regarding the seismic performance of these pocket connections, additional research was required to develop practical and reliable pocket connections. As a result of the research project, pocket connections are found to be a useful way to join precast columns and pier caps together. Through their literature review research, it was discovered that if the bent cap is properly designed, the effects of pockets, with regards to the seismic performance of the cap, are negligible and the connection simulated a cast-in-place column connection. Based on the lessons learned from the research, five details for precast pocket connections are shown in Figure 5. Some of the previous precast cap beam models that were constructed with a pocket connection yielded. The failure of the pocket connections is a result of inadequate design. The use of precast pocket Alt-5 connections, shown in Figure 5, reduced the onsite construction time by 75%. The other pocket connections reduced the onsite construction time by 42%.



(a) Cast-in-Place Pocket Connections



(b) Precast Pocket Connection

**Figure 5. Details for Bent Cap Pocket Connections (courtesy of Tazarv and Saiidi 2015a)**

Tazarv and Saiidi (2015b) also investigated mechanical bar splices located in the plastic hinge. One of the precast columns is shown in Figure 6. Their research revealed that the performance of a coupler is dependent upon the loading rate and the manufacturer of the coupler. It is also concluded that careful placement of large couplers in the column is crucial to obtaining the ultimate capacity of the coupler. In most cases, the seismic performance of smaller couplers is determined to be adequate. Finally, it is estimated that incorporating the mechanical bar splices at both ends of a precast column can reduce the construction time by nearly 60%.



**Figure 6. Precast Column for Testing Mechanical Bar Splices (courtesy of Tazarv and Saiidi 2015b)**

Kim et al. (2016) developed two types of cast-in-place concrete-filled hollow precast concrete columns to reduce the weight of large precast concrete columns and to increase the structural integrity of the cap beam to column joints. The two proposed types of hollow precast concrete columns are shown in Figure 7. Cyclic loading tests were performed on the two columns and a conventional reinforced concrete column to measure the seismic resistance of the columns. The results from the test procedure showed that the stiffness and the maximum strength of the experimental test columns are comparable to the controlled conventional reinforced column. However, the displacement ductility of the experimental columns is lower. The energy dissipated from the experimental columns is slightly lower than the controlled reinforced column. The experiment also concluded that the hollow core sections reduced the weight of the precast elements by 62% and 51%.

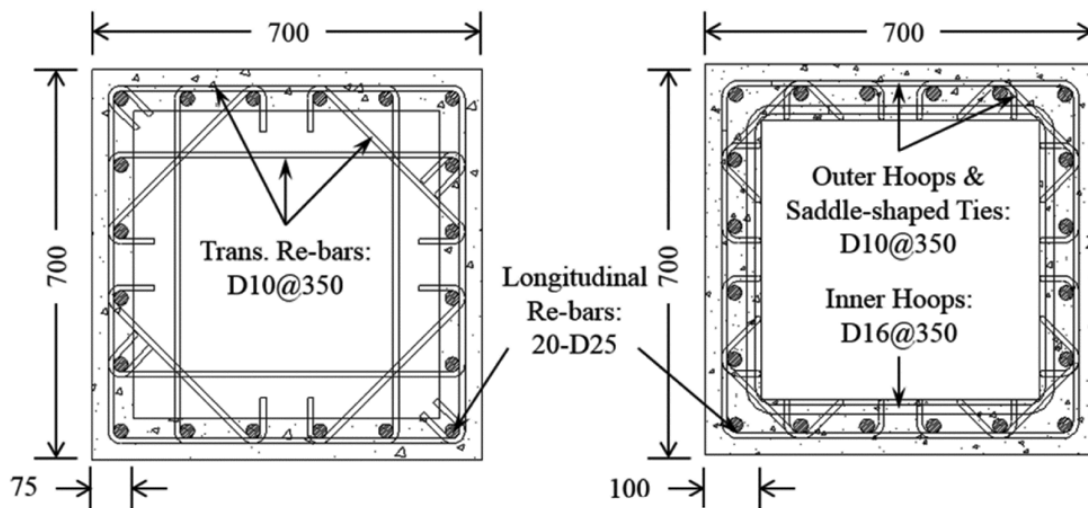


**Figure 7. Hollow Precast Concrete Columns (courtesy of Kim et al. 2016)**

Ameli et al. (2016) performed tests on seismic column-to-footing connections using grouted splice sleeves. The location of the connection is in either the column or footing, depending on the test specimen. The

grouted splice sleeves are selected to be tested because they have good construction tolerances and offer a bond-related load transfer mechanism. Figure 8 shows a typical grouted connection located in the plastic hinge of the column. To test the connections, three half-scale precast cantilever column test specimens and one cast-in-place cantilever control test specimen were tested under quasi-static cyclic loads. The results from the test demonstrated that the columns with grouted splice sleeves located in the plastic hinge of the column had a lower displacement ductility capacity compared to the conventional cast-in-place column. The results improved for the columns with grouted splice sleeves located in the footing. To expand the test results, the reinforcing bars inside of the footing were intentionally de-bonded a length equal to eight times the diameter of the reinforcing bars. Displacement ductility is any performance of the connection past the yielding point without a significant decrease in the structure, or column, lateral capacity.

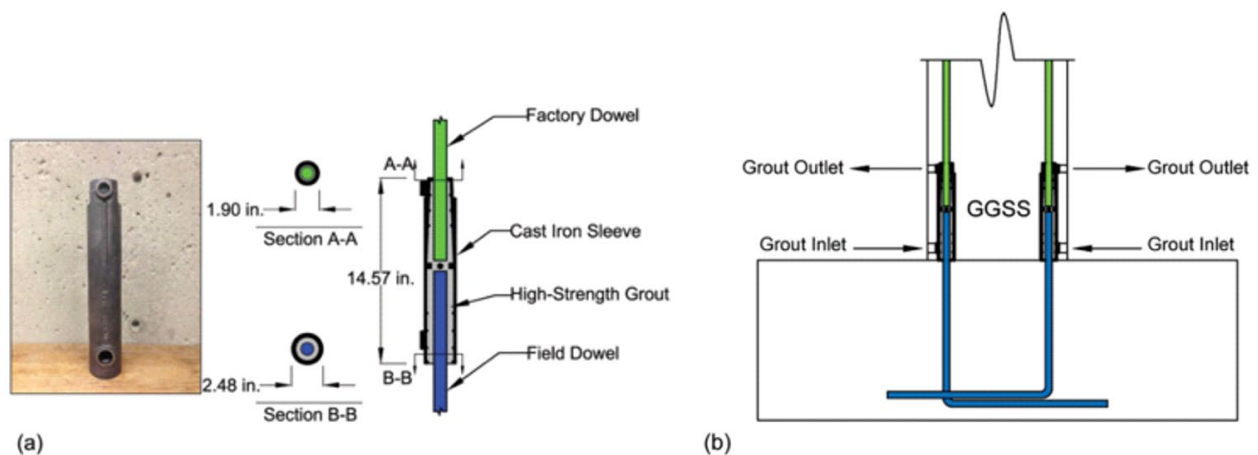


**Figure 8. Grouted Splice Sleeve Connection Located in the Plastic Hinge of the Column (courtesy of Ameli et al. 2016)**

Galvis and Correal (2017) investigated the characterization of the seismic behavior of a column foundation connection for Accelerated Bridge Construction. This research indicated that grouted duct connections have the potential to be improved. Several challenges arise during the design and construction of grouted ducts, such as construction tolerances and large diameter bars. An alternative to the grouted duct connections is a pocket connection. The pocket connection investigated is created from a corrugated steel tube and non-shrinkage grout that bonds all of the longitudinal reinforcing bars together. The benefit of using a pocket connection is large construction tolerance. A disadvantage to using a pocket connection is a large amount of connecting materials and the foundation's reinforcement details are complex. Another alternative to grouted ducts is a socket connection. A socket connection allows the column to be installed without any additional connecting members between the column and footing. To improve the bond strength of the column and footing, the pre-cast column has a roughened surface where it is in contact with the footing. A benefit of using the proposed socket connection is there are not any reinforcing bars extruding out of the base which makes transporting and handling the precast elements easier. A disadvantage of using the socket connection is the same as the pocket connection discussed prior (e.g., placing of footing rebars). A drawing of both the pocket and socket connections are shown in Figure 9.

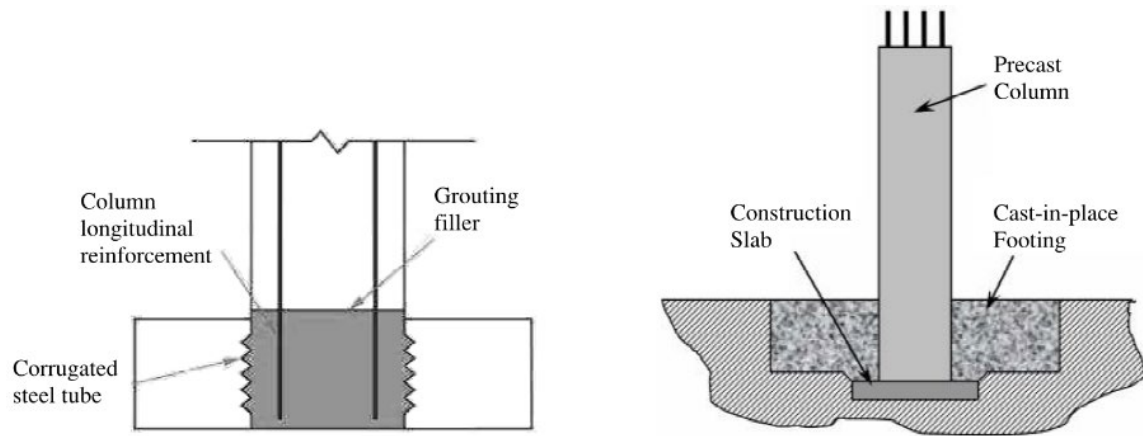


**Figure 9. Column to Footing Connection Alternatives: a) Socket Connection, b) Pocket Connection (courtesy of Galvis and Correal 2017)**

Mehraein and Saiidi (2016) examined the seismic performance of bridge column-pile-shaft pin connections. The experimental test specimens for this project are two bent assemblies. The cap beam is precast, which is connected to columns via a pocket connection. One of the columns in each of the bents is cast-in-place, while the other is constructed using a precast shell. The reinforcement for each of the columns is shown in Figure 10. The shake table testing results confirmed that the proposed precast shell design satisfies the safety and performance requirements outlined in the code.

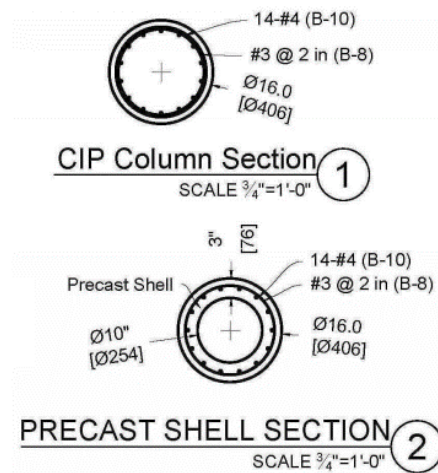


**Figure 10. CIP and Precast Bent Column Details (courtesy of Mehraein and Saiidi 2016)**

Mashal and Palermo (2019a) performed experimental work investigating a non-emulative low-damage seismic design for ABC. The project intends to minimize the amount of damage imposed on precast bridge elements during an earthquake. The experiment utilized dissipative controlled rocking connections between the precast column and the footing or cap beam as shown in Figure 11. The use of the dissipative controlled rocking connections keeps the traditional plastic hinges located at the column to footing and column to cap beam interfaces from forming. The connection utilizes an unbonded post-tensioned tendon

located inside of the precast column to encourage the column to centering itself to its original position after a seismic event. The dissipaters located on the exterior of the column are used to dissipate the seismic kinetic energy. A steel jacket armor is used to increase the confinement of the concrete and reduce any damage that may occur during a seismic event. After several cycles of quasi-static testing of the connection, there was no damage or measurable post-seismic displacement. As a result of the experiment, the design was used in the Wigram-Magdala Link Bridge located in Christchurch, New Zealand. The bridge continues to stand today after enduring through a 7.8 magnitude earthquake in 2016, just months after it was built. Although, the epicenter of the earthquake was far away from the bridge, the bridge is expected to perform well during future seismic events.



**Figure 11. Low-Damage Seismic Design (courtesy of Mashal and Palermo 2019a)**

Mashal and Palermo (2019b) also performed experimental work investigating the use of two different types of connections in a single precast column. The two connections are a member socket connection at the base connecting the columns to the footings and a grouted duct connection at the top connecting the columns to the cap beam. A half-scale test specimen is constructed with the intent to simulate a cast-in-place connection. Quasi-static cyclic loading is used during testing. The results from the experiment showed similar amounts of energy being dissipated in the plastic hinges of the columns. Several large cracks developed where the member socket connections are located and only a few large cracks at the grouted duct locations. The member socket connections exhibited a larger amount of strength deterioration than the grouted duct connections which is a result of the starter bars intentionally being de-bonded a length of 100 mm during the construction. The results indicate that including an unbonded length of the starter bars at the connection can reduce the amount of spalling and strength degradation in the plastic hinges. Figure 12 depicts an accurate representation of the tested column.

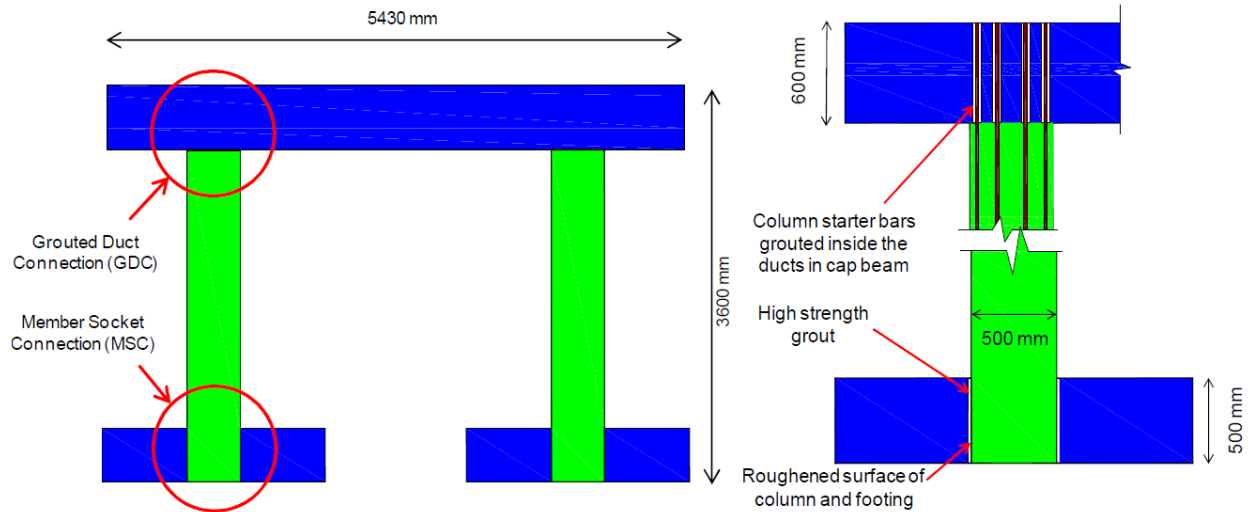


**Figure 12. Precast Bent with Member Socket and Grouted Duct Connections (courtesy of Mashal and Palermo 2019b)**

Zaghi and Saiidi (2010) experimented with the use of a pipe-pin connection. A pipe-pin connection is essentially a concrete-filled steel tube embedded at the end of a column. More details of the connection are shown in Figure 13. The observations and conclusions from this research are numerous. An observation for the experimentation is that the column can rotate significantly without altering the performance of the connection. The mode of failure that is assumed when designing the test specimens is a shear failure. However, if the pipe thickness is large the connection can fail in shear or result in bearing failure of the concrete surrounding the pipe. One of the conclusions from the experiment is that the bearing strength of concrete against the pipe is two to six times the axial compressive strength of the concrete. After the experiment had concluded, the pipe-pin connection was disassembled, and the pipes were straight, intact, and damage-free; while the steel exterior can receive small dents located where the pipe came in contact with it. The finite element analysis used to model the pipe-pin connections returned results that are within 5% of the actual experimental data.

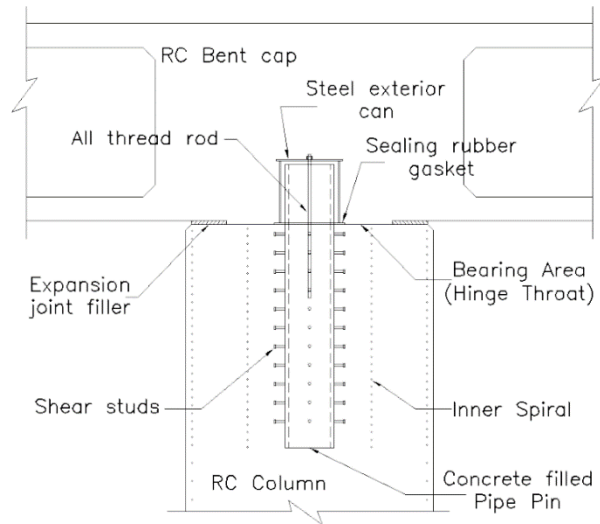


**Figure 13. Pipe-Pin Connection Detail (courtesy of Zaghi and Saiidi 2010)**

## Conclusion

A significant amount of research has been conducted to improve and expand the ABC scope and knowledge in seismic regions. The connections discussed include thin-walled steel columns, high strength precast concrete, pocket connections, socket connections, grouted ducts, grouted splice sleeves, mechanical bar splices, hollow precast reinforced concrete, precast shell column, dampers, and pipe-pin connections. Research for ABC in seismic regions continues to be performed to improve and/or simplify the construction of bridges. The research presented in this report aims to present a simple alternative to the current grouted duct, pocket, socket, and pipe-pin connections.

# 3. Experimental Investigation

## Cantilever Column: Cast-In-Place

### Introduction

This section presents the design, construction, and testing of a cast-in-place cantilever column. The purpose of a cast-in-place cantilever column is to set a benchmark to compare the experimental precast cantilever column. The design discussed in this chapter follows the 2017 AASHTO LRFD Design Specifications (AASHTO 2017). This chapter also presents a prototype structure and the testing arrangement for both the cast-in-place and precast columns.

### Prototype Structure

Details of a typical bridge located in Idaho, US-95 over US-20/26, are shown in Figure 14 and are used to determine reasonable dimensions for the prototype structure. The prototype structure can be assumed to be built in South-East Idaho which is the most seismically active region in the state. To obtain the height and diameter of the prototype structure, the typical bridge details are scaled by a factor of approximately 0.25. The 0.25 scale is used to accommodate for the height restraints within the Idaho State University Structural LAB (SLAB). Applying the approximately 0.25 scale to the typical drawings reduces the height from 40 ft-10 in. to 10 ft-2.5 in. and the diameter from 6 ft-0.75 in. to 1 ft-6.2 in., as shown in Figure 15.

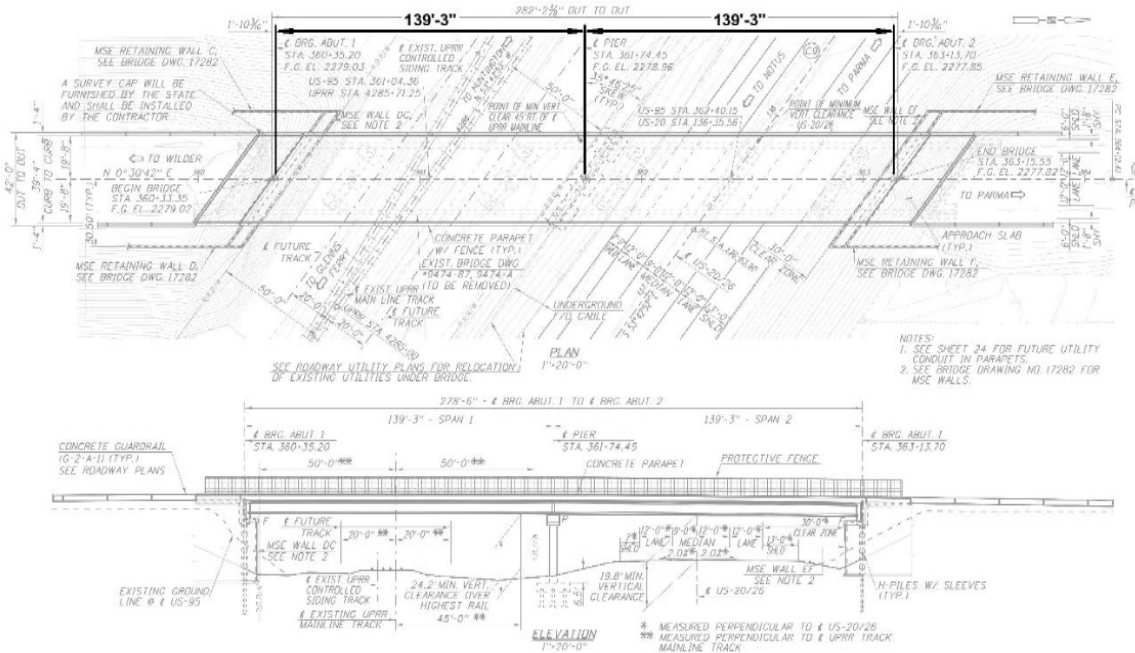
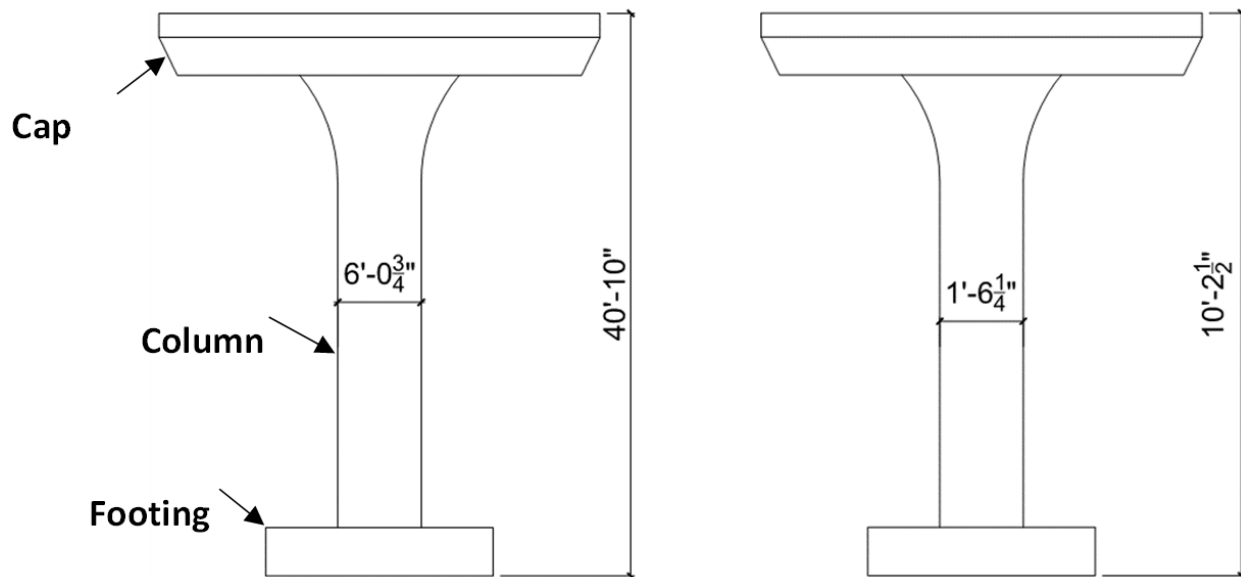


Figure 14. Detail Views of a Typical Bridge in Idaho



**Figure 15. Scaling of a Typical Column, a) Full-Scale Typical Column, b) 0.25 Scale Typical Column**

After the typical drawings are appropriately scaled, the dimensions of the prototype column and footing are determined. The prototype structure will have an overall height of 10 ft-4 in. The footing size is 4 ft. x 4 ft. x 3 ft. (L x W x H). The logic behind the proposed dimensions is a result of the SLAB's strong floor sleeve spacing and to ensure the footing will not fail before the column. The column is octagonal, having a diameter of 18 in., and a height of 7 ft-4 in. measured from the top of the footing up. Using a footing height of 3 ft., the distance from the top of the footing to the center of the actuator is 6.5 ft.

### Testing Arrangement and Design Considerations

The 0.25 (1/4<sup>th</sup>) scale cantilever columns are tested via a uniaxial lateral load. Using a uniaxial load to test the column represents a seismic event pushing and pulling the piers in the transverse direction. In this type of loading, the abutments are assumed to resist the loads in the longitudinal direction of the bridge. A 50-kip axial load is applied to the column throughout the entire testing procedure. The axial load is expected to vary slightly and is kept as close to a constant value as possible (deviation of less than approximately 5%). The deviation of the axial load is inconsequential to the testing results. This axial force corresponds to about 5% of the ultimate axial capacity of the column (axial ratio in % =  $\frac{50 \text{ kips}}{A_g f'_c} = 5\%$ ) where  $A_g$  is the gross cross-sectional area of the column and  $f'_c$  is the compressive strength of the concrete. The footing is assumed to be rigidly fixed to the ground (e.g., no soil-structure interaction). The appropriate loads are shown in Figure 16.

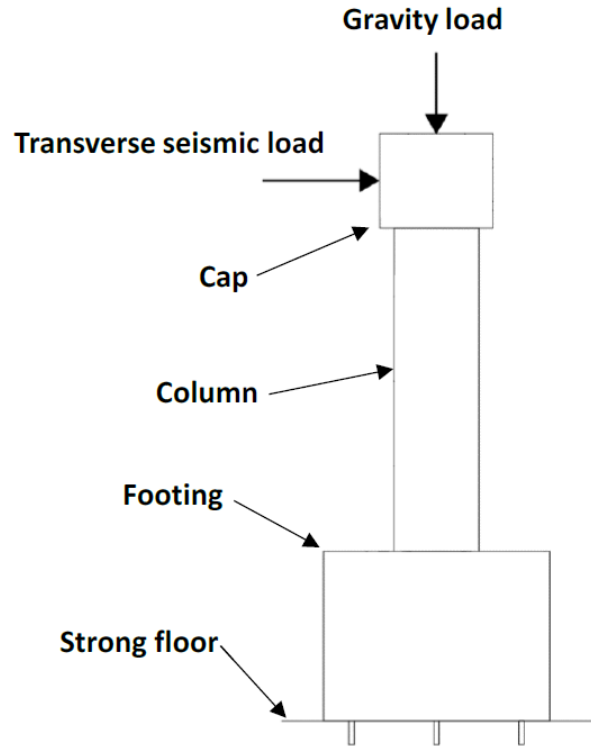


**Figure 16. Testing Arrangement**

The loading protocol established for the experiment is obtained from the American Concrete Institute (ACI) (ACI Committee 374 2013) which is a quasi-static cyclic loading protocol. The loading protocol begins at 0.5 of the yield displacements then proceeds to 1, 2, 3, 4 times of the yield displacement until failure, as shown in Figure 17.

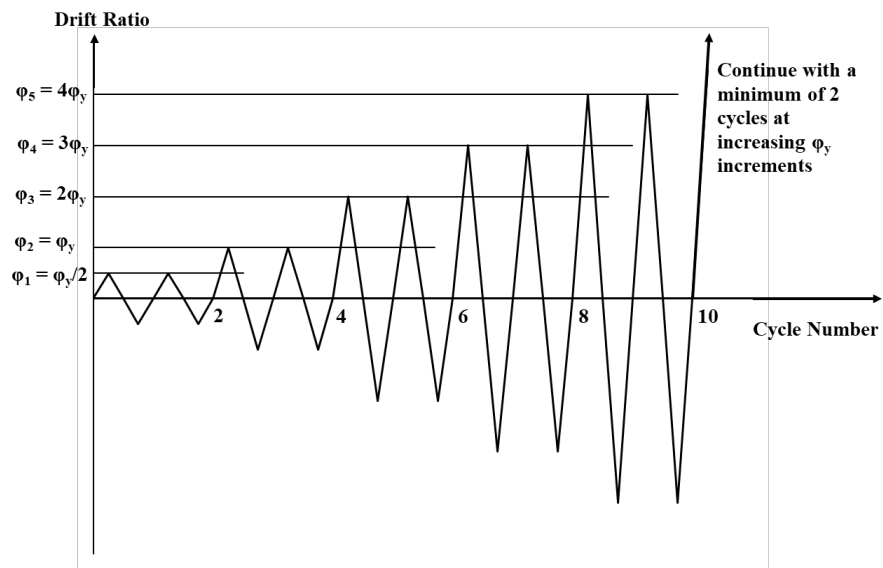


**Figure 17. ACI Testing Protocol**

The testing procedure is stopped when the column lateral capacity is reduced to 50% of the ultimate lateral force. The yield displacement is calculated using the following equation from Priestley et al. (2007):

$$\Delta_y = \frac{\varphi_y (H + L_{sp})^2}{3}$$

Where:

$\varphi_y$  = Yield curvature

H = Height of the column, inches

$L_{sp}$  = Strain penetration length, inches

The yield curvature is calculated using the equation shown below:

$$\varphi_y = \frac{2.25(F_{ye})}{E_s D}$$

Where:

$F_{ye}$  = Effective yield strength of the steel, i.e., 110% of yield strength of the steel, ksi

$E_s$  = Modulus of elasticity of the longitudinal rebars, ksi

D = Column diameter, inches

The strain penetration is calculated using the following equation:

$$L_{sp} = 0.15(F_{ye})d_{bl}$$

Where:

$d_{bl}$  = Diameter of the longitudinal rebars, inches

$F_{ye}$  = Effective yield strength of the steel, i.e., 110% of yield strength of the steel, ksi

Yield displacement equation becomes:

$$\Delta_y = \frac{0.000284 * (78 + 7.7425)^2}{3} = 0.692 \text{ in.}$$

Figure 18 shows a graphical representation of the loading protocol used during the testing procedure. The loading protocol from ACI is primarily developed for buildings. There is no load protocol for bridges at the moment because it depends on seismicity. So, the loading protocol that is used, is the minimum required from ACI. It is common in some places, e.g., Alaska uses 3-cycles; however, the idea is to account for strength degradation from the test. This can be achieved from the loading cycle as in Figure 18. The loading rate of the lateral actuator is 1 mm/sec with appropriate pauses to allow adequate time to observe and record any changes in the column during testing.

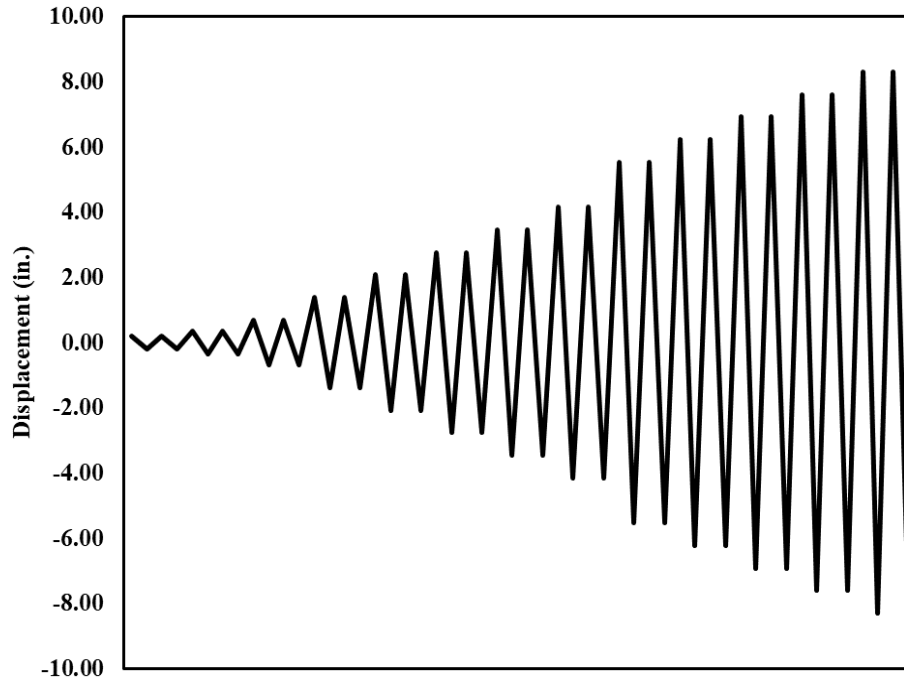


**Figure 18. Loading Protocol**

Once the dimensions of the prototype structure have been established, the reinforcing steel is appropriately selected. The design of the reinforcing steel located in the column and footing is in accordance with the 9<sup>th</sup> edition of AASHTO LRFD Bridge Design Specifications (AASHTO 2020).

The column base shear is selected so it does not exceed the capacity of the equipment in the SLAB. The base shear force has been selected to be 25-kip. Using this base shear, the longitudinal reinforcing has been determined to be twelve #6 rebar equally spaced in a circular pattern. For confinement purposes, a spiral having a pitch of 1.5 in. is used along the entire length of the column except where the footing reinforcing crosses the longitudinal bars. Where the footing reinforcement crosses the longitudinal bars, a mechanical splice is used on each side of the reinforcing bars. The minimum cover requirements of the spiral are 1.5 in. Guidelines on rebar hooks, bends, and development lengths are conservatively considered with all the rebar in the column.

The footing has reinforcing bars in each direction on both the top and bottom using #6 rebar. The rebar will have a spacing of roughly 3.5 in. between parallel bars and a minimum cover of 2 in. Guidelines on rebar hooks, bends, and development lengths are conservatively considered with all the rebar in the footing.

The moment capacity of the proposed cantilever column has been determined for a base shear of 25-kip. In the calculations, an 18 in. diameter column having 1.5 in. of cover, twelve #6 rebar, with #3 spirals are used. The compression strength of concrete,  $f'_c$ , is taken to be 4 ksi. The rebar properties are 60 ksi for the yield strength and 29,000 ksi for the modulus of elasticity. Using Response-2000 and SAP-2000 the yield moment capacity of the round column is calculated to be approximately 165 kip-ft without an axial load.

Adding the 50-kip vertical axial force the moment capacity of the column increases to 187 kip-ft. A comparison of the two programs, before the axial load, is shown in Figure 19. Using a moment arm of 6.5 ft., the shear demand from the moment capacity is approximately 25-kip which is the targeted base shear.

Referring to Figure 19, the reason why Response-2000 obtained a lower curvature is that the program does not have the capability to introduce spiral stirrups. Response-2000 thinks of the shear reinforcing as hoops compared to spirals which provide more confinement and ductility. Response-2000 does not have a confined model and is not typically used for seismic. In terms of capacity, the values from both programs are comparable. It should be noted that SAP-2000 uses a fiber model to compute the moment-curvature. A fiber model is a model with the capacity to perform an analysis with nonlinear behavior distributed across the cross-section of the element in the model.

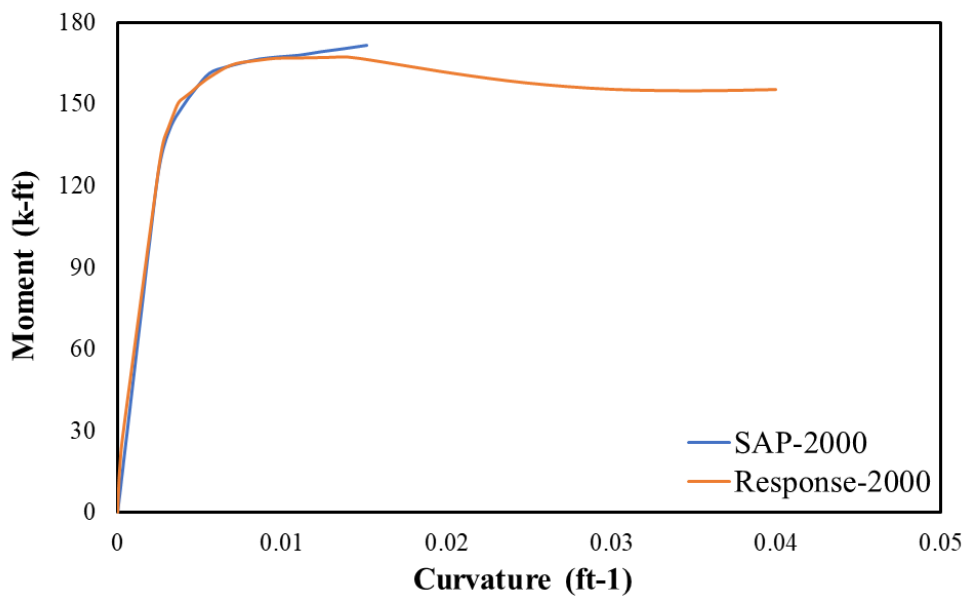


**Figure 19. Comparison of SAP-2000 and Response-2000**

The parameters used to calculate the moment capacity of the footing are  $f'_c$  equal to 4 ksi, ten #6 rebars in both the top and bottom reinforcing layers with 2 in. of cover, rebar yield strength of 60 ksi, and a modulus of elasticity of 29,000 ksi. Using these values, the moment capacity is calculated to be 1,000.2 and 998.5 kip-ft using SAP2000 and Response2000, respectively. An image depicting the footing is shown in Figure 20.

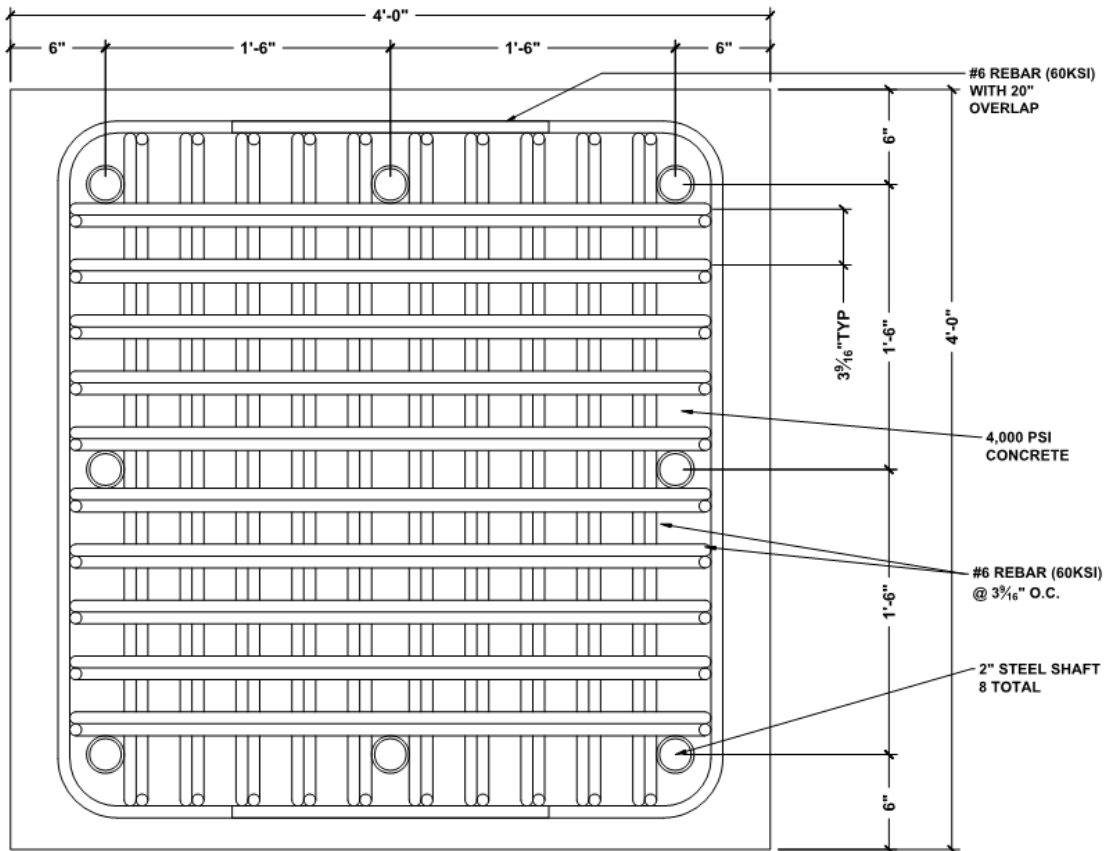


**Figure 20. Cast-In-Place Footing Reinforcing Rebar Layout**

In summary, the column is octagonal with a diameter of 18 in. The longitudinal reinforcement is comprised of twelve #6 rebar equally spaced and a #3 spiral having a pitch of 1.5 in. to confine the concrete. The calculated moment capacity of the column has been determined to be 165 kip-ft.

The footing is 4 ft. x 4 ft. x 3 ft. with ten #6 rebar reinforcing the top and bottom in each direction while maintaining a spacing of approximately 3.5 in. between the bars and 2 in. of cover. The moment capacity of the footing has been calculated to be roughly 1,000 kip-ft. Comparing the column moment capacity to the footing moment capacity, the column should reach its ultimate strength before the footing is yielded. Figure 21 provides a visual representation of the test specimen.

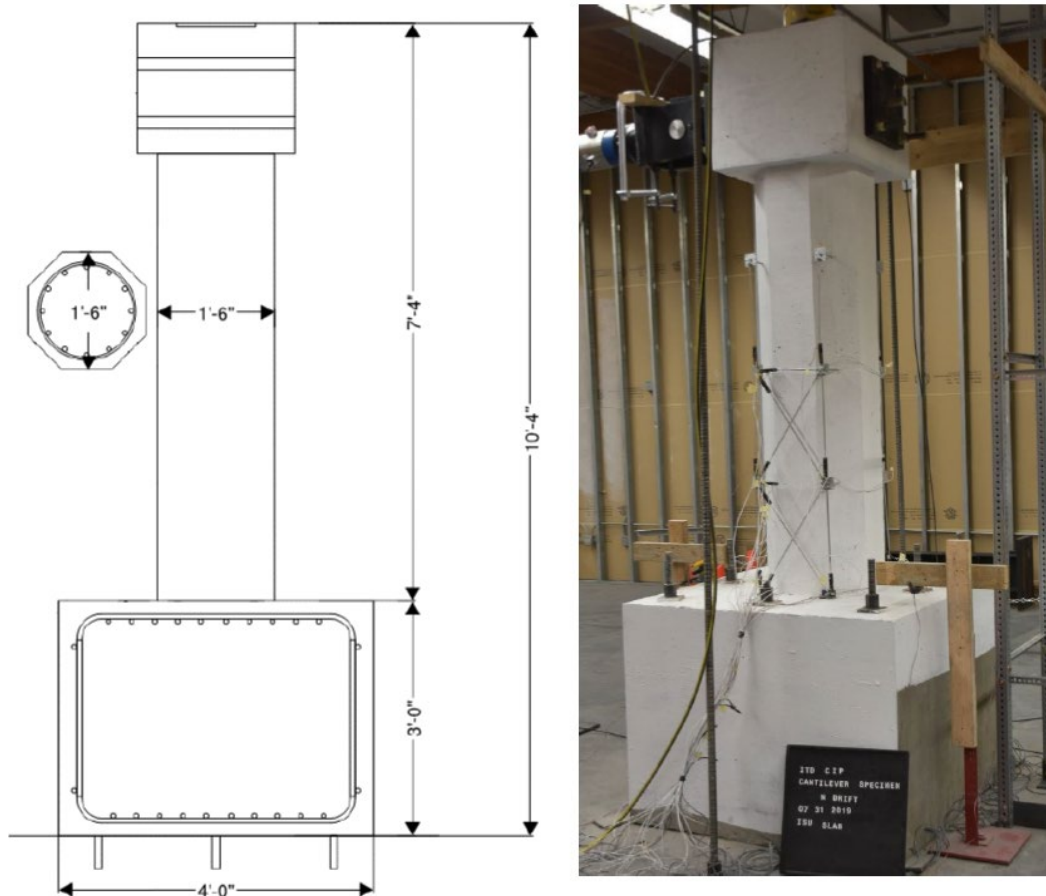


**Figure 21. Cast-In-Place Test Specimen**

## Construction

Now that the design criteria have been determined, the construction of the cast-in-place cantilever column is next. To begin, the formwork is built. After the formwork is complete, rebar is cut to the required lengths and bent appropriately. Next, the rebar is tied together, and the formwork is secured around the tied rebar (Figure 22a). Once the rebar and formwork are set, the concrete for the column footing is poured via Pocatello Ready Pour and ISU civil engineering students as shown in (Figure 22b). The footing is allowed to cure for three days before the formwork is removed. After the formwork is removed the concrete is covered with burlap and plastic and wetted daily to allow the concrete to continue curing in the most ideal conditions (Figure 22d). Once the footing reached seven days of curing, the footing is moved to the structural laboratory, the column formwork is assembled, column cap reinforcement is tied in place, then the column concrete is poured (Figure 22e). The column is allowed to cure for three days, then the formwork is removed. The column is then covered with burlap and plastic to ensure ideal curing conditions are present for 28 days. After the 28 days, the column is uncovered, painted, and instrumented in preparation to be tested. Images of the construction progress are shown in Figure 22.



**Figure 22. CIP Construction: a) Completed Rebar Cage, b) Footing Pour, c) Finished Footing, d) Footing Curing, e) Column Formwork Setup, f) Finished Test Specimen**

## Material Properties

The 28-day compressive strength of concrete,  $f'_c$ , is designed to be 4,000 psi. The yield strength of the longitudinal and transverse reinforcement of the rebar is 60,000 psi with a modulus of elasticity of  $29 \times 10^6$  psi. The actual compressive strength of the concrete on the test day is summarized in Table 3.

**Table 3. Actual  $f'_c$  values (psi)**

	Test 1	Test 2	Test 3	Test 4	Average
Footing	3,980	4,740	4,450	5,330	4,630
Column	5,280	4,680	4,970	4,460	4,850

## Test Setup and Instrumentation

A Campbell Scientific data acquisition system is used to collect important data points from the instruments such as load cells, strain gauges, and linear potentiometers to analyze data after the testing procedure. A total of 39 instruments are used and are discussed in the following paragraphs and summarized in Figure 23. The testing arrangement is shown in Figure 24.

The lateral and vertical loads are measured using load cells. The lateral load cell is mounted between the hydraulic ram and the end of the actuator. The vertical load cell is mounted between a hydraulic jack and a steel beam which is resisting any vertical movement of the hydraulic jack.

Lateral displacement at the top of the column is measured by string potentiometers shown as “IPC”, “OPC”, and “ASP” in Figure 23 and representing in-plane, out-of-plane, and actuator displacements, respectfully. The string potentiometers are mounted to a steel structure that is independent of the testing arrangement. Each of the instruments is connected to the column at the centerline of the actuator.

The footing displacement is monitored using horizontally and vertically mounted string potentiometers shown as “FHI”, “FHO”, “FVN” and “FVS” in Figure 23 and representing footing horizontal in-plane, footing horizontal out-of-plane, footing vertical on the north end, and footing vertical on the south end of the footing, respectfully. The string potentiometers are also mounted independently of the testing arrangement. String potentiometers are positioned on the footing to measure any sliding or rocking of the footing that may occur. Data collected from these instruments are used to correct the lateral displacement at the top of the column.

The column deformation is obtained by using rod potentiometers, these are shown as “A”, “B”, and “C” symbols in Figure 23. The rod potentiometers are attached to the face and back of the column in three distinct zones: Zone A measured from the top of the footing to 18 in., Zone B measured from 18 in. to 36 in., and Zone C measured from 36 in. to 54 in. This deformation data is used to calculate the curvature of the section up the height of the column.

Elongation of the rebar within the column is monitored by strain gauges. The strain gauges are attached to the longitudinal rebar at the column to footing interface before pouring the concrete.

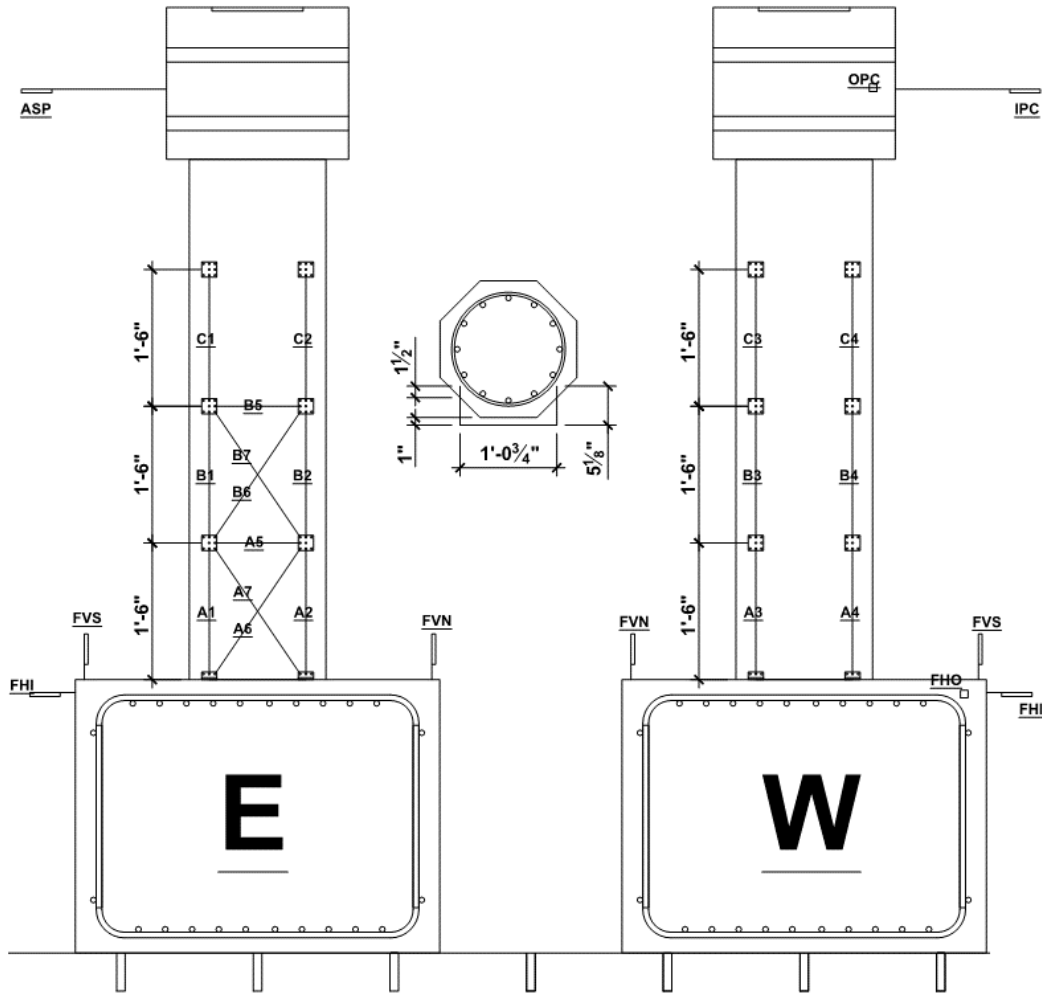
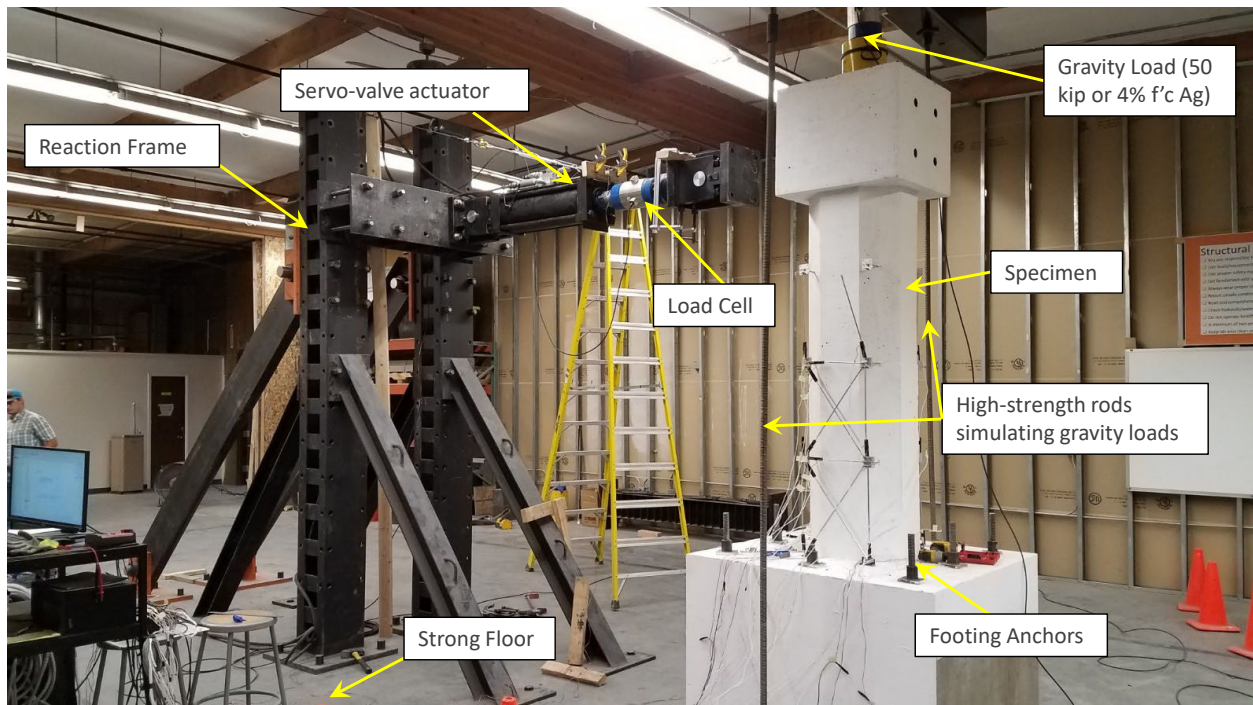


Figure 23. Column Instrumentation



**Figure 24. Typical Test Setup with Load Cells**

## Testing Results

On the first cycle, hairline cracks appeared on the column within the first 0 – 18 in. from the base of the column where the plastic hinge is expected to form. During the second cycle, hairline cracks spread into the 18 – 36 in. of the column. By the third cycle, hairline cracks spread above the 36 in. mark and other lower cracks continued to spread and get larger. On the fourth cycle, a crack approximately 1mm wide is seen at the column-footing interface. During the fifth and sixth cycles, cracking continued to develop with the base crack opening up to 4mm and the concrete began to spall. For the eighth, ninth, tenth, and eleventh cycles; all of the cracks continued to develop and the column concrete near the footing had all spalled off. During the twelfth cycle, there was a loud pop followed by a significant drop in lateral force. The drop-in force was not significant enough to discontinue the test. The thirteenth cycle resulted in two additional loud pops which are followed by a significant drop in lateral force. The drop in lateral force was significant enough to terminate the testing procedure. The loud pops are a result of a longitudinal rebar breaking and the locations where they occurred are shown in Figure 25. Figure 26 shows images of the lower half of the column during the testing procedure.

Throughout the testing procedure, the programmed displacement is not the actual displacement of the column. As a result of this, there is a cycle missing between cycles eight and nine to achieve the desired displacement. One of the reasons why the programmed displacement values are not the same as the actual values is because during the testing procedure the reaction frame is deflecting. Another reason is that the footing is sliding a little throughout the testing procedure. The sliding of the footing is documented via

the instruments placed on the footing before the testing procedure. Using the collected data, the sliding of the footing is removed from the column displacement to obtain the column displacement relative to the footing. A summary of the loading protocol is shown in Table 4.

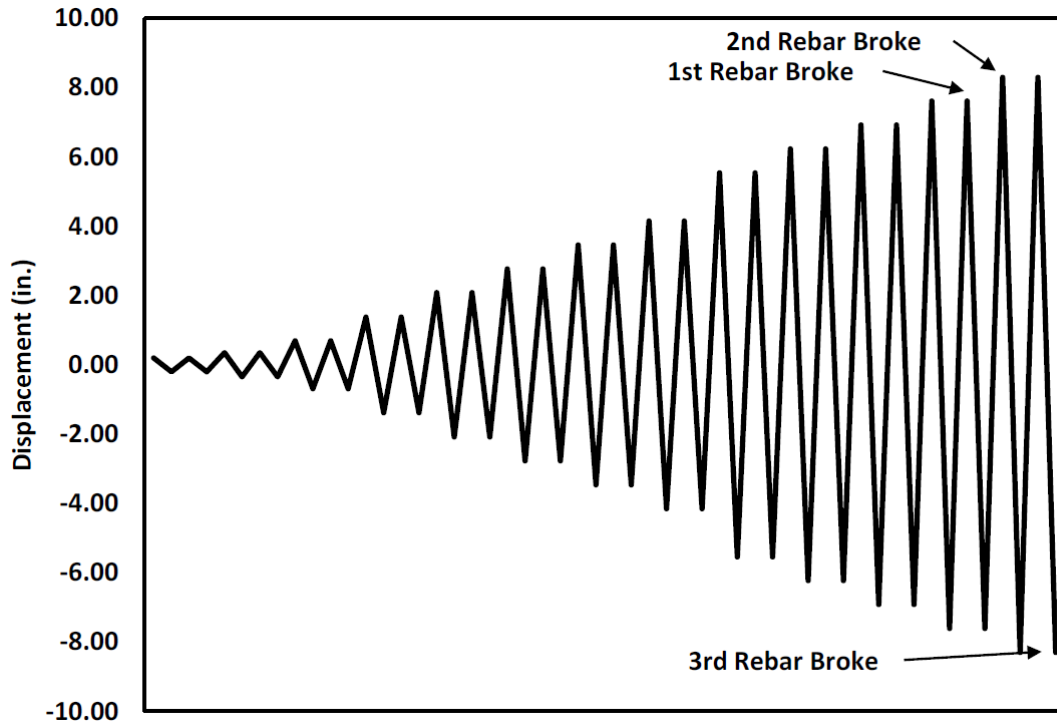


**Figure 25. Loading Protocol for the Cast-In-Place Column**

**Table 4. Summary of the Cast-In-Place Loading Protocol**

Cycle	Programmed Displacement (in.)	Programmed Drift (%)	Actual Displacement (in.)	Actual Drift (%)
1	0.20	0.26	0.16	0.20
2	0.35	0.45	0.26	0.33
3	0.69	0.88	0.46	0.59
4	1.38	1.77	0.86	1.10
5	2.08	2.67	1.50	1.93
6	2.77	3.55	2.15	2.76
7	3.46	4.44	2.84	3.64
8	4.15	5.32	3.50	4.49
9	5.54	7.10	4.86	6.23
10	6.23	7.99	5.54	7.10
11	6.92	8.87	6.23	7.99
12	7.61	9.76	6.94	8.90
13	8.30	10.64	7.71	9.89

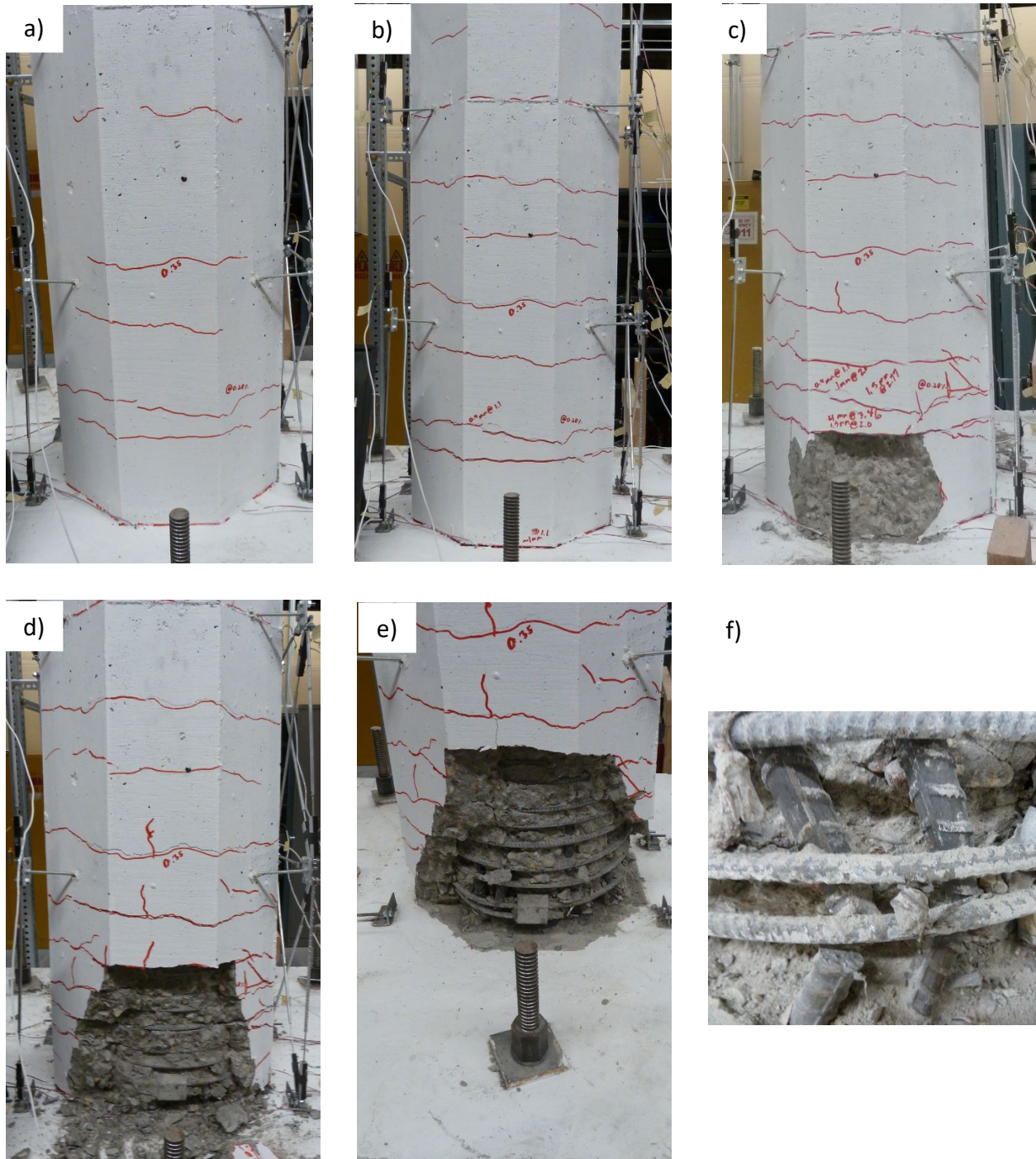


**Figure 26. CIP Specimen at a) 0.45% drift, b) 2.67% drift, c) 5.32% drift, d) 8.87% drift, e) 10.64% drift, f) Ruptured Bar**

After the testing procedure has concluded the data is analyzed. The maximum displacement of the column during the testing procedure is 7.7 in. The maximum load applied to the column during the testing

procedure is 37.8 kip which corresponds to a 245.7 kip-ft moment capacity. Plots showing the Force vs. Displacement and Drift during the test are shown in Figure 27 and Figure 28, respectively. These plots show the yield displacement of the column and the corresponding base shear. The column reached its design flexural capacity at 25-kip and behaved in a ductile manner. Rebar ruptures can be identified on the plots as a sudden reduction in capacity in the first quadrant. The backbone curve is also shown in Figure 29. Table 5 and Table 6 show significant values from the cast-in-place column testing procedure.

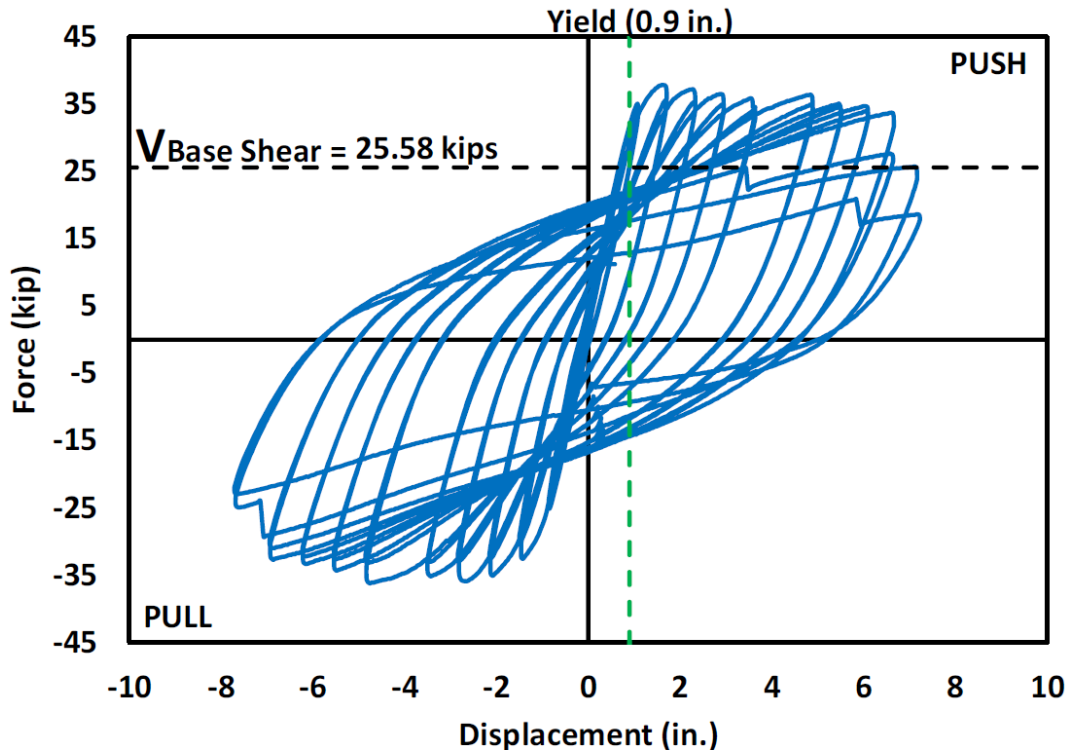


Figure 27. Force vs. Displacement Plot for the Cast-In-Place Column

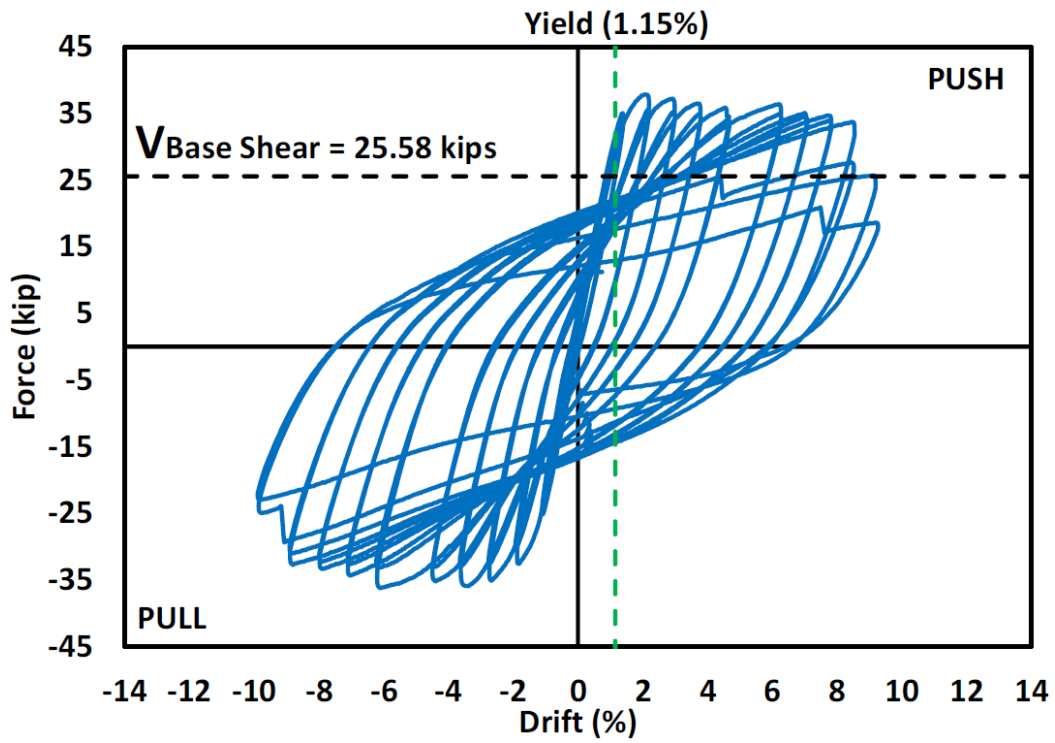


Figure 28. Force vs. Drift Plot for the Cast-In-Place Column

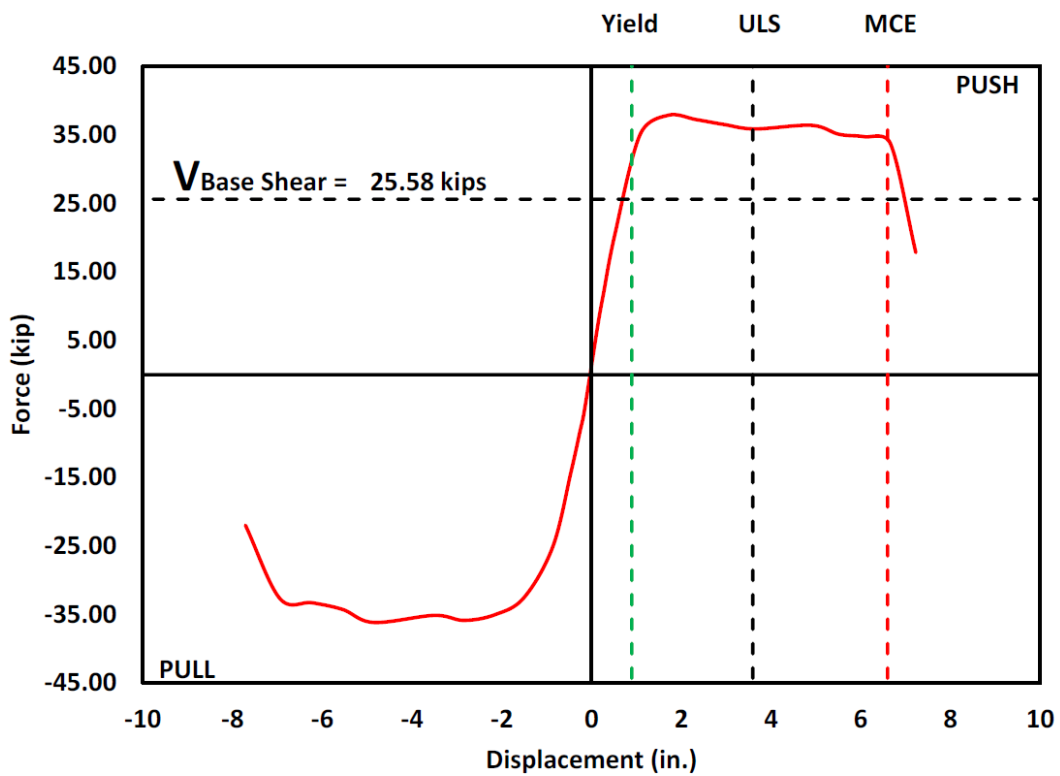


Figure 29. Backbone Curve for the Cast-In-Place Column

**Table 5. Damage Observation from Testing of the CIP Column, Drift %**

Cracking	Spalling	1 <sup>st</sup> Bar Rupture	2 <sup>nd</sup> Bar Rupture	3 <sup>rd</sup> Bar Rupture	End of Testing
0.2 %	4.49%	8.9%	9.89%	9.89%	9.89%

**Table 6. Summary of the Performance Points from Testing of the CIP Column**

Yielding Predicted Drift (%)	Yielding Predicted Base Shear (kips)	Yielding Experimental Drift (%)	Yielding Experimental Base Shear (kips)	Ultimate Strength Experimental Drift (%)	Ultimate Strength Experimental Base Shear (kips)	Ultimate Strength Experimental Ductility*
0.88	25.58	1.15	35.1	9.89	37.8	7.4

Note: \*Displacement ductility ( $\mu$ ) was 7.4 at the end of testing

The distribution of curvature along the height of the first 54 in. of the column is shown in Figure 30. The column is expected to yield and fail within the plastic hinge of the column. The plastic hinge is calculated by the following equation from Priestley et al. (2007):

$$L_p = 0.08H + l_{sp}$$

Where:

H = Height of the column, inches

$l_{sp}$  = Strain penetration length, inches

Strain penetration can be calculated using the following equation from Priestley et al. (2007):

$$l_{sp} = 0.15F_{ye}d_{bl}$$

Where:

$F_{ye}$  = 1.1 times the longitudinal bar yield strength, ksi

$d_{bl}$  = Diameter of the longitudinal bar, inches

Using a yield strength of 60 ksi and a bar diameter of 0.75 in, the strain penetration becomes 7.4 in. Using a column height of 78 in. the plastic hinge can be calculated to be 13.7 in. Figure 30 shows that yielding occurred in the bottom 18 in. of the column. From 18 in. to 36 in. the column approached the yield point but never reached it. Because the region from 18 in. to 54 in. never reached the yield point, this region essentially remained elastic throughout the testing procedure.

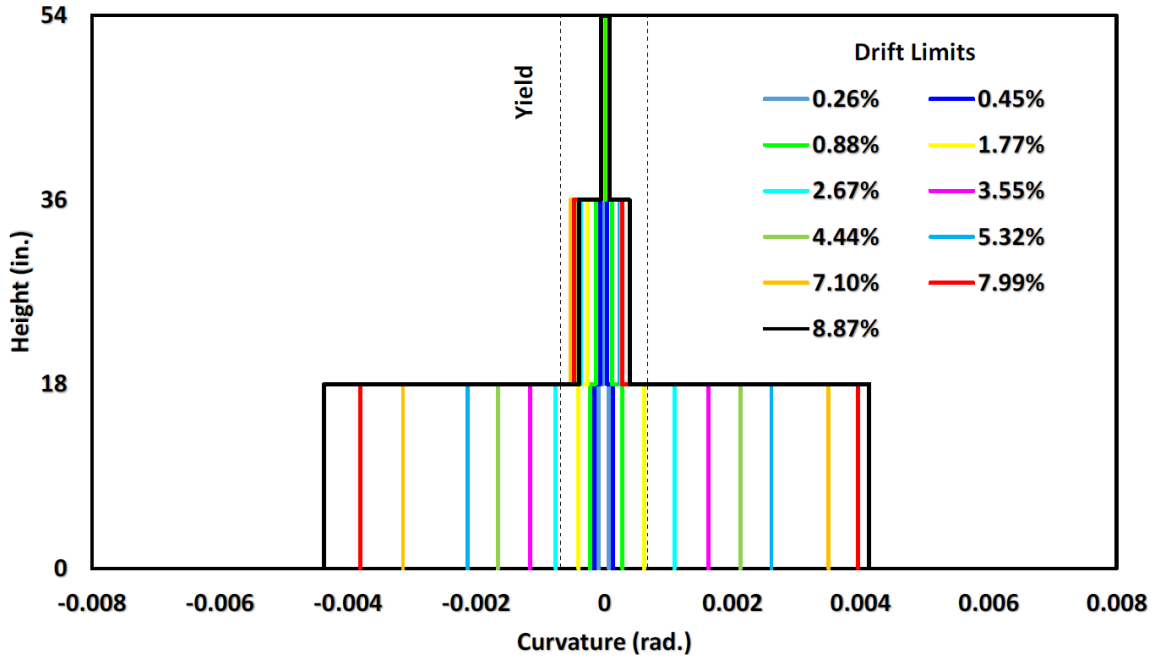


**Figure 30. Cast-In-Place Curvature Distribution**

The dissipated energy plot is shown in Figure 31. The dissipated energy is obtained by finding the area of each loop in the force versus displacement plot. The area is obtained using a MATLAB program. Each of the loops represents the total energy dissipated in a single cycle. Using input units of newtons and meters, the output energy units are of joules. For each drift cycle, the first loop dissipated more energy than the second because the column becomes weaker with each push-pull cycle. The largest difference in dissipated energy occurred during the 12<sup>th</sup> and 13<sup>th</sup> cycles which corresponds to the longitudinal rebars rupturing. The total dissipated energy during the testing procedure is 336,328 ft-lb (456 kJ).

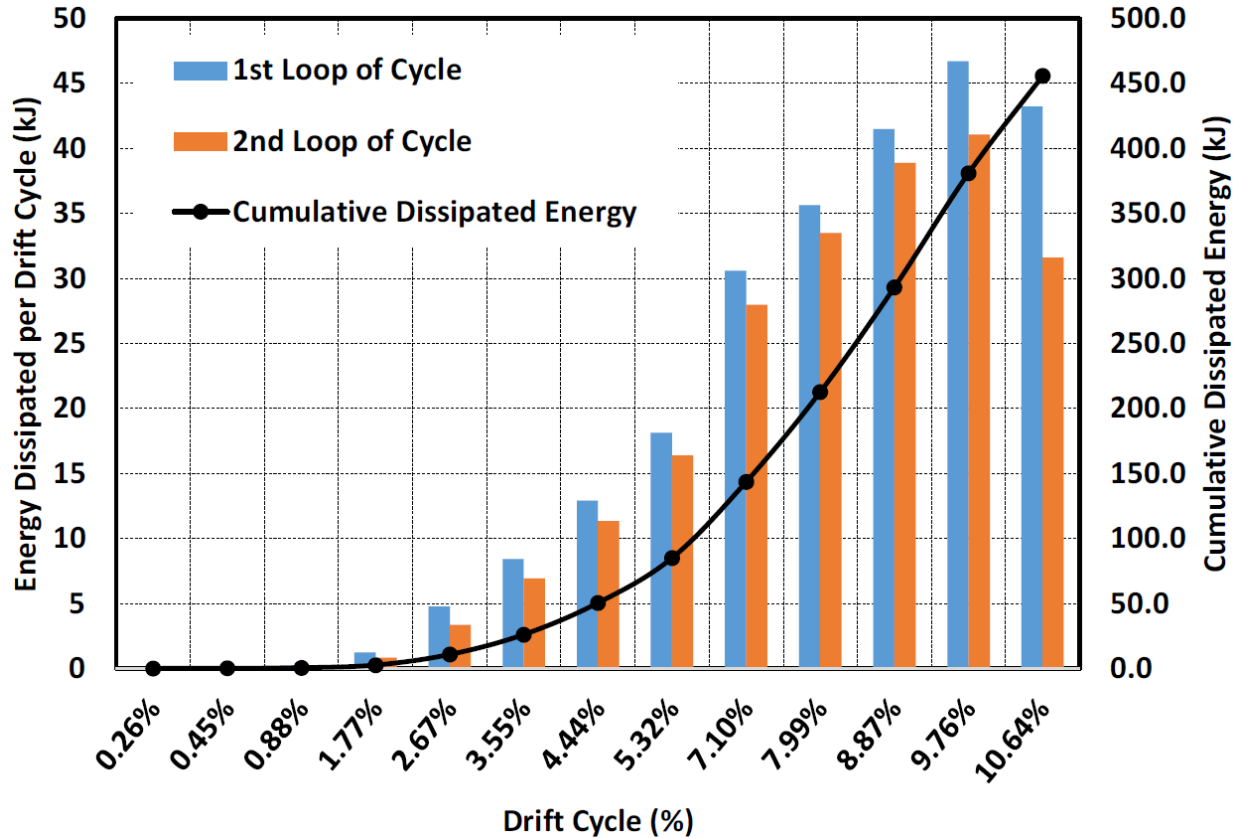


Figure 31. Dissipated Energy Plot for the CIP Column (1 kJ = 737.56 ft-lb)

The area-based hysteretic damping is calculated using the following equation from Chopra (2017):

$$\xi_{area-based} = \frac{A_h}{2\pi F_m \delta_m}$$

Where:

$A_h$  = Area of a loop in the force vs. displacement plot, N-m

$F_m$  = Maximum force in the loop, N

$\delta_m$  = Maximum displacement in the loop, mm

To compare the hysteretic damping values to a theoretical model, a correction factor should be applied to convert the values to an equivalent time-history-calibrated hysteretic damping. The equation used to convert the area-based damping values to the time-history-calibrated hysteretic damping values is shown below from Priestley et al. (2007):

$$\xi_{hyst} = \xi_{area-based} [-0.018\xi_{area-based} + (0.0875\mu + 0.723)]$$

Where:

$\mu$  = Displacement ductility

$\zeta_{area-based}$  = Area based hysteretic damping

Displacement ductility is used to characterize the seismic response of a structure (Vielma and Mulder 2017) and is calculated using the following equation from Priestley et al. (2007):

$$\mu = 0.01(\%Drift) \frac{H}{\Delta_y}$$

Where:

- $\mu$  = Displacement ductility
- H = Height of the column, m
- $\Delta_y$  = Yield displacement, m

A corrected area-based hysteretic damping plot is shown in Figure 32. As a comparison, the Takeda Fat, Takeda Thin, Elastic-Perfectly Plastic (EPP), and Ramberg-Osgood (RO) models have also shown in Figure 32. The Takeda Fat model represents a ductile reinforced concrete frame structure. The Takeda Thin model represents a ductile reinforced concrete wall or column structure. The Elastic-Perfectly Plastic (EPP) model represents an elastic model and the Ramberg-Osgood (RO) model represents a ductile steel structure (Priestley et al. 2007). The equivalent viscous damping coefficients used are summarized in Table 7 which are used in the following equation to obtain the hysteretic damping models from Priestley et al. (2007):

$$\xi_{hyst} = a \left( 1 - \frac{1}{\mu^b} \right) \left( 1 + \frac{1}{(T_e + c)^d} \right)$$

Where:

- $\xi_{hyst}$  = Hysteretic damping
- $T_e$  = Effective period representing one column, 1 sec
- $\mu$  = Displacement ductility

**Table 7. Equivalent Viscous Damping Coefficients for Hysteretic Damping Component**

Model	a	b	c	d
EPP	0.224	0.336	-0.002	0.250
Takeda Thin	0.215	0.642	0.824	6.444
Takeda Fat	0.305	0.492	0.790	4.463
Ramberg-Osgood	0.289	0.622	0.856	6.460

Figure 32 shows the cast-in-place column having a relatively linear trend between the displacement ductility and the hysteretic damping. The hysteretic damping is approximately equal to the Takeda Thin model until a displacement ductility of 3.5. The cast-in-place column hysteretic damping curved achieved a value of 24.7% when the testing procedure is terminated.

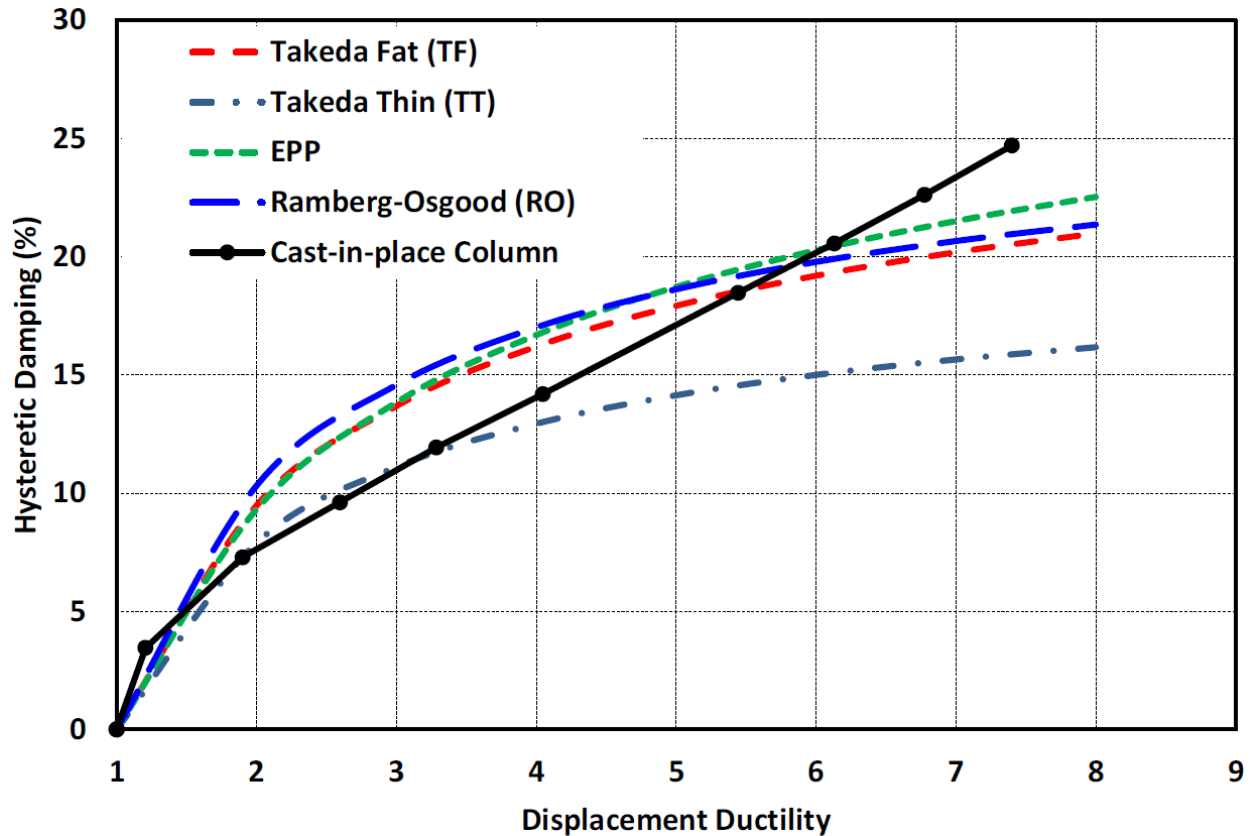


Figure 32. Corrected Area-Based Hysteretic Damping for the CIP Column

## Summary

The cast-in-place specimen is intended to be the benchmark for the precast solution. The cast-in-place column is designed following the latest version of the AASHTO LRFD Bridge Design Specifications. The footing and column are constructed using traditional methods and materials. The column is tested under quasi-static loading until failure. The column behaved in a ductile manner. The column achieved its design base shear of 25-kip. The maximum base shear obtained during the testing procedure is 37.8-kip. The maximum displacement achieved is 7.7 in. which corresponded to a ductility of just below 7.5. Damage to the column during the test is within the first 18 in. of the column which is the expected plastic hinge length for a well detailed and confined section. The total energy dissipated during the testing procedure is 456 kJ. A hysteretic damping plot showed that the column had similar values to a Takeda-Thin model up to a displacement ductility of slightly lower than 3.5. Above that, the column had higher values of hysteretic damping compared to a Takeda-Thin model.

# Cantilever Column: Precast

## Introduction

This section presents the design, construction, and testing of a precast cantilever column. The precast cantilever column is intended to have the same capacity as the cast-in-place column in terms of resisting lateral force and drift capacity. Using precast elements will increase the rate of construction and reduce overall construction costs. One of the foreseeable issues is with regards to the proper alignment of the hollow structural section (HSS) made from steel that is incorporated into the design of the column. Proper alignment is crucial because small errors can have a significant impact during the assembly of the precast members. The design discussed in this chapter closely follows the 2019 WSDOT Bridge Design Manual (WSDOT 2019). The overall structural dimensions, testing arrangement, and instrumentation are identical to the cast-in-place column.

## Overview

As shown in Figure 1 of Chapter 1: Introduction, the pipe connection incorporates two HSS members which is a representation of the pipe connection assembly. One of the HSS members is installed at the end of the precast column and the other is embedded into the footing. Approximately half of the column HSS is extending out of the precast column and with centering fins welded to the outside edge of the pipe and provides flexural capacity, shear capacity, and confinement for the concrete at the plastic hinge zone. The centering fins are for inserting the column into the footing and are not structurally important. Headed rebars are used to develop the strength of the rebar during a seismic event. Inserting the precast column into the footing is made possible by the footing HSS member. The footing HSS member will remain hollow until the column is inserted into it. An unbonded length on the column HSS member is provided to reduce the stresses in the HSS member and emulate a cast-in-place behavior.

An elastomeric bearing pad is placed between the column and footing to eliminate any undesired concentrated loading between the two elements and allows the column to rock during smaller earthquakes to prevent cracking. After the protruding HSS column member has been inserted into the footing HSS member, the remaining voids between the two elements are filled using a non-shrinkage grout via PVC pipes strategically placed to allow the grout to fill all the desired voids without compromising the integrity of the footing or column before the grouting procedure. The grout is poured or pumped into the grout inlet pipe while the grout vent provides an escape for air that would otherwise be trapped. The gap between the two HSS members is approximately 1 in. to 2 in. to ensure the grout performs properly. Any of the rebars in the footing that are impeded by the HSS member in the footing are terminated using a welding bar coupler or hooks. The column and footing design that is not impeded by the HSS members follows the AASHTO LRFD Bridge Design Specifications (AASHTO 2017).

## Material Properties

For the proposed pipe connection, WSDOT design manual (WSDOT 2019) was referred. The WSDOT design manual (WSDOT 2019) specifies materials to be used in the design of the concrete-steel tube members. First, the concrete should be class 5000P which is 5,000 psi concrete. The second material specification is to use ASTM A 709 GR 50 steel. ASTM A 709 GR 50 steel has a specified tensile strength of 65,000 psi and a yield strength of 50,000 psi (Chapel Steel 2018).

In this study, the 28-day compressive strength of concrete ( $f'_c$ ) is 4,000 psi. Through trial and error, the HSS member selected to obtain a moment capacity approximately equal to the cast-in-place member is HSS8.625x0.625. The properties of an HSS8.625x0.625 member is 42,000 psi yield strength ( $F_y$ ), 58,000 psi ultimate strength ( $F_u$ ), and a modulus of elasticity ( $E$ ) of  $29 \times 10^6$  psi. The dimensions of the HSS member are 8.625 in. for the outside diameter and a pipe thickness of 0.581 in. The actual compressive strength of the concrete and grout on the test day is summarized in Table 8.

**Table 8. Actual  $f'_c$  Values for the Precast Column (psi).**

Element	Test 1	Test 2	Test 3	Average
Footing/Column	3,800	4,180	3,930	3,970
Grout	5,410	5,420	5,370	5,400

## Design of Precast Specimen

The Concrete Filled Steel Tube (CFST) at the interface of the column and footing (e.g., where the CFST is unbonded) is the ductile link. This section is designed to provide flexural and shear capacities as well as confinement for the plastic hinge. The footing and the section of the column above the unbonded region are designed to remain elastic. For a simplified approach, the contribution of the unconfined cover concrete towards the flexural resistance of the CFST section is ignored. The size of the CFST for the ductile link was selected to closely match the flexural capacity of the cast-in-place specimen (e.g., similar base shear).

The flexural design procedure for CFST has several resistance factors to use for a variety of situations. The resistance factor used in this design is equal to one, which is used for an extreme event limit state. To ensure the pipe is not subject to local buckling before developing the strength of the pipe, the WSDOT (2019) advises the use of the following equation for members subject to plastic forces:

$$\frac{D}{t} \leq 0.15 \frac{E}{F_y}$$

Where:

D = Outside diameter, inches

t = Wall thickness of HSS member, inches

For the selected HSS member the D/t is equal to 14.85 and  $0.15E/F_y$  is equal to 103.57. In common practice, both D and t should be adjusted for corrosion but due to the short life of the testing timeline, this is considered irrelevant. Most importantly, the equation from WSDOT (2019) was adopted in this research for CFST to be used in columns and not piles. The nominal compressive strength of the concrete filled HSS member is determined by using the following equation:

$$P_0 = 0.95f'_c A_{concrete} + F_{y,steel} A_{steel}$$

Where:

$f'_c$  = Compressive strength of a concrete, ksi

$A_{concrete}$  = Area of concrete, in<sup>2</sup>

$A_{steel}$  = Area of steel, in<sup>2</sup>

$F_{y,steel}$  = Yield strength of the steel, ksi

For the selected HSS member  $P_0$  has been calculated to be 949 kips. The equation used to determine the nominal moment capacity is shown below:

$$M_n(y) = \left( c(r_i^2 - y^2) - \frac{c^3}{3} \right) * 0.95f'_c + 4ct \frac{r_m^2}{r_i} F_y$$

Where:

$c$  = One half cord length of the compressive block

$r_i$  = Mean radius of internal reinforcement, in

$r_m$  = Mean radius of HSS member, in

$y$  = Vertical distance of neutral axis from center of HSS in plastic stress distribution method, in

$f'_c$  = Compressive strength of the concrete

$t$  = thickness of HSS member

$c$  is calculated using:

$$c = r_i \cos \theta$$

Where:

$r_i$  = Mean radius to the inside of the steel tube

$\theta$  is calculated using:

$$\theta = \sin^{-1} \left( \frac{y}{r_m} \right)$$

Where:

$y$  = Distance from the centroid of the specimen to the neutral axis during a seismic event, in

$r_m$  = Radius to the center of the steel tube, in

Because the neutral axis is expected to be equal to the centroid the variable  $y$  is taken equal to zero. Once  $y$  is determined, the variables  $\theta$  and  $c$  are calculated to be  $0^\circ$  and 3.73 in., respectfully. The nominal moment capacity is calculated then to be 1842 kip-in. or 142.5 kip-ft.

The variable  $y$  can be used if the centroid and neutral axis are not equal. If this is the case, the column is not perfectly vertical. Determining the variable  $y$  is difficult if the column is not vertical and is more of a guess. Figure 33 shows the plastic stress distribution of the steel and concrete when the variable  $y$  is not equal to zero. Material forces can be obtained by solving the following equations simultaneously.

$$\sum F_x = P + T_s - C_c - C_s = 0$$

$$\sum M_0 = \frac{(C_c + C_s)(r + y)}{2} - \frac{T_s(r - y)}{2} = 0$$

$$A_s = A_{sc} + A_{st}$$

$$T_s = A_{st}F_y$$

$$C_c = 0.95A_{cc}f'_c$$

$$C_s = A_{sc}F_y$$

Where:

- P = Axial load, kips
- $T_s$  = Resultant force of the steel in tension, kips
- $C_c$  = Resultant compressive concrete forces, kips
- $C_s$  = Resultant compressive steel forces, kips
- $r_m$  = Radius to the center of the steel tube, in
- $A_{st}$  = Area of steel in tension, in<sup>2</sup>
- $A_{cc}$  = Area of concrete in compression, in<sup>2</sup>
- $A_{sc}$  = Area of steel in compression, in<sup>2</sup>
- $r$  = Radius of the pipe measured to the outside of the pipe, in
- $f'_c$  = Compressive strength of the concrete, ksi
- $F_y$  = Yield strength of the steel, ksi

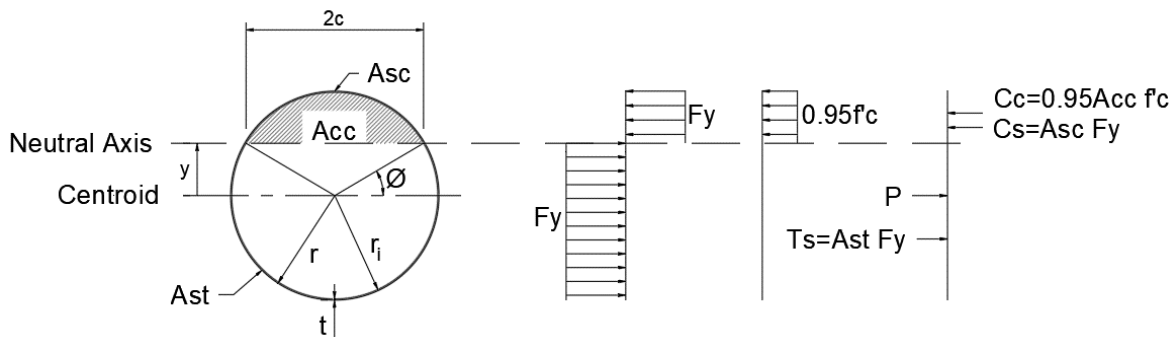


**Figure 33. Plastic Stress Distribution**

To calculate the base shear, the following equations were used:

$$\phi V_n = \phi (V_c + V_s)$$

Where:

$\phi$  = Capacity reduction factor, 0.75  
 $V_n$  = Net shear, kips  
 $V_s$  = Shear in the HHS steel member, kips  
 $V_c$  = Shear in the concrete, kips

$V_c$  is calculated using the following equation from McCormac (2014):

$$V_c = 2\lambda\sqrt{f'_c}b_wd$$

Where:

$\lambda$  = Modification factor, 1.0  
 $f'_c$  = Compressive strength of concrete, ksi  
 $b_wd$  = Area of concrete

Using appropriate values, the equation becomes:

$$V_c = 2(1)\sqrt{4000}(43.74) = 5,532 \text{ lb}$$

$V_s$  is calculated using the following equation from AISC (2011):

$$V_s = 0.6F_y A_g/2$$

Where:

$F_y$  = Yield strength of steel, ksi  
 $A_g$  = Gross cross-section area of the member, in<sup>2</sup>

Using the appropriate values, the equation becomes:

$$V_s = \frac{0.6(42,000)(14.68)}{2} = 184,968 \text{ lb}$$

And the net shear equation becomes:

$$\phi V_n = 0.75(5,532 + 184,968) = 142,875 \text{ lb}$$

Two methodologies are considered to determine the embedment of the pipe into the column and footing. The methodologies used are proposed by WSDOT and Edward P. Wasserman (Wasserman and Walker 1996). The WSDOT equation includes an annular ring, as shown in Figure 34, and is used to ensure full plastic behavior of the concrete-filled steel tube is as follows:

$$l_e \geq \sqrt{\frac{D_0^2}{4} + \frac{5.27DtF_u}{\sqrt{f'_c}}} - \frac{D_0}{2}$$

Where:

$l_e$  = Calculated embedment length, in  
 $D_0$  = Outside diameter of the annular ring, in  
 $D$  = Diameter of the embedded pipe, in  
 $t$  = Wall thickness of the embedded pipe, in  
 $F_u$  = Ultimate strength of the embedded pipe, ksi

$f'_c$  = Compression strength of the concrete, ksi

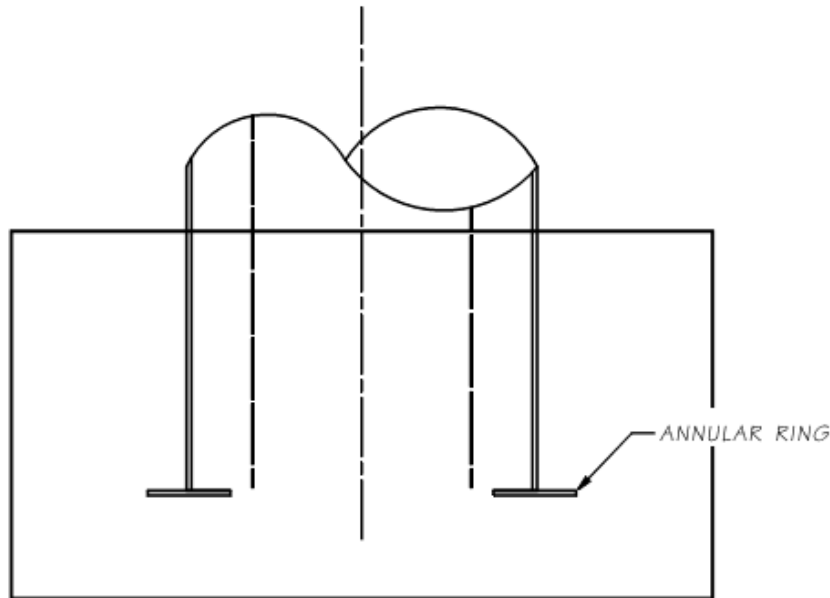


**Figure 34. Embedment Length with Embedded Ring (courtesy of WSDOT)**

Eliminating the annular ring from the equation, e.g.,  $D_0 = 0$ , the equation becomes:

$$l_e \geq \sqrt{\frac{5.27DtF_u}{\sqrt{f'_c}}}$$

Incorporating the appropriate values into the equation an embedment length of 27.7 in. is adequate. For the embedment length proposed by Wasserman, the following equations are used:

$$l_e = \frac{2F_y Z}{\sqrt{700f'_c b}}$$

$$b = \frac{d\sqrt{\pi}}{2}$$

Where:

$F_y$  = Yield strength of the embedded pipe, ksi

$Z$  = Plastic section modulus of the embedded pipe, in<sup>3</sup>

$f'_c$  = Compressive strength of the concrete, ksi

$d$  = Outside diameter of the embedded pipe, in

Incorporating these values into the equations an embedment length of 23.7 in. As a result of these two equations an embedment length of 2 ft-3 in. is used as the HSS embedment length.

The column longitudinal reinforcing is comprised of twelve #6 headed rebars equally spaced in a circular pattern. For confinement purposes, a spiral having a pitch of 1.5 in. is used along the entire length of the

column with a mechanical splice located at each end of the spiral. The spiral should maintain 1.5 in. of cover.

A portion of the HSS member just inside the concrete column is left unbonded. The unbonded length is a way to force the HSS over a certain length above the footing and encourage a rocking type (gap opening) motion at the base of the column during smaller movements (e.g., small earthquakes) without yielding of the CFST. Also, during larger movements/earthquakes, the unbonded length distributes the inelastic strain over a longer length of the CFST which enhances the low-cycle fatigue performance and ultimate displacement ductility of the connection. Leaving unbonded length is optional, if there are concerns about durability of the HSS, the unbonded length can be avoided.

In absence of experimental data on debonding of CFSTs, the unbonded length of the HSS member is determined using PRESSS Design Handbook (Pampanin 2010). All of the equations from the PRESSS Design Handbook are in metric units. To begin the elongation of the mild steel from the cast-in-place column testing procedure is determined to be roughly 0.88 in. (22.4 mm). The strain penetration is then calculated using the following equation:

$$l_{sp} = 0.15F_{ye}d_{bl}$$

Where:

- $F_{ye}$  = 1.1 times the yield strength, ksi
- $d_{bl}$  = Pipe thickness, in
- $f'_c$  = Compressive strength of the concrete, ksi
- $d$  = Outside diameter of the embedded pipe, in

Using a value of 60 ksi (413.7 MPa) for  $F_y$  and 0.75 in. (19.05 mm) for  $d_{bl}$ , the strain penetration is calculated to be 7.43 in. (188.7 mm). Strain in the steel is then calculated using the following equation:

$$\varepsilon_s = \frac{\Delta}{l_{ub} + 2l_{sp}}$$

Where:

- $\Delta$  = Elongation of the rebars, in
- $l_{ub}$  = Unbonded length, in
- $l_{sp}$  = Strain penetration length, in

The elongation of the rebars during the cast-in-place testing procedure was determined to be 0.81 in., from the data collected at an 8.87% drift. Using a value of 0 for the unbonded length and 0.81 in. (22.4 mm) for the elongation of the rebars, the strain is calculated to be 5.90% for the cast-in-place column. Using  $\Delta = 0.81$  in. (22.4 mm),  $F_y = 42$  ksi (289.6 MPa),  $d_{bl} = 0.581$  in. (14.76 mm) or the pipe thickness, and an unbonded length of 3 in. (76.2 mm), the strain in the HSS member is determined to be 7.75%. As a result of this calculation, the unbonded length is determined to be 3 in. It should be noted that this procedure is a rough estimate and more experimental and analytical data are required to quantify the exact unbonded length of the HSS. Another proposed method of estimating the unbonded length is that the unbonded length would equal 30-35% diameter of the HSS. For states such as Idaho where corrosion

risk is not such high as Pacific northwest, California, or areas around the coast; there should not be a major concern regarding the debonding steel. However, for the areas where moisture ingrain or corrosion is likely to occur are factors, then the unbonded length can be avoided for better durability.

Figure 35 shows the details of the precast column. The reason behind using the volumetric reinforcement ratio of about 2.4%, i.e., #3 spiral rebars although CFST gets shear to simulate the CIP as close as possible for the sake of good comparison with CIP until further research is available on what should be the volumetric reinforcement ratio for the system. The tapered fins that are used in pipes are not structural, they can be simple fillet welds because they are intended for the alignment and are not performing any structural function.

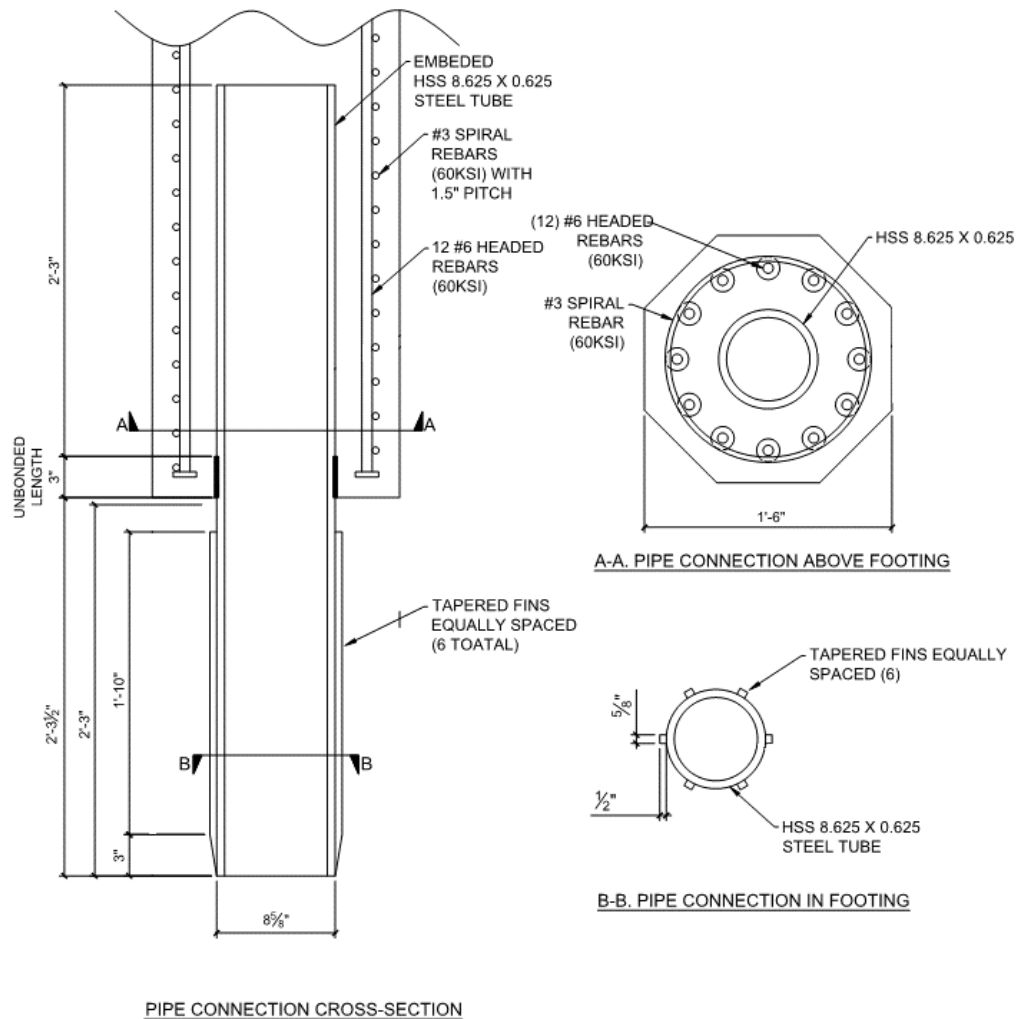


**Figure 35. Precast Column Detail**

After the precast testing procedure, the gap opening for the precast column is measured to be 0.55 in. (13.97 mm) on cycle 10 or 5.96 in. (7.64% drift) after which the instruments were removed from the

column. Using the values previously discussed, the actual strain in the HSS member is determined to be 5.29%.

The elastomeric bearing pad is designed according to the AASHTO LRFD Bridge Design Specifications (AASHTO 2017). The elastomeric bearing pad is designed for a column with a diameter of 18 in., 50-kips axial load, and has a 10.5 in. diameter hole through the center of the bearing pad. Using these parameters and shear modulus of 0.13 ksi, a plain elastomeric bearing pad with a thickness of 0.5 in. is determined to be sufficient. Further information can be found in AASHTO M251 (Standard Specification for Plain and Laminated Elastomeric Bridge Bearings). For this research project, under consultation of ITD a ½ in. of this material was deemed to be suitable.

The footing for the precast column was designed to remain elastic throughout testing. The footing design is similar to the cast-in-place column. The changes that are made to the footing are to accommodate for assembling the column to the footing. An HSS10.75x0.5 having a length of 28 in. is installed into the top of the footing such that the top of the HSS member is level with the top of the footing. All of the footing reinforcing rebars that are affected by the HSS member are adjusted by incorporating a 90° bend with an appropriate amount of development length to accommodate this change. Guidelines on rebar hooks, bends, and development lengths are conservatively considered with all the rebar in the footing. An image depicting the precast column assembly to the footing is shown in Figure 36.



## Construction

For the construction of the precast specimen, the formwork from the cast-in-place test specimen is modified slightly to accommodate for the HSS members and is reused. Rebar is cut to the required lengths and bent appropriately. Next, the rebar is tied together, and the formwork is secured around the tied rebar (Figure 37a). Before installing the HSS members, the exposed surfaces are sandblasted to remove paint and roughen the surface to obtain a better bond with the concrete. The precast column is poured horizontally because of the restrictions over dropping height for concrete as well as difficulty in keeping the column standing upright with a pipe protruding from the end (Figure 37b). Once the HSS members, rebar, and formwork are set, the concrete for the column and footing is poured (Figure 37c-d). Both the footing and column are allowed to cure for three days before the formwork is removed. After the formwork is removed the concrete is covered with burlap and plastic and wetted daily to allow the concrete to continue curing in the most ideal conditions. Once the concrete reached seven days of curing, the concrete footing is moved to the Structural LAB (SLAB). After another seven days, the column is also moved to the structural laboratory and grouted into place, painted, and instrumented in preparation to be tested. Images of the construction progress are shown in Figure 37. Before the column assembly, the exposed surfaces of the HSS member embed in the footing is roughened and lightly wetted in preparation for the grouting process. The grout used to fill the void between the two HSS elements is SikaGrout®-328. After mixing the grout per the grout mixing instructions, the mixture is promptly pumped into a Polyvinyl Chloride (PVC) pipe that extended from the top of the footing grout inlet pipe. After a few moments grout is observed to be pouring out of both of the grout outlet pipes (Figure 37). The grout is allowed to flow freely through the grout vent ducts for approximately 30 seconds to remove any air pockets that may be trapped. Once the grout had flowed for approximately 30 seconds the PVC pipe valves are closed and the grout is allowed to cure for 7 days before the testing protocol is initiated. Figure 37f shows the completed precast specimen.

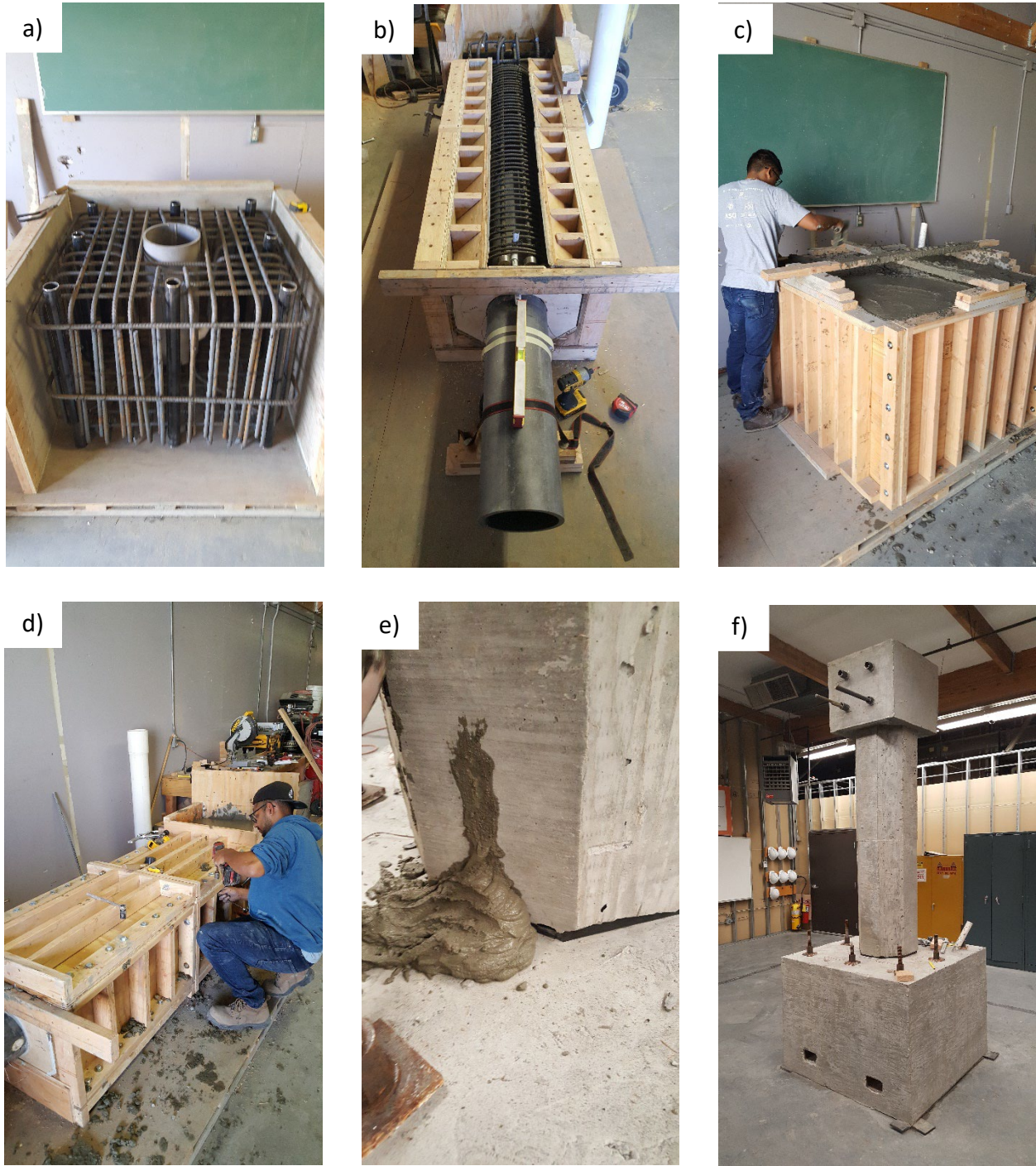


**Figure 37. Precast Column Construction: a) Footing Rebar Cage, b) Column Rebar Assembly, c) Finished Footing, d) Finished Column, e) Grout Flowing out of Grout Vent, f) Finished Test Specimen**

## Test Setup and Instrumentation

The testing protocol and arrangement for the precast column is similar to that of the cast-in-place column. The instrumentation of the precast column is similar to the cast-in-place; however, the precast column had a total of four strain gauges, two on each side, located on the column HSS member at the extreme push and pull locations. On each extreme location of the HSS member, a strain gauge is placed on the exposed surface about one inch from the surface of the concrete and the other was placed approximately one inch inside of the concrete surface as shown in Figure 38. Arranging the strain gauges in this manner makes so each of them is one inch from the column to footing interface.

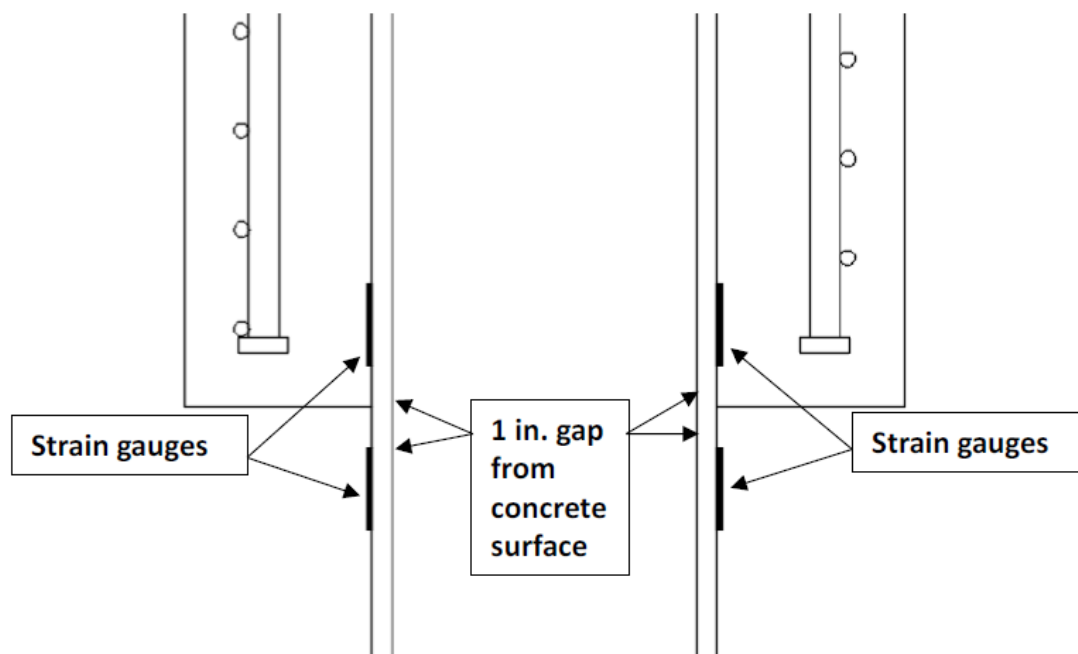


Figure 38. Location of Strain Gauges on the HSS Member

## Testing Results

After testing began, for the first two cycles, there are no visible hairline cracks. On the third cycle, hairline cracks are visible below the first 0 – 36 in. of the column which continued to develop into the fourth cycle. During the fifth cycle, concrete spalling began to occur on the north face of the column and by the seventh cycle, spalling occurred on the south face as well. Cracking and spalling continued to develop until the 11<sup>th</sup> cycle. On the 11<sup>th</sup> cycle, the unbonded length of the pipe is visible on both the north and south faces of the column. On the 13<sup>th</sup> cycle, an “elephant leg” behavior is observed on the exposed HSS member. During the 15<sup>th</sup> cycle, approximately 10 kips of lateral force is lost as a result of the pipe beginning to degrade. On the 16<sup>th</sup> cycle, another significant drop in lateral force is observed due to a fracture of the pipe on one side and the testing procedure was terminated due to safety reasons. The fracture is located very close to the interface, the buckling of the pipe is obvious on the other side as shown in Figure 39.



**Figure 39. Pipe Failure During the Testing Procedure.**

Figure 40 shows the loading protocol used during the testing procedure. Similar to the cast-in-place column, the programmed displacement is not the actual displacement due to the actuator frame deflecting and the footing sliding. The actual deflection of the column for the push and pull cycles are within 0.05 in. of each other. To keep the same loading protocol as the cast-in-place there is a missing cycle between cycles eight and nine as shown in Figure 40. The same procedure is followed to correct the column displacement data which is summarized in Table 9. Figure 41 shows images of the lower half of the column during the testing procedure.

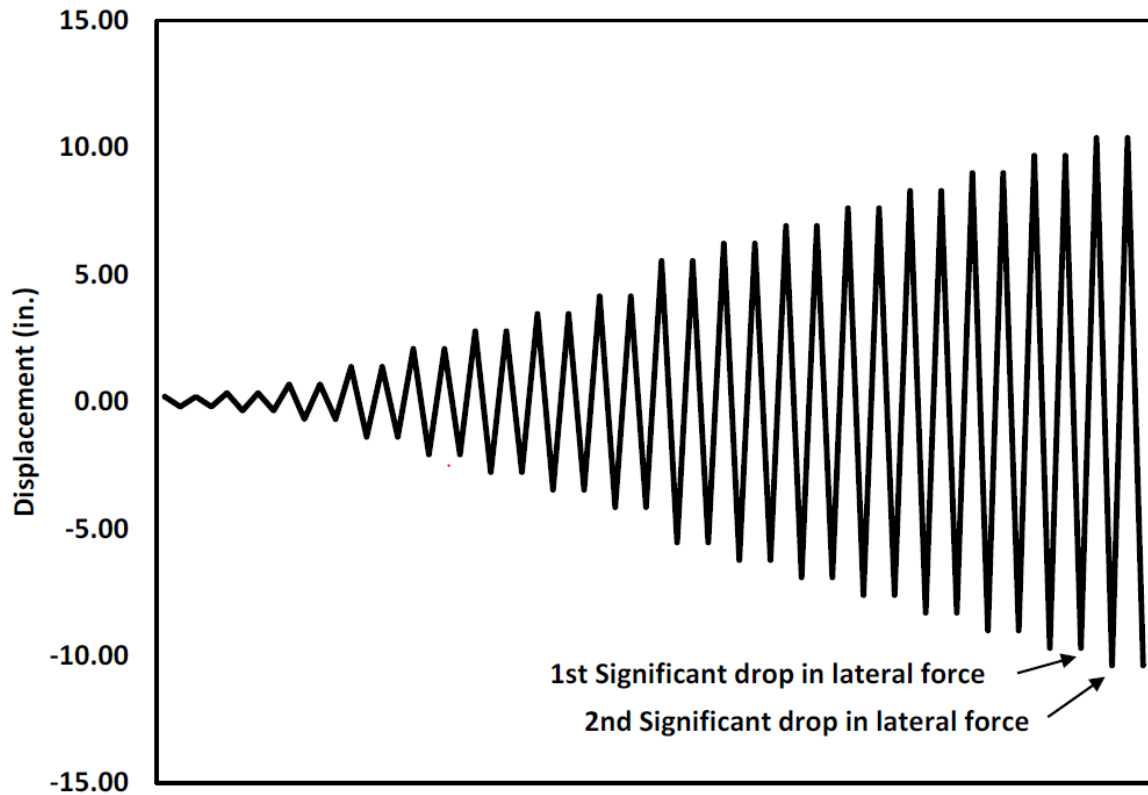


**Figure 40. Loading Protocol for the Precast Column**

**Table 9. Summary of Performance Values from Testing of the Precast Column**

Cycle	Programmed Displacement (in.)	Programmed Drift (%)	Actual Pull Displacement (in.)	Actual Pull Drift (%)
1	0.20	0.26	0.14	0.18
2	0.35	0.45	0.23	0.29
3	0.69	0.88	0.47	0.60
4	1.38	1.77	0.92	1.19
5	2.08	2.67	1.53	1.96
6	2.77	3.55	2.15	2.75
7	3.46	4.44	2.82	3.62
8	4.15	5.32	3.36	4.30
9	5.54	7.10	4.87	6.24
10	6.23	7.99	5.37	6.89
11	6.92	8.87	6.09	7.80
12	7.61	9.76	6.78	8.69
13	8.30	10.64	7.45	9.55
14	9.00	11.54	8.14	10.44
15	9.69	12.42	8.87	11.37
16	10.38	13.31	9.57	12.27



**Figure 41. Precast Specimen During Testing at: a) 0.45% Drift, b) 2.67% Drift, c) 5.32% Drift, d) 8.87% Drift, e) 13.27% Drift, f) Failed HSS Member**

After the testing procedure has concluded the data is analyzed. The maximum displacement of the column during the testing procedure is 9.57 in. which corresponds to a 12.27% drift ratio. The maximum load applied to the column during the testing procedure is 41.2 kip which corresponds to a 267.8 kip-ft moment capacity. The column showed a stable response with significant energy dissipation. When the column reached the peak load, a reduction in the lateral load is observed as a result of the column engaging the cover concrete. The lateral load continues to slowly decrease with each cycle because the HSS pipe is experiencing low-cyclic fatigue. As the testing procedure progresses a significant drop in lateral force is

observed which is a result of the pipe buckling or “elephant leg” behavior. On the next cycle the lateral force approaches the same lateral force then decreases as the pipe fails. Plots showing the Force vs. Displacement and Drift during the test are shown in Figure 42 and Figure 43, respectively. These plots show the yield displacement of the column and the design base shear of the column which was reached before the pipe failed. The backbone curve is also shown in Figure 44. The initial kink in the backbone curve is a decompression point or point at which a gap began to open as a result of the column rocking. Table 10 and Table 11 show significant values from the precast column testing procedure.

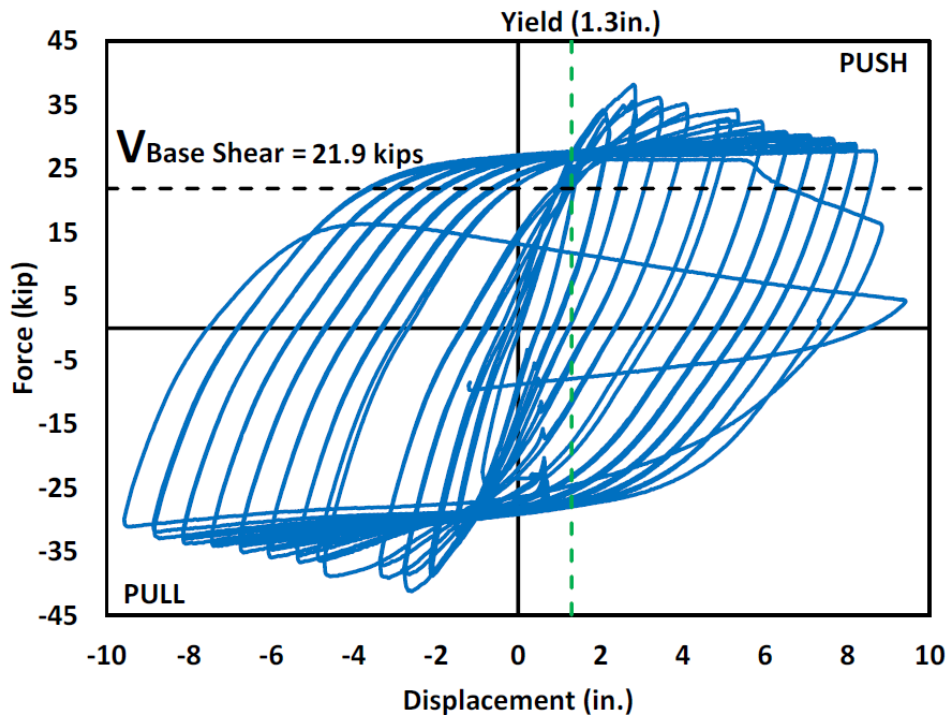


Figure 42. Force vs. Displacement plot for the Precast Column

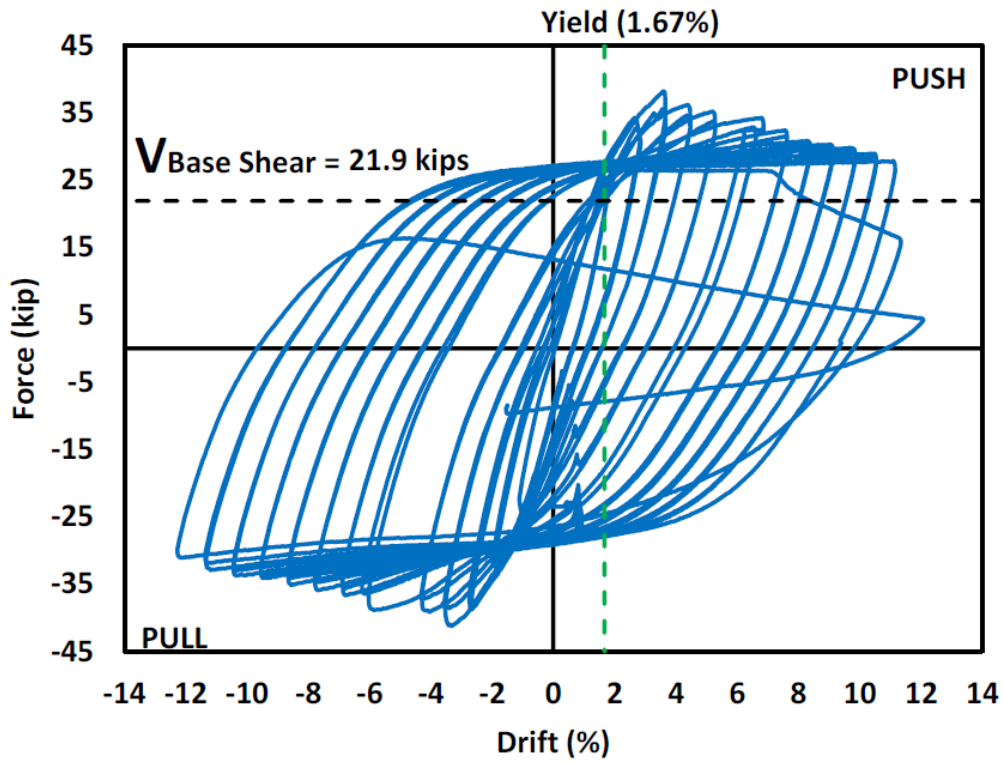


Figure 43. Force vs. Drift Plot for the Precast Column

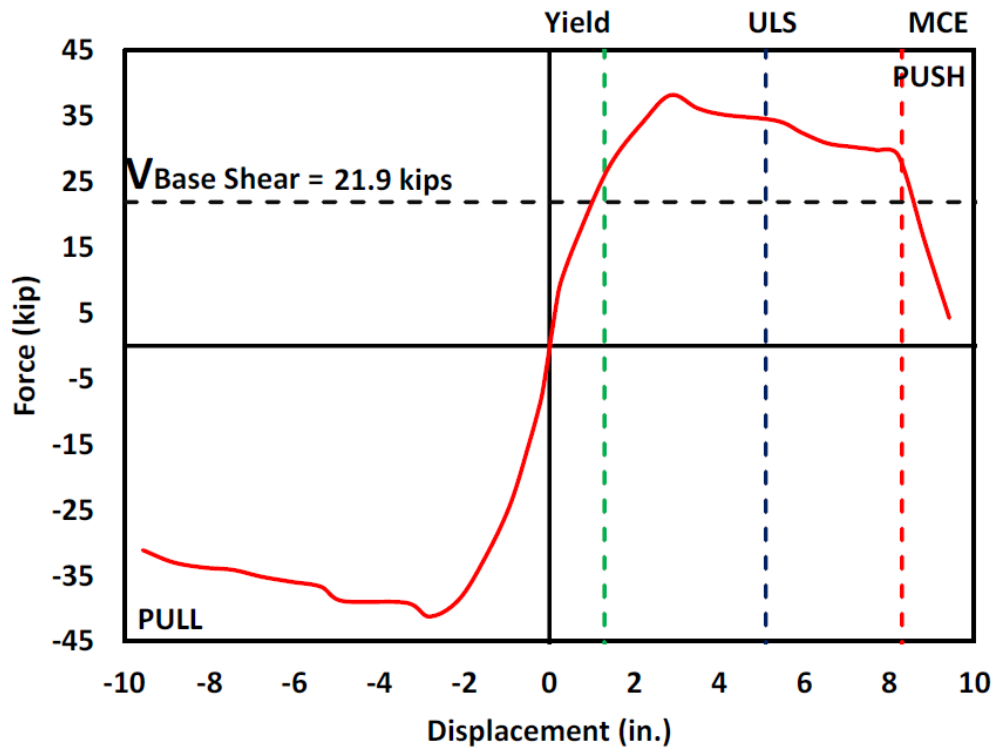


Figure 44. Backbone Curve for the Precast Column

**Table 10. Damage Observation from Testing of the Precast Column, Drift (%)**

Cracking	Spalling	Significant Elephant-Leg Buckling	Fracture of the Pipe	End of Testing
0.6 %	4.42 %	8.7 %	10.5 %	12.27 %

**Table 11. Summary of the Performance Points from Testing of the Precast Column**

Yielding Predicted Drift (%)	Yielding Predicted Base Shear (kips)	Yielding Experimental Drift (%)	Yielding Experimental Base Shear (kips)	Ultimate Strength Experimental Drift (%)	Ultimate Strength Experimental Base Shear (kips)	Ultimate Strength Experimental Ductility*
0.88	21.9	1.7	27.2	12.27	41.2	6.3

Note: \*Displacement ductility ( $\mu$ ) was 6.3 at the end of testing

The distribution of curvature along the height of the first 54 in. of the column is shown in Figure 45. Like the cast-in-place column, the column is expected to yield and fail within the plastic hinge of the column. The plastic hinge for the precast column can be calculated using the same equation as the cast-in-place column from Priestley et al. (2007):

$$L_p = 0.08H + l_{sp}$$

Where:

H = Column height, in

$l_{sp}$  = Strain penetration length, in

Using the strain penetration discussed earlier in this chapter and column height of 78 in. the plastic hinge is calculated to be 13.07 in. Result showed that yielding occurred in the bottom 18 in. of the column. From 18 in. to 36 in. the column approached the yield point but never reached it. Because the region from 18 in. to 54 in. never reached the yield point, this region essentially remains elastic throughout the testing procedure.

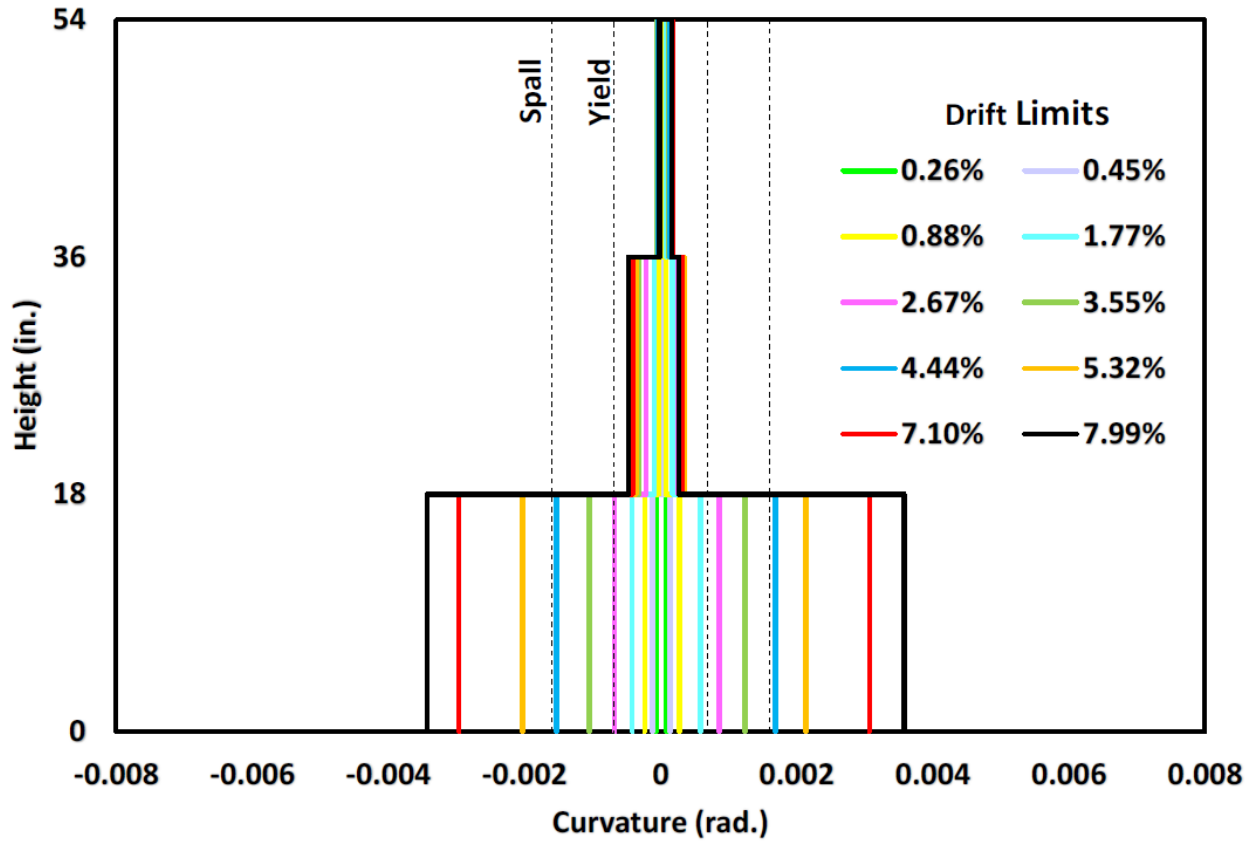


**Figure 45. Precast Curvature Distribution**

The dissipated energy plot is shown in Figure 46. The dissipated energy is obtained using the same procedure as the cast-in-place column. The largest difference in dissipated energy occurred during the 15<sup>th</sup> and 16<sup>th</sup> cycles which corresponds to the HSS member located in the column buckling and fracture. The total dissipated energy during the testing procedure is 756,001.2 ft-lb (1025 kJ).

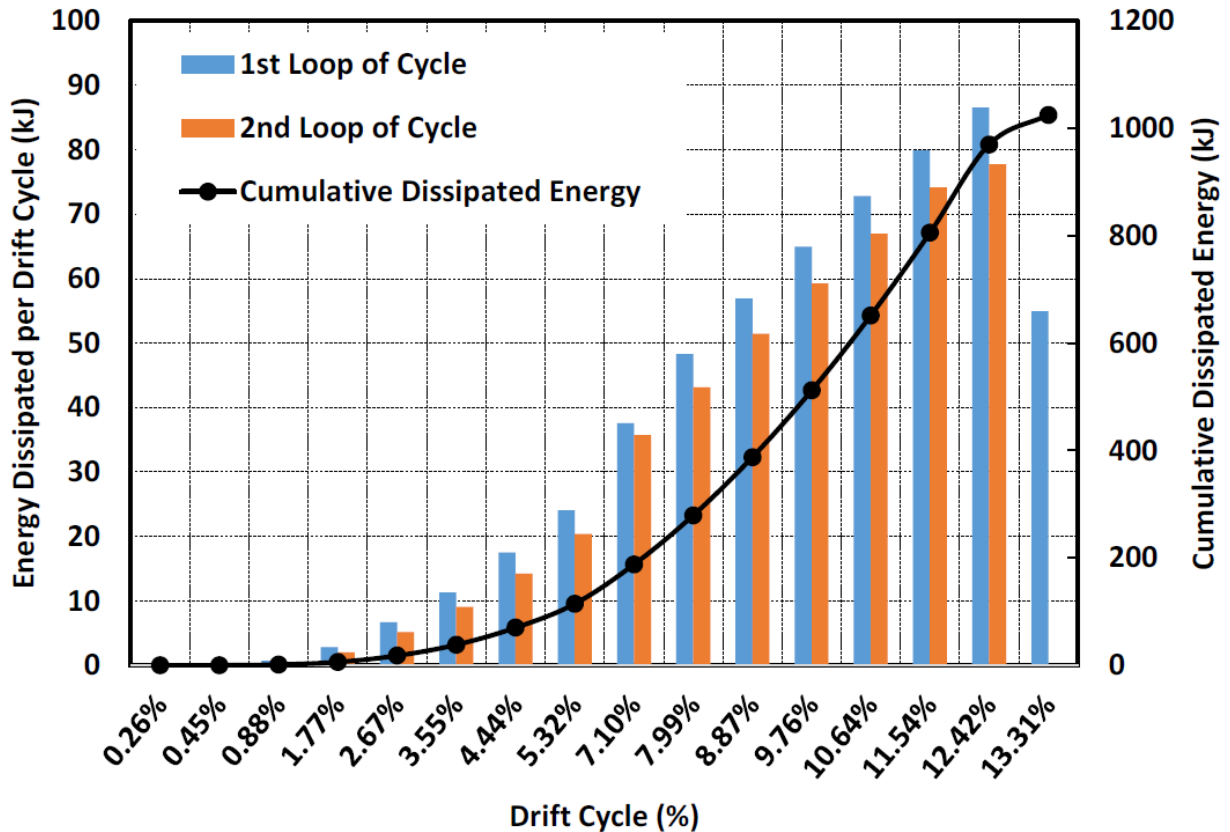


**Figure 46. Dissipated Energy Plot for the Precast Column (1 kJ = 737.56 ft-lb)**

An area-based hysteretic damping plot is shown in Figure 47. The area-based hysteretic damping is calculated using the same procedure as the cast-in-place column. The plot shows the precast column having a relatively parabolic trend for the majority of the testing procedure. The column had higher hysteretic damping at the beginning of the testing procedure because of the elastomeric damping pad (e.g., contact damping) allowing the column to move without significantly increasing the load at the top of the column. The precast column hysteretic damping is just below the Takeda Fat model after the capability of the elastomeric bearing pad is exceeded, then approximately equal to the Takeda Fat model from a displacement ductility of 4 to 5.5 after which the column hysteretic damping approached the Ramberg-Osgood model until the testing procedure was ended.

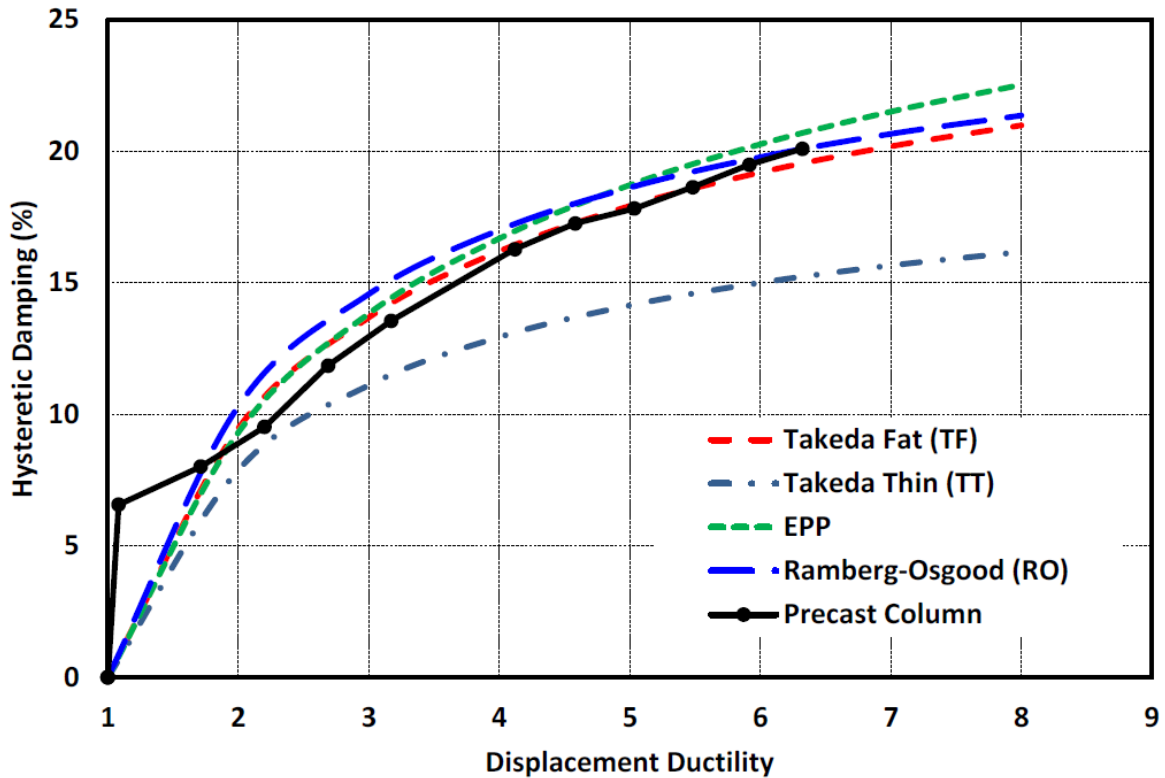


Figure 47. Area-Based Hysteretic Damping for the Precast Column

### Summary

The precast specimen is designed to match the capacity and ductility of the cast-in-place benchmark. The precast footing and column are constructed incorporating HSS members. The Concrete Filled Steel Tube (CFST) at the interface of the column and footing provides flexural and shear resistance as well as confinement. The specimen is designed using the CFST equations provided in the WSDOT Bridge Design Manual and the latest version of AASHTO LRFD Bridge Design Specifications. The contribution of the unconfined concrete cover at the interface was ignored for the flexural design of the column. An elastomeric pad is provided at the column and footing interface to prevent cracking during smaller drift ratios and allow rocking of the column. The embedment length of the pipe is selected such to develop the plastic capacity of the column pipe without any premature failure or pullout. An unbonded length of the pipe is provided to distribute inelastic strain during larger drift ratios and to improve the low-cycle fatigue performance of the pipe. The unbonded length region was designed to be the ductile link in the specimen. The footing and other parts of the column are designed to be capacity protected regions. Testing results show good performance of the precast column with enhanced energy dissipation. Damage to the column during the test was observed to be within the first 18 in. of the column which thought to be the plastic hinge region. The loss of the cover concrete occurred during the 4.42% drift ratio. This was later than what was observed in the testing of the cast-in-place benchmark. The failure mechanism for the connection started with an “Elephant-Leg” buckling of the pipe over the unbonded region, followed by the fracture

of the pipe on one side. There was a rapid decrease in the lateral capacity of the column when the buckling increased. The maximum force obtained during the testing procedure was 41.2-kip which was approximately 10% higher compared to the cast-in-place benchmark. The maximum displacement achieved was 9.4 in. which is about 20% higher compared to the cast-in-place benchmark. The ultimate displacement ductility is just below 6.5. The lower value of ductility compared to cast-in-place (7.5) was the fact that the precast column had a higher yield point compared to cast-in-place. The total energy dissipated during the testing procedure was 1,025 kJ. This was 2.25 times of the cast-in-place benchmark. The hysteretic damping plot showed that the precast column, overall, had similar values of hysteretic damping of Takeda-Fat and Ramberg-Osgood models. This is thought to be due to enhanced confinement (e.g., Concrete Filled Steel Tube) and detailing considerations. The precast column reached a hysteretic damping of 20% at the failure point.

## **Cantilever Columns: Precast vs. Cast-In-Place**

Both columns are designed from the same prototype structure and as a result, are designed and built with the same overall dimensions. The columns had a height of 7 ft-4 in. and a diameter of 18 in. The designed moment capacity of the cast-in-place column is 165 kip-ft, after the AASHTO LRFD Bridge Design Specifications (AASHTO 2017), and the moment capacity of the precast column pipe connection is 143 kip-ft, after the WSDOT LRFD Bridge Design Manual (WSDOT 2019).

The testing setup and procedures are identical for each of the columns except the precast column endured through more cycles to reach its failure point. The cast-in-place column reached 50% degradation of the highest observed lateral force on the 13<sup>th</sup> cycle, which corresponds to 7.7 in. of displacement and 9.9% drift after the displacement of the footing is removed from the data. The precast column reached 50% degradation of the highest observed lateral force on the 16<sup>th</sup> cycle, which corresponds to 9.57 in. of displacement and 12.3% drift after the displacement of the footing is removed from the data. The loading protocol for the cast-in-place and precast columns is shown in Figure 25 and Figure 40 respectively. Figure 26 and Figure 41 show images of the cast-in-place and precast columns, respectively during the testing procedure at approximately the same displacements.

The cracking drift ratio for the cast-in-place and precast columns are 0.2% and 0.6%, respectively. The precast column exhibited flexibility during smaller drift ratios to prevent cracking to the column.

The maximum displacement of the cast-in-place column during the testing procedure is 7.7 in. which corresponds to a 9.9% drift. The maximum load applied to the cast-in-place column during the testing procedure is 37.8 kip which corresponds to a 245.7 kip-ft moment capacity. The maximum displacement of the precast column during the testing procedure is 9.6 in. which corresponds to a 12.3% drift. This is 20% higher compared to the cast-in-place benchmark. The maximum load applied to the precast column during the testing procedure is 41.2 kip which corresponds to a 267.8 kip-ft moment capacity. This is 9% higher compared to the cast-in-place benchmark. The Force vs. Displacement plots for the cast-in-place and precast testing procedures are shown in Figure 27 and Figure 42, respectfully. The Force vs. Drift plots are shown in Figure 28 and Figure 43 for the cast-in-place and precast testing procedures, respectively.

Looking at each of the hysteresis plots, it is obvious that the area of the loops for the precast column is larger compared to the cast-in-place column. In each of the plots, the enclosed area values are larger for the precast column than the cast-in-place column. It can be observed that the cast-in-place column yielded sooner compared to the precast column. The precast column had a yield drift which was 30% higher compared to the cast-in-place column.

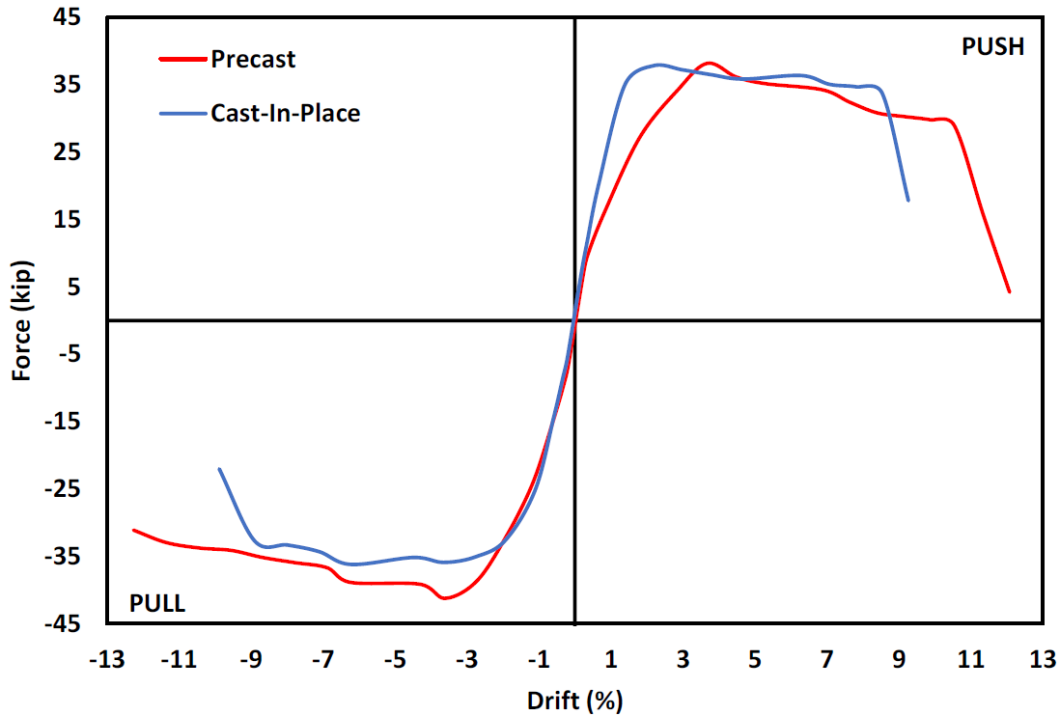


**Figure 48. Backbone Curve for the Cast-In-Place and Precast Columns**

The backbone curve for both testing procedures is shown in Figure 48. It can be observed that the precast column has a lower stiffness compared to the cast-in-place column. The cast-in-place column had a consistent stiffness of 36.7 kips/in. The precast column begins with a stiffness of 42.4 kips/in., transitions to 16.44 kip/in., then has a stiffness of 8.5 kips/in. before achieving the maximum lateral load. Comparing the values, the precast column initially has a stiffness 16% higher, then 45% lower, next 23% lower compared to the cast-in-place benchmark column. However, the precast column reached the capacity of the cast-in-place column at about a 3% drift ratio. The lower stiffness of the precast column is due to the rocking movement to allow flexibility and prevent concrete cracking at lower drift ratios. The ultimate displacement ductility for the precast column was nearly 6.5 which was slightly lower than the cast-in-place (e.g., 7.5) This was mainly due to larger yield drift for the precast column. Table 5 and Table 6 shows significant values from the cast-in-place testing procedure while Table 9 and Table 10 show significant values for the precast column testing procedure.

The curvature distribution along the height of the first 54 inches of the cast-in-place and precast columns are shown in Figure 30 and Figure 45, respectively. Each of the columns is expected to yield and fail within the plastic hinge of the column. The plastic hinge of the cast-in-place column is 13.7 in. The plastic hinge

for the precast column is 13.07 in. Each of the curvature figures shows that yielding occurred in the bottom 18 inches of the column. From 18 inches to 36 inches, the columns approached the yield point but never reached it. Because the region from 18 inches to 54 inches never reached the yield point, this region deformed elastically throughout of the testing procedures. The maximum calculated curvature the cycle corresponding to the 10<sup>th</sup> cycle or 7.99% drift for the cast-in-place column is 0.0038 radian compared to 0.0036 radians for the precast column. These values are nearly identical. There were several large cracks in the plastic hinge length of the cast-in-place column. However, for the precast column, there was essentially one large crack (e.g., gap opening) in the beginning until the spalling of the cover concrete.

The dissipated energy is obtained by finding the area of each loop in the Force vs. Displacement plot after the units are converted to newtons and meters. The area of each loop represents the total energy dissipated in units of joules. The total dissipated energy during the cast-in-place testing procedure is 456 kJ (336,327 ft-lb). The total dissipated energy during the precast testing procedure is 1025 kJ (755,999 ft-lb) which is more than 2.2 times the cast-in-place column. However, comparing the cumulative dissipated energy plots at the end of the cycle just before the cast-in-place column's first rebar break, 8.87% drift, the cast-in-place column dissipated 293 kJ (216,105 ft-lb) compared to 388 kJ (286,173 ft-lb) for the precast column. Figure 49 and Figure 50 show the dissipated energy for both the columns. One reason why the dissipated energy is higher for the precast column is that there is more steel at the column connection which makes the column more ductile and able to absorb more energy. Also, the precast column had better confinement (e.g., presence of a steel shell) compared to the cast-in-place benchmark.

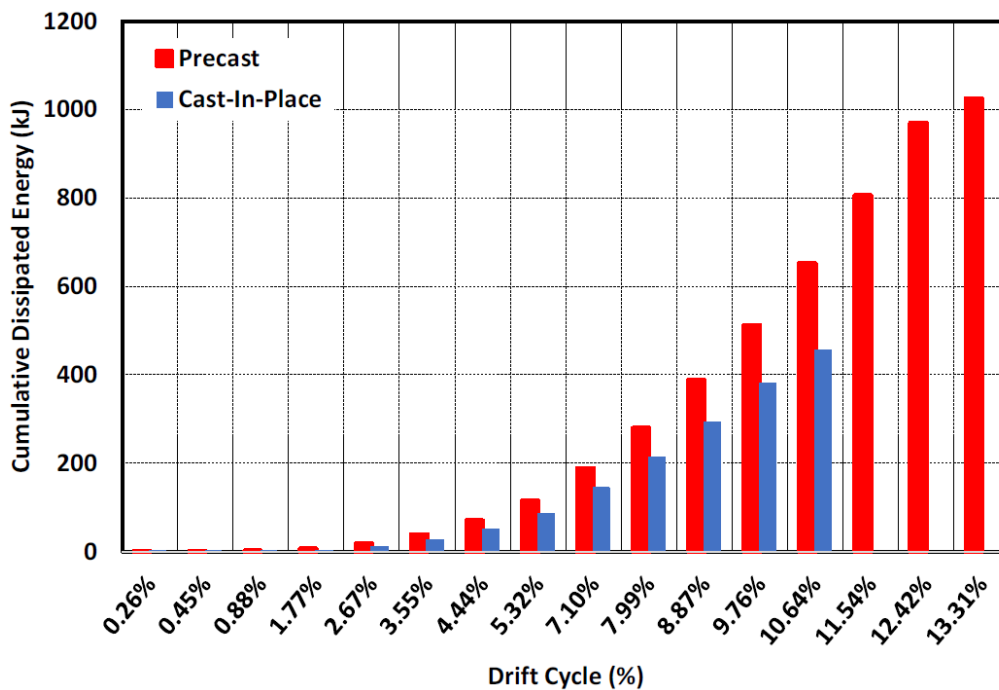
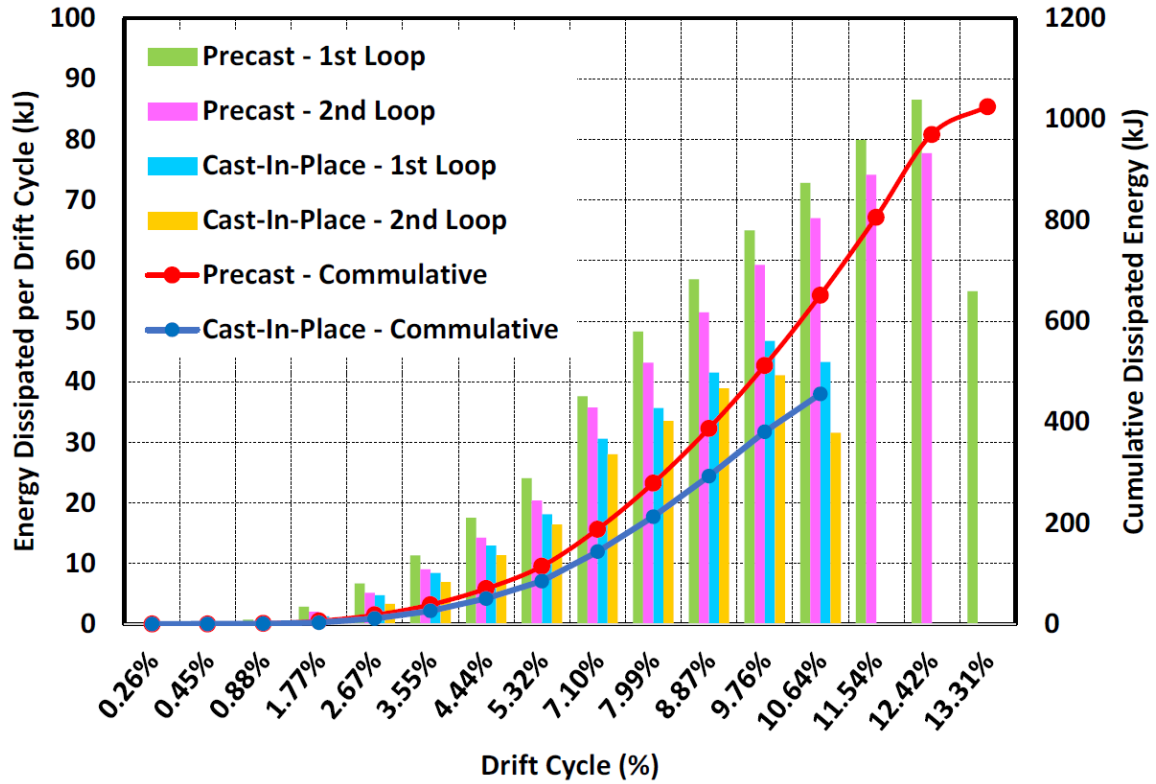
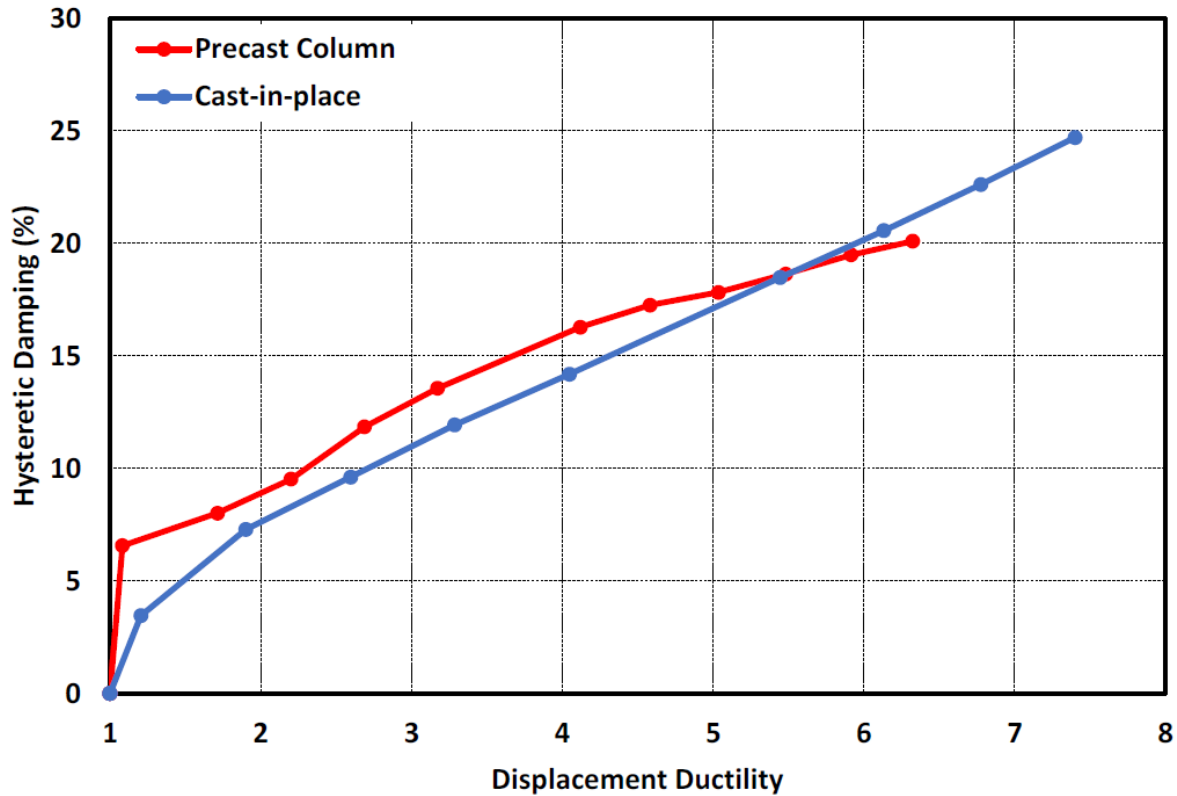


Figure 49. Cumulative Dissipated Energy for Both Columns (1 kJ = 737.56 ft-lb)



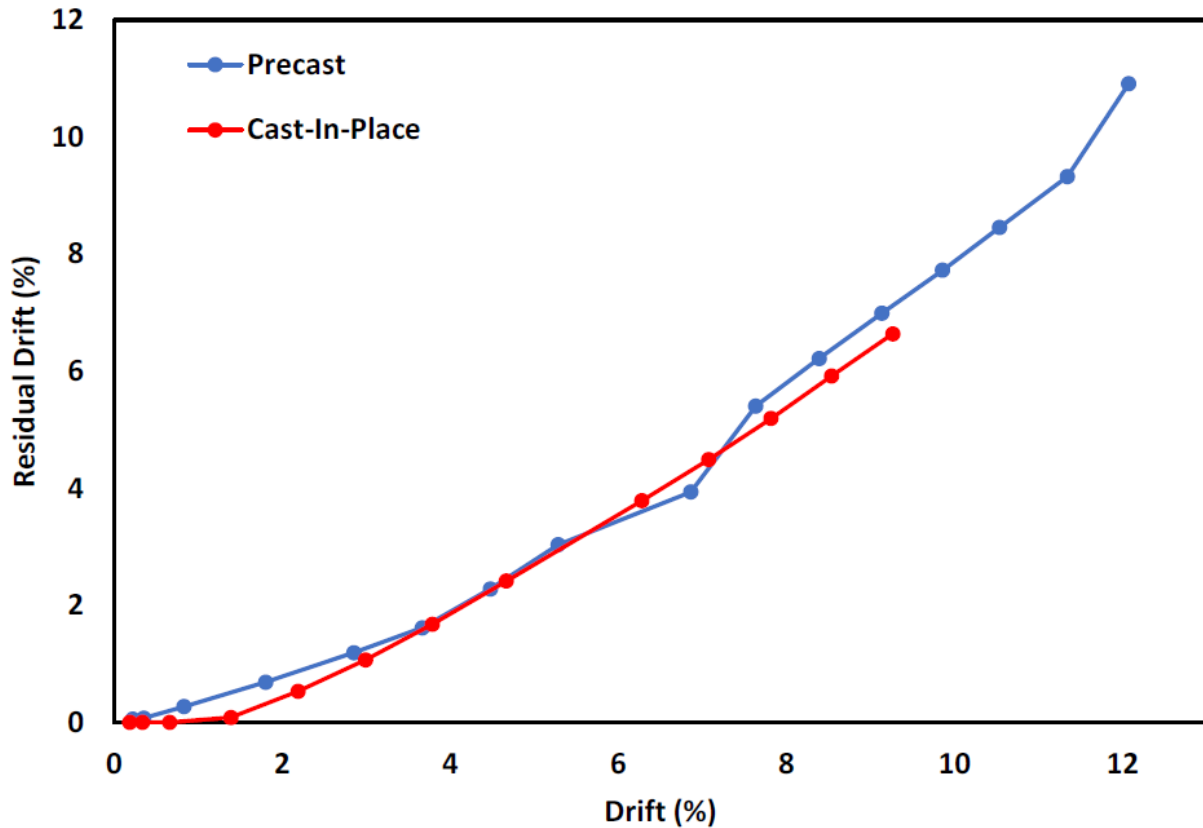
**Figure 50. Dissipated Energy for Each Cycle for Both Columns (1 kJ = 737.56 ft-lb)**

Figure 51 shows the corrected area-based hysteretic damping plots for both the cast-in-place and precast columns. It can be observed that the precast column had higher values of hysteretic damping compared to the cast-in-place column up until a ductility of nearly 5.5. The initial jump in the hysteretic damping plot of the precast column is due to contact damping provided by the elastomeric pad. The effects reduce as the pipe starts yielding with increasing displacement ductility.



**Figure 51. Corrected Area-Based Hysteretic Damping for Both Columns**

Figure 52 shows the residual drift for the cast-in-place and precast columns. Looking at the image, the two columns follow a similar trend line throughout their testing procedures. The residual drift of the cast-in-place column on the last cycle of the testing procedure is 6.64% compared to the 9.27% drift that the column was pushed. This corresponds to the column maintaining 70% of the displacement applied to the column when the lateral force was equal to zero. The residual drift of the precast column was 10.91% compared to the 12.08% drift that the column was pushed or 90% of the displacement of the column was maintained when the column lateral force was equal to zero. If the cast-in-place column could continue through more of the test cycles, the residual drift results are expected to continue following the precast cast column results.



**Figure 52. Residual Drift for the Cast-In-Place and Precast Columns**

Each of the cantilever columns is designed and constructed having the same overall dimensions and approximately similar capacities. The cast-in-place and precast columns are tested using identical loading protocols and displacement progression for each cycle. The columns perform similarly throughout the testing procedures. The precast column, however, continued through more loading cycles and as a result, achieved higher deflections and cumulative dissipated energy. Overall testing shows better performance of the precast column compared to the cast-in-place column. It reached higher displacements with good strength. The residual deformation for both columns is comparable. Table 1 summarizes some of the key data from the testing of the two columns.

## **Bent Pier System: Cast-In-Place**

### **Introduction**

This section presents design, construction, and experimental testing of a Cast-In-Place (CIP) bent system with the intention of establishing a performance level in which to compare the precast bent system using the proposed pier connection. A review of the construction process is thus presented discussing the challenges faced during a CIP construction project and the work required. The full testing arrangement used for the experimental work is presented and discussed. Followed by the experimental testing carried out on the system and its resulting performance.

### **Prototype Structure**

The first steps in developing the specimen is the determination of the overall size of the specimen. As the research aims to test the proposed connection at a large scale, the specimen sizing is determined near the maximum capacity of the testing facility, Idaho State University Structural Laboratory (SLAB). The overall specimen itself is considered to be sized as a scaled version of a typical mid-to-long span bridge constructed in south-east Idaho. South-east Idaho is proposed to be the place of construction as it is the most seismically active area of the state where the proposed connection is to be used. An example of a typical mid span bridge in south-east Idaho is presented in Figure 53. This particular bridge is constructed over the Bear River near Preston, Idaho about 70 miles south of Pocatello, Idaho.

The bridge consists of two 137 ft spans. Each span is set between the bridge's abutments and a center bent system located approximately in the center of the river. The bent system is comprised of three octagonal columns measuring 4 ft. in width and having an overall height of 29ft-3in. The column cap measuring 40 ft. in length, 5 ft. wide, and 4 ft-6 in. deep and the foundation being 40 ft. in length, 22 ft. wide, and 5 ft-6 in. deep. A detail of the bent is provided in Figure 54.

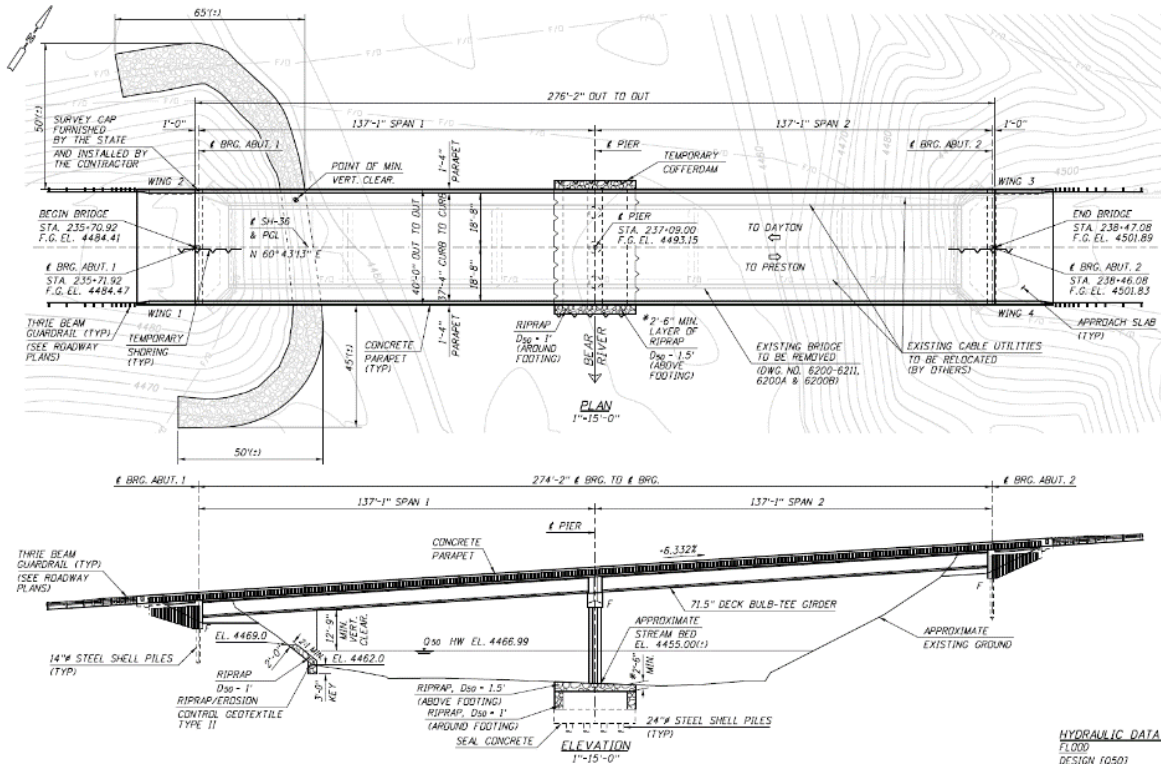


Figure 53. Elevation and Top View of SH-36 Bridge Over Bear River

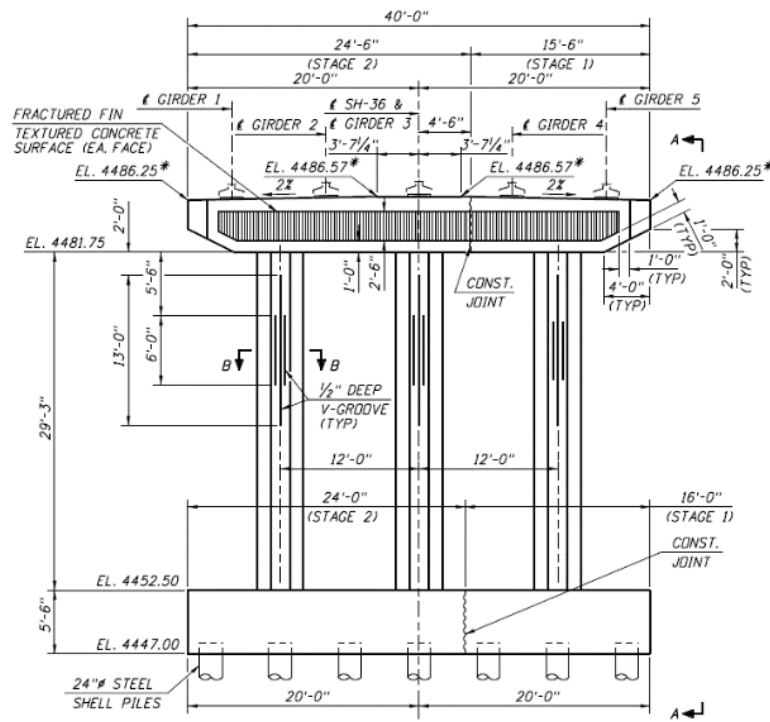
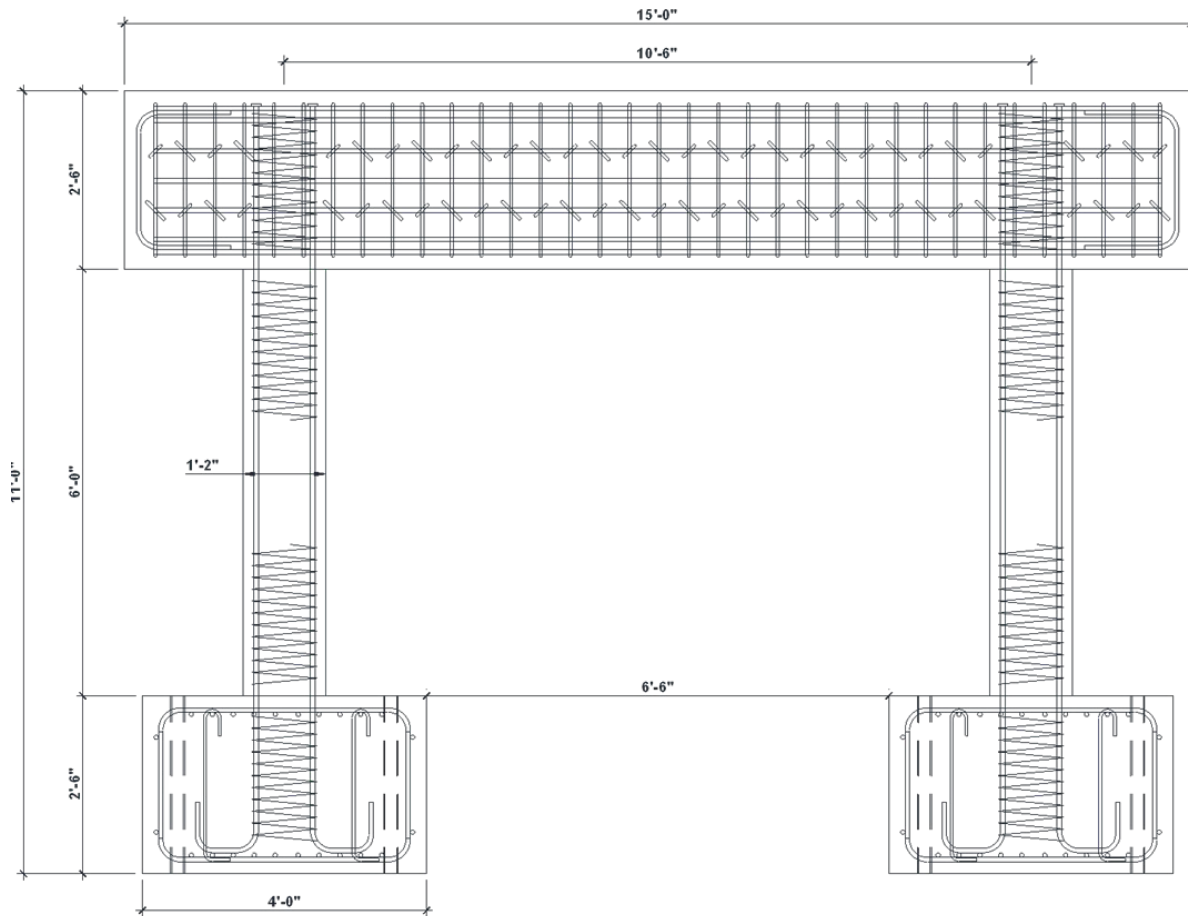


Figure 54. Bear River Bent System Elevation View

Through the consideration of the capabilities within the SLAB, maximum dimensions were established for a height of the specimen and associated setup to not exceed 13 ft. and the specimen's overall length not to exceed 15 ft. After factoring in the items required for loading and monitoring the specimen during testing the specimen height was determined to be 11 ft. in total height and have a pier cap length of 15 ft. For determining the depth of the pier cap and footing segments consideration of the embedment required by the HSS pipe in the proposed precast connection had to be considered in order to achieve similar dimensioning between the CIP and precast bent systems. Through this a required depth of 2 ft-6 in. is necessary for both the footing and pier cap. The footing width and length is determined based on the layout of the SLAB strong floor which has embedded anchors in an 18 in. x 18 in. square pattern throughout the floor. Considering the centrally located pier in each footing and providing adequate anchorage the footings are required to be 4 ft. x 4 ft. square.

For sizing of the columns, past experiments performed in the lab were considered to determine the final width. Previous experiments on single piers acting as cantilevers had been performed with a column width of 18 in. with steel reinforcing ratios of 2% ( $r=2\%$ ). While also attempting to match the capacity of the previous experiments a reduced column width of 14 in. was determined suitable as the bent system would produce higher demands during testing than previous cantilever columns tested. From the column width and consideration of cap reinforcing and cover concrete a 2 ft. width for the cap is necessary. Through consideration of the lab limitations, past experiments, typical bent ratios, and requirements for the both the CIP and precast specimen the resulting specimen depicted in Figure 55 is determined.

The reason behind using much stiff beams and footing is to make sure no non-linear deformation occur in those elements as cap beam and footing are capacity protected elements. The cap beam and footing was made rigid.



**Figure 55. CIP Bent Specimen**

### Design of the CIP Specimen

After establishing the overall specimen dimensions to accommodate the limitations and experimental goals, the design of the system is performed. For properly designing the bent the 8<sup>th</sup> Edition of AASHTO LRFD Bridge Design Specification (AASHTO 2017) is considered. Through the design process the reinforcing steel is determined for accomplishing the targeted strength of system. An analysis of the lab capabilities and past experiments deemed a safe target strength of 60-70-kip force applied during testing as an achievable target force applied to the bent system.

Considering each individual pier as an individual system comprised of two connections, footing-to-column and column-to-cap, each contributing to the overall strength of the bent system, an approach which considers each connection to constitute 25% of the overall pushover force required for the system was established. Considering the previously established safe operating force for the lab (60-70-kip) a target force of 15-kip is considered for the design of each pier connection. This 15-kip force is considered as the base shear force for each connection. With a reinforcing ratio of 2% the longitudinal reinforcing steel is

determined to be seven #6 Grade 60 rebar. Grade 60 rebar has a yield strength of 60 ksi and modulus of elasticity of 29,000 ksi. Additionally, in accordance with AASHTO design a continuous reinforcing spiral is provided throughout the length of the column. The #3 Gr. 60 reinforcing spiral is broken at both the footing-to-column and column-to-cap interface, with the spiral continuing in both the footing and cap for the full length of the longitudinal reinforcing. The #3 spiral is terminated at each end by mechanical splice. The #3 spiral is spaced at a constant pitch of 1.5 in. throughout the full length of the longitudinal reinforcing. The required cover concrete of 1.5 in. is provided between the reinforcing spiral and column surface.

The resulting connection capacity is thus calculated considering a normal weight concrete with compressive strength,  $f'_c$ , of 4,000 psi. The column design moment capacity of approximately 61.7-kip-ft. is calculated. Considering the loading height to the actuator center of 83-3/4 in. from the footing surface, the resulting design base shear is 8.8-kip. The ultimate base shear is 13.6-kip which is 91% of the target base shear per connection as discussed above. Note threaded terminators are used in the cap to develop the required embedment strength where reinforcing congestion makes it difficult to utilize hooks or bends for producing development length. A column cross-section is provided in Figure 56 below, with a column detail in Figure 57.

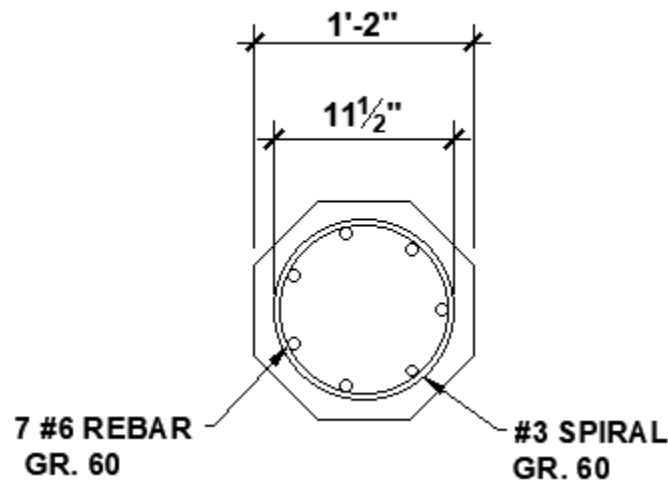
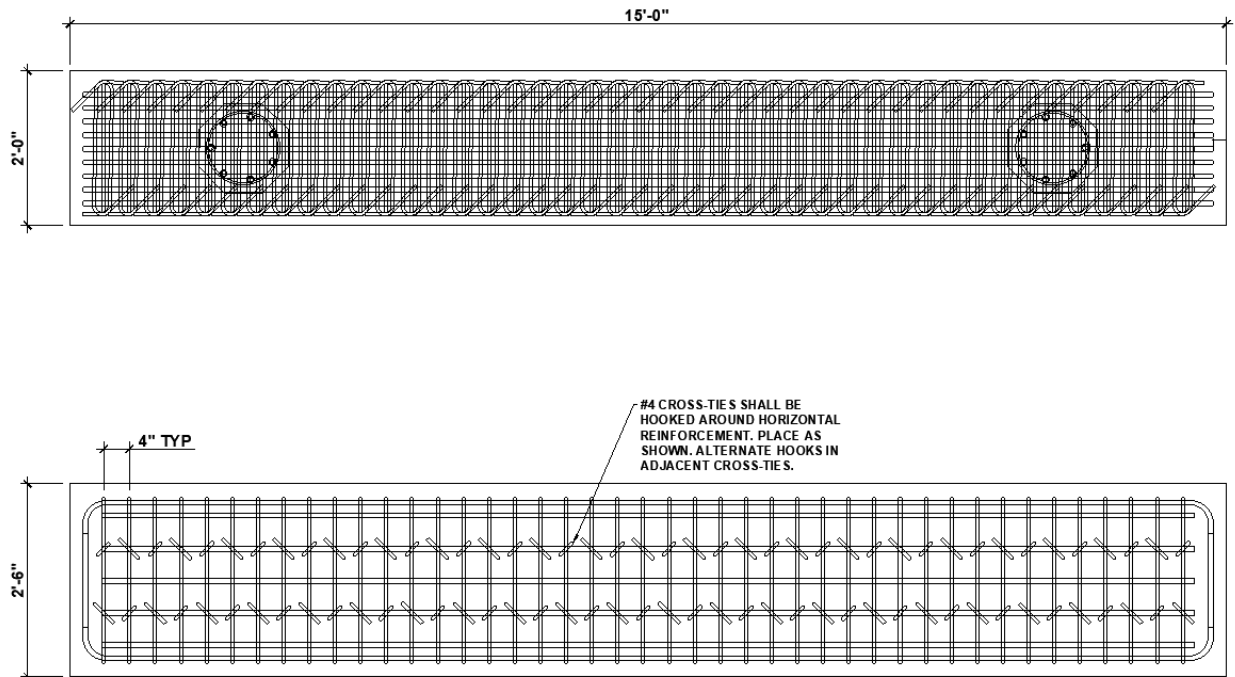


Figure 56. CIP Pier Detail



conservative approach is taken to ensure failure is forced to the columns the design moment and shear is taken to be 500-kip-ft. and 150-kip, respectively. The design process using concrete of compressive strength of 4,000 psi, yields a required 11 #6 Gr. 60 rebar be provided at the top and bottom with #4 Gr. 60 stirrups provided at 4 in. center-to-center spacing. Additionally, as per ITD general practice two alternating #4 Gr. 60 cross-ties are provided for each stirrup. Figure 58 and Figure 59 provide the final CIP cap beam drawings. Cap beam and cap beam to column panel zone or connection can be designed using strut and tie method for shear reinforcing.



**Figure 58. CIP Cap Beam**

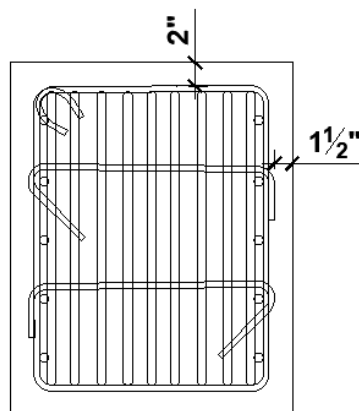


**Figure 59. CIP Cap Beam Cross-Section**

The footings are similarly designed in a conservative fashion to ensure failure is forced into the columns. As the footing dimensions are largely controlled by the lab and proposed precast connection requirements, the reinforcing is determined as 10 #6 Gr. 60 rebar provided at the top and bottom in each direction. Using Response-2000 the footing is calculated to have an ultimate moment capacity of 532-kip-ft providing a significant factor of safety over the moment demand created by the pier connection. Figure 60 provides a top view of the footing and rebar layout for the bent system.

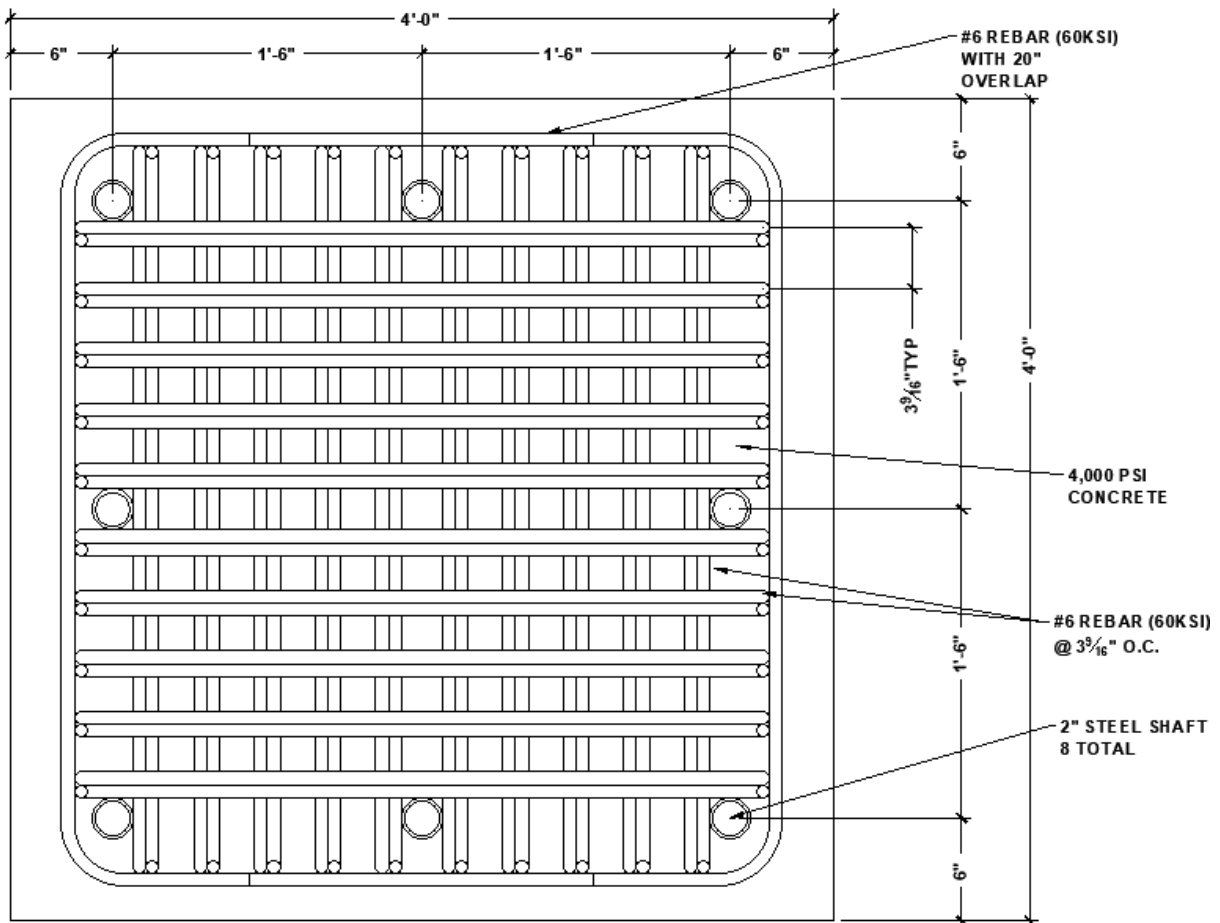
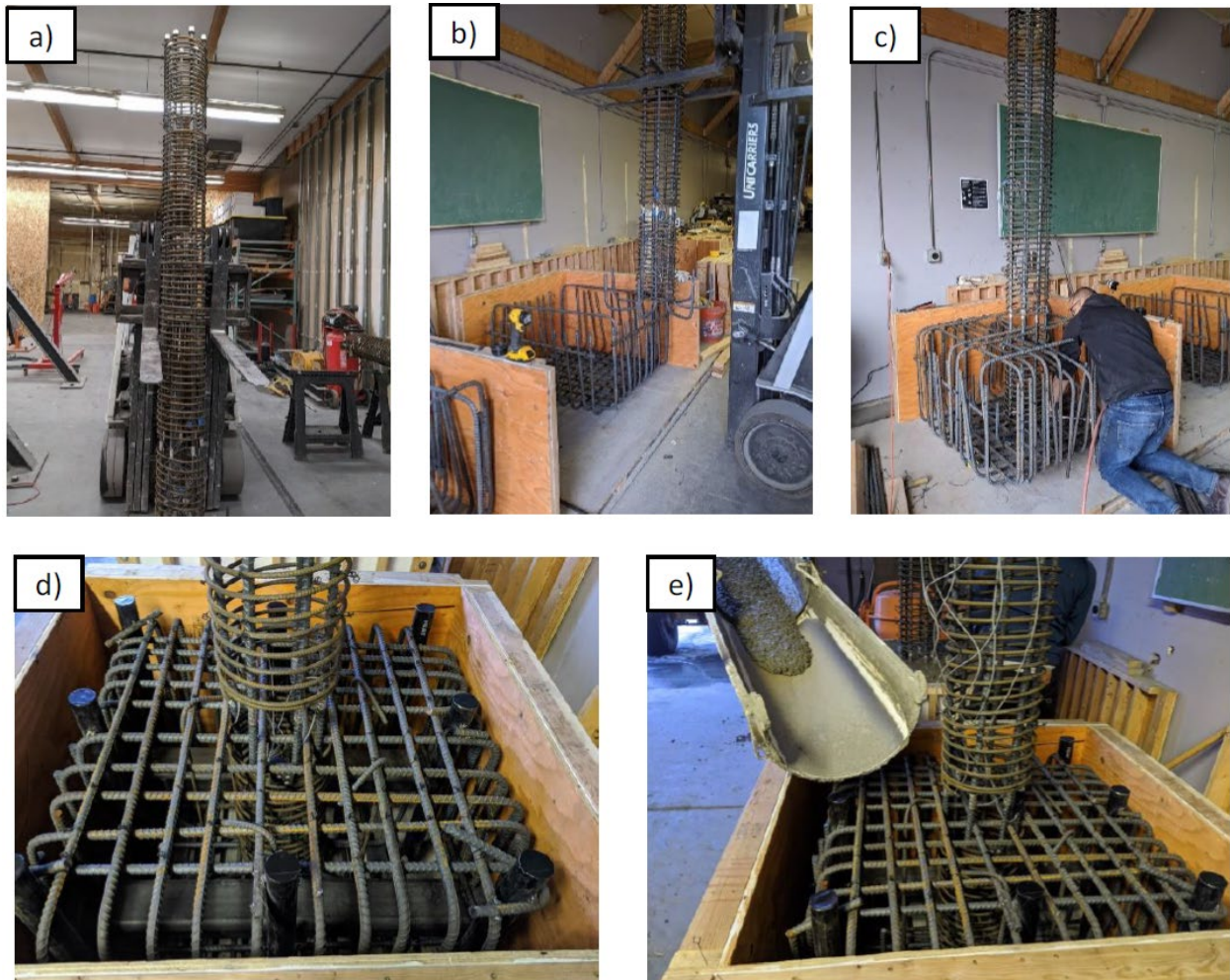


Figure 60. CIP Footing

## Construction

After determining the final dimensioning and design details, the CIP construction began. Typical CIP construction is performed completely onsite with multiple in-place concrete pours taking place. For construction of a bent substructure there are three main pours, footing, columns, and cap. Forming and rebar fabrication are performed simultaneously throughout the construction. Wood form work is determined as a suitable material as it can serve for both the bents constructed and is considerably more cost effective and less labor intensive than producing steel forms for two specimens.

The footing, longitudinal, and spiral reinforcing in the column is prepared as a singular cage for each individual pier (Figure 61). The column cage is prepared and then lifted into the lower rebar mat of the footing (Figure 61a, b) with the upper mat finished last (Figure 61c). After the footing and column are completed, the sleeves are placed for the floor anchors (Figure 61d). Finally, the concrete is placed, courtesy of Pocatello Ready Mix, finishing the footings up to the footing-to-column interface (Figure 61e) The interface where the column is to be poured is left rough to assist in bonding. The total concrete order for pouring of the footings was 3.25 cubic yards.



**Figure 61. CIP Footing Construction: a) Column Cage, b) Place Column Cage, c) Tying Top Mat, d) Anchor Sleeves, e) Footing Pour**

After footings have adequately cured the form work is removed and the footings are relocated to the SLAB where they are anchored in place (Figure 62). The column spiral is checked for proper placement and secured. For the pouring of the columns in order to follow proper concrete placing procedures the pier form work is built in two 3 ft. segmental sections, which can be assembled during pouring. This ensures the concrete is not dropped at too great a distance resulting in segregation and proper vibrating is accomplished throughout the full column. The full 6 ft. of the two columns are poured so as not to have

a cold-joint present in the length of the column. At 7 days the pier formwork is removed allowing for the cap pour preparation to begin (Figure 63). The pour for the two columns was a total of 1 cubic yard.



**Figure 62. CIP Footing Placement**

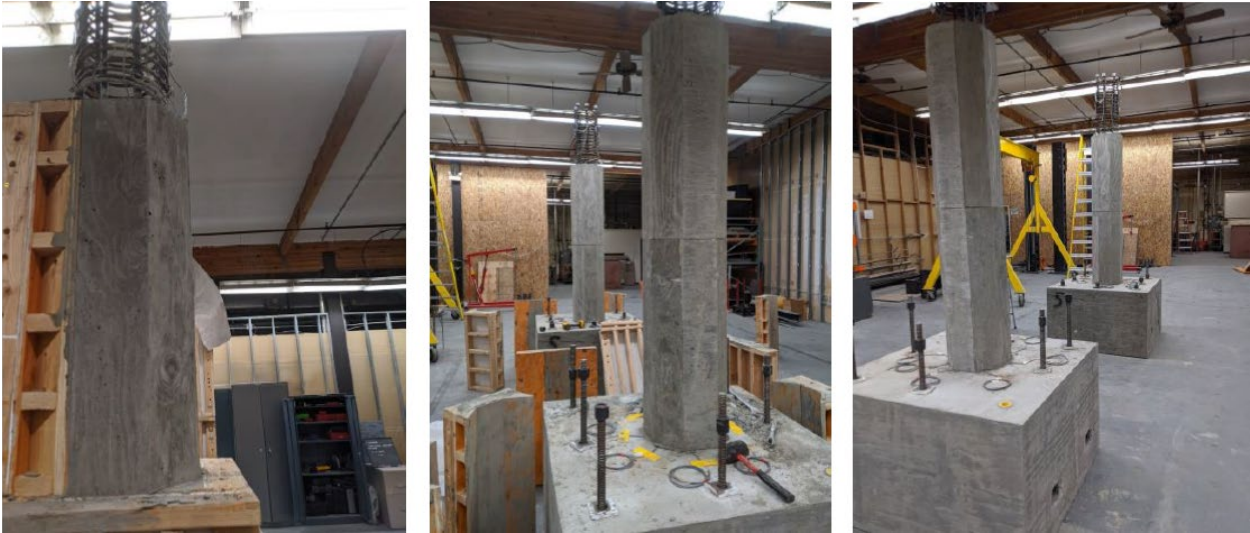


**Figure 63. Completed CIP Pier**

As the cap has to be poured in the lab at a height of 8 ft-6 in., false-work for supporting the concrete during initial curing is necessary. Making use of existing items in the lab proved the most efficient way to construct false work. Figure 64 provides a view of an assortment of reaction frames and sections serving to provide the necessary false work for completing the cap pour. The cap reinforcing cage is started on the ground (Figure 65a) and lifted into place over top the longitudinal column reinforcing (Figure 65b). Then the final stirrups, cross-ties, form-work, and false-work is placed for pouring (Figure 65c)



Figure 64. Cap False-Work



Figure 65. CIP Cap Construction: a) Cap Cage, b) Cap Cage Placement, c) Cap Complete False-Work, Cage, and Formwork

The full cap, measured to be a total of 75 cubic feet of concrete and estimated to weigh 11,000 lbs., is completed in a single pour to eliminate cold joints (Figure 66). The completion of the cap marked the final pour required for the construction of the CIP bent system. The total CIP bent is constructed of approximately seven cubic yards and estimated to weigh in the range of 26,500 lbs. to 28,000 lbs. After the cap had adequately cured the false-work and formwork is removed, the specimen is painted, and prepared for instrumentation (Figure 67).



**Figure 66. Completed Cap Pour**



**Figure 67. CIP Bent Prepared for Instrumentation**

## Testing Arrangement

After the CIP bent construction is completed the testing arrangement is erected. For the purposes of testing the connection, a uniaxial load is applied in the transverse or perpendicular direction of the bridge deck. The purpose for loading in this direction is due to a full bridge structure being weak in the transverse direction. This is based upon the assumption that a full bridge, including the superstructure, has significantly higher resistance to loading parallel to the superstructure as the bridge integral abutments provide adequately stable resistance to such loading. An additional vertical load is applied to the system during the entire testing procedure serving as a gravity simulant.

The lateral load is applied cyclically in accordance with the American Concrete Institute (ACI) (ACI Committee 374 2013) via a hydraulic servo-valve actuator. The actuator is a 2.5 gallon-per-minute (gpm) servo-valve actuator with a total achievable stroke of 24 in. A 225-kip tension/compression loadcell is mounted in-line with the horizontal actuator in order to monitor the actuator force during the experiment. The actuator is mounted horizontally to the reaction frames. The reaction frames are comprised of two identical columns fabricated of steel channel, C12x30, laced together with 0.25 in. flat plate. Additional channel and wide flange angle bracing are provided to support the columns. In total the reaction frame is anchored to the floor via twenty-four 1 in. diameter high strength threaded rods (Figure 69). The head of the actuator is attached to the cap beam using four 1 in. diameter 120 ksi all thread. During casting of the cap, embedded anchors were fabricated into the cap end. The embedded anchors were provided additional anchoring support in the cap via high strength threaded rod connected to an anchoring plate embedded 12 in. into the cap beam (Figure 68). The specimen itself is secured rigidly to the SLAB strong floor using nine 1 in. rods. The foundations are assumed to be rigidly fixed disallowing soil-structure interaction effects during the testing.

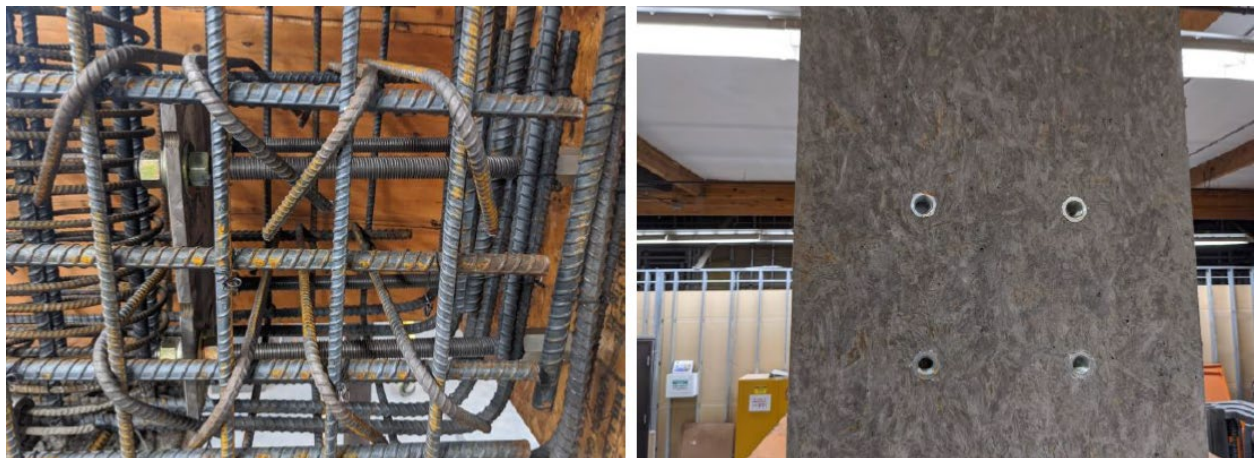


**Figure 68. Actuator Cap Anchors**

The final phase of the testing arrangement is the application of the gravity load applied vertically at the center of the cap beam. The vertical force of the gravity load corresponds to 4.5% of the axial compressive capacity of the columns. Typically, the target gravity load is 5% of the axial compressive capacity of the

specimen, but due to equipment limitations and the limited 3000 psi hydraulic pump the highest achievable axial ratio is 4.5%. For the two 14 in. columns of 4 ksi concrete, the gravity load is determined as approximately 60-kips. The equation for determining the gravity force is given as:

$$\text{Gravity Force} = 0.045(A_g f'_c)$$

Where:

$A_g$  = Gross cross-sectional area of the two columns, in<sup>2</sup>

$f'_c$  = Compressive strength of the concrete, ksi

The gravity force is applied using a 100-ton 4 in. hollow jack. The jack is placed on the bent cap, a 225-kip tension/compression loadcell is stacked on top of the jack, and a reaction beam is placed across the top of the loadcell. Two high strength all thread bars are used to bolt the reaction beam to the floor to provide the resisting downward force to the cap. The full test setup is provided in Figure 69 below.

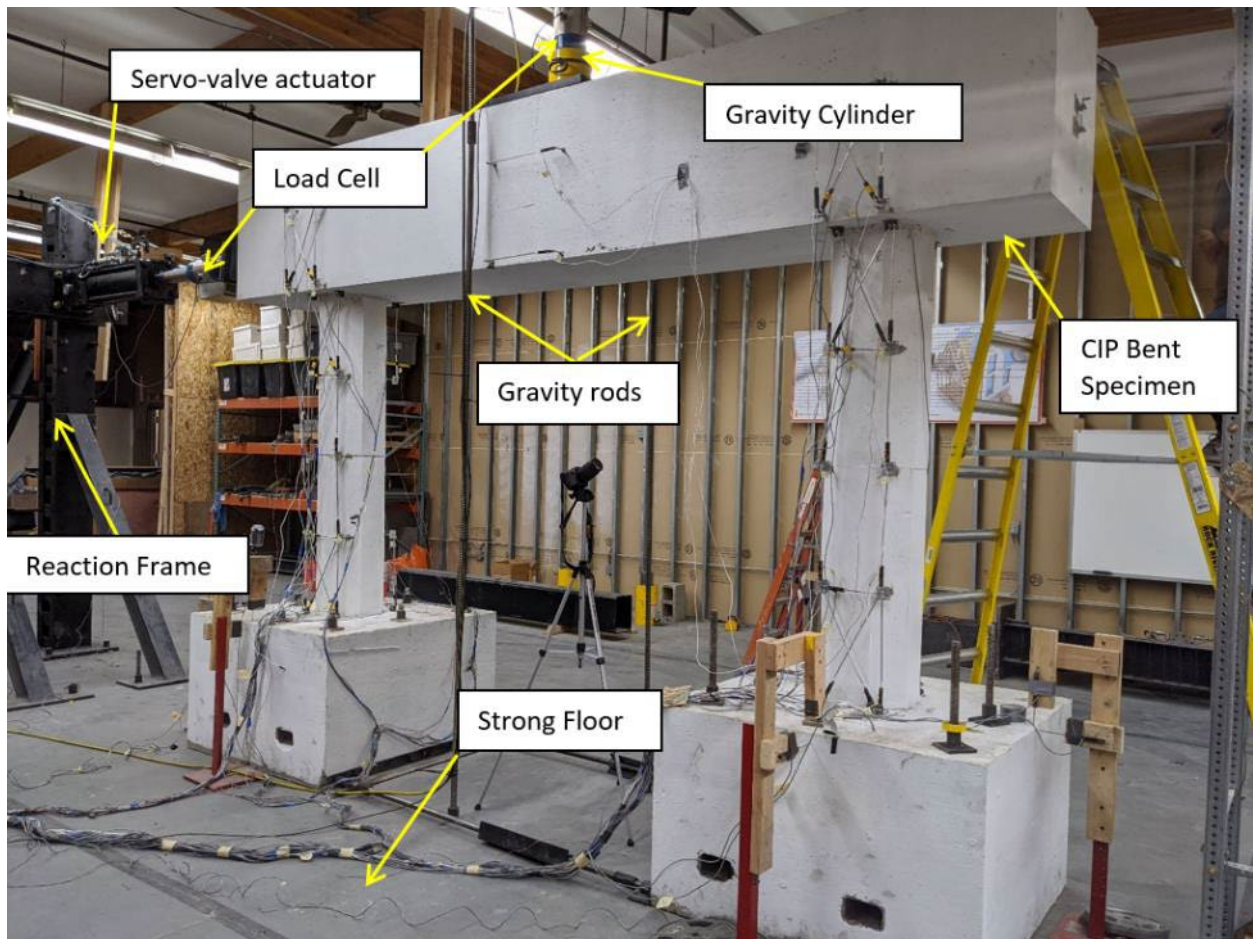


**Figure 69. CIP Bent Testing Arrangement**

## Instrumentation

Throughout the experiment specific measurements of the system are monitored in order to document the specimen's response and characterize its overall performance. Various instruments are used including loadcells, linear potentiometers, string potentiometers, and strain gages. The instruments are programmed using a Campbell Scientific data acquisition system. The system is uniquely programmed for all the instruments and set to take five readings per second throughout the experiment. A total of 95 total instruments are used during the experiment. Figure 70 to Figure 72 provides a visual of the instrumentation layout on the CIP specimen. Note all instrumentation specifically associated with either the north or south pier are indicted as "XX-N" and "XX-S", respectively.

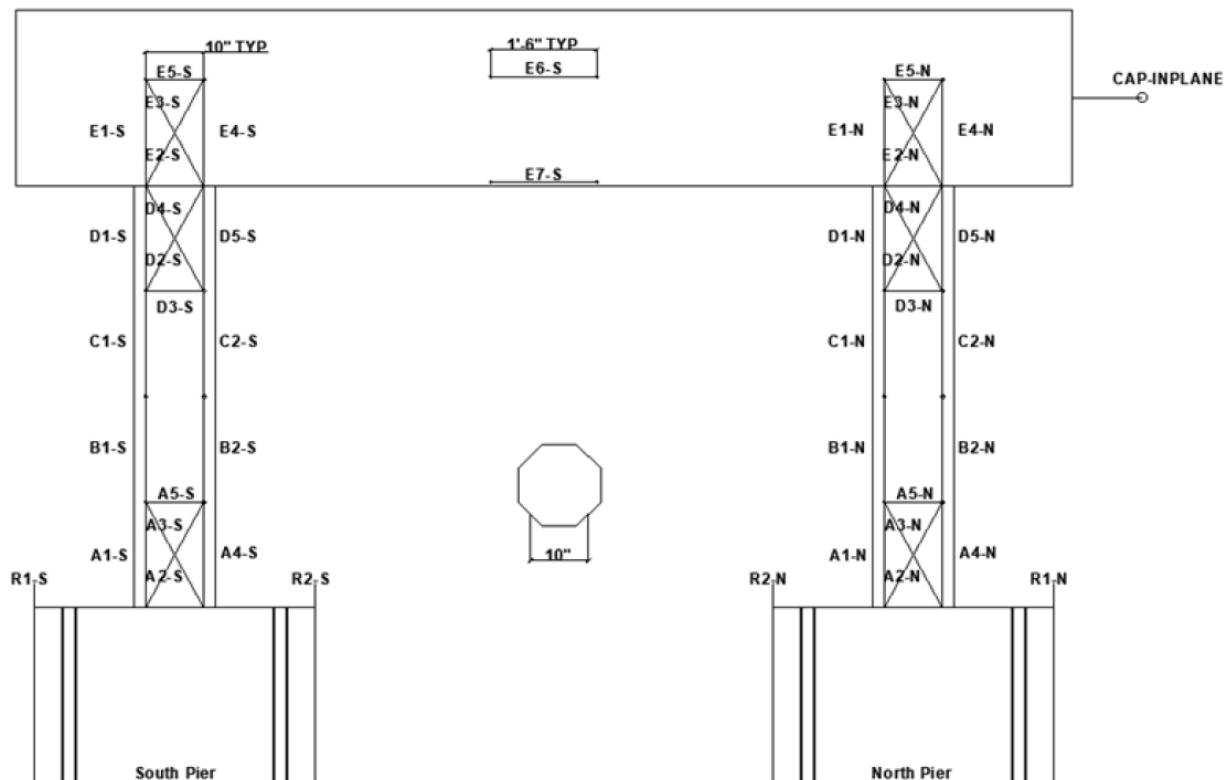
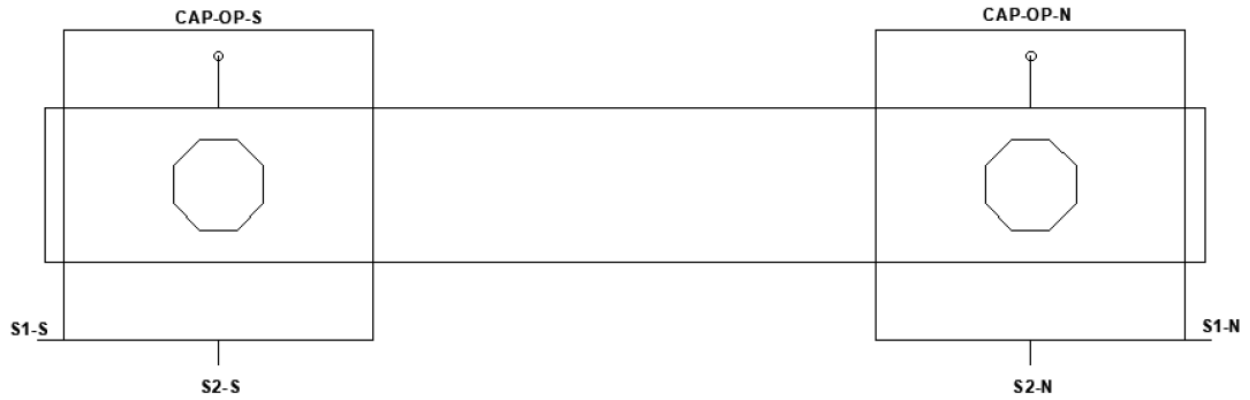
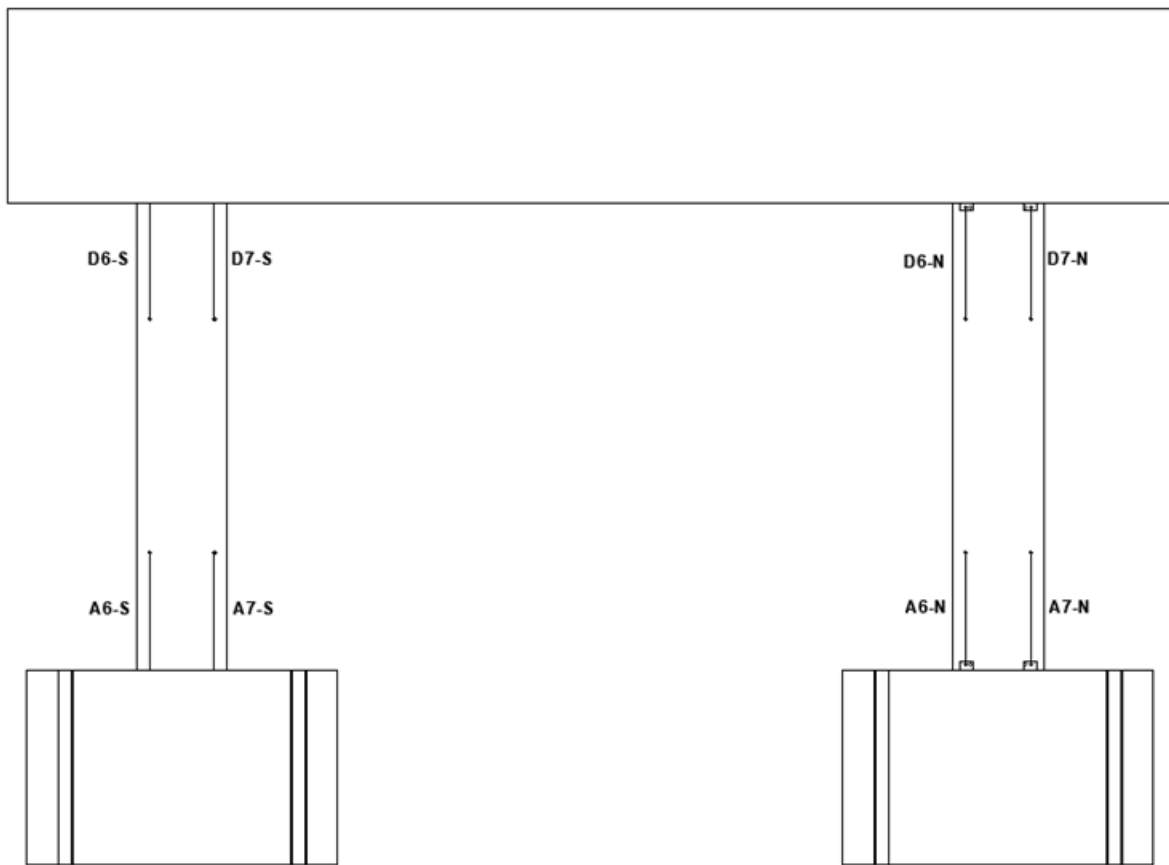


Figure 70. CIP Instrumentation Layout: Front Elevation View



**Figure 71. CIP Instrumentation Layout: Top View**



**Figure 72. CIP Instrumentation Layout: Rear Elevation View**

Specific instruments are mounted as such to measure the global movement of the specimen. These instruments are mounted independent of the specimen and test arrangement in order to provide a true displacement of the specimen. The instruments mounted independently include CAP-INPLANE, CAP-OP-S, CAP-OP-N, R1-N, R2-N, R1-S, R2-S, S1-N, S2-N, S1-S, and S2-S. The instrument labeled CAP-INPLANE is a

string-potentiometer, used to measure the true displacement of the cap. It is mounted directly at the center of the actuator on the opposite end of the cap beam. As it is assumed the cap does not experience any noticeable compression during testing, this measurement is used as the true displacement of the specimen. CAP-OP-S and CAP-OP-N are string potentiometers used to monitor the out-of-plane motion of the cap. These measurements are predominately monitored to ensure the cap does not move excessively to one side or the other during testing. Monitoring of this measurement reaffirms the stability of the specimen throughout the experiment and helps to monitor the risk of out-plane collapse. Linear spring potentiometers are used for measurements R1-N, R2-N, R1-S, R2-S, S1-N, S2-N, S1-S, and S2-S. The “R” refers to “rocking” as these instruments are mounted vertically, or parallel to the piers, to monitor any lifting of the footing edges, both in- and out-of-plane. Similarly, “S” refers to “sliding” as these potentiometers are used to monitor sliding of the footing in both the direction of loading and the transverse direction. Additionally, a string potentiometer is attached to the actuator to confirm the true stroke of the actuator itself. As this is a non-independently mounted instrument it is simply used to confirm the motion of the actuator head.

Instruments occupying groups “A” through “E” are comprised of both linear spring potentiometers and linear potentiometers with aluminum extensions. The group “A” potentiometers monitor the plastic hinge zones located at the base of each column. Group “D” and “E” potentiometers monitor the plastic hinge zones located at the top of each column. Groups “B” and “C” are used to monitor any curvature experienced by the column falling outside of the plastic hinge zones.

Additionally, two 225-kip tension/compression loadcells are used to monitor the lateral load and vertical gravity load induced on the specimen. Finally, elongation of the rebar is monitored using strain gages. Strain gages are attached to the longitudinal reinforcing bars just above the footing-to-column interface and just below the cap-to-column interface prior to pouring concrete.

## **Loading Protocol**

As mentioned earlier the loading protocol for the specimen is determined in accordance with the ACI (ACI Committee 371 2013). The quasi-static cyclic loading protocol is based off the yield displacement of the bent itself. Figure 73 shows the loading protocol given as a graph of cycle number versus the drift ratio.

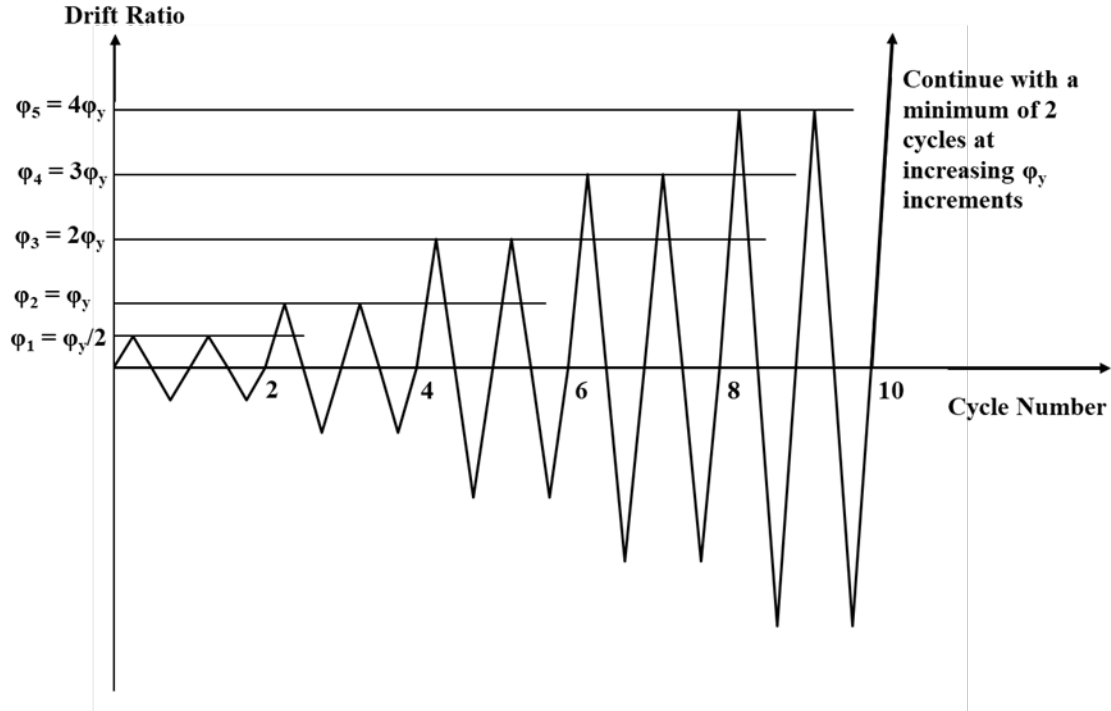


**Figure 73. ACI Loading Protocol**

Determination of the yield displacement is derived using an equation provided by the Priestley et al. (2007) as shown Figure 74. Given the following two equation yield displacement,  $\Delta$ , is calculated:

$$\Delta_y = \Delta_{y1} + \Delta_{y2}$$

$$\Delta_{y1} = \phi_y \frac{(L_1 + L_{sp})^2}{3}$$

$$\Delta_{y2} = \phi_y \frac{(L_2 + L_{sp})^2}{3}$$

Where:

$\Delta_{y1}, \Delta_{y2}$  = Yield drift for each short column, in.

$\phi_y$  = Curvature in the column corresponding to the first bar yield point, in<sup>-1</sup>

$L_1$  = Column height, in.

$L_{sp}$  = Strain Penetration Length, in.

$\phi_y$  and  $L_{sp}$  were then obtained for a conventional CIP constructed column using equations below:

$$\phi_y = 2.25 \frac{F_{ye}}{ED}$$

$$L_{sp} = 0.15 F_{ye} d_b$$

Where:

- $F_{ye} = 1.1$  times the yield strength of steel; Yield strength of steel, 60 ksi
- $E =$  Modulus of elasticity of steel, 29,000 ksi
- $D =$  Diameter of the column, 14 in.
- $d_b =$  Diameter of reinforcing longitudinal bar, in.

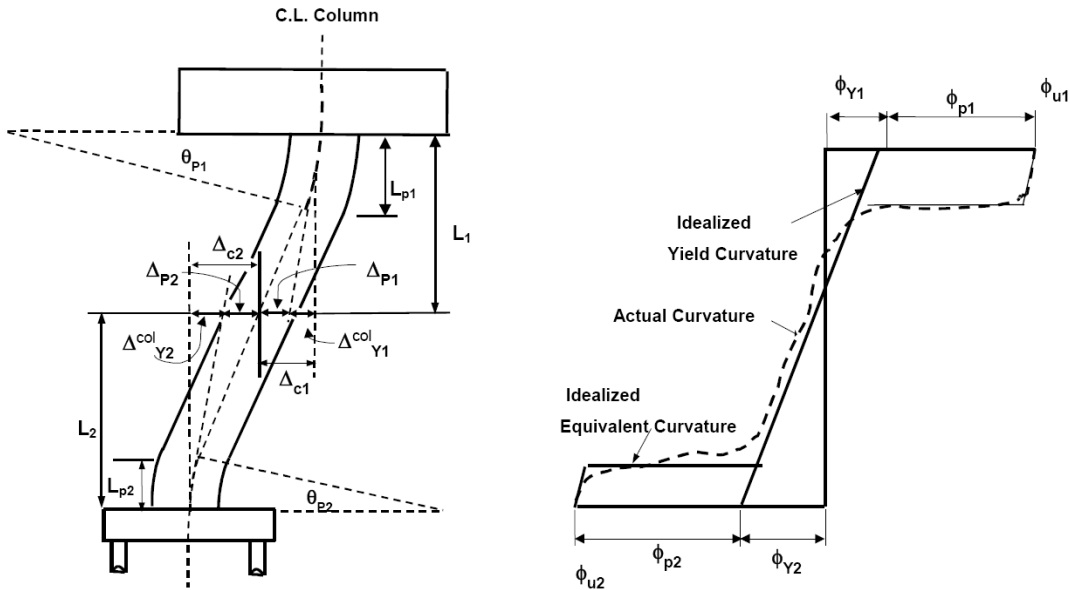


**Figure 74. Displacement Capacity of a Pier in a Bent with Fixed-Fixed Supports (Caltrans 2013)**

Considering the above equations as applied to the CIP specimen with a column diameter of 14 in. (for design) and comprised of #6 longitudinal reinforcing, a resulting yield drift total of 0.46 in. is determined. So, 0.35 in. is used for the programming of the actuator controller to ensure two cycles are performed prior to reaching yield for instrumentation and test set up tests.

From the determination of the yield displacement the final loading protocol used is determined and graphed, as shown in Figure 75. During the testing, a loading rate of 1 mm/sec is used. As the yield displacement is multiplied for each set of additional cycles, time is taken to observe the response of the specimen during each two-cycle set. The cycles are continually increasing in displacement magnitude until the bent demonstrates a 20% degradation in strength or is determined to be unsafe for continued loading due to possible collapse.

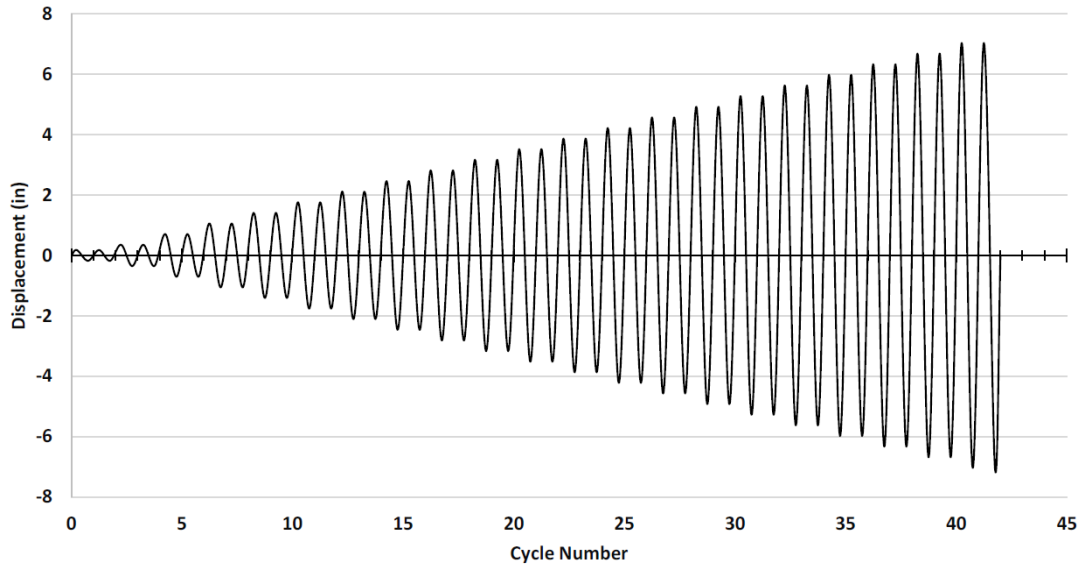


**Figure 75. CIP Bent Loading Protocol**

## Material Properties

Following the completion of testing, the concrete samples prepared during each stage of pouring had to be tested to confirm the concrete properties on test day. Three concrete samples from the footing, pier, and cap pours were tested to verify the respective compressive strength of the concrete. Also, two split tension cylinder samples were tested. The 28-day compressive strength of concrete,  $f'_c$ , is targeted to be 4000 psi. However, the laboratory testing of the concrete did not show the desired compressive strength of columns and cap which could be because of the problems associated with the way concrete was mixed in the concrete yard which is common. Table 12 and Table 13 provide a summary of the test day compressive strength and split tension results, respectively.

**Table 12. CIP Bent Test Day Compressive Strength**

Sample	1	2	3	Average (psi)
Footing	6974	7186	7121	7094
Columns	2994	3211	3535	3247
Cap	3084	3276	3266	3209

**Table 13. CIP Bent Test Day Split Tension**

Sample	1	2	Average (psi)
Footing	533	603	568
Columns	352	427	390
Cap	443	374	409

## Testing Results

Starting the experiment at the first cycle of  $\pm 0.18$  in., cracks formed at the interface of the column-to-footing and column-to-cap (Figure 76a). Hairline cracking began in only the face of the column away from the actuator, noted as the “North” pier for instrumentation purposes, during the second cycle. The interface cracks widened during this cycle as well. During the third cycle hairline cracking developed at all connections, with the furthest forming up to 19 in. from the interface (Figure 76b). During the fourth cycle cracks measuring 0.0157 in. (0.4 mm) began to open within 12 in. of the interfaces (Figure 76c). Additionally, hairline cracking was extended up to 26 in. from the interface. The cracks at the interface then continued to widen. During the fifth cycle spalling began developing at the column top connections with cracks developing continuing throughout the column. The cracks in the column face were opening as wide as 0.0394 in. (1 mm) while in tension. The sixth, seventh, and eighth cycles saw continued crack development up to 0.0984 in. (2.5 mm) and additional slight spalling at the connection faces (Figure 76d). The ninth cycle is the first which concrete spalling developed at the base column connections (Figure 76e). The ninth cycle is also where the largest measured force, approximately 66-kip, takes place. From this point forward, the specimen strength begins to degrade.

The tenth, eleventh, and twelfth cycles saw cracking continue to develop and spalling develop to exposure of the spiral reinforcing at the top of the column near the actuator (Figure 76f). It is during the fourteenth cycle which exposure of the longitudinal reinforcing occurred at the top of the column near the actuator (Figure 77g). The fifteenth and final cycle results in the fracture of longitudinal reinforcing at the top connection of the column nearest the actuator resulting in a significant drop in lateral force (Figure 77h). Having the fifteenth cycle finishing with a max lateral force of 53-kip (80% of greatest lateral force experienced) the test was completed.

An item of note during the test is the flex experienced by the reaction frame. This constituted to a lower achieved specimen displacement that targeted at each cycle. This is due to the inability of the reaction frame to be completely rigid against the lateral force of the actuator. Table 14 provides a recap of the target values programmed for the actuator and the actual displacements experienced by the specimen, as measured by the independent string potentiometer labeled CAP-INPLANE. The ultimate drift achieved by the bent prior to 20% strength degradation was 4.94%. This is comparable to the targeted displacement programmed for the thirteenth cycle. Also, from observing the actual displacements it can be seen that the yield drift was achieved on the third cycle rather than the second as targeted by the program. This is important to note as the specimen experienced an extra cycle at a very low drift of 0.11%.

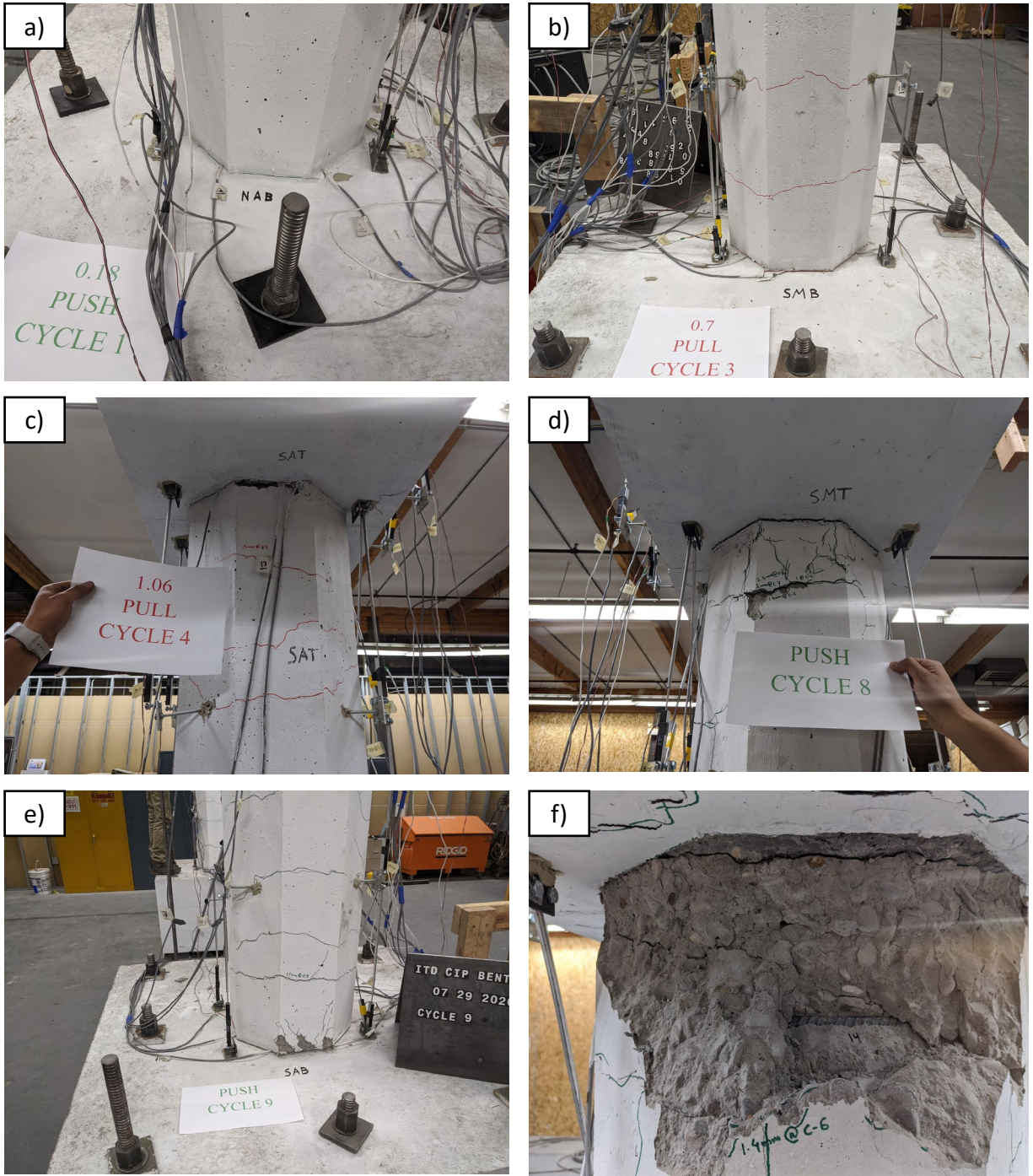


**Figure 76. CIP Bent Testing: a) Cycle 1: Interface Cracking, b) Cycle 3: Hairline Crack Development, c) Cycle 4: 0.0157 in. (0.4 mm) Crack Development, d) Cycle 8: Spalling and 0.0984 in. (2.5 mm) Cracking, e) Cycle 9: Base Connection Spalling, f) Cycle 13: Spiral Exposure**

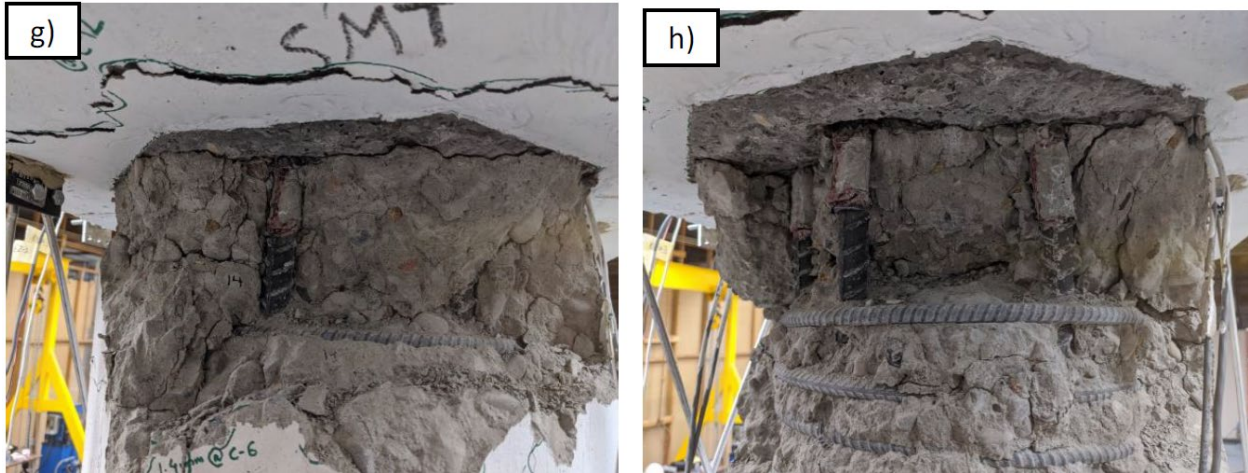


**Figure 77. CIP Bent Testing: g) Cycle 14: Longitudinal Exposure, h) Cycle 15: Longitudinal Rebar Fracture**

**Table 14. CIP Bent Loading Protocol Summary**

Cycle	Programmed Displacement (in.)	Programmed Drift (%)	Actual Displacement (in.)	Actual Drift (%)
1	0.18	0.21	0.09	0.11
2	0.35	0.42	0.15	0.18
3	0.7	0.84	0.35	0.42
4	1.06	1.27	0.56	0.67
5	1.41	1.68	0.86	1.03
6	1.76	2.10	1.08	1.29
7	2.11	2.52	1.4	1.67
8	2.46	2.94	1.73	2.07
9	2.81	3.36	2.06	2.46
10	3.17	3.79	2.4	2.87
11	3.52	4.20	2.75	3.28
12	3.87	4.62	3.1	3.70
13	4.22	5.04	3.44	4.11
14	4.57	5.46	3.78	4.51
15	4.92	5.87	4.14	4.94

The maximums achieved during the testing of displacement and lateral load were 4.14 in. and 66-kip, respectively. The lateral load correlates to total moment capacity of 460-kip-ft. If assumed the four connections shared the lateral load equally, this equates to base shear at each connection of 16.5-kip. Figure 78 and Figure 79 provide Force vs. Displacement and Force vs. Drift hysteresis of the full CIP bent testing. As can be seen the specimen reached its design base shear of 35.2-kip. The hysteresis suggests

the bent yielded at 0.42 in. displacement. Similarly, from the Force-Drift hysteresis it is seen the bent yielded at a drift ration of 0.5%.

As can be noted from the figures, the positive vertical axis shows the specimen in push. As the test began by first pulling the specimen, and continued to begin all cycles in pull, it can be observed the bent had higher strength in pulling than push can be attributed to two factors. The bent underwent softening during the first pull of the cycle thus exhibiting higher strengths in all cycles. Additionally, the reaction frame exhibited slightly higher stiffness during the pulling stage as opposed to experiencing higher displacement during the pushing stage.

Figure 80 provides the resulting Force-Drift backbone curve. The backbone curve is comprised of the peak loads achieved at each cycle. Observation of the curve provides further evidence of the bent performance and its yield progression.

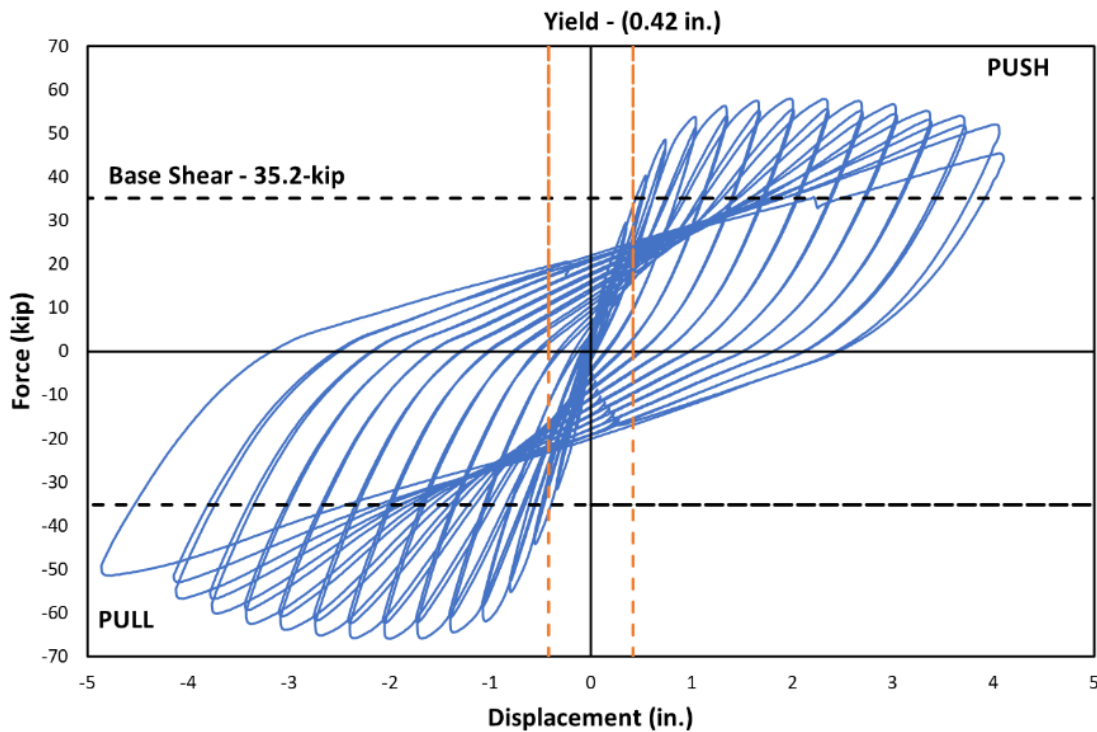


Figure 78. CIP Bent Force-Displacement Hysteresis

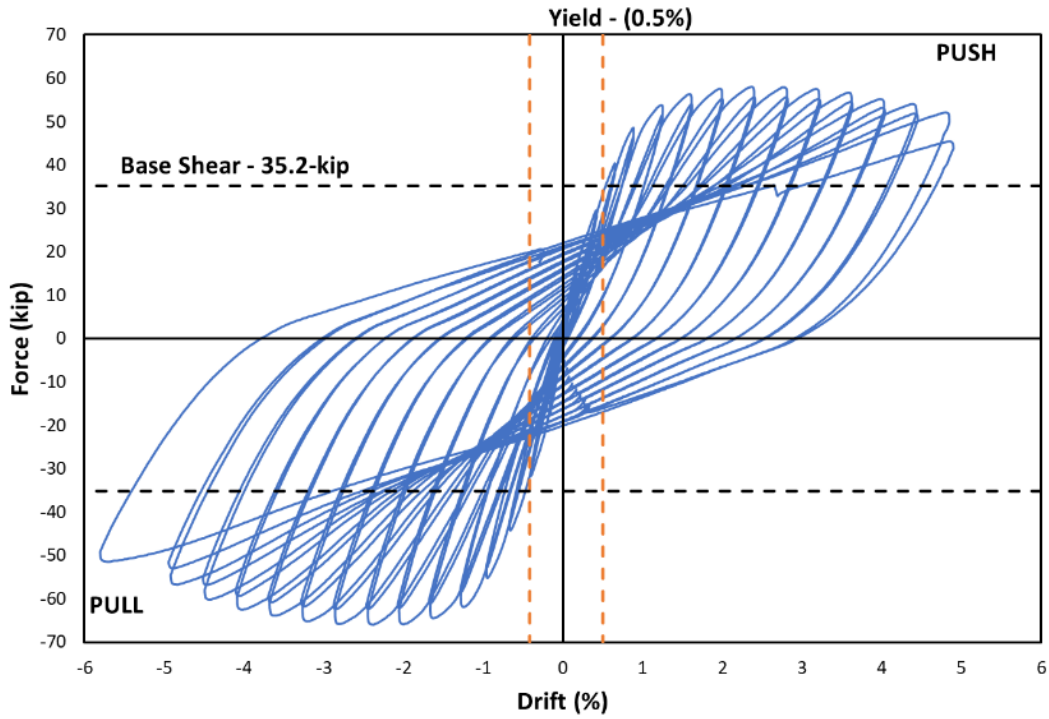


Figure 79. CIP Bent Force-Drift Hysteresis

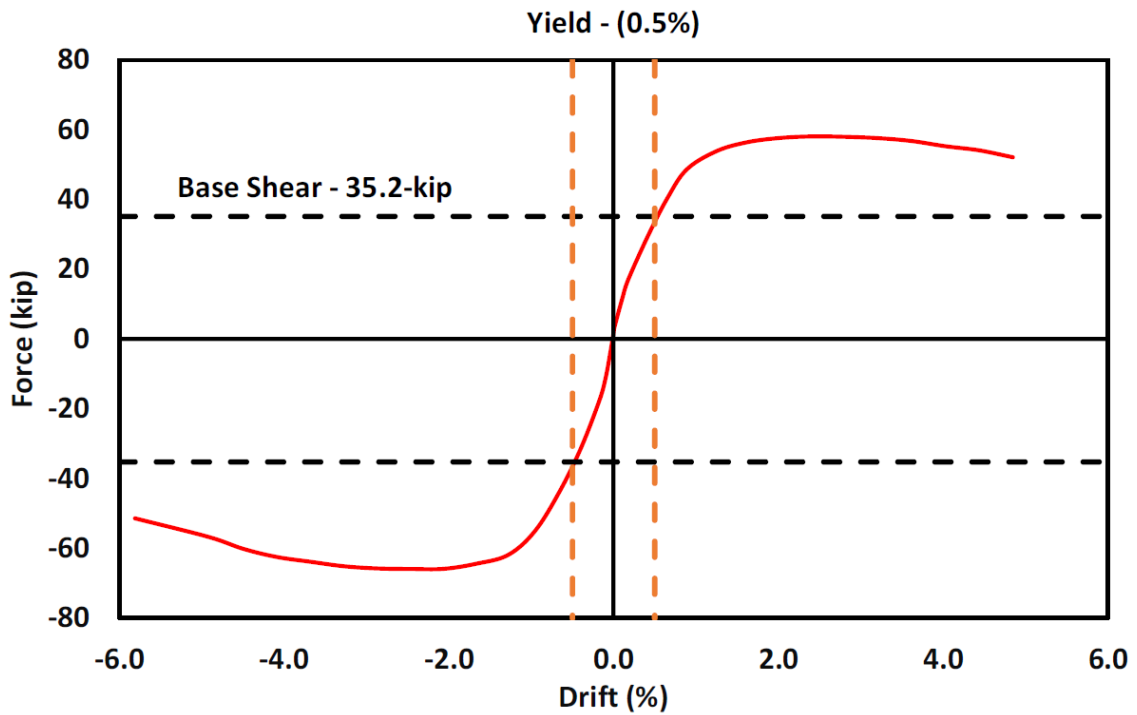
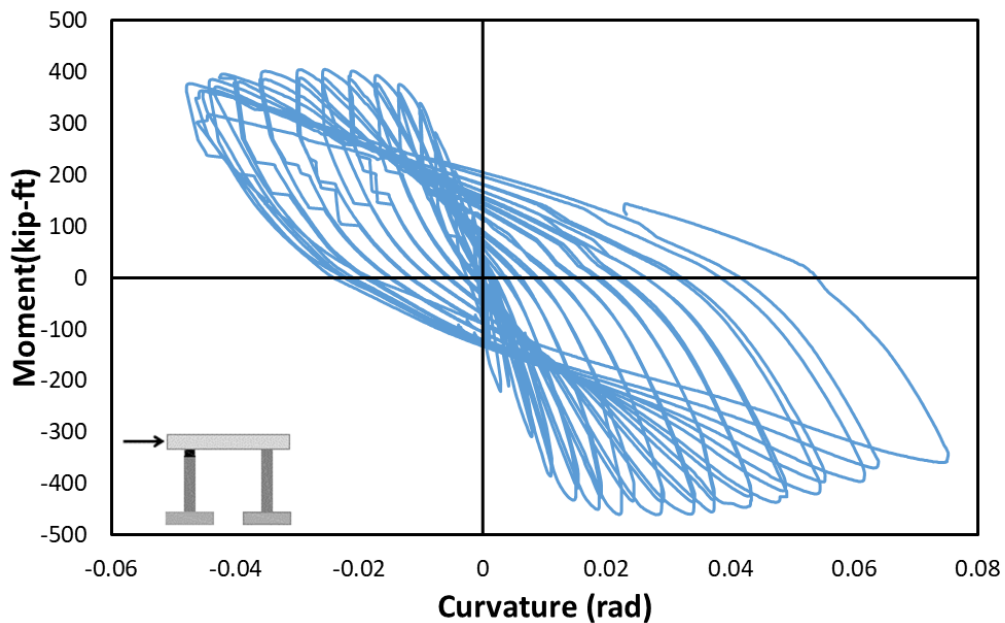


Figure 80. CIP Bent Force-Drift Backbone Curve

Further analysis of the potentiometers, specifically located in the plastic hinge regions (groups A, B, C, and D), provides a close breakdown of each connection's reaction through moment-curvature. The progression of the yield that is captured by the instrumentation at each plastic hinge can be observed in Figure 81 through Figure 84, providing the moment-curvature of each. Observation of the top of the south column (Figure 81) shows a narrower hysteresis produced as opposed to the other connection. This correlates to the level of damage and spalling observed at each connection, with this particular connection being the one to sustain the most and ultimately fail of the longitudinal reinforcing as noted in the previous section. Further observation of the plots shows a consistent increase in the strength degradation at each cycle once the bent reached its capacity. Through comparing the two south column plots to the north plots it can be seen that the south column experienced a higher level of drift correlating to the increased damage observed on the column during testing. Therefore, the observations made during testing have a good correlation with the experimental results collected via the instrumentation.



**Figure 81. South Column: Top (D1-S – D4-S)**

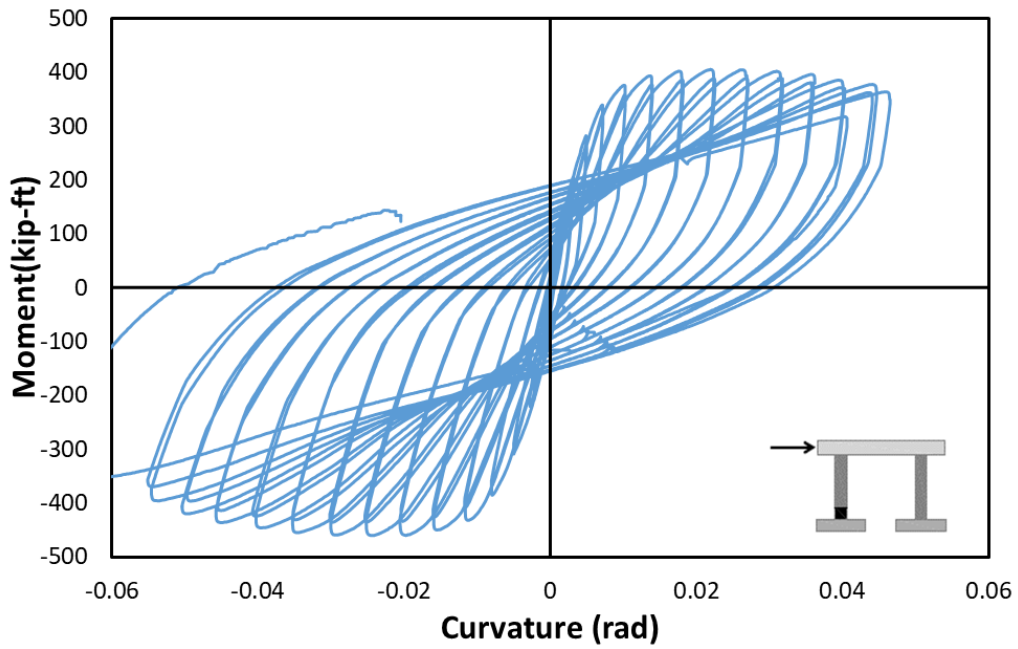


Figure 82. South Column: Bottom (A1-S – A4-S)

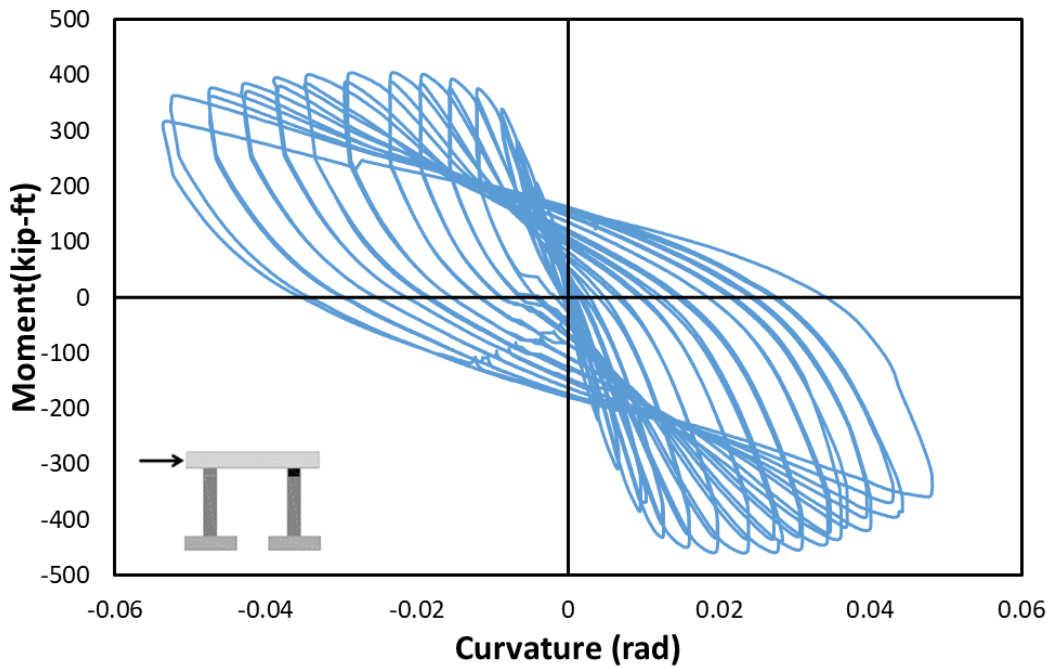
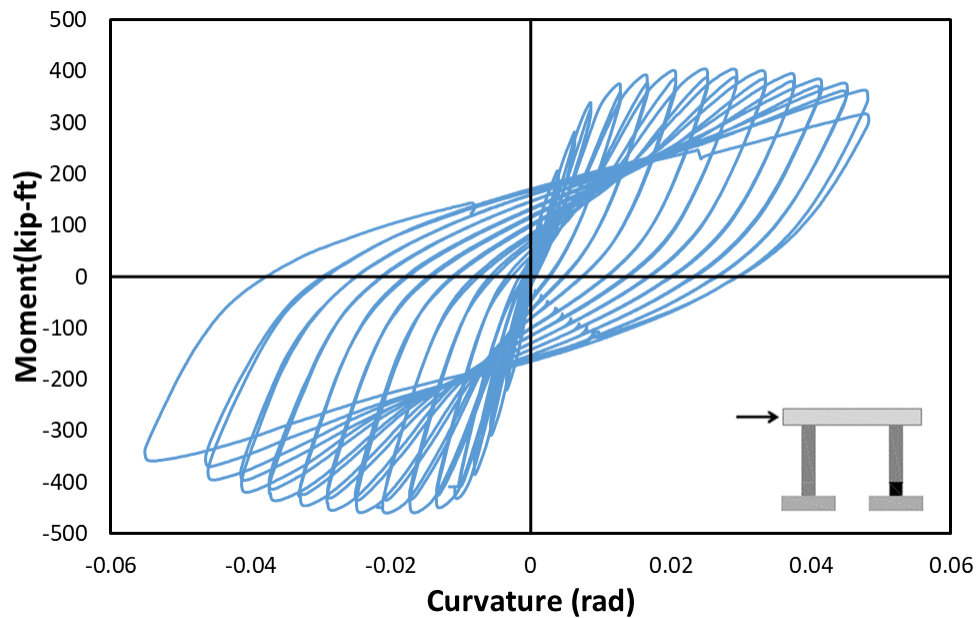


Figure 83. North Column: Top (D1-N – D4-N)



**Figure 84. North Column: Bottom, (A1-N – A4-N)**

The energy dissipated per each cycle drift ratio for the bent is presented in Figure 85. The dissipated energy was calculated using numerical integration of the hysteresis loop at each cycle considering the area enclosed within the loop. To accomplish this a MATLAB program is utilized to break the hysteresis down to individual loops and calculate the enclosed areas, which are then summed together resulting in a “Cumulative Dissipated Energy”. For the CIP bent specimen the resulting cumulative dissipated energy is expressed in kilojoules (kJ). The result is 342 kJ.

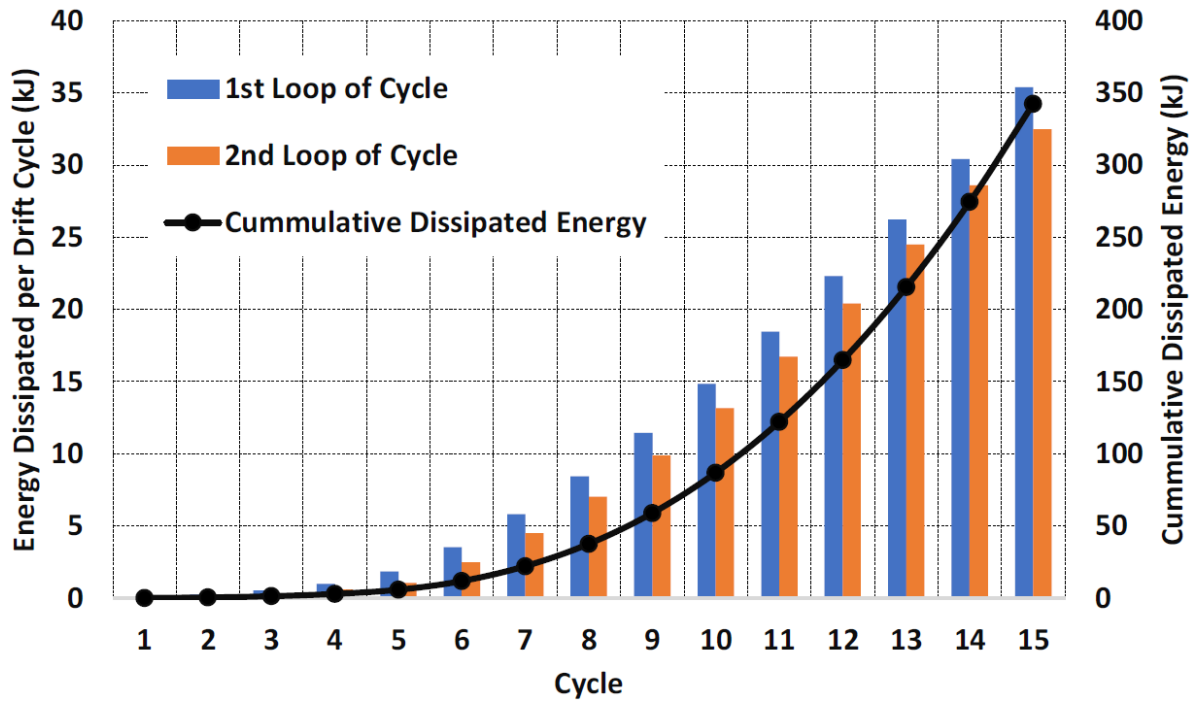


Figure 85. CIP Bent Dissipated Energy per Cycle and Cumulative

Experimental results are used to determine the experimental yield curvature and yield moment by Caltrans Idealized Model (Caltrans 2013). A bilinear approximation similar to the example is provided in Figure 86. The moment capacity can be obtained by balancing the area between the idealized M- $\phi$  and actual. The global yield curvature and yield moment is determined to be  $0.702 \text{ in}^{-1}$  and 380-kip-ft.

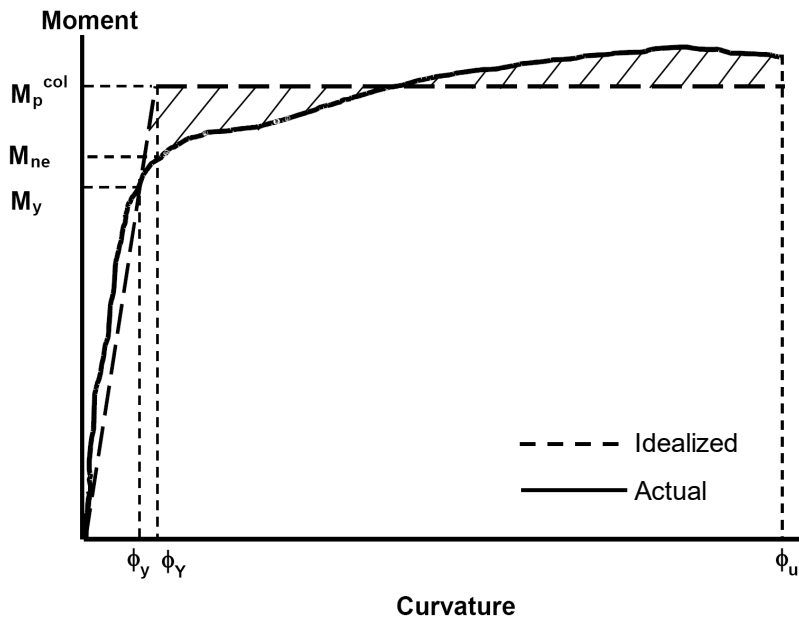
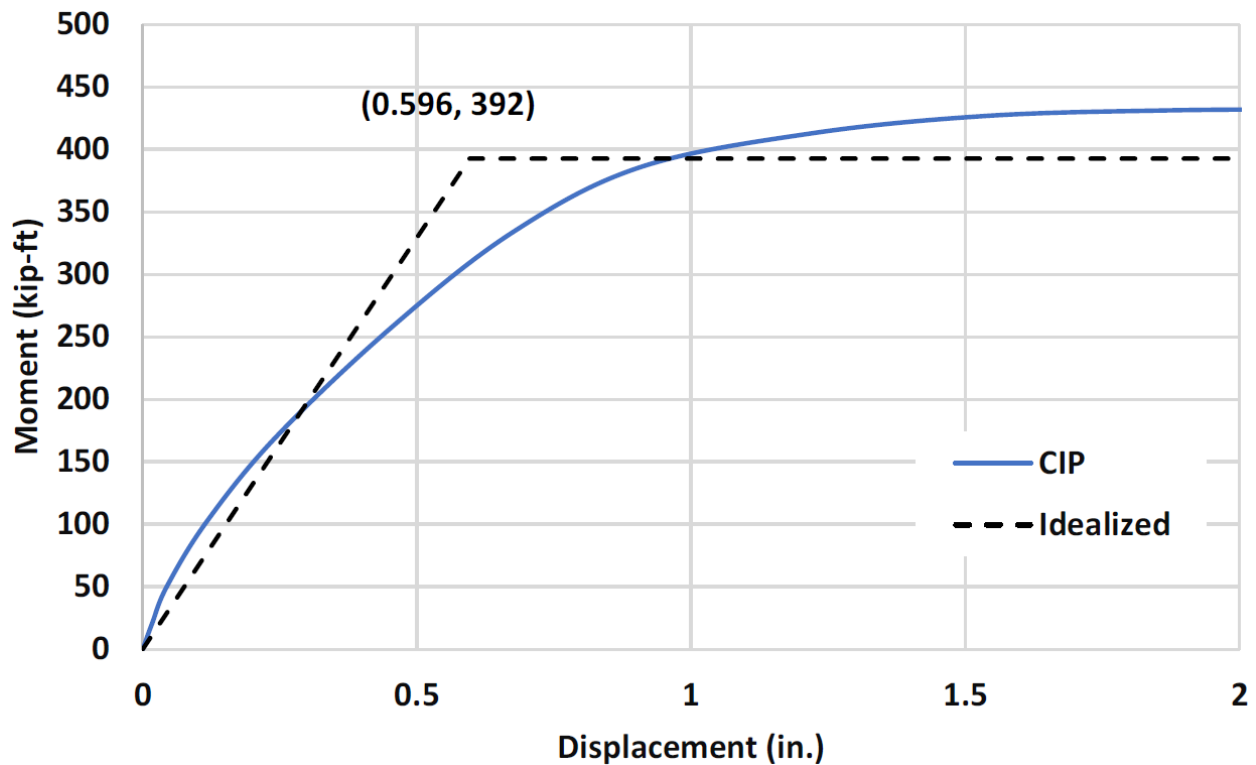


Figure 86. Moment Curvature Curve (Caltrans 2013)

Where:

- $\phi_y$  = Curvature at the first bar yield point ( $\text{in}^{-1}$ )
- $\phi_g$  = Curvature at the global yield point ( $\text{in}^{-1}$ )
- $\phi_u$  = Ultimate curvature at the failure point ( $\text{in}^{-1}$ )
- $M_y$  = Moment capacity at the first bar yield point (kip-ft.)
- $M_p$  = Plastic moment capacity (kip-ft.)

For this experiment the backbone curve is analyzed using displacement in place of curvature providing the following results. The backbone curve average of the push and pull direction is considered. The global yield moment capacity produced from the experimental results is used to obtain the base shear yield of 56.2-kip corresponding to a yield displacement of 0.596 in. The ultimate base shear provided from the backbone curve gives a total base shear of 61.9-kip at a displacement of 2.2 in. The bilinear approximation is shown in Figure 87, below.



**Figure 87. Bilinear Approximation for CIP Bent**

Further analysis of the experimental results allows for the determination of the overstrength factor ( $\Omega_0$ ), an important seismic parameter. The overstrength factor is determined as the ultimate base shear capacity at ultimate ( $V_{ultimate}$ ) divided by the base shear at initial yield ( $V_{yield}$ ). The equation is given below. The resulting overstrength factor of 1.76 is obtained.

$$\Omega_0 = \frac{V_{ultimate}}{V_{yield}}$$

Where:

$V_{ultimate}$  = Ultimate base shear capacity at ultimate, kips

$V_{yield}$  = base shear at initial yield, kips

$\Omega_0$  = Overstrength factor

Displacement ductility is calculated in a similar fashion as seen in the equation below and provides further seismic parameters on the performance of the CIP bent.

$$\mu = \frac{\delta}{\delta_y}$$

Where:

$\mu$  = Displacement ductility

$\delta$  = Displacement at the ultimate base shear point on the backbone plot (in.) for the displacement ductility at the ultimate base shear capacity

$\delta$  = Displacement at  $0.8V_{ultimate}$  in the backbone plot (in.) for the ultimate displacement ductility

$\delta_y$  = Deflection at yield (in.)

Resulting in a displacement ductility of 3.69 for ultimate base shear and 7.48 at failure point.

The residual drift of the CIP bent is presented in Figure 88, reflecting the permanent deformation of the columns after the completion of each cycle. At the point of failure, the CIP bent was maintaining 61.5% (3.04% drift ratio) of the drift applied, 4.94%.

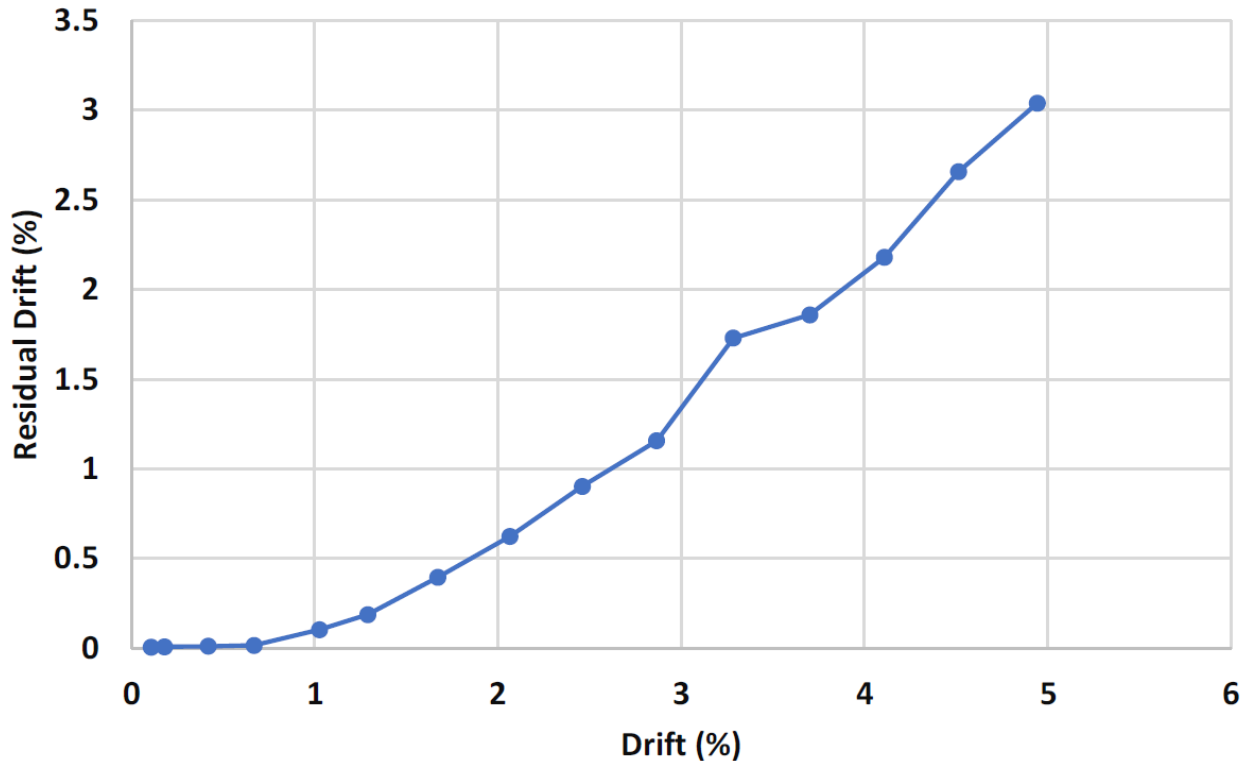


Figure 88. Residual Drift of CIP Bent

## Summary

The CIP bent is fully constructed to simulate the traditional construction and design of a typical mid to long-span Idaho bridge. For this reason, the design followed closely the requirement in AASHTO LRFD Bridge Design Specifications (AASHTO 2017). Similarly, the full specimen is poured in a staged fashion that is seen on a typical CIP construction project using traditional materials and methods. The experimental loading program determined from ACI “Guide for Testing Reinforced Concrete Structural Elements under Slowly Applied Simulated Seismic Loads” resulted in a ductile specimen response. The CIP bent achieved the design base shear of 35.2-kip, correlating with yield drift ratio of 0.5% (0.42 in.) at first yield, with an approximated global yield point of 0.7% (0.596 in.). The system achieved a maximum base shear and total displacement of 66-kip and 4.14 in., respectively. The bent responded similarly in all four column connections, as similar plastic hinges developed at each connection. Ultimately, as the experiment progressed the column nearest the lateral loading actuator began to experience an accelerated degradation of cover concrete thus, on further loading, the longitudinal reinforcing ruptured at the top connection. The failure of the longitudinal reinforcing resulted in a significant strength loss bringing the strength degradation to more than the targeted 20%. With a shear failure eminent in the top connection, the experiment was terminated to ensure a proper level of safety was maintained. The Force-Displacement and Force-Drift plots show the specimen had higher strength in pull as compared to push. This is because the pull cycle is performed first resulting in a softening effect observable in the push of the cycles. This difference in strength is also due to the reaction frame being stiffer in pull than push. Additionally, the total energy dissipated during the experiment by the CIP bent resulted in a total of 342 kJ. The CIP bent resulted in an overstrength factor of 1.76 and displacement ductility values of 3.69 and 7.48 for ultimate base shear and failure point, respectively. Overall, the CIP bent performed as expected.

# Bent Pier System: Precast

## Introduction

This chapter presents the design, construction, and experimental testing of a precast bent system using a proposed column connection by ITD. A review of the construction process is presented discussing the challenges faced during the precast construction and the implementation of the proposed connection and its accompanying aspects. As the proposed connection is comparable to that of CFSTs; a similar approach which closely follows the 2019 WSDOT Bridge Design Manual (WSDOT 2019), is used for design. As a comparison to the CIP bent is to be made aspects such as overall specimen dimensions, testing arrangement, loading protocol, and instrumentation are repeated as they were carried out for the benchmark CIP bent.

## Overview

The proposed connections are to be tested as a precast ABC technology used in bridge substructure column connections. The technology makes use of HSS pipe, suggested to be similar pipe as used in structural piles, with a pipe embedded in both the column and footing/cap. The column pipe is typically protruding half its length from the pier end (Figure 90). The footing/cap has a fully embedded pipe insert of larger diameter designed to accommodate the column pipe into the footing/cap. Figure 89 provides a typical footing detail suited for the proposed connection. The full connection assembly provided in Figure 1 shows a typical footing connection. As opposed to traditional CIP pier it can be seen there is no longitudinal reinforcing to bridge the interface of the two elements. HSS pipe is the only item passing through the footing-to-column interface. The HSS provides the flexural capacity, shear capacity, and confinement for the connection. Figure 2 similarly provides the proposed connection detail for the column-to-cap connection.

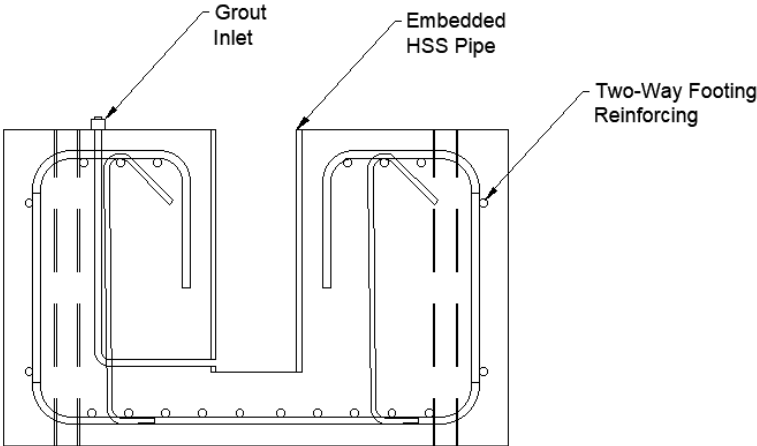


Figure 89. Proposed Connection: Precast Footing Detail

The precast footing was placed directly against the floor. The base connection for this specimen were assumed to be fixed connection and no soil-structure interaction was considered in this research. Since the footing is over designed and is bulky, there was no compression strut because the footing was designed to take that.

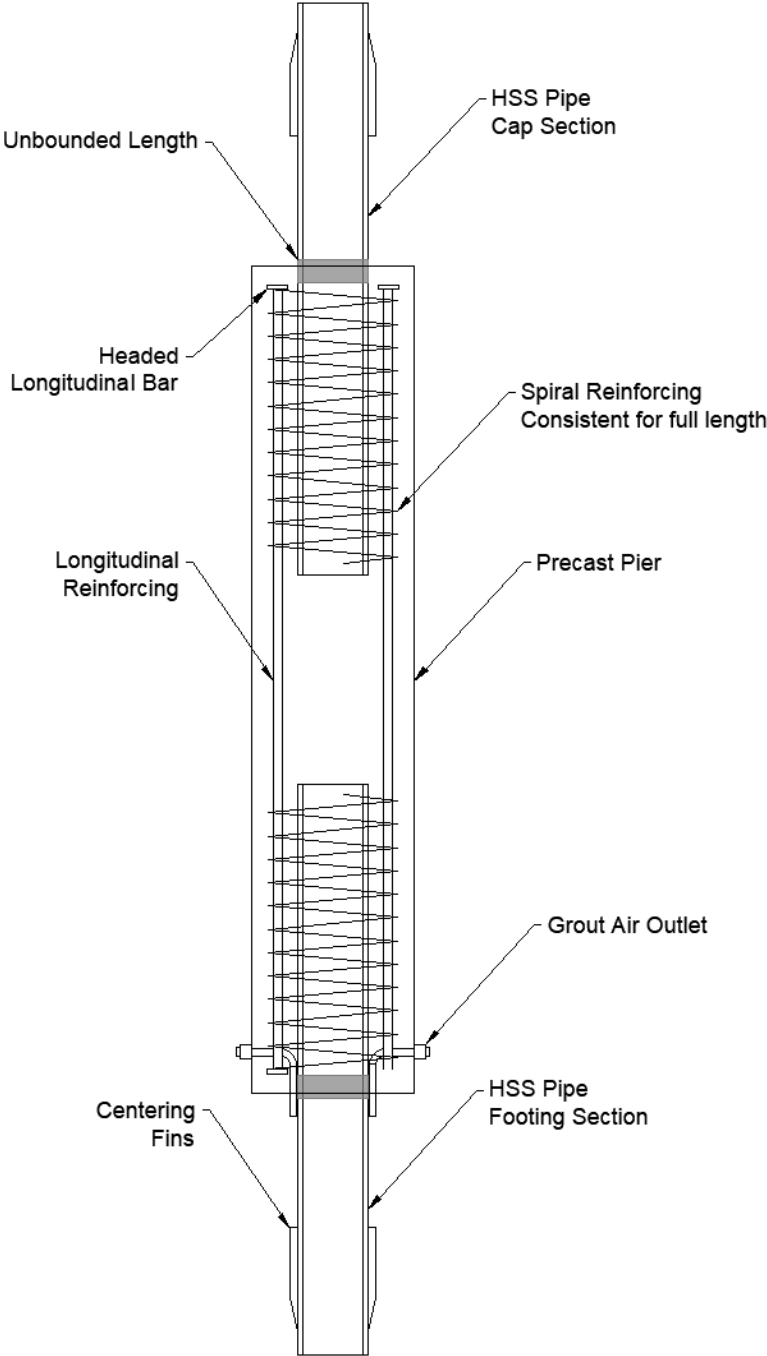


Figure 90. Proposed Connection: Precast Column Detail

As this connection provides similar total steel area at the interface of the connection in a more condensed arrangement than typical CIP connections, consideration for a greater yielding of steel must be accounted for. The pipe is precast into the center of the column which requires a smaller diameter as opposed to traditional longitudinal reinforcing. For this an unbonded length of the pipe is provided in order to establish a greater yield area of the steel to be activated during higher seismic loading. This unbonded length is identified in Figure 1, Figure 2, and Figure 90 on the column HSS and is positioned just above and below the interface of the footing and cap, respectively.

Additionally, an elastomeric pad is provided at each interface. The requirement for the elastomeric pad is due to the grouted state of the precast connection after completion. The connection is finished with a grout poured between the two pipes filling the gap to the interface at the pier. A non-rigid material is desired to help eliminate any voids that would be present in a dry concrete-to-concrete interface. The bearing pad helps to seal this connection for the completion of the grout pour and from natural elements (water, road salt, etc.) during the life of the connection. The bearing pad also allows for slight non-destructive movement of the connection during low level loading. Resulting in decreased cracking and spalling during low cycle seismic activity.

As mentioned above the connection is completed using a grout fed into the footing and pushed up through the void until sufficient flow out the air outlets is achieved. For the cap connection the grout can be fed from the top of the cap down into the void until similar sufficient flow is produced out the air valve in the top of the cap. The grout to be used must be non-shrink with a low metallic content to reduce interaction with HSS pipe in regard to corrosion. For all the HSS pipe it is suggested that all surfaces are sand-blasted or similarly prepped prior to concrete or grout application. The gap provided around the column pipe inserted into the embedded pipe is dependent upon the grout specifications and as to allow for full flow of the grout throughout the connection.

Regarding the footing and cap reinforcing interrupted by the embedded HSS sections, sufficient development is to be supplied via rebar bends or terminators to ensure full development of the bar. The remaining elements of the substructure are designed in accordance with the AASHTO LRFD Bridge Design Specifications (AASHTO 2017) as similar to the CIP bent benchmark specimen as possible.

## **Precast Bent System Design**

The steps taken to design the proposed connection for the purposes of this experiment are considered to be similar to CFSTs. The concrete filled HSS pipe is the ductile element at the interface of the connection. The remainder of the pier is designed to remain elastic throughout loading and is designed as a traditional pier. A consideration made for the proposed connection is the assumption that the unconfined concrete cover cast around the HSS pipe does not contribute to the flexural capacity of the connection. The footing and cap are designed as traditional members with no contribution of strength from the reinforcing interrupted by the embedded HSS pipe.

As mentioned, following WSDOT (2019) the pier HSS pipe is first sized. As the design relies on a variety of resistance factors, a factor of one is selected because the bent is to be tested to an extreme limit state. Sizing of the HSS pipe is begins by ensuring it is not subjected to local buckling prior to developing the pipe strength. WSDOT (2019) offers the use of the below equation for determination of member sizing as to assure ductile behavior/buckling criteria:

$$\frac{D}{t} \leq 0.15 \frac{E}{F_y}$$

Where:

D = Outside diameter, inches

t = Wall thickness of HSS member, inches

The selected pipe is determined through a combination of strength capacity, column rebar spacing, and other requirements. The selected HSS section is determined as an HSS6x0.500, with properties of 42 ksi yield strength, an ultimate strength ( $F_u$ ) of 58 ksi and modulus of 29,000 ksi. The actual design pipe thickness is 0.465 in. For this particular HSS pipe D/t is equivalent to 12.9 and  $0.15E/F_y$  is equivalent to 103.6.

After confirmation that the selected HSS meets the buckling criteria, the moment capacity of the connection must be determined. The equation provided is used:

$$M_n(y) = \left( c(r_i^2 - y^2) - \frac{c^3}{3} \right) * 0.95f'_c + 4ct \frac{r_m^2}{r_i} F_y$$

Where:

c = One half cord length of the compressive block

$r_i$  = Mean radius of internal reinforcement, in

$r_m$  = Mean radius of HSS member, in

y = Vertical distance of neutral axis from center of HSS in plastic stress distribution method, in

$f'_c$  = Compressive strength of the concrete

t = thickness of HSS member

c is calculated using:

$$c = r_i \cos \theta$$

Where:

$r_i$  = Mean radius to the inside of the steel tube

$\theta$  is calculated using:

$$\theta = \sin^{-1} \left( \frac{y}{r_m} \right)$$

Where:

y = Distance from the centroid of the specimen to the neutral axis during a seismic event, in  
r<sub>m</sub> = Radius to the center of the steel tube, in

As the neutral axis is expected to be equal at the centroid the variable, y is taken to equal zero. Once y is determined the variables  $\theta$  and c are calculated as 0° and 2.54 in., respectively. The final resulting moment capacity of the connection is 56.7-kip-ft. The testing arrangement is identical to the CIP bent which has a loading height off the top of the footing of 83.75 in. to the center of the actuator, the resulting base shear is taken as 8.1-kip; with a total design base shear of 32.5-kip when considering all four column connections present in the precast bent system.

A further design element required for the proposed connection is the embedment length of the HSS pipe into the footing, cap, and column. For this, two approaches from literature are considered. The two methodologies are proposed by Edward P. Wasserman (Wasserman and Walker 1996) and WSDOT (2019). Wasserman and Walker's approach is based on "Design of Integral Abutments for Jointless Bridges" by Edward P. Wasserman (1996). The following proposed equation was derived from a method used for application to develop the plastic moment capacity of piles used in bridge abutments. The original derivation used  $3.78f'_c$  for the concrete bearing capacity, based on research performed by Burdette, Jones, and Fricke. The derivation used below uses a much more conservative value of  $0.7f'_c$ , as allowed by AASHTO for concrete bearing pressure (C5.5.4.2, Pages. 5-30). The resulting proposed equation is:

$$l_e = 2 \left( \frac{M}{(0.7f'_c b)^{\frac{1}{2}}} \right)$$

$$M = Z * F_y$$

$$b = \frac{d}{2} \sqrt{\pi}$$

Where:

$l_e$  = Required embedment depth, in  
M = Plastic pipe moment, lb-in  
 $f'_c$  = Compressive strength of concrete, psi  
d = Outside diameter of the pipe, in  
Z = Gross plastic section modulus, in.<sup>3</sup>  
 $F_y$  = Yield strength of the pipe, ksi

Note that the equations above are empirical and require the parameters to be in the proper units.

The method used by the WSDOT was developed experimentally at the University of Washington by Dawn E. Lehman and Charles W. Roeder in "Rapid Construction of Bridge Piers with Improved Seismic Performance", published January 2012 (Lehman and Roeder, 2012). The method was developed for use

with CFSTs for foundation connections and bridge piers. The connection uses a steel pipe with an annular ring, as shown in Figure 91, imbedded into a pocket connection either preformed or formed with a corrugated steel pipe and grouted in place.

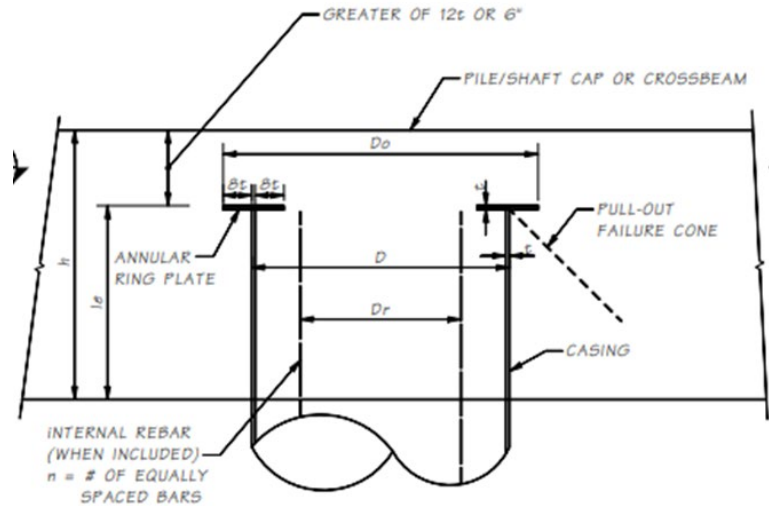


**Figure 91. WSDOT Pipe Embedment Cross-Section**

WSDOT Proposed equation to ensure full plastic behavior of the CFST:

$$l_e \geq \left( \frac{D_o^2}{4} + \frac{5.27DtF_u}{\sqrt{f'_c}} \right)^{\frac{1}{2}} - \frac{D_o}{2}$$

Where:

- $l_e$  = Calculated embedment length, in
- $D_o$  = Outside diameter of the annular ring, in
- $D$  = Diameter of the embedded pipe, in
- $t$  = Wall thickness of the embedded pipe, in
- $F_u$  = Ultimate strength of the embedded pipe, ksi
- $f'_c$  = Compression strength of the concrete, ksi

Again, the equation is empirical. This equation can be reduced for the proposed connection as an annular ring is not used. The resulting simplified equation is:

$$l_e \geq \left( \frac{5.27DtF_u}{\sqrt{f'_c}} \right)^{\frac{1}{2}}$$

For the purpose of conservative construction for the experimental investigation of the proposed connection both methodologies are considered with the greater resulting value used for construction. The controlling resulting embedment length is determined to be 22 in. This results in an HSS section with

an overall length of 49 in.; 22 in. is required in the footing or cap; an additional 2.5 in. is considered for the elastomeric bearing pad and unbonded length. This leaves 24.5 in. to extend into the column which ensures effective bonding of the HSS pipe section. For the embedded elements within the cap and footing the HSS pipe section is required to be a total length of 23 in. to accommodate for the full 22 in. embedment required and an additional 1 in. for grout flow. Similar to the CIP bent the remainder of the column is designed as a traditional CIP section. Resulting in 7 #6 Gr. 60 longitudinal reinforcing, and a #3 Gr. 60 spiral with a pitch of 1.5 in. running the full length of the column. However, the longitudinal reinforcing is required to terminate within the column as opposed to running continuously, as in the CIP columns. For this, threaded terminators are used at either end of the longitudinal reinforcing within the column. The full bent detail is provided in Figure 92.

The elastomeric bearing pad used was 0.5 in. This can be designed in accordance with the AASHTO M251 (Standard Specification for Plain and Laminated Elastomeric Bridge Bearings) for thickness, select material for durability, and shear performance of it. They can be designed to be replaceable. We are not relying on the elastomeric bearing pad structurally but does provide damping on smaller earthquake when it starts rocking and dampens the motion. We are neglecting this damping and is simply referred to be a contact damping.

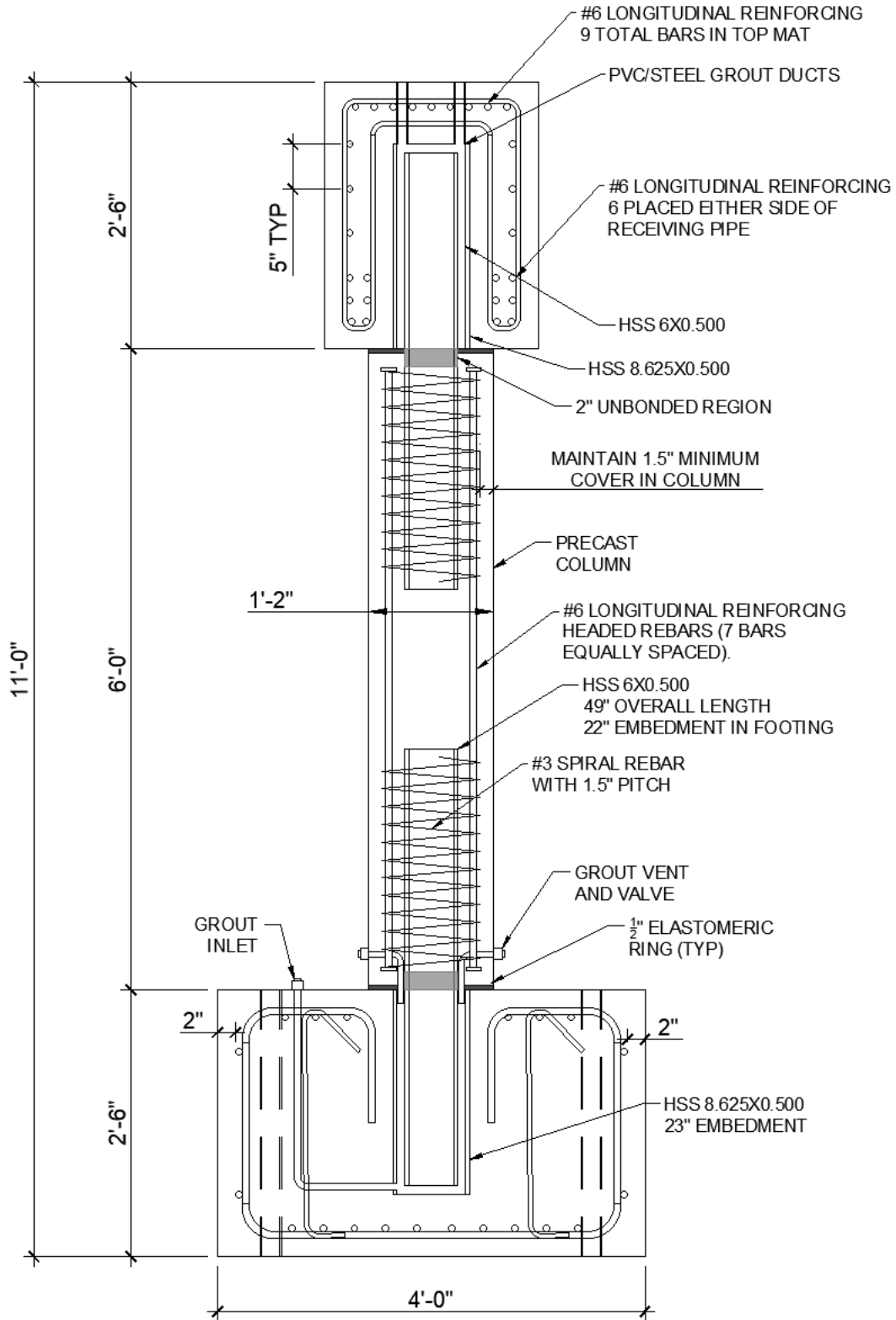


**Figure 92. Precast Bent Cross-Section**

Further examination of Figure 92 provides details to the footing and cap sections. The footing and cap embedded HSS8.625x0.500 are selected based on the calculated column pipe diameter and the clearance required for grout flow in the void. This size provides 7/8 in. clearance around the column pipe when sitting centered in the embedded insert. Beyond the pipe the footing and cap are dimensioned exactly as the CIP bent specimen was. The footing measures 4 ft. x 4 ft. x 2.5 ft. and the cap measures 15 ft. x 2 ft. x 2.5 ft. (L x W x D). With the presence of the embedded pipe, adjustments to the top reinforcing and bottom reinforcing of the footing and cap, respectively, had to be made. For the footing this was simply accomplished through adequate 90° rebar hooks for any of the interrupted top mat reinforcing with the bars falling outside of the embedded HSS pipe constructed as normal.

The cap design required a unique approach as the experiment aimed to ensure failure occurs in the column. With the requirement that none of the reinforcing interrupted by the embedded HSS be considered to constitute to the cap's moment capacity, the cap is considered to be comprised of two individual concrete beams on either side of the HSS pipe. This results in design of a beam having a cross-section of 7.7 in. x 30 in. to conservatively handle one half of the targeted moment capacity of 500-kip-ft. As can be seen in the cap cross-section in Figure 93, the resulting beam is comprised of three layers of two #6 Gr. 60 rebar on either side of the HSS pipe with a resulting moment capacity of 608-kip-ft. Additionally, the top reinforcing is similar to the CIP bent cap with 9 #6 Gr. 60 rebar provided. The cap is designed with #4 Gr. 60 stirrups provided 4 in. center-to-center spacing. As in the CIP bent specimen and in compliance with ITD's general practice, two alternating #4 Gr. 60 crossties are provided for each stirrup. Also seen in the cap cross section is the grout polyvinyl chloride (PVC) pipe inlet and air vent at the top of the HSS pipe.

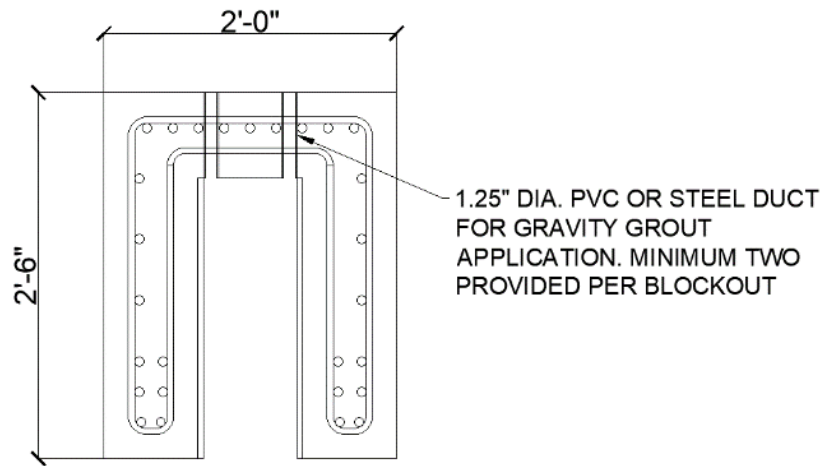


**Figure 93. Precast Bent Cap Detail**

The final resulting precast bent, having the same overall dimensions as the CIP bent, is shown in Figure 94. The figure shows the full detail of bent, with the implementation of the proposed connection.

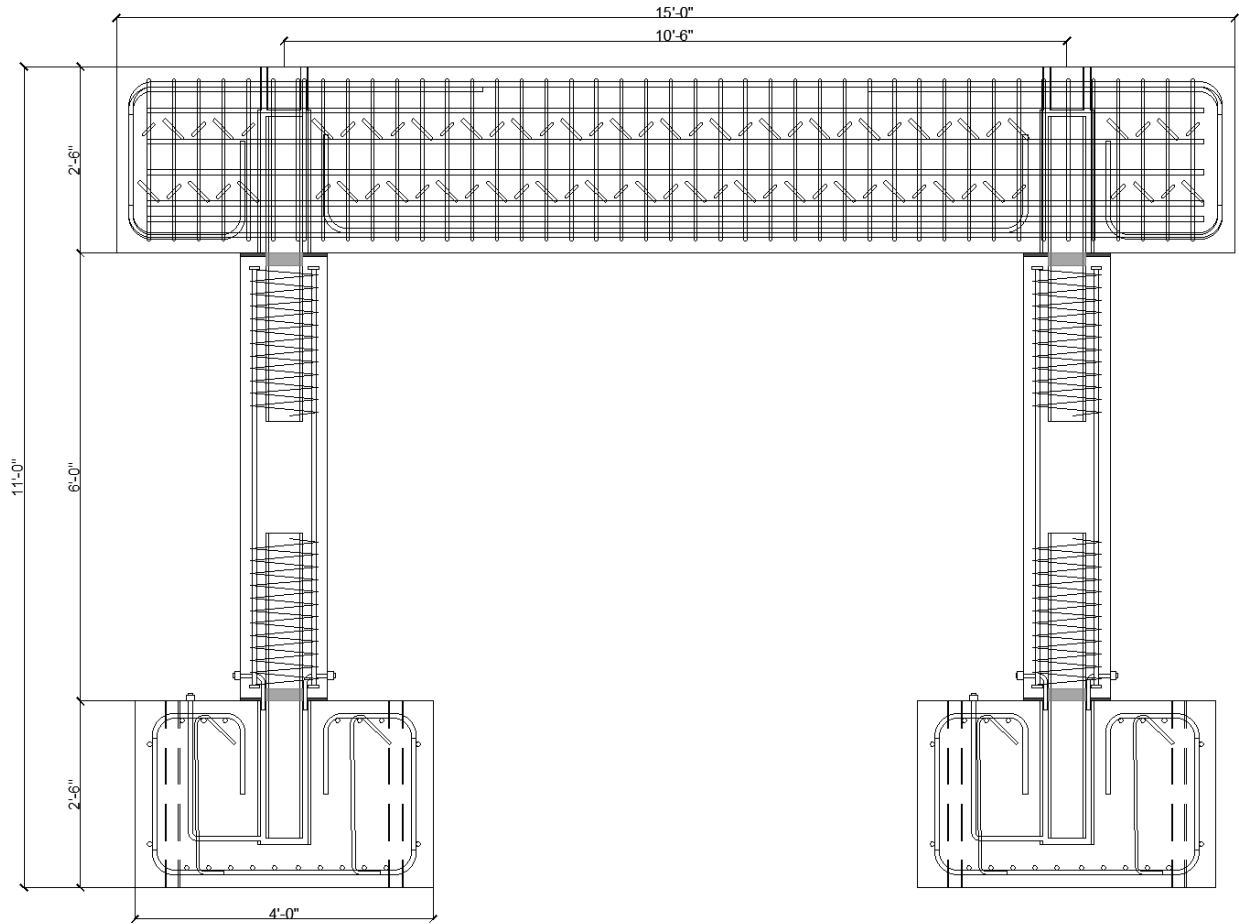


**Figure 94. Precast Bent Specimen**

## Construction

The construction of the precast bent is done completely outside the lab with each element, footing, columns, and cap, poured and moved into the lab for assembly as would be performed on a true bridge project. The cages for each respective element are constructed and placed in the form work reused from the CIP bent. The reuse of the form work for the footing is simply done as the footing forms are not required to be altered or reworked. The HSS pipe is first sand blasted, for improved bond with both the concrete and grout, then fabricated with suitable rebar risers in order to be secured and sit at the proper height for pouring. The grout inlet is also secured in place prior to placement. Finally, a wood block is fixed to the bottom pipe end and sealed with caulk to ensure concrete does not rise into the embedded pipe. The rebar risers, grout inlet and wood block are all shown in Figure 95 after fabrication and installation. The welds in Figure 95 are fillet welds which is only intended for the ease of construction or alignment and does not do anything structurally. Figure 96 shows the completed footing elements after the full installation of the embedded HSS pipe, grout inlet, rebar cage, and anchoring sleeves.



**Figure 95. Embedded HSS Pipe Prepared for Installation**



**Figure 96. Precast Bent Footing Elements**

The pier construction is carried out independently of the footing construction as opposed to the traditional CIP method used for the benchmark specimen. The rebar cage and HSS pipe sections are fabricated and placed in the forms for pouring. The columns for the precast bent are poured horizontally

as opposed to vertically for the CIP bent. This greatly reduces the labor involved and increases safety as all work can be completed on the ground as opposed to lifting concrete to the finished pier height. The forms from the CIP bent construction are simply reduced to three sides because the piers are poured on a casting bed outside the lab (Figure 97).



**Figure 97. Precast Bent Column Prepared for Concrete**

Following the completion of the footing and columns, the cap construction began. Due to available space on the casting bed the items had to be cast in separate pours. Whereas a true precast operation can likely handle producing the items at one time or as is necessary for the project. The cap is poured similar to the CIP bent cap but is constructed and poured on a casting bed making the full process much simpler and safer. The forms from the CIP bent are again used and are placed after the rebar cage is completed. The HSS pipe embedment's are placed and sealed to the precast bed. The rebar cage is then lowered into place (Figure 98) with the forms and grout ducts placed last. Rebar lifting hooks are also installed to assist with handling and erecting of the cap. The construction of each element is followed by pouring of the concrete, form removal, and relocating of the elements.



**Figure 98. Cap Rebar Cage Placement**

The footings are placed and anchored to the floor followed by the erection of the columns. The columns are firstly fitted with alignment fins to ensure proper centering of the columns within the HSS pipe embedded in both the footing and the cap. The alignment fins also serve to ensure a minimum gap is maintained on all sides of the column pipe to ensure grout application is possible. The columns are then lowered into place (Figure 99). After placement, the grout air vents located in the base of columns are ensured to not be blocked by the elastomeric pad and allow air flow for grout application.



**Figure 99. Precast Bent Column Erection**

The cap is then prepared for placement. Due to limitation in the lab the 10-kip forklift had to be fitted with an extension frame to place the cap. The extension frame allowed for the cap to reach the necessary height to pass over the column HSS pipe extending from the column tops and be lowered down (Figure 100). After the placement of the precast cap the connections are grouted using SikaGrout 328. SikaGrout

328 is determined as a suitable material due to its ability to be highly flowable, non-shrink, non-metallic content, and it has an extended working time. As the grout is applied through a gravity feed method the extended working time ensured the full void is filled. After sufficient flow is achieved through the grout vents the specimen is allowed to cure and is prepared for testing.

Practical limits on full size cap beams weight, lifting and shipping can be determined for individual projects by the precasters. If the weight exceeds what's allowed on the highways, the cap might have to be made hollow or partial-solid. If there are limitations in the size, it can be made in sections. The precast pier system as in Figure 100 is proposed for short to medium span bridges. The size of the cap beam and the weight of it should not exceed at least for short span bridges. A shallower cap can be used only if further research is available on the development length of CFST. The joints for the cap beam, at least the shear reinforcing can be design using strut and tie method.

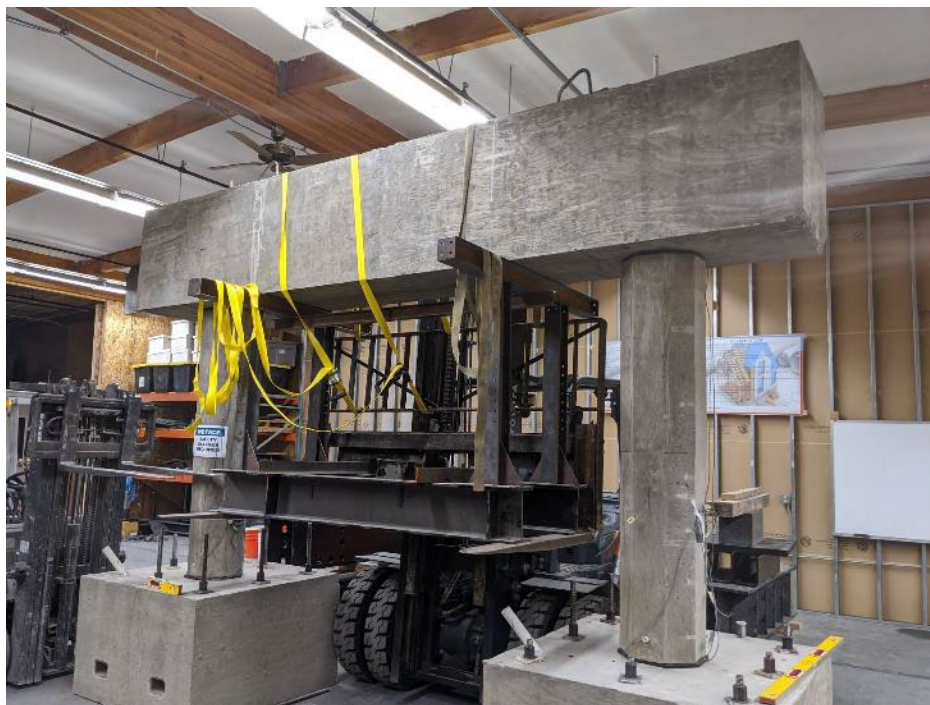


**Figure 100. Precast Bent Cap Erection**

## **Testing Arrangement**

The test arrangement, instrumentation, and loading protocol for the precast bent is setup and done the same as that of the benchmark CIP bent. The one exception in the instrumentation is the strain gages present on the longitudinal reinforcing in the column of the CIP bent. As the longitudinal reinforcing in the precast columns does not pass through the interface of the connection, the HSS pipe at each connection is instrumented with a total of 16 strain gages. The placement of the strain gages can be seen in Figure 38. Refer to the test arrangement, instrumentation, and loading protocol sections of CIP Bent for the full details.

## Testing Results

The test started with a first cycle targeted displacement of +/- 0.18 in. achieving a maximum of 0.15 in. No visible cracking developed. The second cycle again developed no visible cracking. A slight gap opening at the elastomeric pad is observable during the second cycle. On the third cycle hairline cracking appeared within 18 in. of the footing and cap interfaces on the column face (Figure 101a). The fourth and fifth cycles resulted in additional hairline cracking expanding up and down the full length of the columns and the development of vertical hairline cracks near the ends of the columns (Figure 101b). Additionally, slight spalling developed at the top connections resulting in quarter sized concrete pieces. During the sixth cycle, more top connection spalling developed, and crack development continued with maximum cracks of 0.0157 in. (0.4 mm) (Figure 102c). The gap opening at the elastomeric bearing on the tension side was widening to approximately 3/16<sup>th</sup> in. gap (Figure 102d). The seventh, eighth, and ninth cycles continued crack development with spalling at the base connections resulting during the ninth cycle. Overall crack development is significantly less than that of the CIP bent. Cracking frequency is reduced with few large cracks developing after initial hairline crack development resulting in large slab like spalling. It is during the ninth cycle the maximum lateral force of 71.4-kip is achieved. Figure 102e demonstrates the significant slab spalling developed during the ninth cycle. The spalling resulted in an approximately 3-kip drop in force and exposure of spiral reinforcing. The tenth cycle resulted in minimal additional spalling and continued crack development. The eleventh cycle resulted in continued spalling of slabs, with significant increase spalling at the column top connections (Figure 102f). At this point the north pier away from the lateral actuator experienced the majority of spalling. During the twelfth cycle the south pier developed significant spalling at the bottom connection (Figure 102g). The fourteenth and fifteenth cycles resulted in continued spalling and crack development with the gap opening at the elastomeric bearing having increased to approximately 1/2 in. (Figure 102h). At this point both piers had developed spalling at both, top and bottom, connections resulting in exposed spiral and longitudinal reinforcing. Additional cracking had stopped developing with existing cracking continuing to widen. The HSS pipe had yet to be exposed.

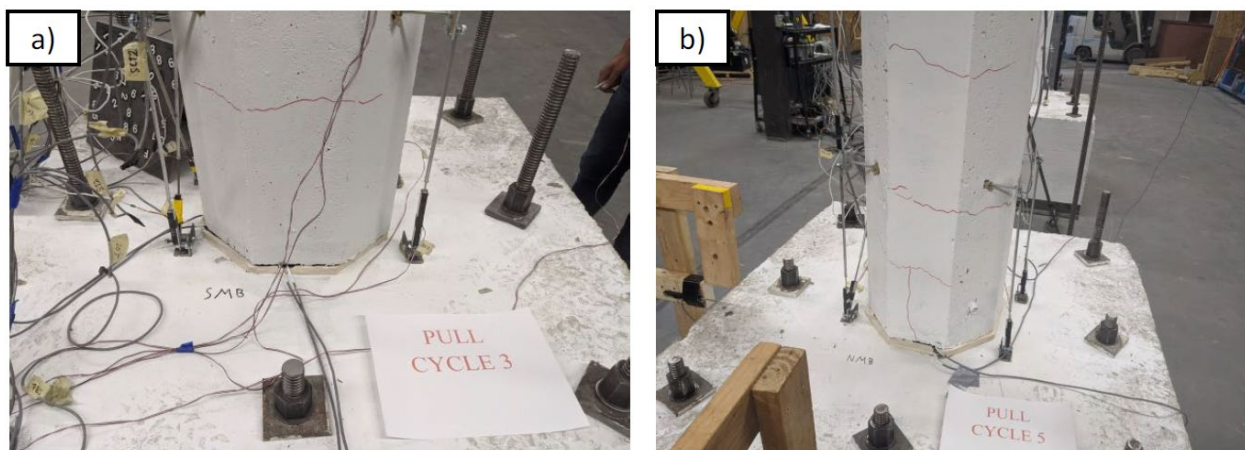


**Figure 101. Precast Bent Testing: a) Cycle 3: Hairline Cracking, b) Cycle 5: Vertical Hairline Cracking**

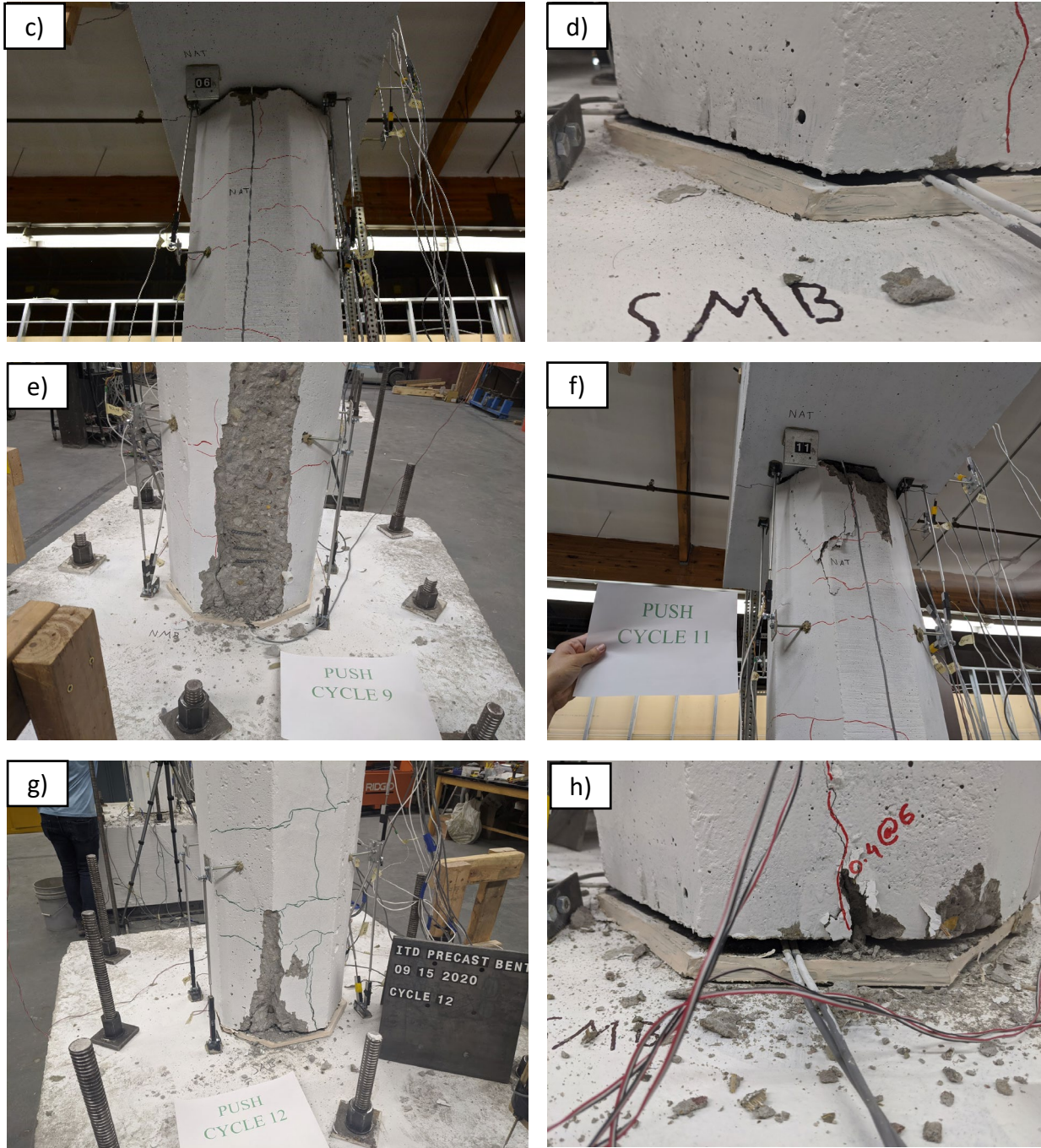


**Figure 102. Precast Bent Testing: c) Cycle 6: Spalling Development, d) Cycle 6: Gap Opening 3/16-inch, e) Cycle 9: Slab Spalling Bottom, f) Cycle 11: Slab Spalling Top, g) Cycle 12: Slab Spalling North, h) Cycle 14: Gap Opening 1/2 inch**

Spalling continued to develop at all connections from the sixteenth to eighteenth cycles. Exposure of the pipe resulted on the eighteenth cycle (Figure 103a). During the nineteenth cycle development of a vertical crack in the column face perpendicular to the loading actuator developed significantly (Figure 103b). The vertical crack continued to develop over the following cycles indicating the spiral reinforcing losing

confinement allowing the column concrete to begin separating from the HSS pipe (Figure 103c). During the twenty-fourth cycle the maximum force achieved dropped to 55-kip, achieving the targeted 20% strength degradation. Figure 103d provides an image of the north column bottom connection at failure.



**Figure 103. Precast Bent Failure: a) Cycle 18: HSS Pipe Exposure, b) Cycle 19: Perpendicular Face Cracking, c) Cycle 24: Confinement Failure, d) Cycle 24: Failure**

The HSS pipe had not been exposed enough to evaluate it at the time the test was terminated. Additional concrete was removed manually to better observe the HSS pipe. Exposed HSS pipe revealed that the top connections resulted in a higher level of deformation. Figure 104 provides images of the observed deformation. A significant bulge of the HSS section developed below the cap for both top connections. An additional observation is the separation of the HSS pipe and grout. The separation is the result of the HSS pipe fracturing just inside the interface of the cap. The HSS pipe underwent “necking” while in tension causing it to separate and fracture just inside the interface.

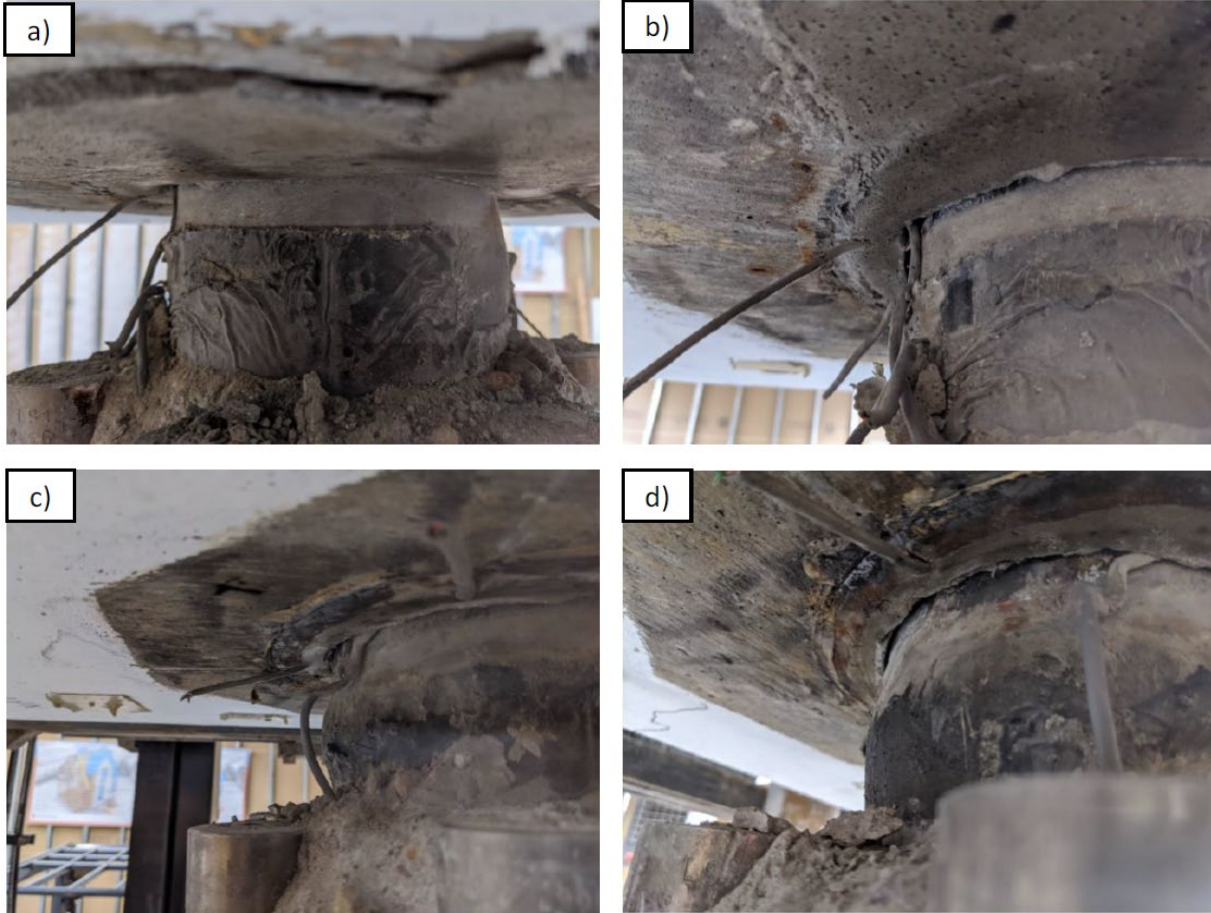


**Figure 104. Precast Bent Top Connection Post Test: a) Bulging HSS Pipe, b) HSS and Grout Separation, c) HSS Bulging, d) HSS Bulging and Separation**

The bottom pier connection exhibited far less damage and deformation. Slight bulging was present but minimal in comparison to the top connections. Figure 105a provides a view of the minimal bulging that resulted. The bottom connection did not exhibit any signs of the HSS necking. No separation of the grout and HSS pipe was observed.

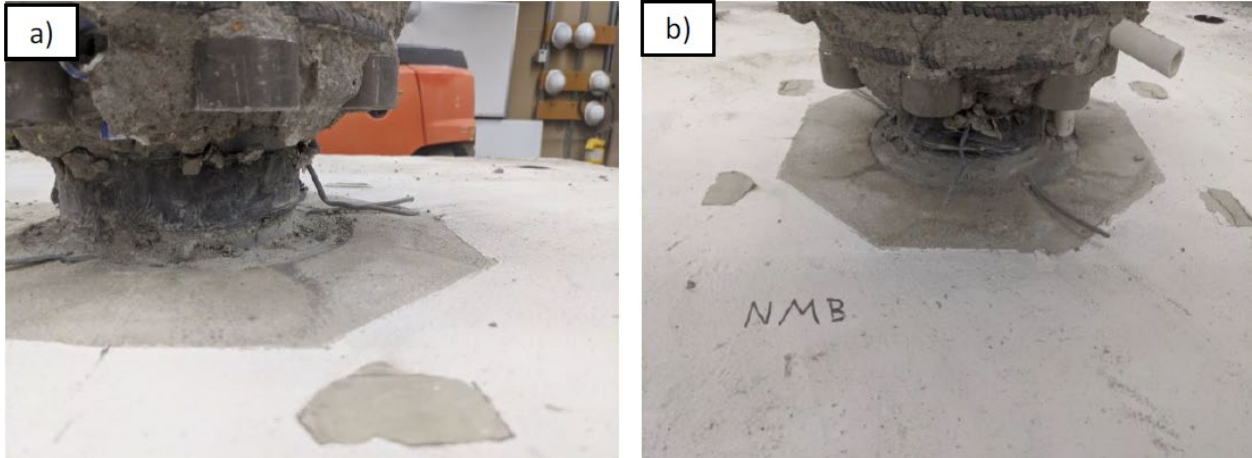


**Figure 105. Precast Bent Bottom Connection Post Test: a) South Column, b) North Column**

During the testing, the bent performed a total of 24 cycles resulting in a maximum actual peak displacement of 7.6 in. A side view of the bent is provided in Figure 106 showing the bent at the maximum pushed state during the 24<sup>th</sup> cycle. The targeted displacement during the 24<sup>th</sup> cycle is 8.4 in., but similar to the reaction frame flex during the CIP bent test the frame was not acting completely rigid. Table 15 provides the targeted displacement and drift ratios and the actual values achieved during the testing of the precast bent.



**Figure 106. Cycle 24 Peak State**

**Table 15. Precast Bent Loading Protocol Summary**

Cycle	Programmed Displacement (in.)	Programmed Drift (%)	Actual Displacement (in.)	Actual Drift (%)
1	0.18	0.21	0.15	0.18
2	0.35	0.42	0.27	0.32
3	0.7	0.84	0.53	0.63
4	1.06	1.27	0.78	0.93
5	1.41	1.68	1	1.19
6	1.76	2.10	1.28	1.53
7	2.11	2.52	1.55	1.85
8	2.46	2.94	1.92	2.29
9	2.81	3.36	2.25	2.69
10	3.17	3.79	2.61	3.12
11	3.52	4.20	3.06	3.65
12	3.87	4.62	3.38	4.04
13	4.22	5.04	3.7	4.42
14	4.57	5.46	4.03	4.81
15	4.92	5.87	4.37	5.22
16	5.27	6.29	5.04	6.02
17	5.62	6.71	5.38	6.42
18	5.97	7.13	5.71	6.82
19	6.32	7.55	6.05	7.22
20	6.67	7.96	6.39	7.63
21	7.02	8.38	6.7	8.00
22	7.37	8.8	7.04	8.41
23	7.72	9.22	7.4	8.84
24	8.07	9.64	7.66	9.15

The data captured during the precast bent test is presented in this section in a similar layout as that for the CIP bent specimen. The maximum values achieved during the testing of displacement and lateral load were 7.66 in. and 71.4-kip, respectively. The peak lateral load correlates to a total moment capacity of 498-kip-ft. The precast bent demonstrates a stable response through the test progression resulting in significant energy dissipation. The degradation of strength is fairly stable and consistent through the end of the cycles. As assumed for the CIP bent, the four connections shared the lateral load equally, this equates to base shear at each connection of 17.9-kip. Figure 107 and Figure 108 provide the resulting precast bent Force vs. Displacement and Force vs. Drift hysteresis. The Force-Displacement hysteresis suggest the precast bent achieved design base shear of 32.5-kip, correlating to a yield displacement of 0.95 in. Similarly, from the Force-Drift hysteresis it is seen the bent yielded at a drift ration of 1.13%. Figure

109 provides the Force-Drift backbone curve developed during testing, highlighting the peak force and displacements achieved throughout the test. The curve exhibits a stable consistent degradation of the precast bent strength as the test progressed.

It should be noted for the figures the positive vertical axis shows the specimen in push. The test began by first pulling the specimen and continued to begin all cycles in pull. It can be observed the bent exhibited higher strength during pulling as opposed to pushing, which can be attributed to two factors. The bent underwent softening during the first pull of the cycle thus exhibiting higher strengths in all cycles. Additionally, the reaction frame exhibited slightly higher stiffness during the pulling stage as opposed to experiencing higher displacement during the pushing stage.

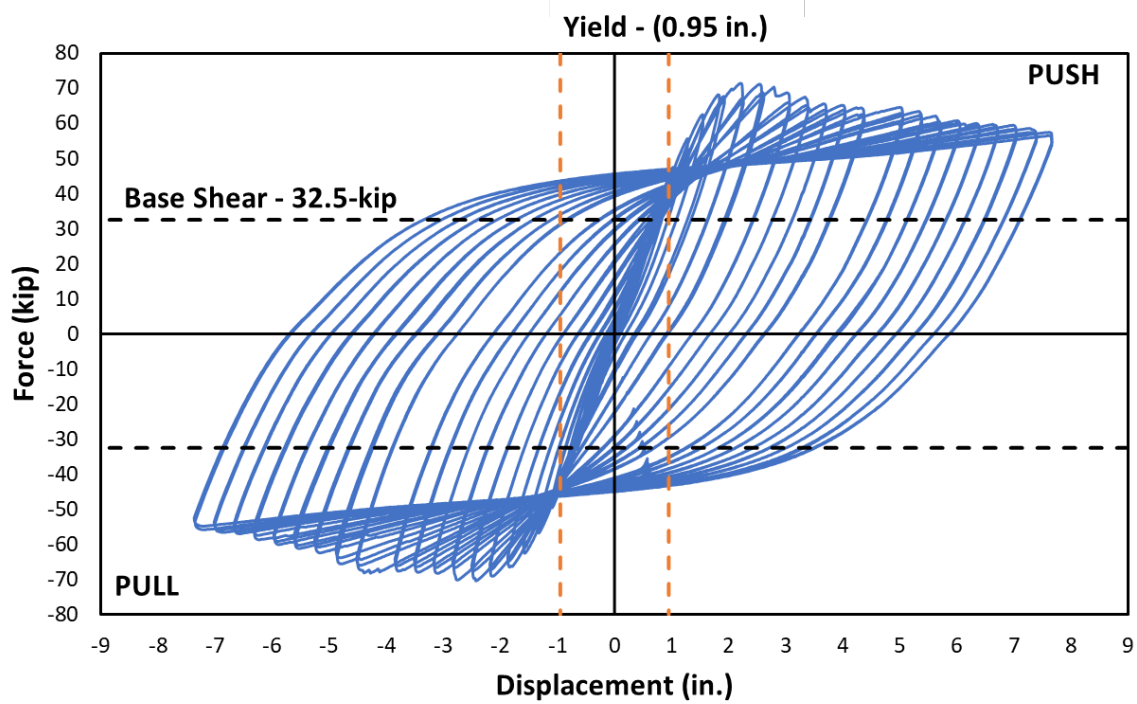


**Figure 107. Precast Bent Force-Displacement Hysteresis**

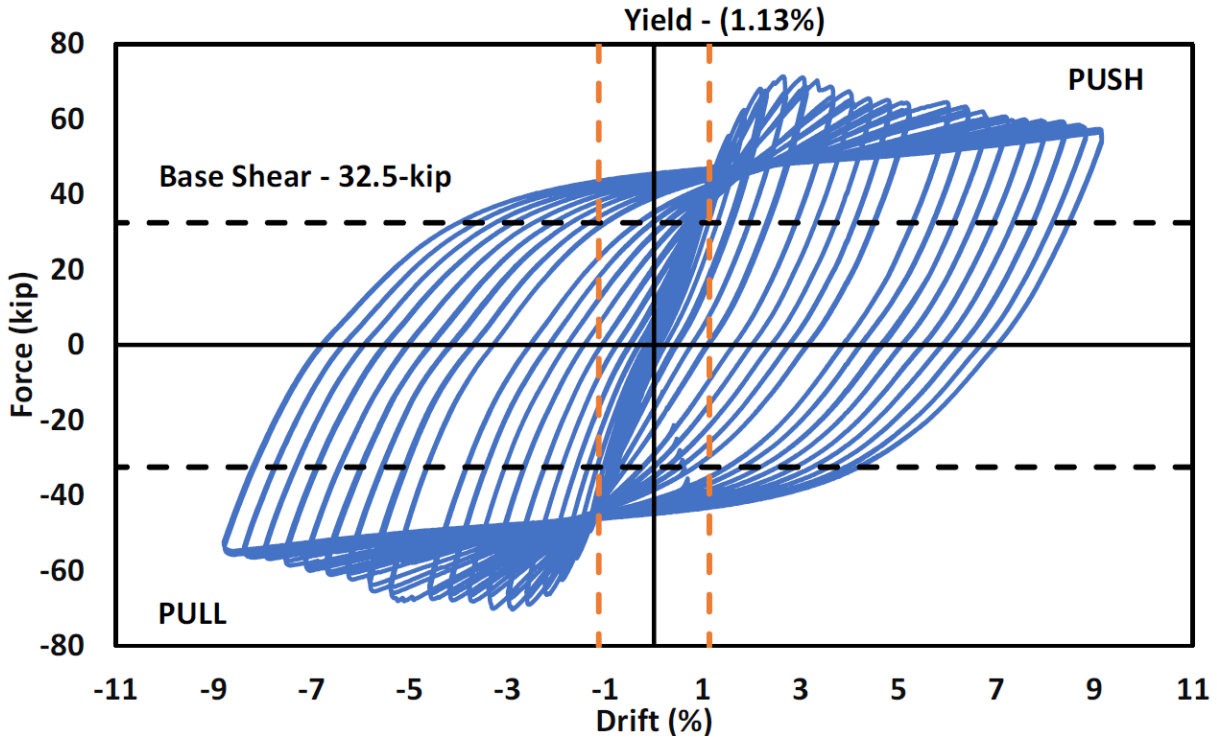


Figure 108. Precast Bent Force-Drift Hysteresis

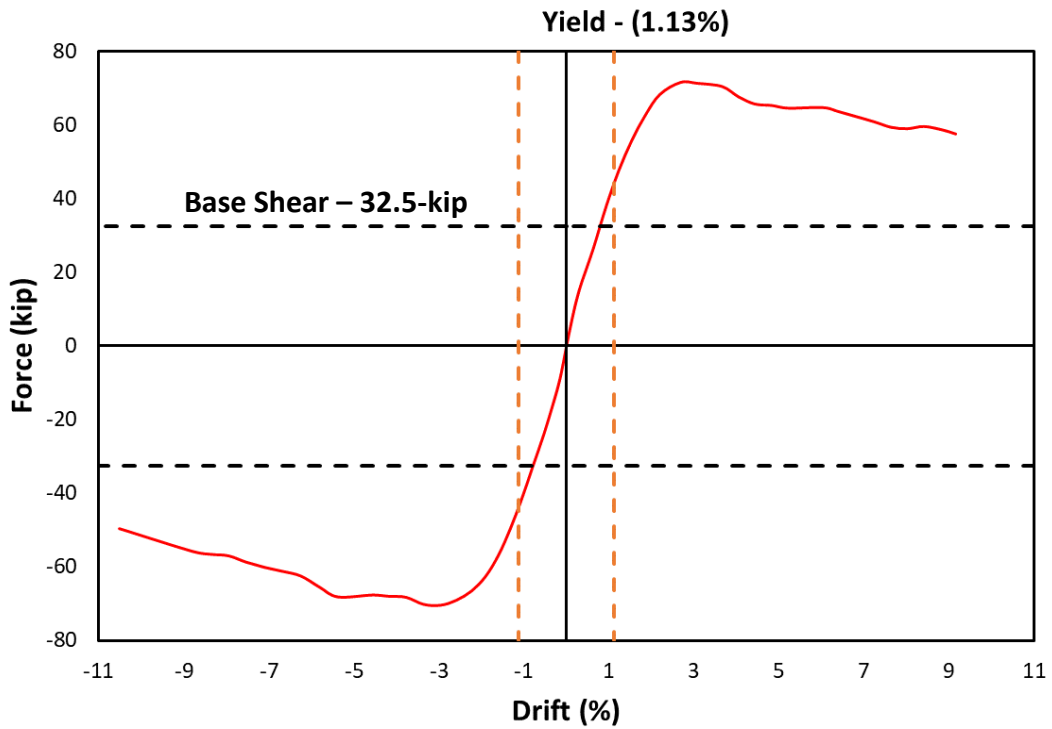


Figure 109. Precast Bent Force-Drift Backbone Curve

Analysis of the potentiometers, specifically located in the plastic hinge regions (groups A, B, C, and D), again provide a close breakdown of each connection's reaction through moment-curvature. The progression of the yield, captured by the instrumentation at each plastic hinge, can be observed in Figure 110, which provides the moment-curvature of each. Observation of four plots shows great stability and consistency across all four connections. Each connection demonstrated a significant amount of energy dissipation. All four moment-curvature hysteresis provide easy identification of the 3-kip drop in force which took place during the ninth cycle. This demonstrates good correlation between the observational data and instrumental data collected during the test. Further observation of the plots shows a consistency in the strength degradation once the precast bent reached ultimate lateral capacity.

Similarly, the final figure provided from the instrumental data is the Dissipated Energy (Figure 114). Similar to the approach for the CIP bent the energy dissipated at each cycle is determined and the cumulative dissipated energy resulting is 2,125 kJ (1,567,320 ft-lb). This is significantly larger than that of the CIP bent due to the ability of the precast bent to perform 23 full cycles as opposed to the 16 cycles performed by the CIP bent.

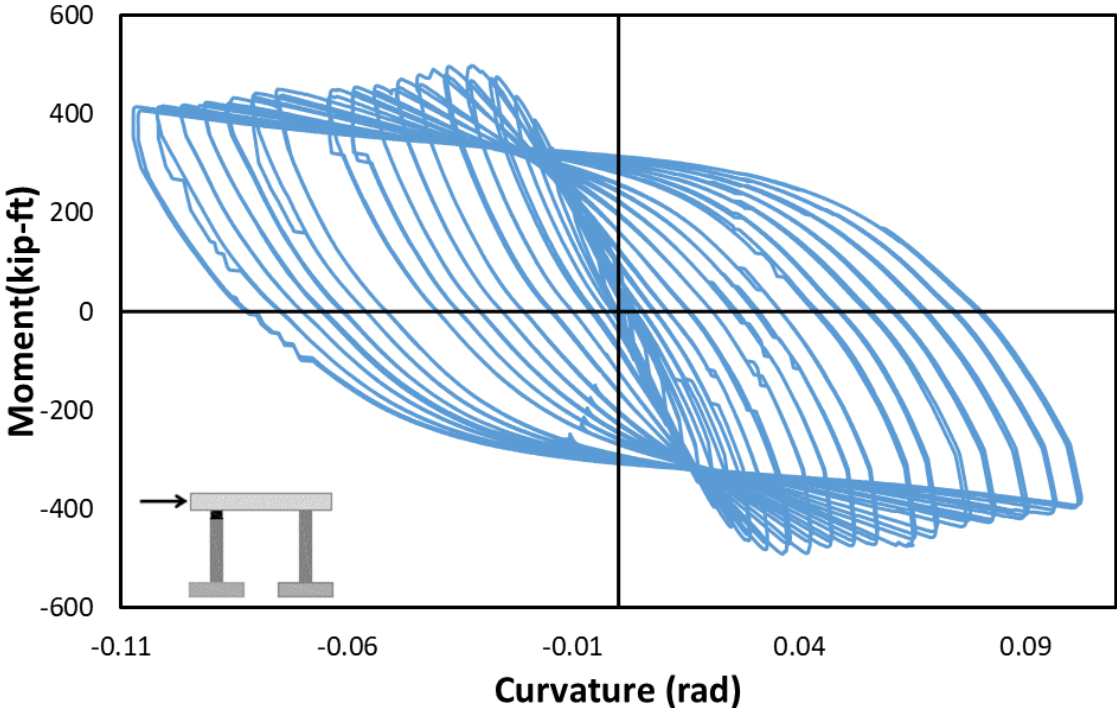


Figure 110. South Column: Top (D1-S – D4-S)

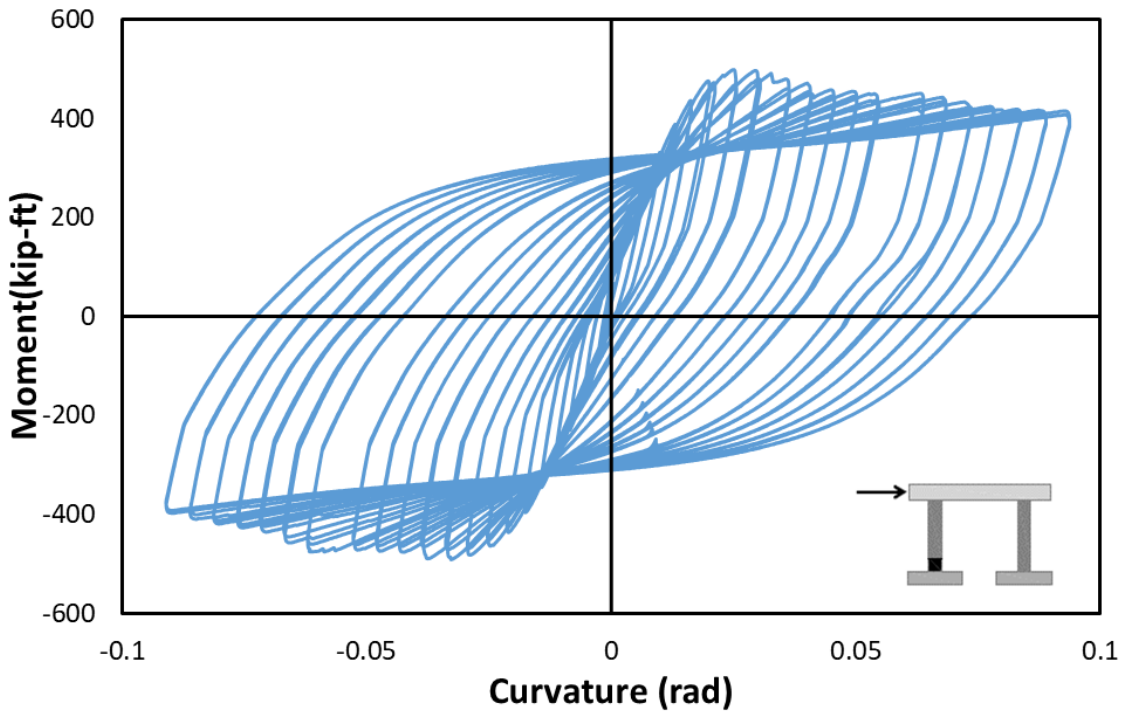


Figure 111. South Column: Bottom (A1-S - A4-S)

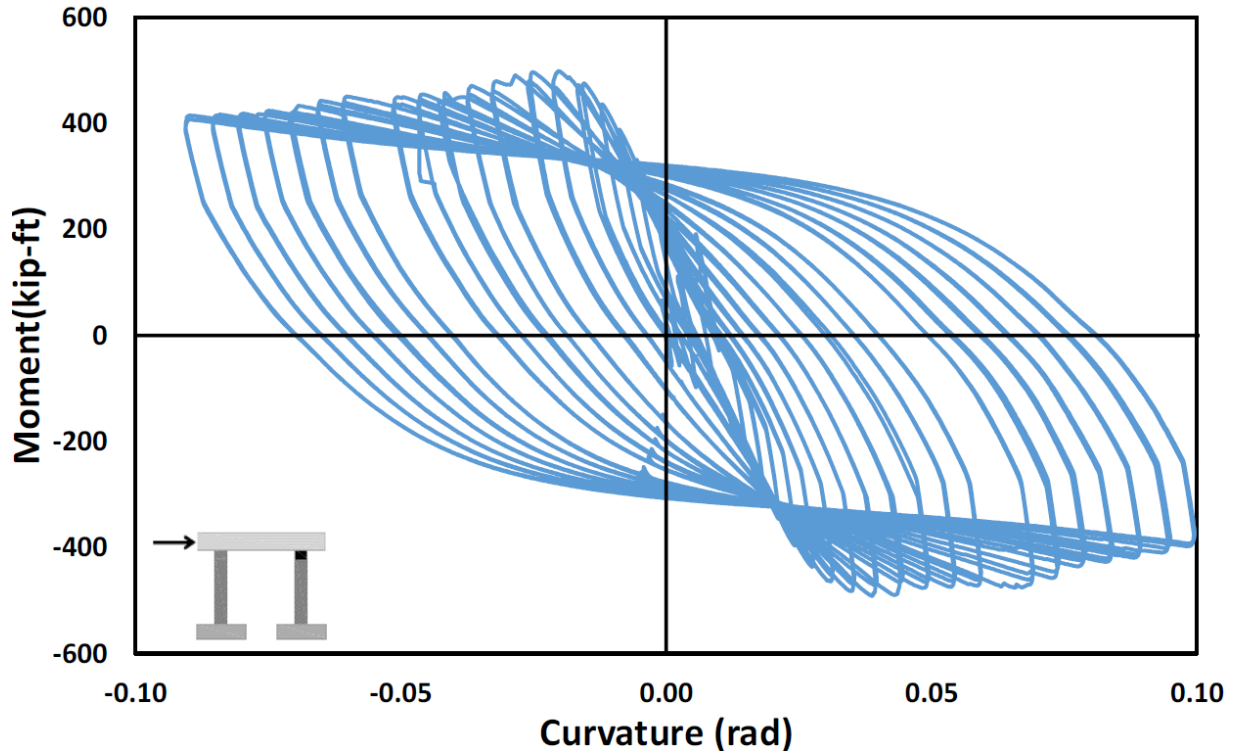


Figure 112. North Column: Top (D1-N - D4-N)

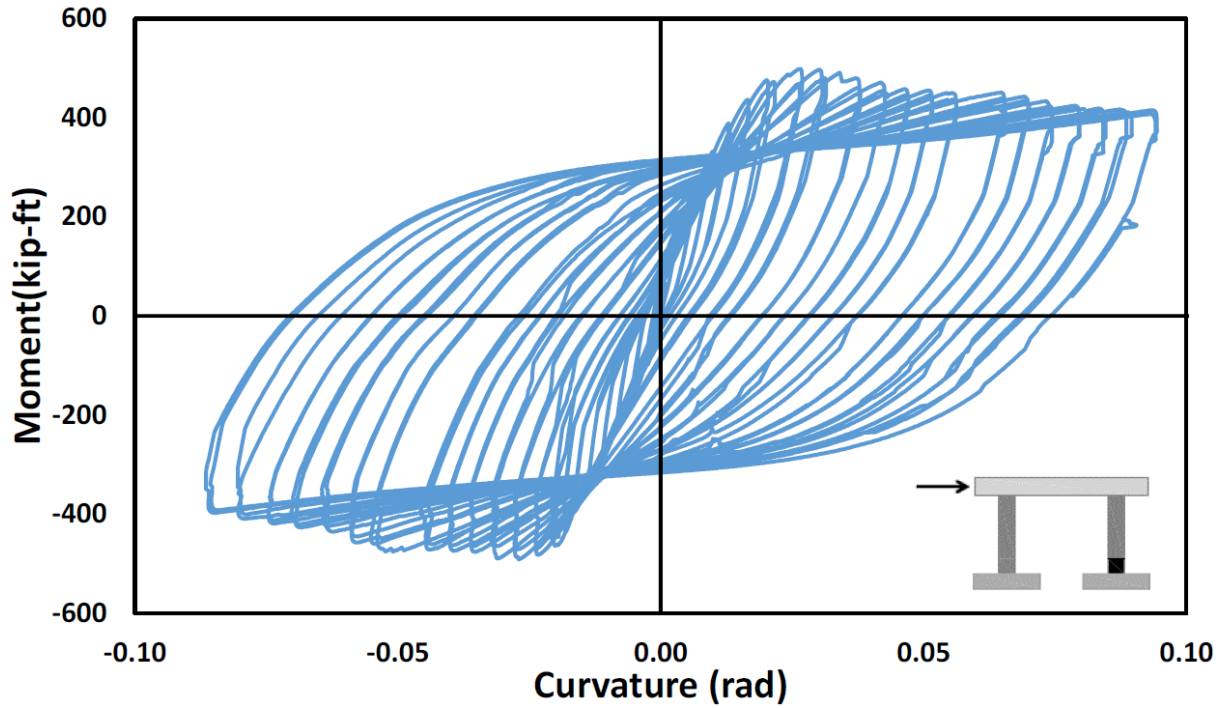


Figure 113. North Column: Bottom (A1-N – A4-N)

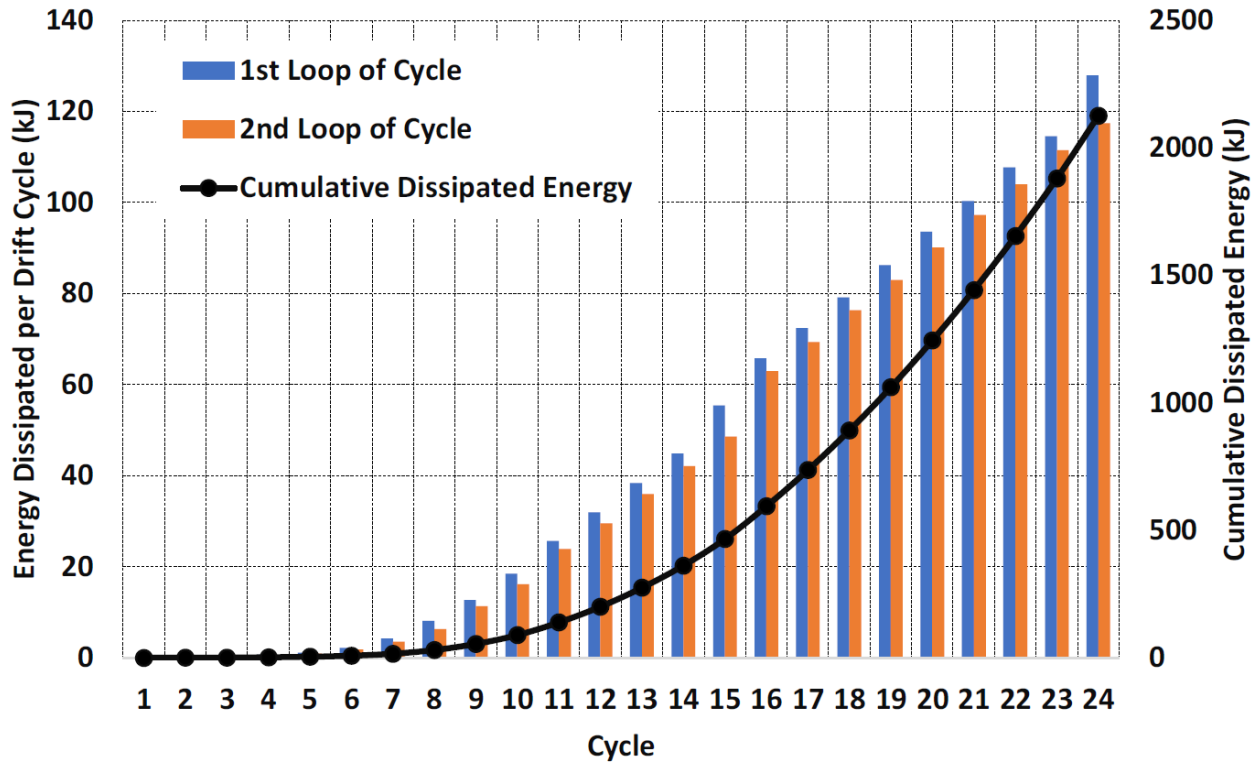
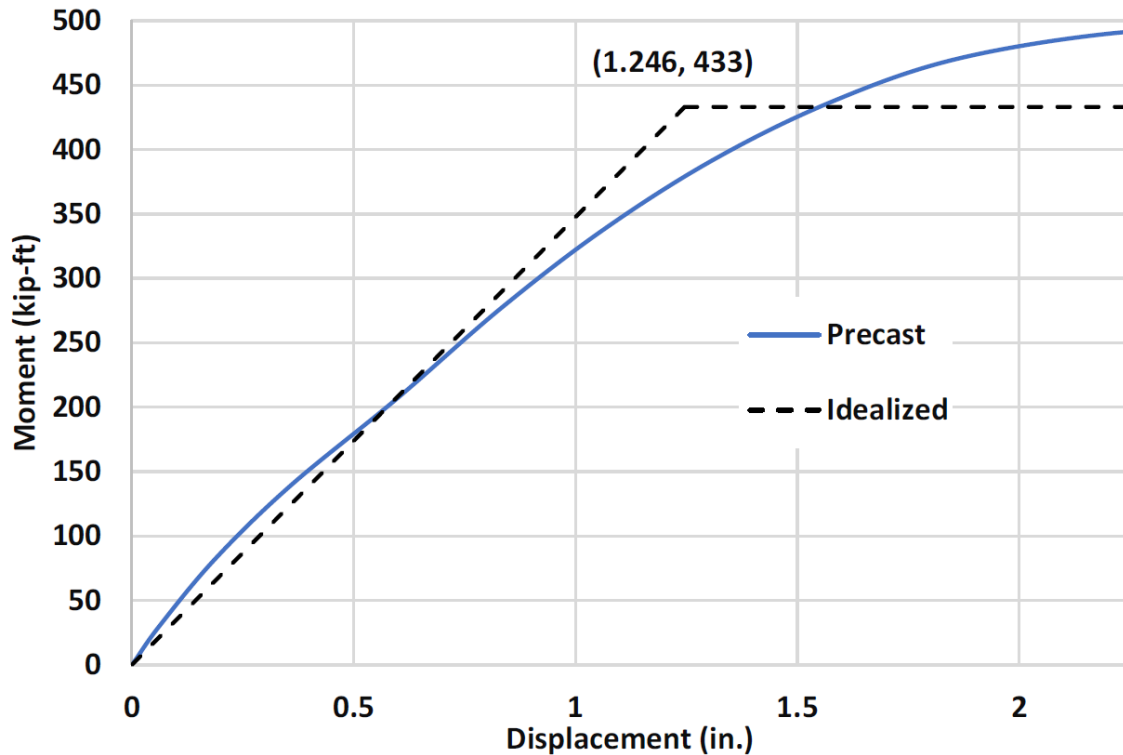


Figure 114. Precast Bent Dissipated Energy Per Cycle and Cumulative (1 kJ = 737.56 ft-lb)

Similar to that of the CIP bent the backbone curve is analyzed using displacement in place of curvature for a bilinear approximation providing the following results. The global yield moment capacity produced from the experimental results is used to obtain the base shear yield of 62-kip corresponding to a yield displacement of 1.246 in. The ultimate base shear provided from the backbone curve gives a total base shear of 70.8-kip at a displacement of 2.53 in. The bilinear approximation is shown in Figure 115. The overstrength factor is calculated in the same fashion as the CIP bent and results in a factor of 2.18 for the precast bent. With accompanying displacement ductility's ( $\mu$ ) of 2.03 at ultimate base shear and 6.02 at failure point.



**Figure 115. Bilinear Approximation for Precast Bent**

The residual drift of the precast bent is presented in Figure 116, providing the permanent deformation of the pier after the completion of each cycle. At the point of failure or test termination, the precast bent was maintaining 74.8% (6.84% drift ratio) of the drift applied, 9.14%.

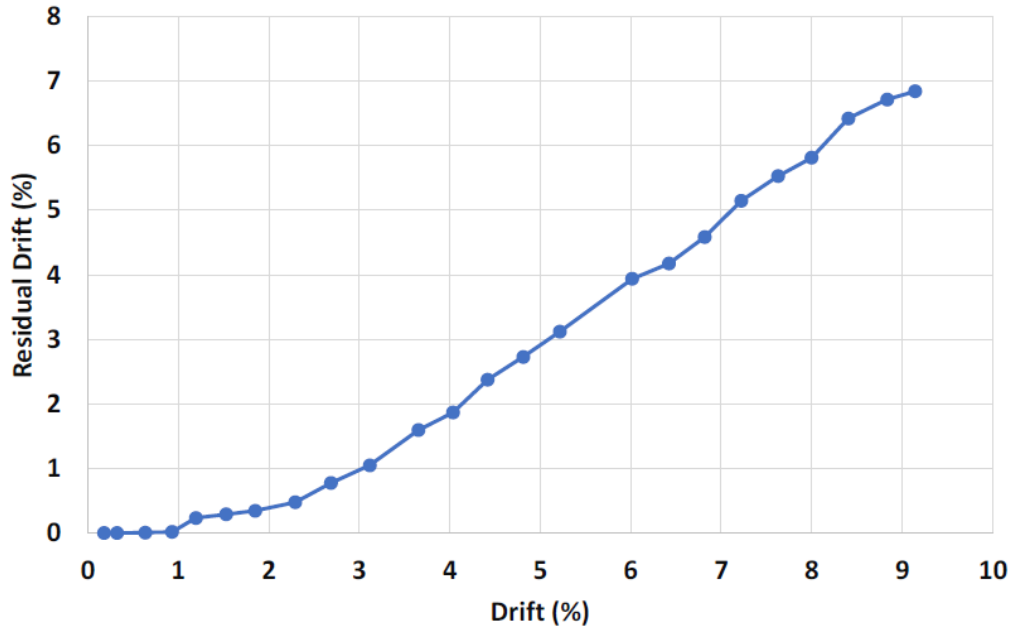


**Figure 116. Residual Drift of Precast Bent**

## Summary

The precast bent designed, constructed, and tested with the proposed connection is intended to emulate a CIP bent under similar conditions. With the proposed connection allowing for the adaptation of ABC in regions of seismicity. Using previously developed design equations for CFSTs from WSDOT Bridge Design Manual and the AASHTO LRFD Bridge Design Specifications, the proposed connection using embedded HSS pipe sections is incorporated into a similarly sized concrete bent as the previously tested benchmark CIP bent, to be tested in SLAB at ISU. Incorporating specific design details in the proposed connection assisted in the connections ability to emulate a CIP connection. The use of an elastomeric bearing pad at the base and top of the piers allows for the piers to have available flexure at small drifts resulting in significantly reduced cracking and spalling and assisting in the ability to develop similar drift capacities as a CIP connection. The embedment of the pipe is determined to ensure full plastic capacity is developed prior to pullout. As the HSS pipe is accountable for providing the full flexural and shear resistance for the column, an unbonded length is provided to allow yielding of the section to take place over a larger area of the HSS pipe. The cap and footings of the bent are designed to be capacity protected members. Each had an embedded HSS pipe section providing a socket for which the column HSS pipe is fitted into using alignment fins for ensuring proper placement and that the gap is maintained for grouting.

The proposed connection proved to provide a safer pour for all elements of the bent as it could be performed completely at ground level. The full precast bent was able to be constructed prior to any grouting with minimal requirement for bracing. The construction did require for additional equipment capable of handling larger elements during assembly. The grouting process was carried out using a highly flowable grout mix that did well to fill the void between the two HSS pipe sections.

The precast bent performed well during quasi-static cyclic loading, as it performed a total of 24 complete testing cycles achieving 20% strength degradation at a drift ratio of 9.15%. The precast bent achieved an ultimate lateral capacity of 71.4-kip, correlating to a moment capacity of 498-kip-ft. Overall, the precast bent demonstrated a stable consistent response through the full progression of testing. The precast bent resulted in less cracking than the CIP bent, but with elevated spalling. The precast bent performance far exceeded expectations and will compare favorably to the CIP bent.

## **Bent Pier System: Precast vs. Cast-In-Place**

The two systems performed as expected and designed, with each exhibiting similar capacity having the same overall dimensions and both being subjected to similar loading. The CIP bent developed significant cracking and failed due to longitudinal reinforcing fracture after a total of 15 cycles. The precast bent using the proposed connection exhibited reduced cracking, in comparison, with increased spalling and failed after 24 total cycles due to the HSS pipe deforming and ultimately tearing. The precast pier demonstrated a reduced stiffness, 38.7 kip/in., approaching ultimate capacity in comparison to the 56.7 kip/in. exhibited by the CIP bent. This reduced stiffness is due to the presence of the elastomeric bearing. The precast bent also achieved a higher ultimate capacity of 71.4-kip than that of the 66-kip achieved by the CIP bent. The two systems exhibited a great difference in the yield displacements. Resulting in initial yield displacement drift ratios of 0.5% and 1.13%, for the CIP and precast bent, respectively. However, in comparing global yield the two systems exhibited differing values. The CIP bent had a global yield of displacement 0.596 in. and a correlating moment of 392-kip-ft, whereas the precast bent exhibited a global yield displacement of 1.246 in. and correlating moment of 433-kip-ft. The two systems also exhibited differences in cumulative energy dissipation. The reduced stiffness of the precast bent caused it to have lower energy dissipation at lower cycles; it slowly cumulated until the stability and added confinement of the HSS pipe allowed it to produce a more stable consistent response to the continued cycles. At the point of failure, the CIP bent demonstrated a cumulative dissipated energy of 342 kJ (252,246 ft-lb), whereas the precast bent at similar cycles (15 total cycles) demonstrated a cumulative dissipated energy of 466 kJ (343,704 ft-lb). As the precast bent was capable of withstanding a total of 24 complete cycles the ultimate cumulative dissipated energy of the systems was 2,125 kJ (1,567,320 ft-lb). Additionally, the precast bent exhibited a slightly greater overstrength factor, 2.18, verse 1.76 for the CIP bent. However, the precast bent exhibited reduced displacement ductility than that of the CIP bent. The precast bent having at minimum matched or exceeded the CIP bent in all categories, except low drift stiffness and displacement ductility due to the elastomeric bearing presence, the proposed connection used is said to have successfully emulated CIP construction under seismic loading. Table 2 provides a summarized comparison of the CIP bent and precast bent.

## 4. Analytical Investigation

### Cantilever Column

This section presents development of appropriate distributed plasticity models for analytical prediction of the two cantilever specimens. Analytical models for both cast-in-place and precast piers are developed using the OpenSees software. Results are compared against experimental data. The analytical prediction in this report is limited in scope and covers only validation of analytical models for the tested specimens. It should be noted that discussion on performance-based design and displacement based seismic design are beyond the scope of project. In this project a force-based seismic design philosophy has been primarily used.

### Cast-In-Place Pier

The analytical models were developed using the OpenSees Finite Element software. Half-scale columns were modeled with nonlinear materials for unconfined concrete, confined concrete, and steel reinforcing bars. Uniaxial fiber-sections were used in the models. Bond-slip spring elements were used to represent the bar slip relative to the concrete in the footing. This slip causes rotation at the column footing interface, resulting in additional displacement (or drift) in the column. The CIP Pier specimen is shown in Figure 117.

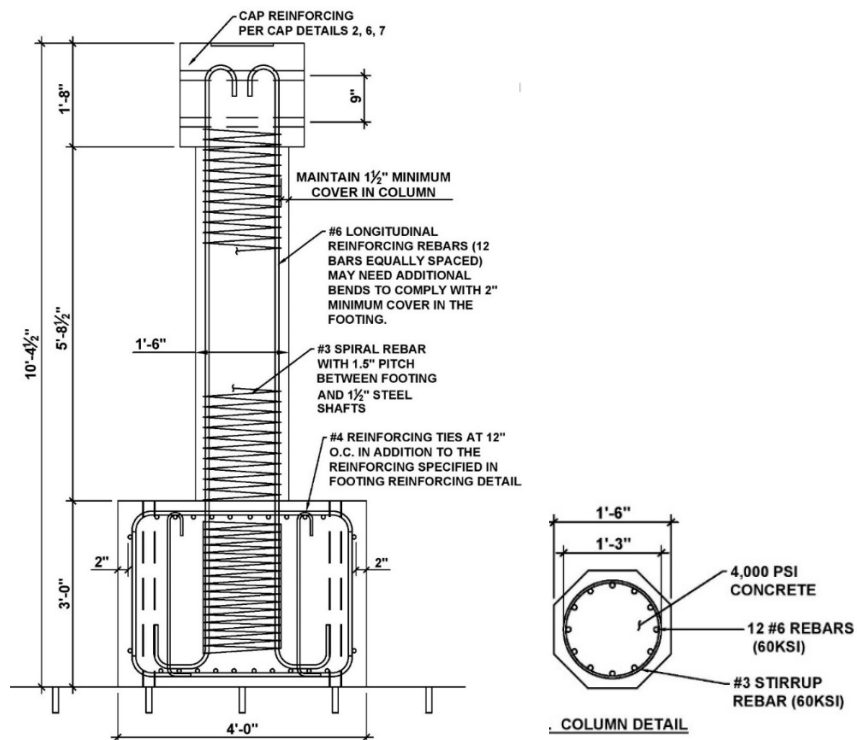


Figure 117. Details of CIP Pier Specimen

In order to duplicate the same results as the experimental study, OpenSees' "Concrete01", "Concrete04", and "Steel02" nonlinear material models were used for unconfined concrete, confined concrete, and longitudinal steel bars, respectively. The computer model uses distributed plasticity frame elements with uniaxial fiber sections.

The model shown in Figure 118 has six nodes and five elements. Two elements are nonlinear, and three elements are linear elastic. The nonlinear element E1 is an OpenSees' "zeroLength" element that represents the bond-slip at the base of the column. The other nonlinear element (element E2) is an OpenSees' "nonlinearBeamColumn" element that uses fiber sections with the three materials noted above. E3, E4, and E5 are OpenSees' "elasticBeamColumn" elements with high stiffness values.

The rotation caused by the bond-slip at the base of the column is modeled using a rotational spring with a "Hysteretic" material behavior. The rotational spring uses a bi-linear curve describing the moment-rotation relationship. The idealized (fitted) bi-linear curve is shown in Figure 119. This process employs the method developed by Wehbe, et al. (1999). The tensile stress and strain in the extreme longitudinal bar and the location of the neutral axis are determined using a moment-curvature analysis (Haber et al. 2013; Ebrahimpour et al. 2016).

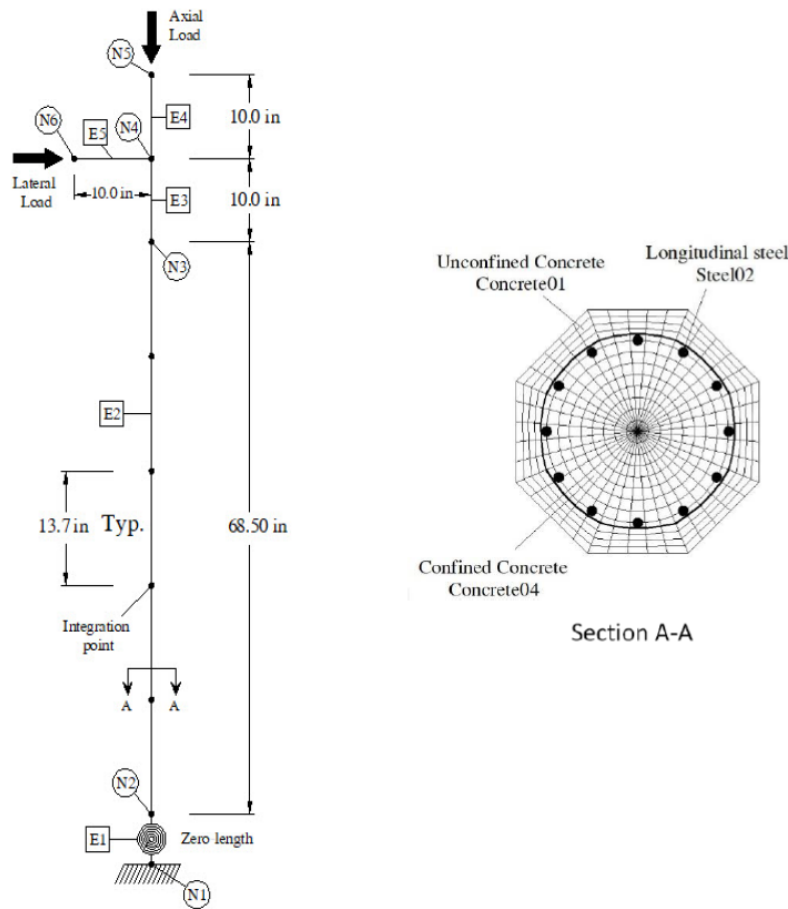
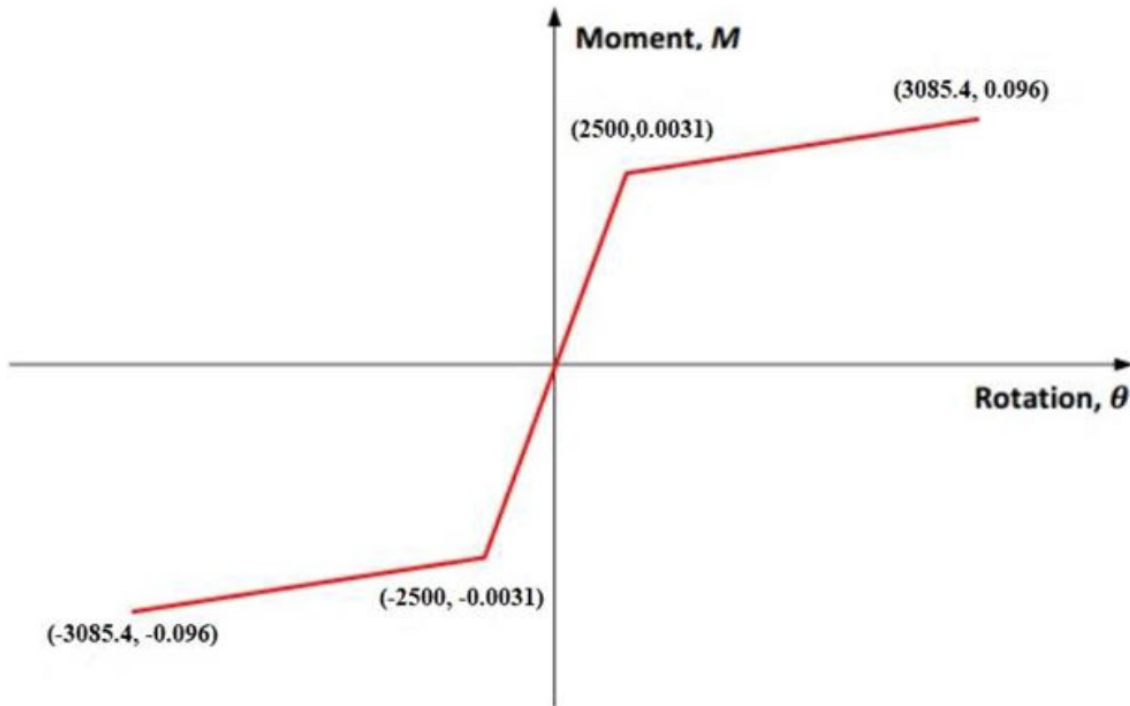


Figure 118. OpenSees Model of the Experimental CIP Column



**Figure 119. Schematic of the Fitted Bi-Linear Curve for the Footing Bond-Slip Moment Rotation**

One of the primary failure mechanisms of reinforced concrete columns subjected to a strong seismic event is low-cycle fatigue fracture of longitudinal reinforcing bars. This assumes that adequate confinement exists to prevent substantial core damage, and longitudinal bar buckling is prevented. Experimental studies on ASTM A706 and A615 bars have indicated that as little as seven full cycles of 0.06 strain can result in low-cyclic fatigue fracture of bars (Hawileh et al. 2010). In order to introduce low-cycle fatigue in OpenSees, the appropriate parameters for the Coffin-Manson curve needed to be introduced.

Brown & Kunnath's (2000) strain values for the number of half-cycles to failure are found to be considerably lower than Hawileh's (2009). Therefore, the number of cycles to failure for ASTM A615 steel were estimated by combining both data from Hawileh and Brown & Kunnath. The experimental data from Hawileh and Brown & Kunnath are shown in Figure 120. The mathematical relation for the combined strain versus number of half-cycles to failure for ASTM A615 plot is shown in Eq. below (Maskey 2017).

$$0.2468(2N_f)^{-0.522}$$

The above equation is for strain versus number of half-cycles to failure. However, OpenSees uses efficients that are for strain versus the number of full cycles to failure. When  $2N_f$  is replaced with  $N_f$  (i.e., the format required by OpenSees), the coefficient of 0.2468 changes to 0.172, but the exponent of -0.522 remains the same. For the pipe section in the precast model (see next section), the coefficients are 0.198 and -0.468.

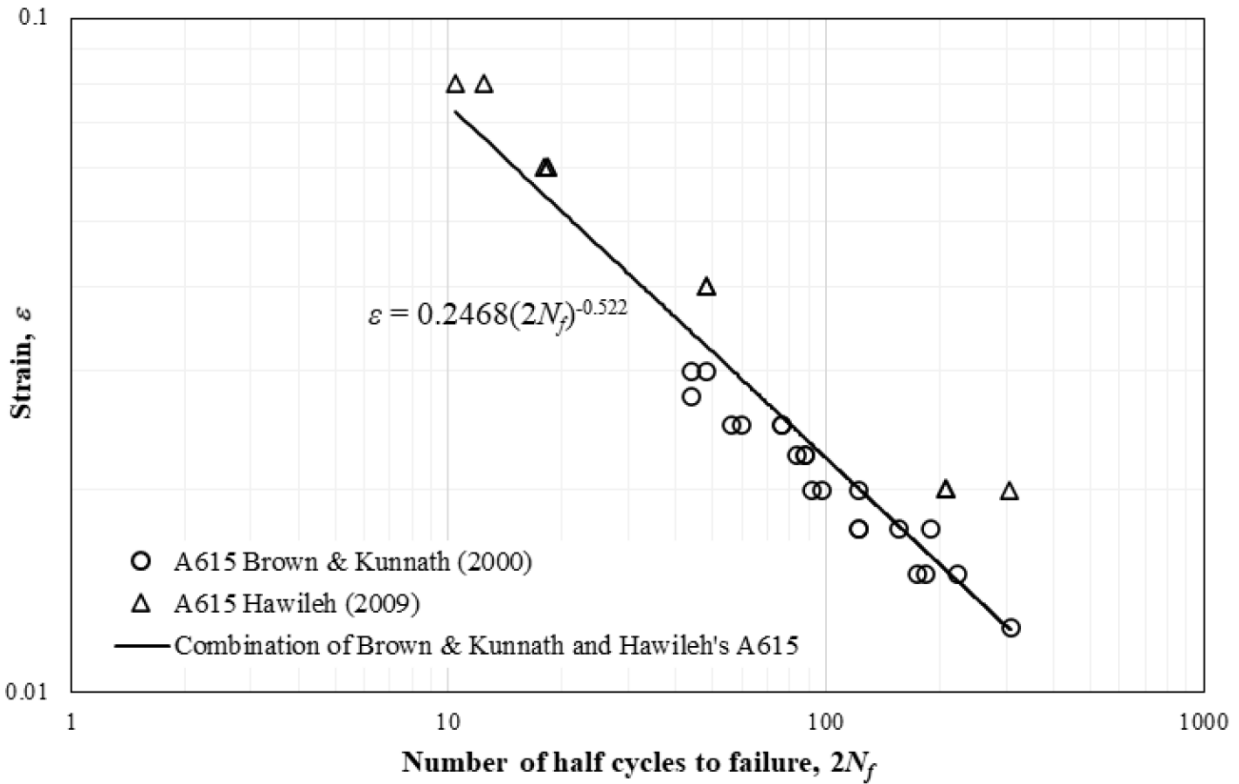


**Figure 120. Combined Strain Vs. Number of Half Cycles to Failure Plot (Based on Brown & Kunnath 2000 and Hawileh, et al. 2009)**

For the model of the cast-in-place column, an axial compressive force of 50 kips is applied at Node 5 shown in Figure 118. Node 6 is subjected to a horizontally applied displacement-controlled increasing cyclic load that was used in the experimental work. The lateral load was applied to the column model in a slow cyclic fashion. For each drift level, two full push and pull cycles were planned. Figure 121 shows the experimentally measured and calculated hysteretic force-displacement curves for the cast-in-place column.

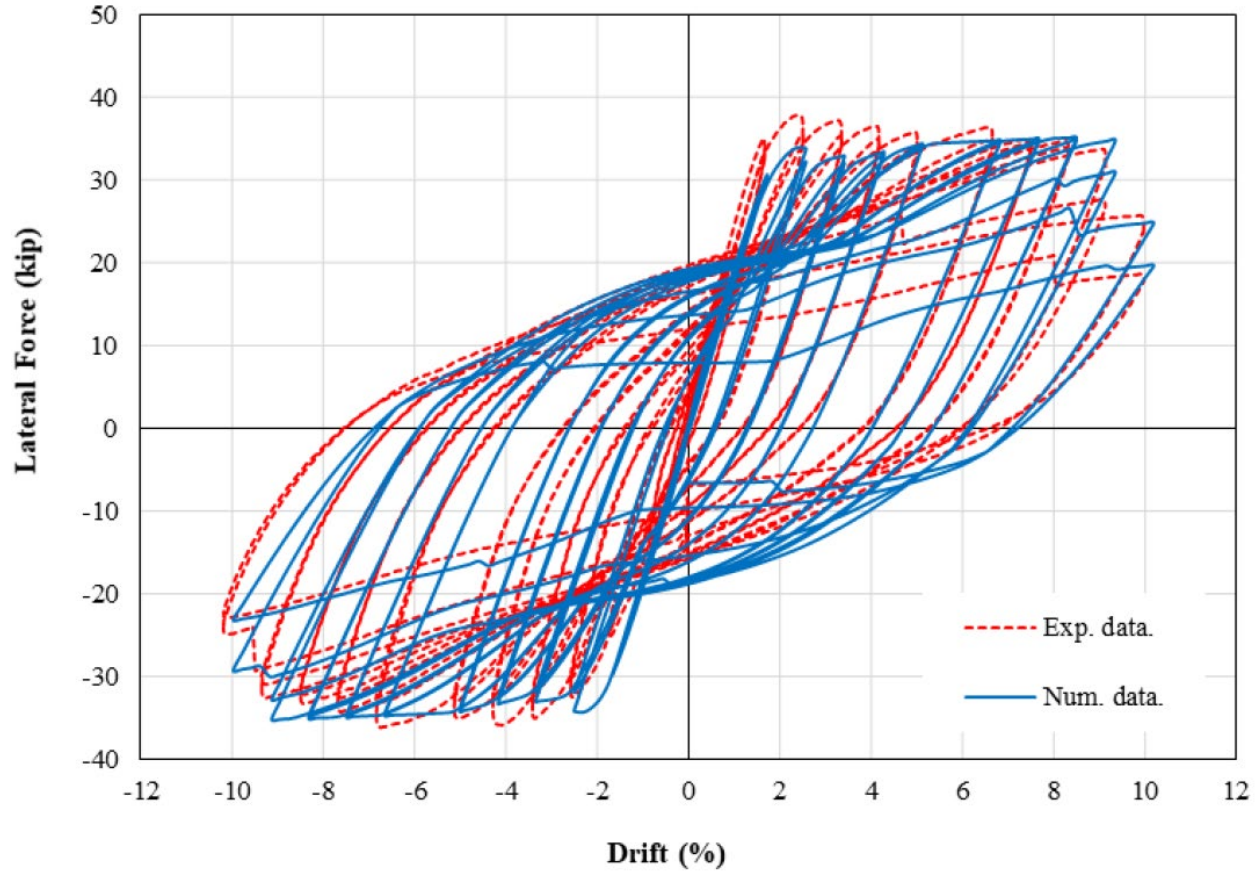


**Figure 121. Numerical and Experimental Hysteresis Force-Displacement for CIP Column**

The result validates the assumptions made for CIP column because the hysteresis loop for both experimental and numerical data are on top of each other.

### **Precast Pier**

Detailed sections of the analytical model for the precast column are shown in Figure 122 and Figure 123. The Zone 1 section of Figure 123 (a) is used for top of the column where there is rebar and concrete. For the middle section of the column where rebar, concrete as well as steel pipe are present, the section shown in Figure 123 (b) is used. At the bottom of the column where there is no rebar and only the pipe is present, the section shown in Figure 123 (c) is used. See Figure 122 for the longitudinal locations of the Zones 1 to 3 of the precast column.

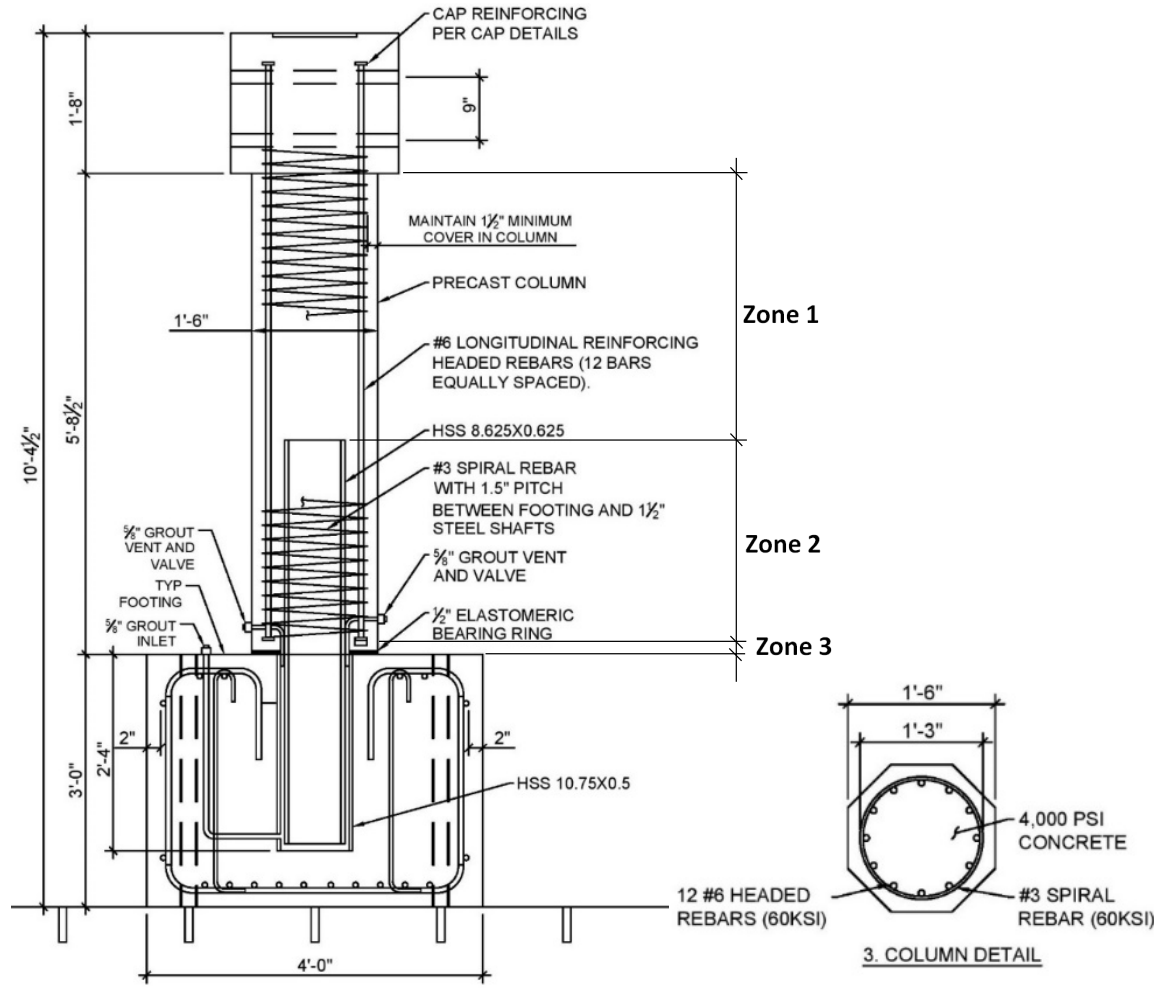


Figure 122. Details of the Precast Pier Specimen

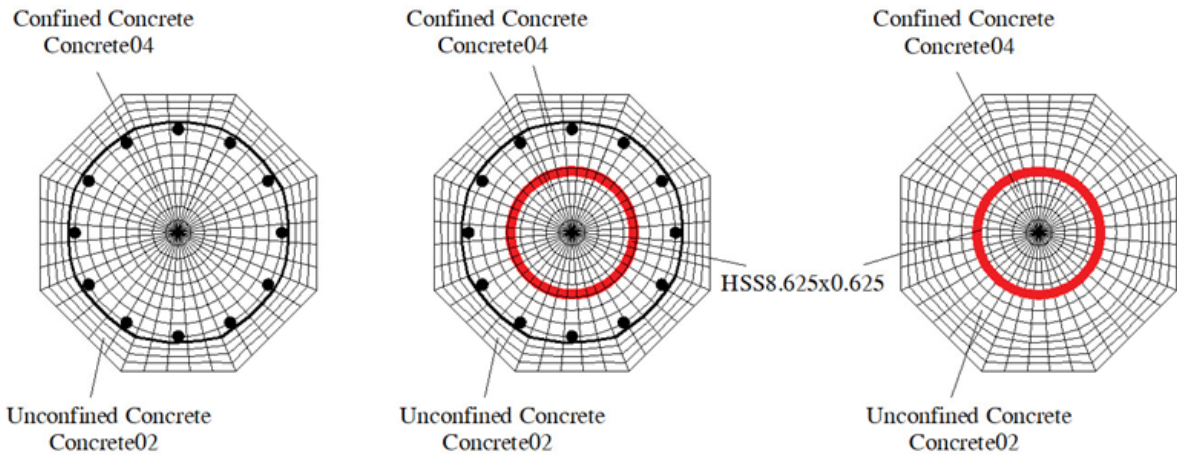
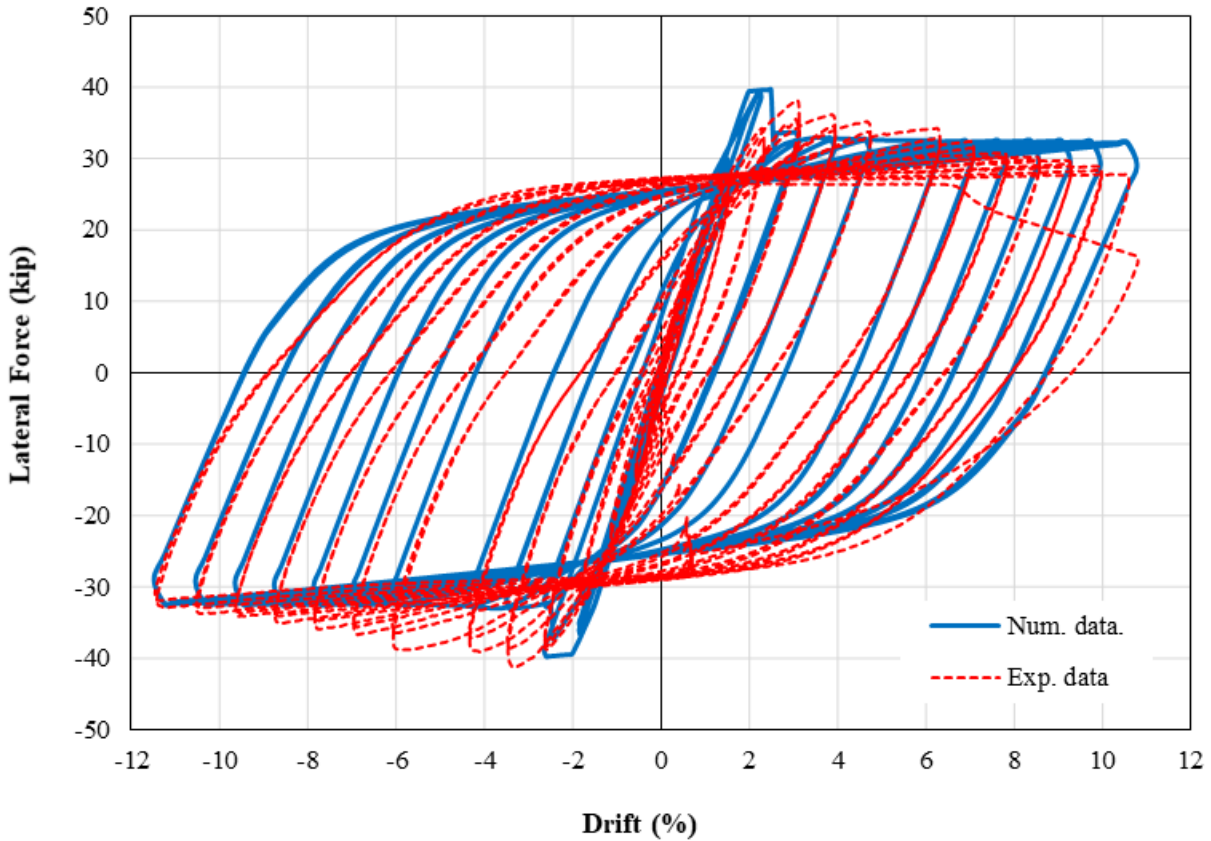


Figure 123. Detailed Sections of the Model for Precast Column: a) Zone 1, b) Zone 2, and c) Zone 3

Figure 124 shows the comparison of the numerical and experimental hysteretic force-displacement results for the precast column. As can be seen, the OpenSees model results match the experimental results until the last cycle in which the pipe buckles right before the complete collapse of the column.



**Figure 124. Numerical and Experimental Hysteresis Force-Drift for Precast Column**

The result validates the assumptions made for precast column because the hysteresis loop for both experimental and numerical data are on top of each other.

# Bent Pier System

Similar to cantilever pier system, analytical models were developed for the cast-in-place and precast bent piers using the OpenSees software.

## Cast-In-Place Bent

The analytical models were developed using the OpenSees finite element software. Half-scale bents were modeled with nonlinear materials for unconfined concrete, confined concrete, and steel reinforcing bars. The dimensions of the bent pier are discussed in the experimental portion of the project in the previous chapter. All the assumptions and modeling procedure are kept identical to the previously discussed cantilever pier system. For the cap beam, the assumption made was that it behaved as an elastic member. Figure 125 shows the experimentally measured and calculated hysteretic force-displacement curves for the cast-in-place bent pier. As it can be observed, the analytical model is in good agreement with the experimental data.

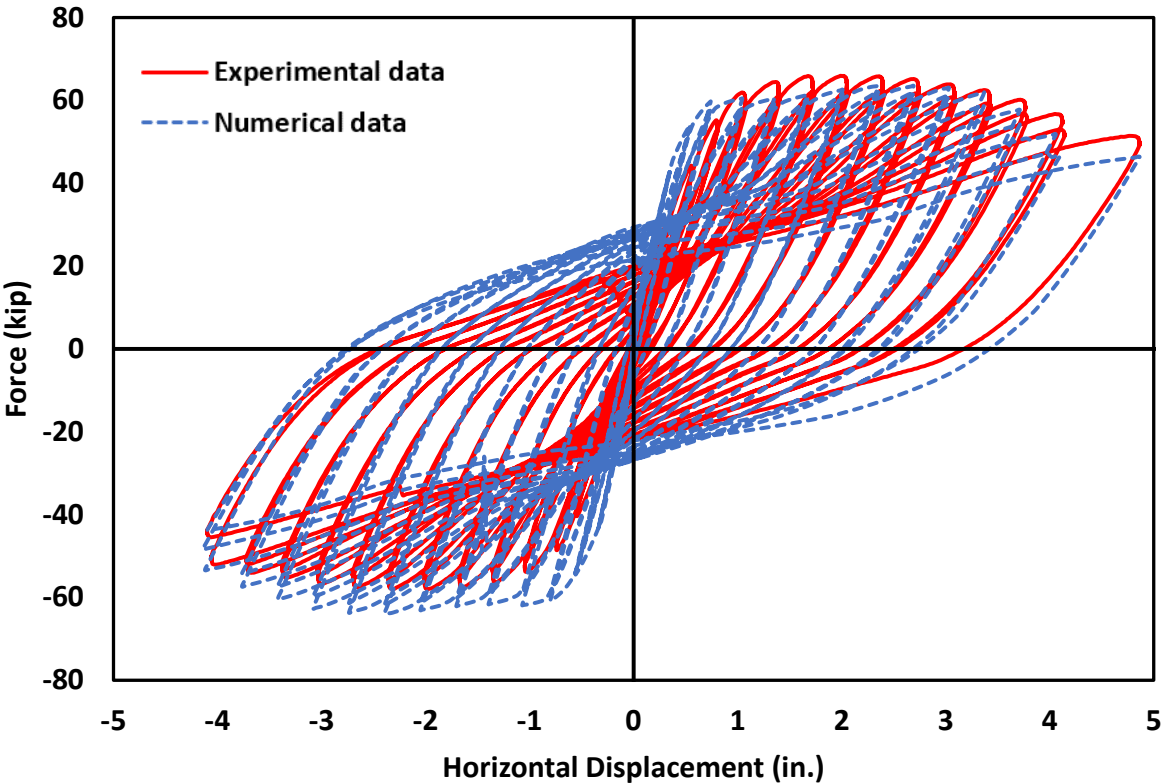


Figure 125. Numerical and Experimental Hysteresis Force-Displacement for CIP Bent Pier

### Precast Bent

Figure 126 shows the experimentally measured and calculated hysteretic force-displacement curves for the precast bent. The analytical force-displacement for the precast bent is in good agreement with the experimental data up to a drift ratio of 6%. During cycles of large drift ratio, the analytical model does not follow the experimental data to a high accuracy. This is thought to be due to excess shear deformation and Bauschinger effects in the HSS which are not easy to capture analytically.

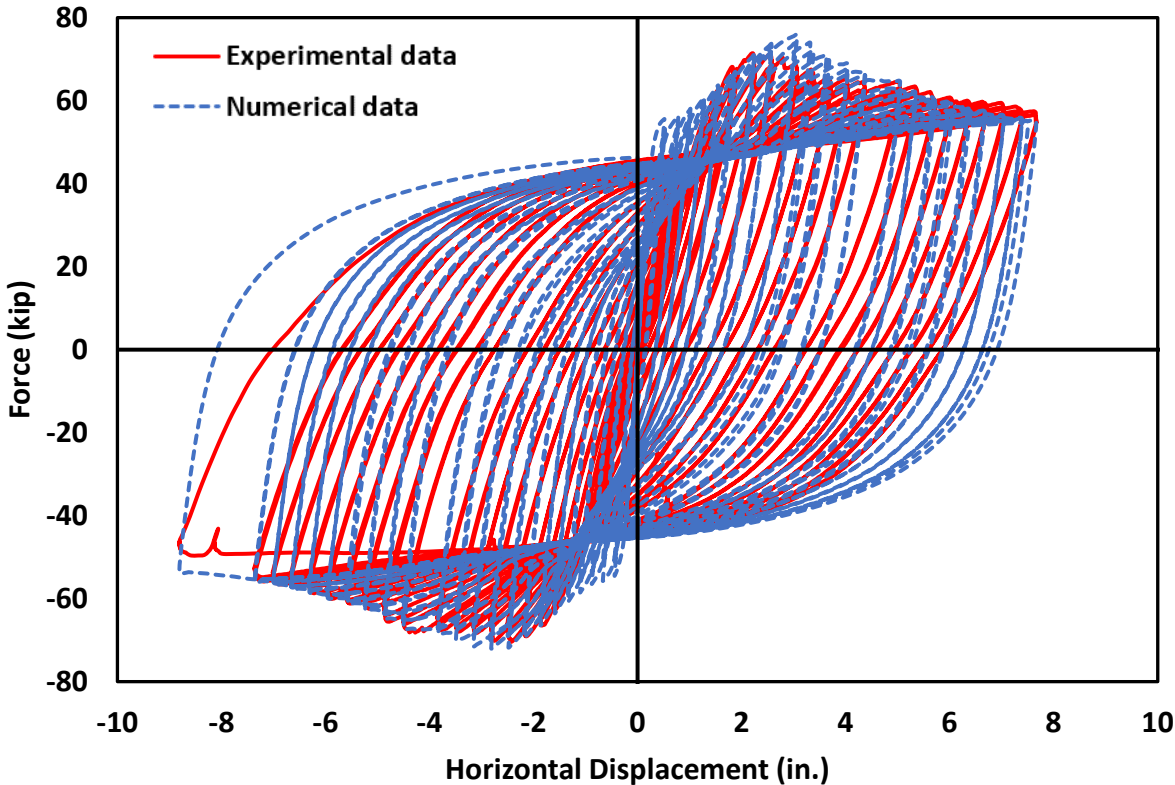


Figure 126. Numerical and Experimental Hysteresis Force-Displacement for Precast Bent Pier

## 5. Parametric Case Studies

This chapter provides some limited parametric case studies for modeling a typical highway bridge (i.e., SH-22 over I-15 at Dubois) in Idaho using OpenSees computer program. Models use both cast-in-place (CIP) and emulative CIP precast piers. The goal is to provide some guidance for the engineer that the proposed ITD connection can be modeled and analyzed very similar to CIP. The size of HSS was selected in order to closely match the capacity of the CIP bridge. For a simplified analysis, the unbonded length of the HSS was not considered in the analysis. Materials properties for the bridge were mostly kept similar for a better comparison. Nonlinear static (pushover) and nonlinear dynamic (time-history analysis) are conducted on the prototype bridge. The global seismic response of the bridge such as formation of plastic hinges, ductility, strength, base shear demand, force-displacement response has been summarized for each CIP and precast model and are compared against each other.

### Description of the Bridge

The bridge on SH-22 over I-15 at Dubois is a two-span bridge with a four-column bent. The superstructure is made up of an 8-in. thick concrete deck that rests on eight steel girders. The substructure is composed of the pier cap, four columns, and footings all cast-in-place (CIP). Figure 127 and Figure 128 show the plan and elevation views of the bridge, respectively. This bridge also has a non-integral superstructure-pier connection. The Columns are 3.5 ft in diameter with a height of 14.05 ft. The column section has 13 No. 11 steel reinforcing bars.

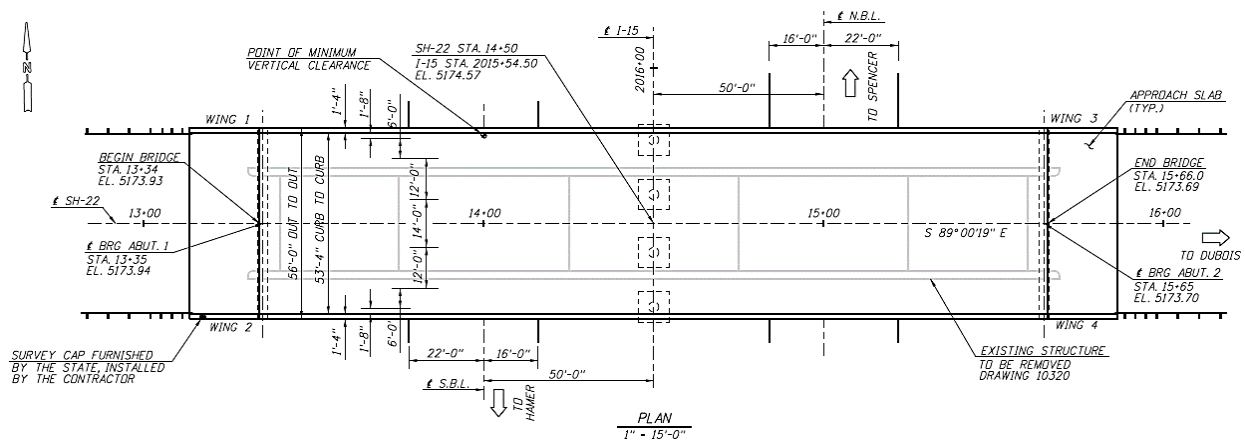


Figure 127. Plan View of the SH-22 over I-15 Bridge at Dubois (NTS)

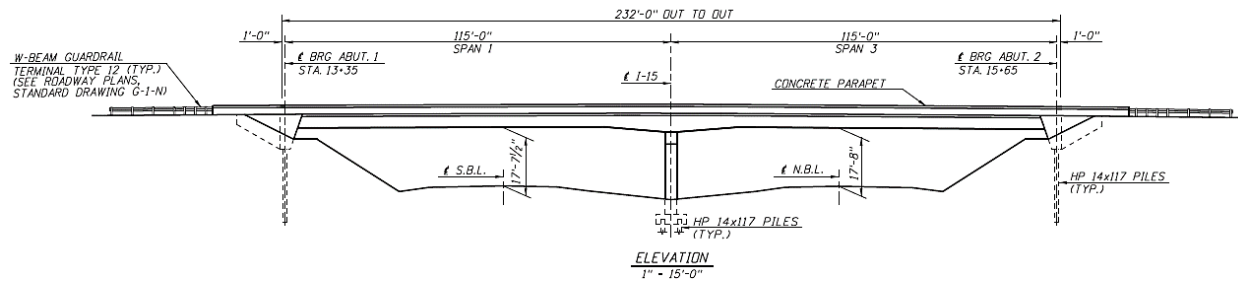


Figure 128. Elevation View of the SH-22 over I-15 Bridge at Dubois (NTS)

## Nonlinear Static Analysis

To keep the analysis simple, the single-mode spectral method was used for the bridge analysis. Since the goal is to compare the behavior of two different types of nonlinear columns (cast-in-place columns versus precast columns with the proposed pipe connection), a more complex analysis is not conducted.

In accordance with the LRFD Bridge Seismic Reference Manual (2014), the use of the uniform load method or single-mode method is one of the two options in “nonlinear static analysis.” Obviously, the procedure in the “nonlinear static analysis” is much less tedious than the “nonlinear dynamic analysis.” Nonlinear static analysis, also known as pushover analysis, is a static procedure that uses a simplified nonlinear technique to estimate seismic structural deformations. Structures redesign themselves during earthquakes. As individual components of a structure yield or fail, the dynamic forces on the building are shifted to other components. A pushover analysis simulates this phenomenon by applying loads until the weak link in the structure is found and then revising the model to incorporate the changes in the structure caused by the weak link.

The nonlinear models of the Dubois bridge with node and element placement are shown in Figure 129 and Figure 130. For the support stiffness in the spring support condition; the assumption made is the springs at abutments with fixed column bases. The abutment type is the seat type. Similarly, for the restraint of superstructure, abutments were modeled with linear springs both in longitudinal and transverse direction along with unrestrained rotation about the z-axis and infinite restraint in all other DOF's.

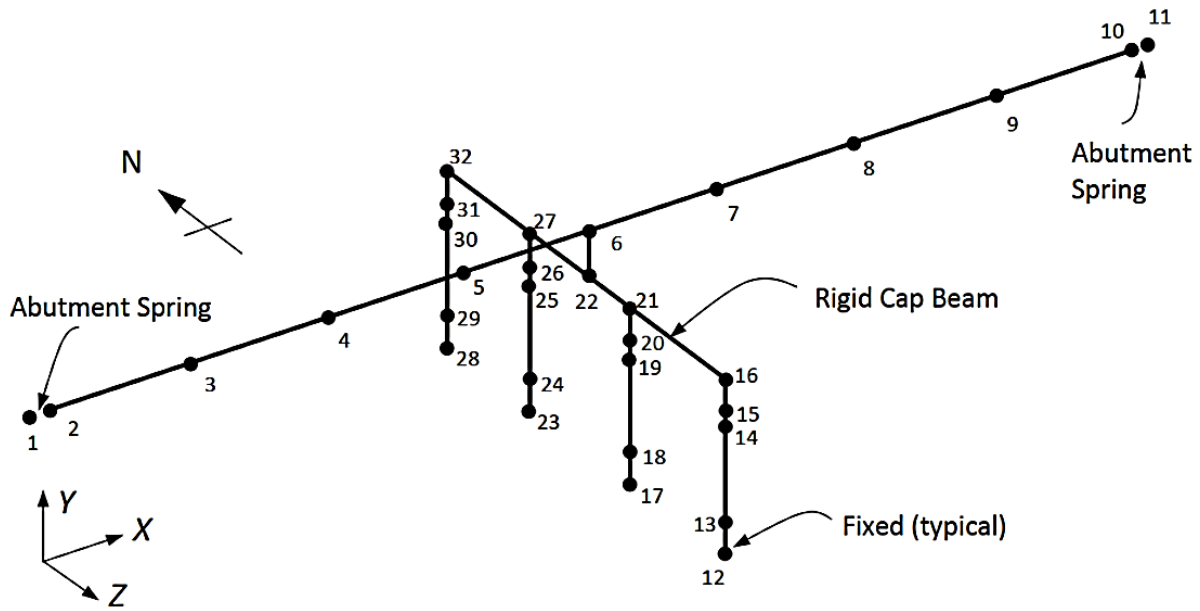


**Figure 129. Dubois Bridge Nonlinear Model with Node Numbers**

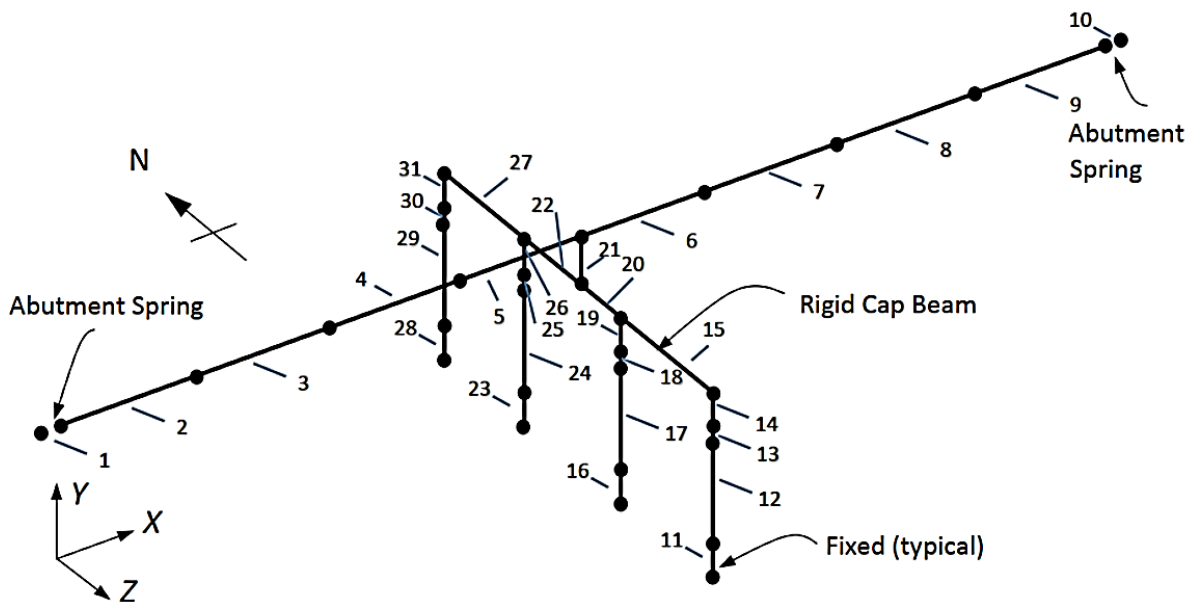


**Figure 130. Dubois Bridge Nonlinear Model with Element Numbers**

From the analysis, a global force-displacement or drift (backbone curve) is obtained (Figure 131). The displacement or drift (X axis) is taken at the center of the gravity of the superstructure and is plotted against the total base shear (Y axis). The curve is extended until hinges form in the piers and collapse, resulting in at least 20% reduction in the total base shear. The hierarchy of plastic hinge formation is shown on the backbone curve to highlight progressive collapse. It can be observed that both bridge

models (CIP and Precast) have similar strength. However, the precast bridge achieves higher displacement capacity compared to CIP.

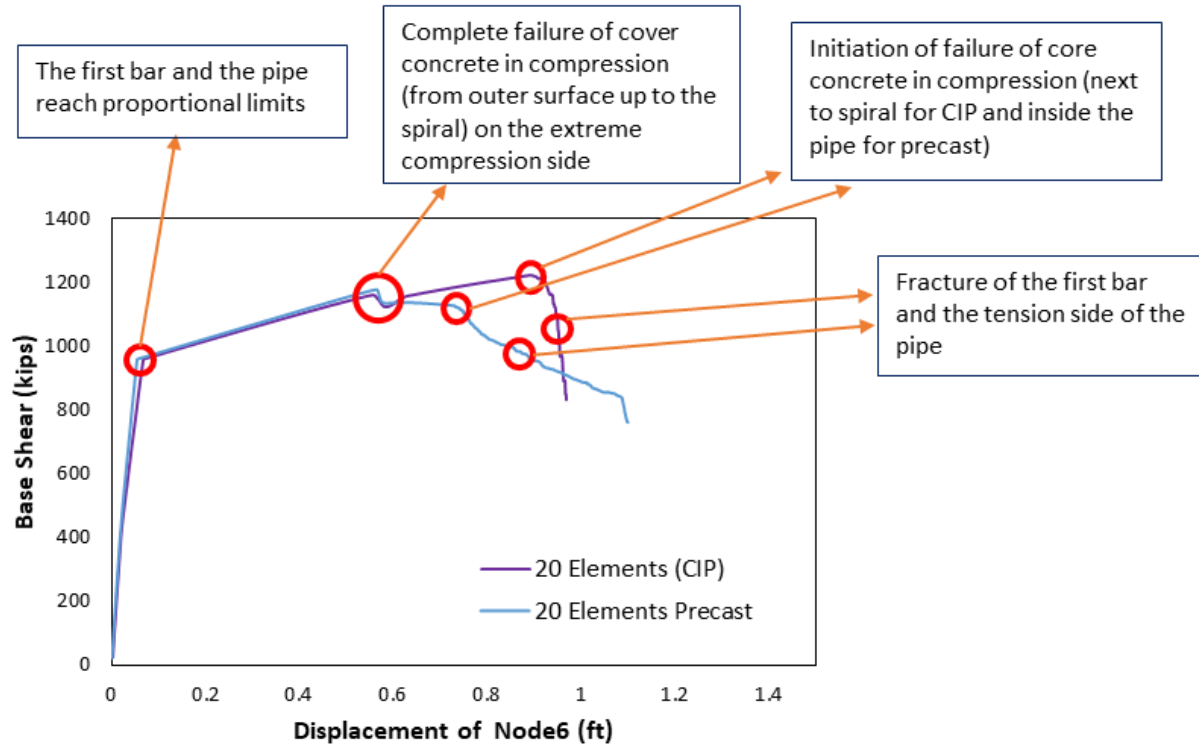
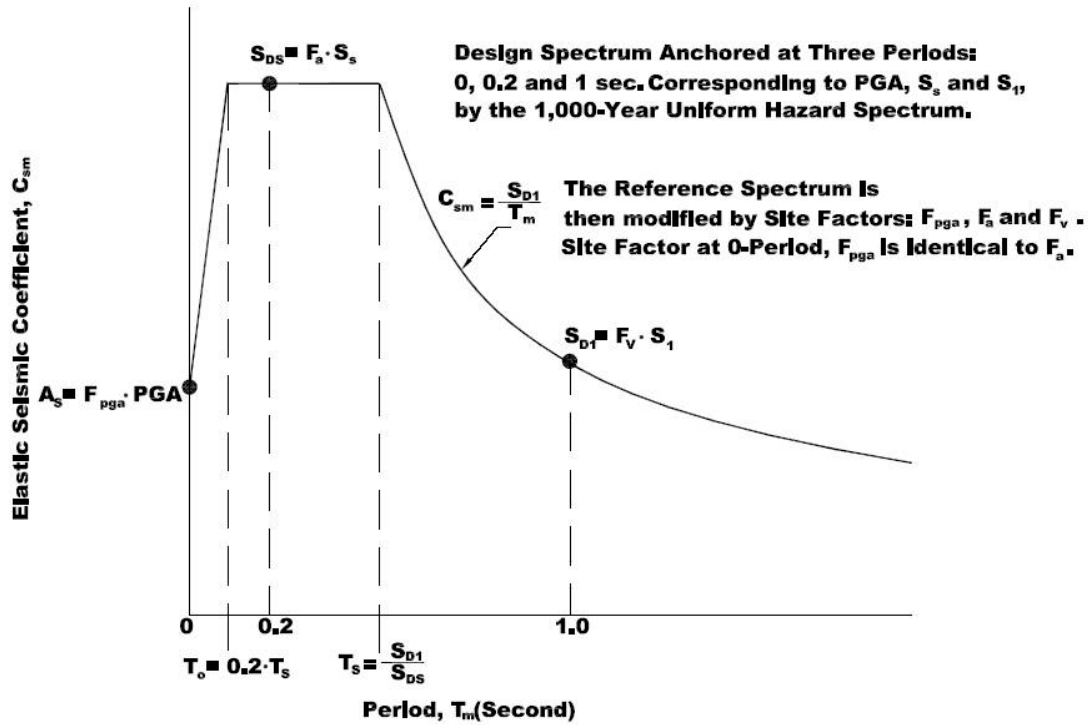


Figure 131. Base Shear Vs. Displacement for both CIP and Precast Column

## Nonlinear Dynamic Analysis

Nonlinear dynamic analysis is carried out to investigate the performance of the bridge with the proposed pipe connection. The goal is to observe how the prototype bridge would perform compared to CIP when subjected to ground motions.

Before selecting ground motion, the bridge is assumed to be located in the most seismically active location in Idaho. The “Step-by-Step Instructions for AASHTO Guide Specifications” and the USGS web site (<https://earthquake.usgs.gov/ws/designmaps/>) were used to obtain the parameters needed to construct the current AASHTO 1000-yr return period response spectrum for the design of a conventional bridge. For the Upper-Level Ground Motion and 7 percent probability of exceedance in 75 years; the return period in accordance with AASHTO is about 1,000 years. Location of the bridge is assumed to be in Montpelier in Idaho (Latitude: 42.32 degrees, Longitude: -111.3 degrees) where soil class is assumed to be D ‘Stiff Soil’. Figure 132 shows the AASHTO recommended three-point method that was used to obtain the design spectrum for the analysis. Similarly, Table 16 shows the data point obtained to construct the uniform hazard spectrum and Figure 133 shows the design spectrum obtained from the data points.



- pga** PGA, the mapped horizontal Peak Ground Acceleration, in units of g
- fpga**  $F_{PGA}$ , the site coefficient for PGA, from Table 3.4.2.3-1 of the seismic design reference document
- as**  $A_s = F_{PGA} \times PGA$  (Equation 3.4.1-1), the design peak ground acceleration, in units of g
- ss**  $S_s$ , the mapped short-period (0.2-second) spectral acceleration, in units of g
- fa**  $F_a$ , the site coefficient for  $S_s$ , from Table 3.4.2.3-1
- sds**  $S_{DS} = F_a \times S_s$  (Equation 3.4.1-2), the design short-period (0.2-second) spectral acceleration, in units of g
- s1**  $S_1$ , the mapped 1-second spectral acceleration, in units of g
- fv**  $F_v$ , the site coefficient for  $S_1$ , from Table 3.4.2.3-2
- sd1**  $S_{D1} = F_v \times S_1$  (Equation 3.4.1-3), the design 1-second spectral acceleration, in units of g
- sdC** SDC, the Seismic Design Category from Table 3.5-1
- ts**  $T_s = S_{D1} / S_{DS}$  (Equation 3.4.1-6), in seconds, for construction of design response spectrum
- t0**  $T_0 = 0.2T_s$  (Equation 3.4.1-5), in seconds, for construction of design response spectrum
- sdSpectrum**  $S_a$ , the design response spectrum from Figure 3.4.1-1 and Equation 3.4.1-4

**Figure 132. AASHTO Seismic Coefficient Design Spectrum Constructed with the Three-Point Method**

**Table 16. Uniform Hazard Spectrum Data Points for Montpelier, Idaho**

<b>Period, <math>T_m</math> (second)</b>	<b>Elastic Seismic Coefficient, <math>C_{sm}</math></b>
0	0.38
0.1072	0.908
0.2	0.908
0.535	0.908
0.6	0.81
0.7	0.694285714
0.8	0.6075
0.9	0.54
1	0.486
1.1	0.441818182
1.2	0.405
1.3	0.373846154
1.4	0.347142857
1.5	0.324
1.6	0.30375
1.7	0.285882353
1.8	0.27
1.9	0.255789474
2	0.243
2.1	0.231428571
2.2	0.220909091
2.3	0.211304348
2.4	0.2025
2.5	0.1944

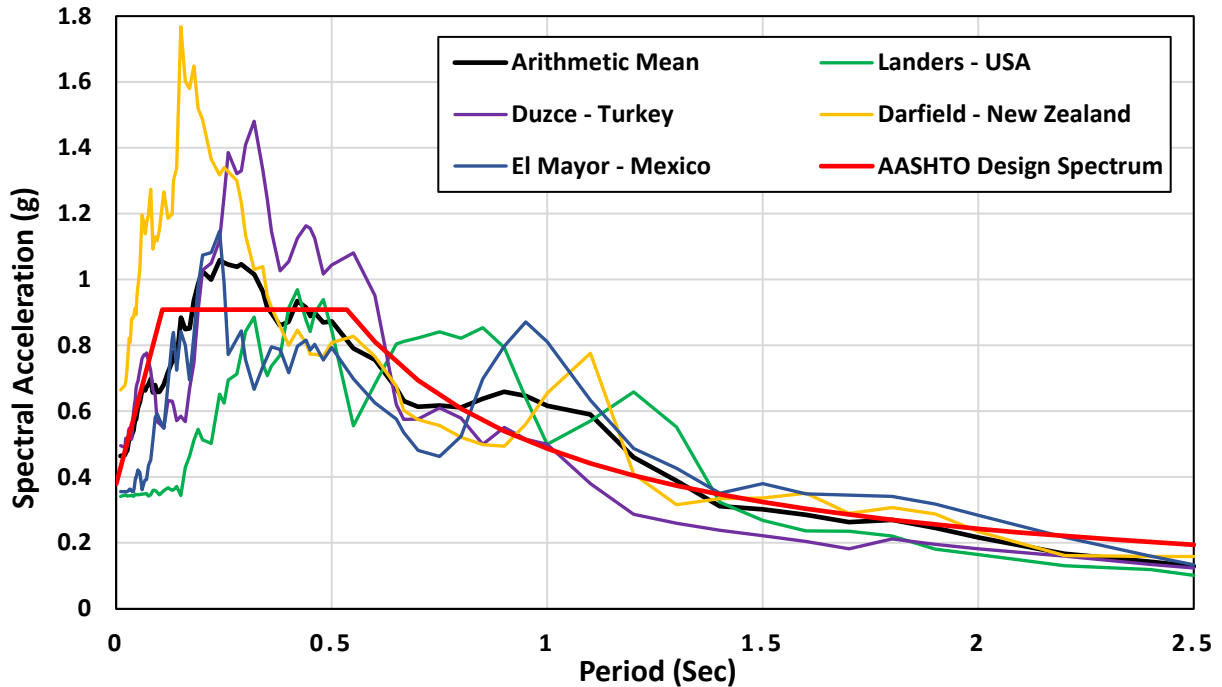


**Figure 133. Design Spectrum**

The Pacific Earthquake Engineering Research Center (PEER) website (<https://ngawest2.berkeley.edu/>) was used to obtain earthquake records and scale the ground motion to the design spectrum. The search criteria for the earthquake records were set as follows:

- Using NGA-West2 database (Western United States)
- Identifying up to 10 ground motion records for strike-slip/normal faults; magnitude 7-7.5; rupture distance ( $R_{rup}$ ) 0-20 km; and any average seismic shear-wave velocity ( $V_{s30}$ )
- Assuming a natural period of 1.5 sec for the bridge (transverse direction); the period of interest for scaling can be taken as  $0.2T_n - 1.5 T_n$  or  $0.3 - 2.25$  sec.
- Spectral ordinate of H1 (not-rotated); 5% damping ratio; arithmetic suite average; and minimize MSE scaling method with weight factor of 1.
- Neglecting vertical excitation and rotational components of ground motions

Four earthquake records from different parts of the world were selected. These records and their scaling factors are summarized in Table 17. The bridge model is subjected to ground displacement from each record for both components of the ground motion (e.g., first run one component in the transverse direction, obtain the results and then run the second component in the transverse direction). Similar procedure for longitudinal direction is carried out.

**Table 17. Earthquake Records form Different Regions**

Scale Factor	Earthquake Name/Location/Station	Year	Magnitude	Mechanism	R <sub>jb</sub> (km)	R <sub>rup</sub> (km)	V <sub>s30</sub> (m/sec)
1.239	Landers – USA - Joshua Tree	1992	7.28	Strike-slip	11.03	11.03	379.32
0.6596	Duzce – Turkey - Bolu	1999	7.14	Strike-slip	12.02	12.04	293.57
1.4092	Darfield - New Zealand - DFHS	2010	7	Strike-slip	11.86	11.86	344.02
1.0718	El Mayor-Cucapah – Mexico - El Centro Array #12	2010	7.2	strike-slip	9.98	11.26	196.88

### Cast-In-Place Bridge Response

A typical dynamic input and response of the model is shown in Figure 134 and Figure 135. In these figures, Direction 1 is a longitudinal direction and Direction 2 is transverse direction. Table 18 provides a summary of the nonlinear dynamic analysis for the CIP bridge. The last column in the table shows the yield stress which is obtained from the static pushover analysis of the bridge explained previously. AASHTO requirement for finding maximum base shear and displacement was used to obtain the load combination for base shear demand as follows:

$$1.0A + 0.3B$$

Where:

- A = Larger displacement or base shear between two directions (longitudinal and transverse)
- B = Smaller displacement or base shear between two directions (longitudinal and transverse)

In this research, matching of horizontal ground motion components to an orientation-independent spectrum (RotDnn) was not considered. However, this could be a good future research to investigate the nonlinear dynamic performance of bridges incorporating such connections.

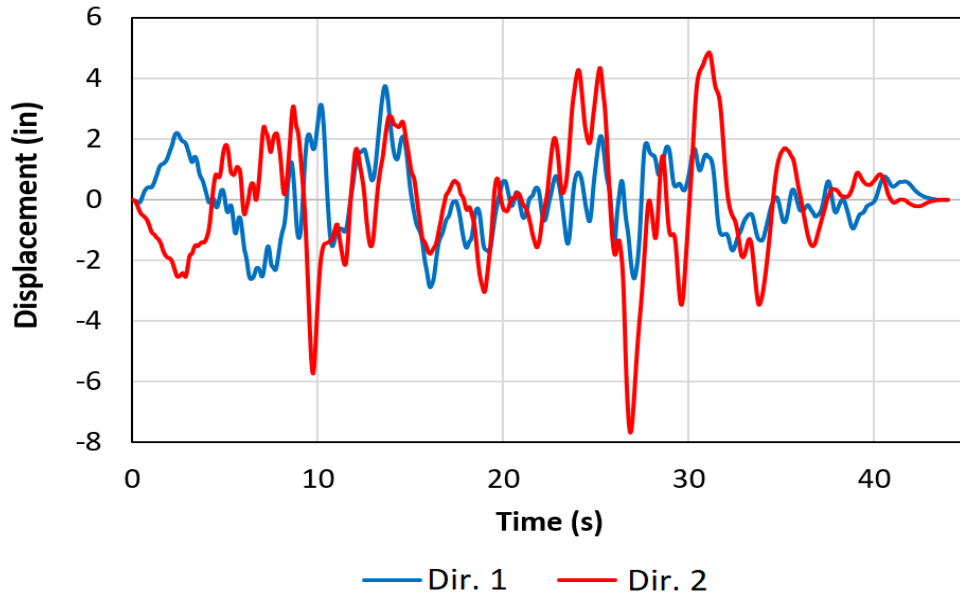


Figure 134. Displacement vs. Time for Landers Earthquake

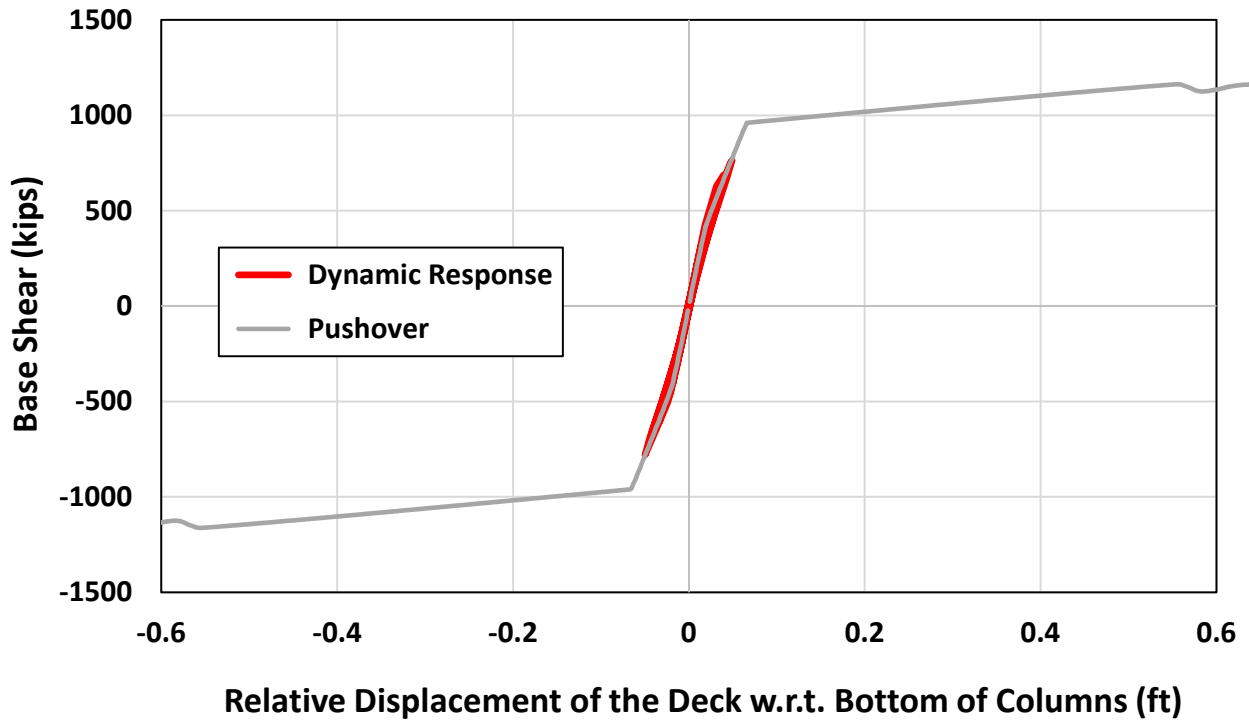


Figure 135. Pushover vs. Dynamic Response for Landers Earthquake for the Bridge with CIP Columns in Direction 2

**Table 18. Maximum Base Shear and Displacement for CIP Bridge (Absolute Values Shown)**

Direction of EQ	Max. Long. Base Shear (kips)	Max. Trans. Base Shear (kip)	Max. Base Shear Demand, Combo (kips)	Max. Long. Displ. (ft)	Max. Trans. Displ. (ft)	Max. Displ. Demand Combo (ft)	Pushover Yield Strength (kips)
<b>Landers</b> Dir1-Long, Dir2-Trans	296	780	869	0.02	0.05	0.056	940
<b>Landers</b> Dir1-Trans, Dir2-Long	413	749	873	0.025	0.047	0.055	940
<b>Duzce</b> Dir1-Long, Dir2-Trans	530	657	816	0.03	0.04	0.05	940
<b>Duzce</b> Dir1-Trans, Dir2-Long	315	974	1067	0.021	0.098	0.1	940
<b>Darfield</b> Dir1-Long, Dir2-Trans	972	966	1262	0.094	0.082	0.12	940
<b>Darfield</b> Dir1-Trans, Dir2-Long	714	978	1192	0.051	0.11	0.05	940
<b>El Mayor</b> Dir1-Long, Dir2-Trans	622	770	957	0.043	0.049	0.062	940
<b>El Mayor</b> Dir1-Trans, Dir2-Long	648	931	1125	0.044	0.067	0.08	940

From Table 18, it can be observed that excluding the Landers record, all other earthquake records pushed the CIP bridge beyond the yield capacity. The displacement demand from all four records are smaller. This is due to the Idaho’s seismicity where earthquakes are not expected to cause large displacements as compared to other locations such as California which has a higher seismic demand.

### **Precast Bridge Response**

Similar to the CIP model, the bridge with precast pier was subjected to the four ground motion records. Results are summarized in Table 19. As it can be observed, all four earthquake records pushed the bridge beyond the yield capacity.

**Table 19. Maximum Base Shear and Displacement for Precast Bridge (Absolute Values Shown)**

Direction of EQ	Max. Long. Base Shear (kips)	Max. Trans. Base Shear (kip)	Max. Base Shear Demand, Combo (kips)	Max. Long. Displ. (ft)	Max. Trans. Displ. (ft)	Max. Displ. Demand Combo (ft)	Pushover Yield Strength (kips)
<b>Landers</b> Dir1-Long, Dir2-Trans	315	872	967	0.02	0.047	0.053	960
<b>Landers</b> Dir1-Trans, Dir2-Long	421	761	887	0.024	0.04	0.047	960
<b>Duzce</b> Dir1-Long, Dir2-Trans	544	696	860	0.029	0.037	0.05	960
<b>Duzce</b> Dir1-Trans, Dir2-Long	340	975	1077	0.02	0.083	0.09	960
<b>Darfield</b> Dir1-Long, Dir2-Trans	977	973	1269	0.088	0.08	0.11	960
<b>Darfield</b> Dir1-Trans, Dir2-Long	788	984	1220	0.05	0.1	0.12	960
<b>El Mayor</b> Dir1-Long, Dir2-Trans	661	965	1163	0.043	0.061	0.07	960
<b>El Mayor</b> Dir1-Trans, Dir2-Long	755	952	1179	0.047	0.054	0.07	960

## Cast-In-Place Vs. Precast Bridge

Results from nonlinear static and dynamic analyses showed that the bridge with the precast pier closely emulates the cast-in-place bridge behavior. Both models had similar strength, ductility, and stiffness. Since the location of the Dubois bridge was assumed to be in Montpelier, nonlinear dynamic analysis showed that both cast-in-place and precast bridge models would reach their yield capacity under the four earthquake records. This is to be expected since the design seismic accelerations for Montpelier are larger than those of Dubois. In summary, existing nonlinear analysis techniques for cast-in-place bridges can be used to perform a system level analysis of a bridge with the proposed ITD connection.

## 6. Design and Detailing Considerations

### Introduction

This chapter discusses flexural analysis, interaction diagrams, design/detailing considerations, construction/assembly technology, limitations, inspection, and potential post-earthquake repair methods for the precast pier.

### Flexural Analysis

Existing resources that can be used to design the precast pier include the AASHTO LRFD Bridge Design Specifications (AASHTO 2017), WSDOT Bridge Design Manual (WSDOT 2019), and Integral Abutments for Steel Bridges (Wasserman and Walker 1996). The AASHTO LRFD Bridge Design Specifications are used as a basis for all footing and column reinforcement. The WSDOT Bridge Design Manual is used to determine the capacity and size the HSS member used to connect the column to the footing. The WSDOT Bridge Design Manual and Integral Abutments for Steel Bridges are used to determine the embedment length of the HSS member.

The first step is to design the column as cast-in-place and identify the required nominal capacity. In the next step, the size of the HSS for the precast solution is identified. The WSDOT Bridge Design Manual provides several equations to select an appropriate HSS member. Appendix D of this report provides a variety of different pipe sizes as a means to quickly determine if a pipe will work and to estimate the moment capacity of an HSS pipe having a yield strength of 42 ksi, ultimate strength of 58 ksi, and compression strength of concrete of either 4 or 8 ksi.

WSDOT (2019) provides equations to check the diameter to pipe thickness ratio and to determine the moment capacity of a CFST. The following equation is used to ensure the pipe is not subject to local buckling before developing the strength of the pipe:

$$\frac{D}{t} \leq 0.15 \frac{E}{F_y}$$

Where:

D = Outside diameter, inches

t = Wall thickness of HSS member, inches

According to WSDOT (2019), the pipe thickness should be reduced as a result of corrosion over a 75-year minimum design life. The corrosion rates vary according to the environment as described in Table 20 and assumes that the soil is not highly corrosive. The minimum corrosion reduction shall be taken as 1/16 in. The interaction diagrams and tables in this report do not incorporate the corrosion reduction factor.

**Table 20. Common Corrosion Rates from WSDOT Bridge Design Manual**

Location	Corrosion Rate
Soil embedded zone (undisturbed soil)	0.001 in./year
Soil embedded zone (fill or disturbed soils)	0.003 in./year
Immersed zone (freshwater)	0.002 in./year
Immersed and tidal zone (saltwater)	0.004 in./year
Splash zone (saltwater)	0.006 in./year
Atmospheric zone	0.004 in./year

In the absence of research data on displacement-based design of the bridges with such connections, the current equation from WSDOT can be used. If future research demonstrates that an expected nominal moment as per AASHTO Seismic Guides can be used for this connection; it would likely influence the presented design guidelines. The equation WSDOT provides to determine the nominal moment capacity is shown below:

$$M_n(y) = \left( c(r_i^2 - y^2) - \frac{c^3}{3} \right) * 0.95f'_c + 4ct \frac{r_m^2}{r_i} F_y$$

Where:

c = One half cord length of the compressive block

$r_i$  = Mean radius of internal reinforcement, in

$r_m$  = Mean radius of HSS member, in

y = Vertical distance of neutral axis from center of HSS in plastic stress distribution method, in

$f'_c$  = Compressive strength of the concrete

t = thickness of HSS member

c is calculated using:

$$c = r_i \cos \theta$$

Where:

$r_i$  = Mean radius to the inside of the steel tube

$\theta$  is calculated using:

$$\theta = \sin^{-1} \left( \frac{y}{r_m} \right)$$

Where:

y = Distance from the centroid of the specimen to the neutral axis during a seismic event, in

$r_m$  = Radius to the center of the steel tube, in

Because the neutral axis is expected to be approximately equal to the centroid when the structure is assembled, the variable y is equal to zero. If the column is not plumb when the column is assembled to the footing, the variable y is used to reduce the column capacity.

To select the column receiving pipe, use a size that will allow a tolerance gap. The gap needs to be large enough to allow the grout to easily flow between the two HSS members. This tolerance gap is larger compared to grouted ducts or similar connections. It is expected that the gap can be up to 2 in. on each side of the pipe without compromising the structural integrity of the connection. For gaps larger than 2 in. experimental and analytical testing should be performed to demonstrate the integrity of the connection beyond the yield point. The gap used in this research was equal to 0.5 in. on each side of the pipe.

## Interaction Diagrams

The equations used to develop the interaction diagram are the same equations that are discussed in the previous section for flexural analysis for CFSTs from the WSDOT Bridge Design Manual (WSDOT 2019). To create the interaction diagram, a variety of different pipe thicknesses, pipe diameters, and two different compression strengths of concrete. The pipe thicknesses used are values found in the American Institute of Steel Construction Manual (AISC Committee 2010) and vary from 0.174 in. to 0.581 in. The Pipe diameters range from 10 in. to 60 in. The compression strength of the concrete used is 4 and 8 ksi and does not account for an axial load. The interaction diagram is shown in Figure 136 and displays the variables used to develop it. Looking at Figure 136, the moment capacity increases as the pipe diameter, pipe thickness, and compression strength of concrete increase. It should be noted that the interaction diagrams in this report do not account for an axial load.

To determine the moment capacity of a specific HSS member, the user only needs to have predetermined the pipe diameter, pipe wall thickness, and the compression strength of concrete. For example, if a 36 in. diameter pipe having a thickness of 0.465 in. were to be selected to be embedded in concrete having a compression strength of 8 ksi, the resulting moment capacity can be determined from Figure 136 to be roughly 4500 kip-ft.

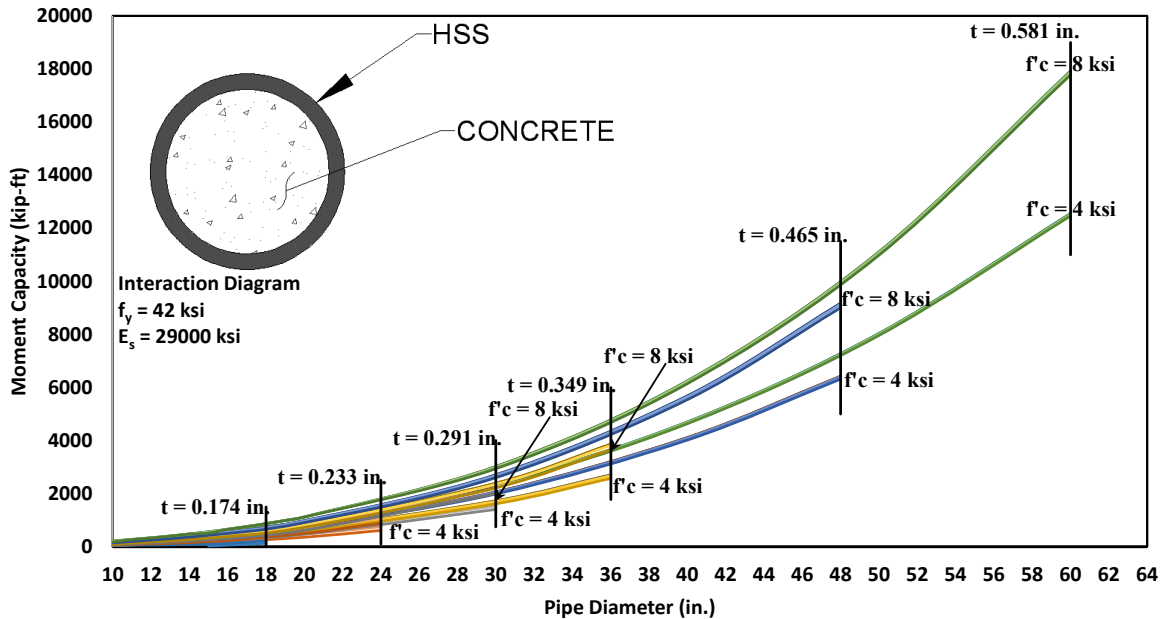


Figure 136. HSS Member Moment Capacity Interaction Diagram

## Embedment Length

In the absence of extensive experimental data on embedment length, two methodologies are proposed to determine the embedment of the pipe into the column and footing. The methodologies used are proposed by WSDOT Bridge Design Manual and (Wasserman and Walker 1996). The equation used in this research is shown below.

$$l_e \geq \sqrt{\frac{5.27DtF_u}{\sqrt{f'_c}}}$$

Where:

- $l_e$  = Calculated embedment length, in
- $D$  = Diameter of the embedded pipe, in
- $t$  = Wall thickness of the embedded pipe, in
- $F_u$  = Ultimate strength of the embedded pipe, ksi
- $f'_c$  = Compression strength of the concrete, ksi

Where,  $l_e$  is the calculated embedment length,  $D$  is the diameter of the embedded pipe,  $t$  is the wall thickness of the embedded pipe,  $F_u$  is the ultimate strength of the embedded pipe, and  $f'_c$  is the compression strength of the concrete with all variables in terms of kip and inches.

For the embedment length proposed by Wasserman, the following equations are used:

$$l_e = \frac{2F_y Z}{\sqrt{700f'_c b}}$$

$$b = \frac{d\sqrt{\pi}}{2}$$

Where:

$F_y$  = Yield strength of the embedded pipe, ksi

$Z$  = Plastic section modulus of the embedded pipe, in<sup>3</sup>

$f'_c$  = Compressive strength of the concrete, ksi

$d$  = Outside diameter of the embedded pipe, in

To select the appropriate embedment length, simply follow the flow chart shown in Figure 137. A summary of embedment lengths for commercially available HSS and pipes are shown in Figure 138 and Figure 139, respectively with  $f'_c$  is 4 ksi,  $F_y$  is 46 ksi, and  $F_u$  is 62 ksi for both graphs.

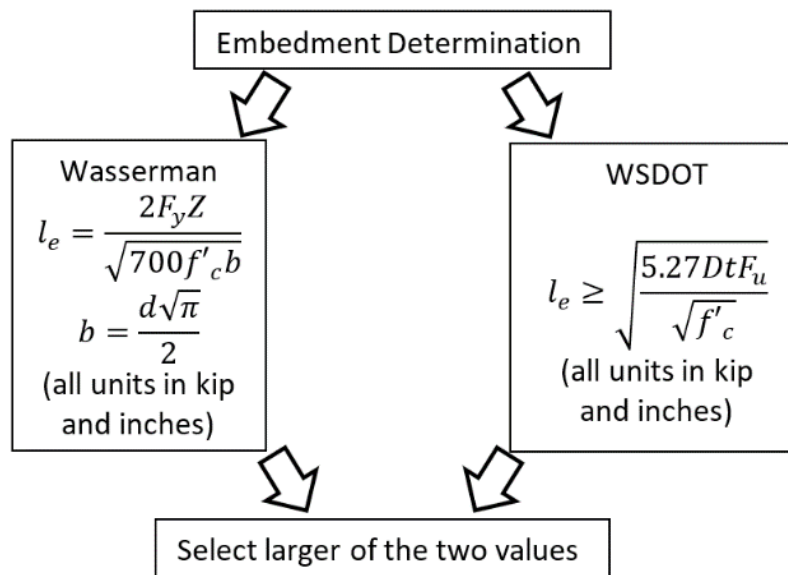


Figure 137. Embedment Length Determination Flow Chart

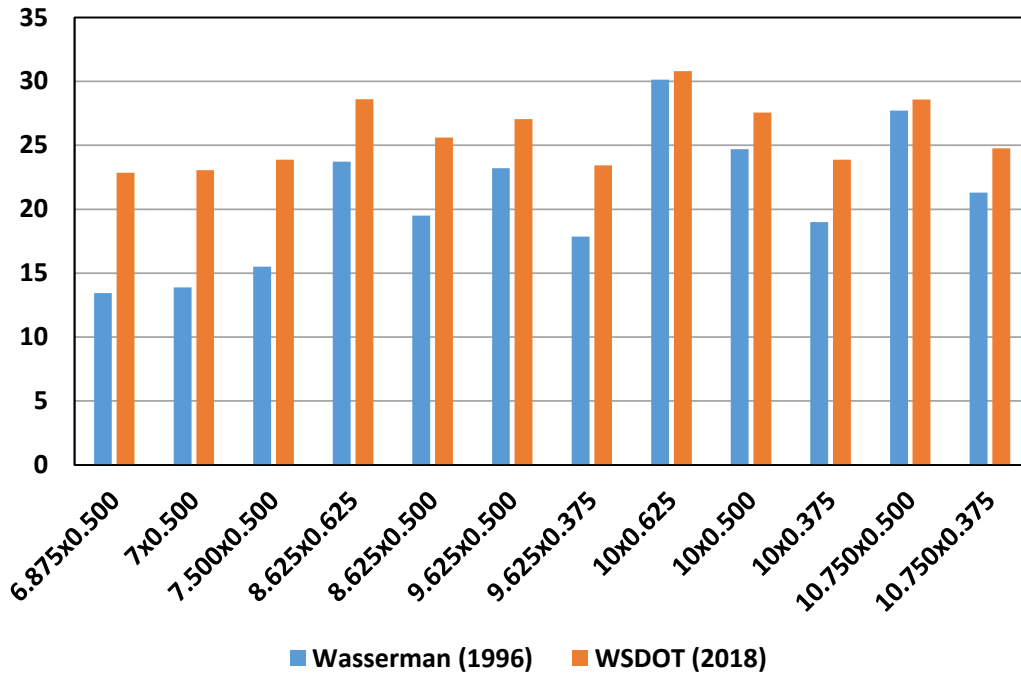


Figure 138. Embedment Length Comparison for HSS Round (in.)

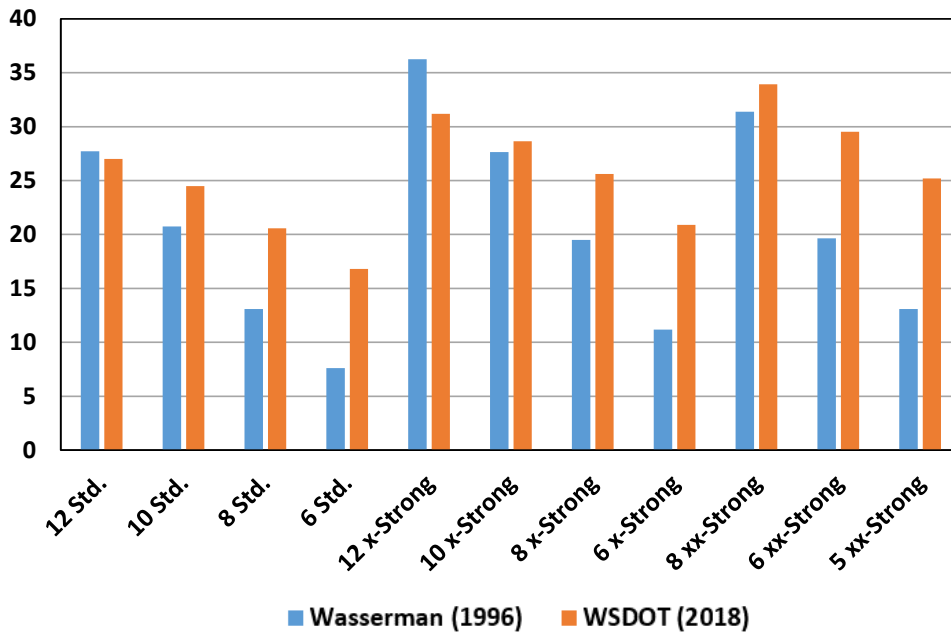


Figure 139. Embedment Length Comparison for Pipe (in.)

## Unbonded Length

The unbonded length in the plastic hinge is a way to force the HSS to yield at a designated location (above the footing) that can be inspected following an earthquake. The unbonded length of the HSS member is determined using the methodology presented in the PRESSS Design Handbook (Pampanin et al. 2010). The unbonded length can be selected such that the strain in the HSS member would be approximately equal to a cast-in-place column or say 6% at the design level. To begin, the strain penetration needs to be calculated using the following equation:

$$l_{sp} = 0.15F_{ye}d_{bl}$$

Where:

- $F_{ye}$  = 1.1 times the yield strength, ksi
- $d_{bl}$  = Pipe thickness, in
- $f'_c$  = Compressive strength of the concrete, ksi
- $d$  = Outside diameter of the embedded pipe, in

Using a value of 60 ksi (413.7 MPa) for  $F_y$  and 0.75 in. (19.05 mm) for  $d_{bl}$ , the strain penetration is calculated to be 7.43 in. (188.7 mm). Strain in the steel is then calculated using the following equation:

$$\varepsilon_s = \frac{\Delta}{l_{ub} + 2l_{sp}}$$

Where:

- $\Delta$  = Elongation of the rebars, in
- $l_{ub}$  = Unbonded length, in
- $l_{sp}$  = Strain penetration length, in

It is important to estimate the elongation of the HSS member to determine an appropriate unbonded length. In this report, data from the cast-in-place column was used to predict the elongation of the HSS member.

Experimental results from testing of the precast piers showed that an unbonded length equal to 30-35% diameter of the HSS/pipe improves the ultimate displacement capacity of the pier. Further experimental and analytical investigations are needed to quantify the unbonded length for various commercially available HSS and pipe sections.

## Construction Technology and Assembly

It is recommended that the materials used in this report be a minimum for practical applications. When constructing the footing, care should be taken to ensure the inside of the receiving HSS member remains clear of concrete. If concrete propagates into the receiving HSS member, the undesired concrete will need to be removed with a grinder before the assembly of the precast column. To keep concrete out of the

footing HSS member, a  $\frac{3}{4}$  in. piece of plywood is sized and secured to the inside bottom edge of the HSS member and gorilla tape is placed at the top of the HSS member (Figure 140 a-c). While the footing is curing, water should not be allowed to pool at the bottom of the receiving HSS member. Any rust that accumulates on the inside of the receiving HSS member should be removed before assembling the precast column and the grouting process.

The precast column is poured horizontally for ease of construction, the restrictions over dropping height for concrete, and to make sure it is not knocked over accidentally while the concrete is being poured or while the concrete is curing. The outside of the HSS pipe is sandblasted before pouring concrete to achieve a better bond between the HSS member to the concrete. The unbonded length of the pipe is accomplished by wrapping the desired unbonded pipe length with gorilla tape. The grout vents used are PVC pipes. The PVC pipes are sealed using gorilla tape while the concrete is being poured to ensure concrete does not enter and clog them. A level should be used to ensure the HSS member is oriented correctly in the formwork (Figure 140 d). If the HSS member is not level before the concrete is being poured, then the column will not be plumb when the precast column is assembled to the cast-in-place footing. Once the concrete is poured, the column should be allowed to cure sufficiently so premature cracking does not occur. The centering fins should be welded onto the protruding HSS member after it is removed from the formwork (Figure 140 e). Refer to Chapter 4 of this report for more construction images.

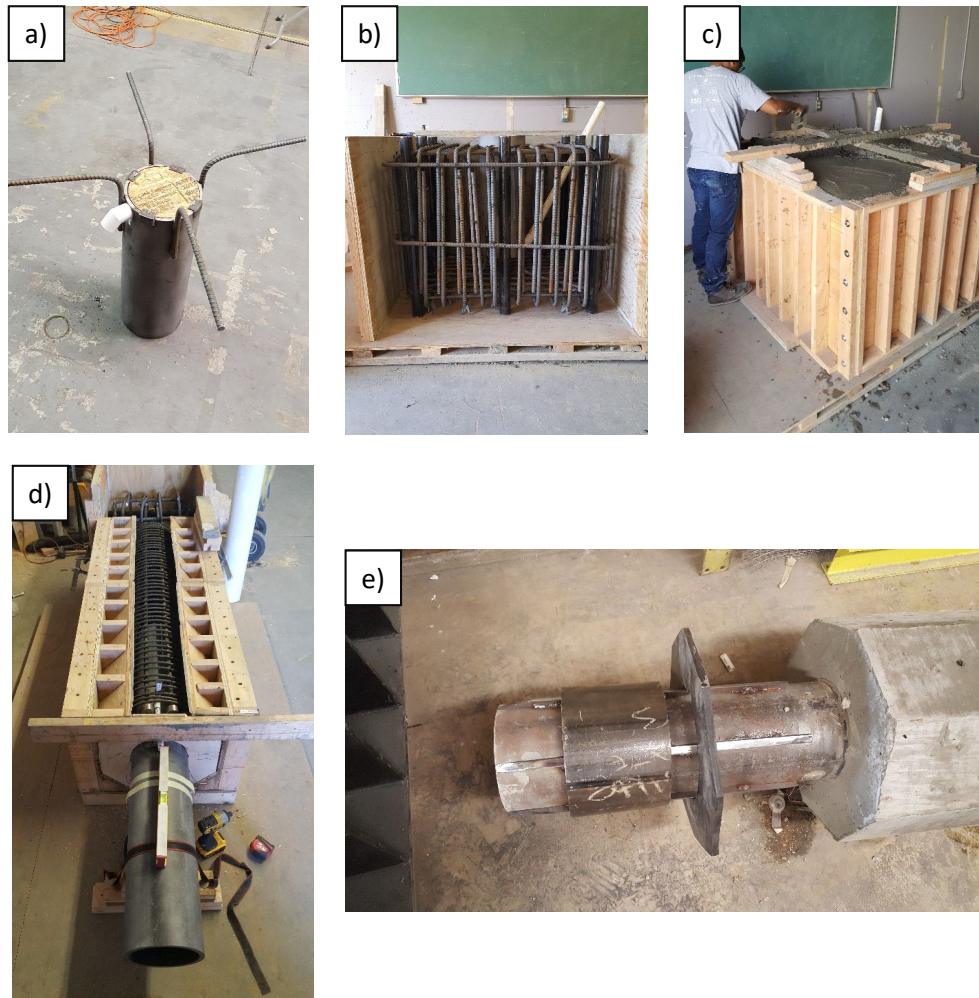


**Figure 140. a) Receiving HSS Member, b) Footing Reinforcement, c) Finished Footing, d) Column Reinforcement, and e) Welded Centering Fins**

For assembly, the precast column needs to be rotated from the horizontal orientation to a vertical orientation. To rotate the column to a vertical orientation, care should be taken to ensure the HSS member that is protruding from the precast column is not damaged. A crane should be used at each end of the column, without coming in contact with the HSS member, until the column is vertical. The HSS member should not come in contact with the ground at any time to prevent any dents or scratches that could compromise the structural performance and long-term durability. Once the column is in a vertical position the precast column's protruding HSS member should be promptly inserted into the cast-in-place footing receiving HSS pipe and grouted into place.

Non-shrinkage grouting should be used to fill the void between the two HSS members that has a higher compressive strength compared to the concrete used in the column and footing. The grout can be either pumped or gravity feed into the footing grout inlet pipe. Once all the voids between the two HSS members are filled, grout would flow out of the grout vents located on each side of the column. Allow the grout to flow unobscured out of each grout vent for approximately 30 seconds to ensure all air pockets are

removed that may have been trapped. Once the grout has been sufficiently cured, the connection is complete.

## Limitations

The limitations of the precast column connection are nearly the same as a traditional cast-in-place column. One of the limitations to the precast column that varies from a cast-in-place column is the column capacity. The capacity of the precast column is controlled by the compressive strength of concrete used, the size of the selected HSS member, and the material properties of the HSS member. Vertical pour of the precast column may not be possible due to concrete drop height restrictions as well as bracings for the formwork. Another limitation is the ability to lift and rotate the column to a vertical position. Equipment capable of lifting the column is required to transport the column to its designated location. As the column height and diameter increase, the total weight of the column also increases, and as a result, larger equipment may be required. For precasting, it is recommended to stay with the available formwork sizes or standardizing the sections so multiple precast columns can be produced using the same formwork. This will help in reducing the cost of the precast columns.

Transportation limitations are likely to govern by the size and height of the precast cap beam. Options for the precast cap range from hollow to partially solid or fully solid. Precasting of the piers would likely require horizontal pour in the factory. Assembly of the pier on-site and any concrete pour (e.g., filling the cap) would be similar to existing precast and cast-in-place practices. Footings will be cast-in-place, welding of rebars to the receiving pipe can be avoided by providing 90-degree bends at the end of the rebars near the pipe (footing or cap socket).

In areas susceptible to chlorides and moisture, further research investigation is required to determine the suitability of the system including its components such as elastomeric joint compounds for wider application.

## Inspection

Inspection during construction and regular service would be similar to a cast-in-place pier with special attention to column-to-cap and column-to-footing interfaces (e.g., damage to elastomeric pad, moisture ingress, cracking etc.) For better durability, leaving unbonded length in the pipe can be eliminated.

The plastic hinges are the hot spots in the proposed precast pier during an earthquake. In post-earthquake inspection, smaller cracks without spalling of cover concrete could indicate the status of the pipe inside the pier. No spalling of the cover concrete can signal that there is little to no yielding of the pipe. However, loss of cover concrete in potential plastic hinge zone may require further intrusive inspection of the pipe by removing the elastomeric pad and cleaning out the debris to inspect the pipe. Non-destructive hardness test of the steel pipe can be carried out to indicate the amount of inelastic deformation during the earthquake and the residual capacity and fatigue life. The “elephant leg” buckling of the pipe would

be an indicator of substantial inelastic deformation of the HSS/pipe. A rupture/crack to the pipe means the need of extensive repair or possible replacement of the pier.

## Proposed Repair Methodologies

If a seismic event were to occur that damaged the precast column, the precast column may be able to be repaired. (Bumstead et al. 2019) explored a variety of repair options for Concrete Filled Steel Tubes (CFST) after a major seismic event. Each of the repair methods used a concrete pedestal, 1.5 times the diameter of the steel tube, and a height equal to the steel tube, around the damaged section of the column. The concrete pedestal is encased in a steel tube to confine the concrete. The three methods are a welded embedded ring, the use of shear studs, and weld beads on the outside of the damaged pipe as shown in Figure 141. Using a finite element model, via ABAQUS software, the three repair methods are analyzed with a damaged concrete steel pipe as shown in Figure 142.

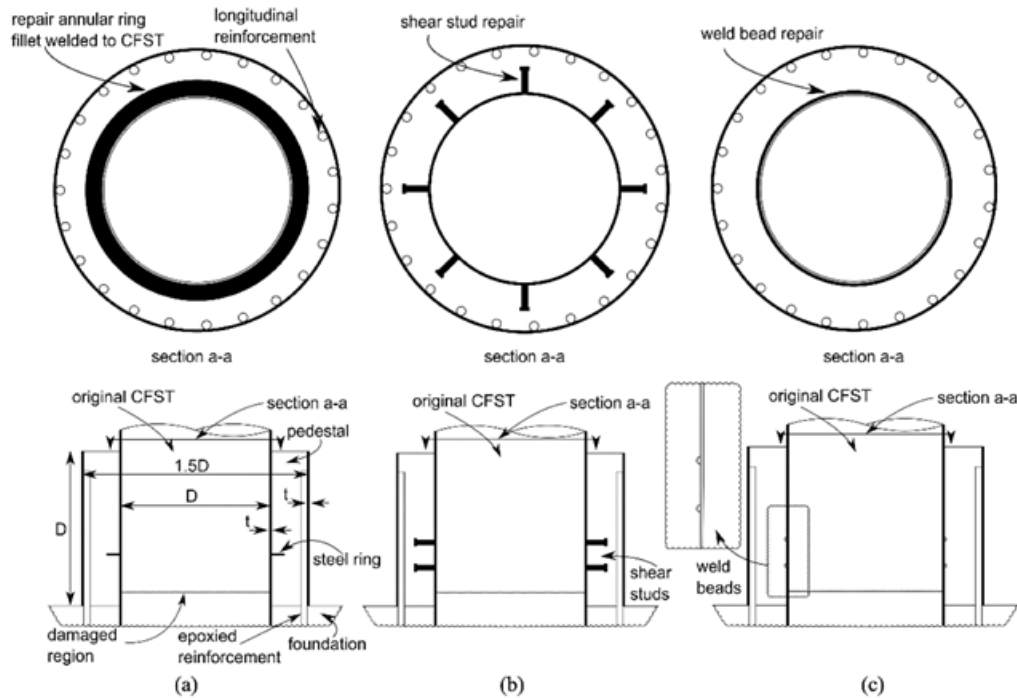


**Figure 141. Repair Methods, a) Embedded Ring Repair, b) Shear Stud Repair, and c) Weld Bead Repair**

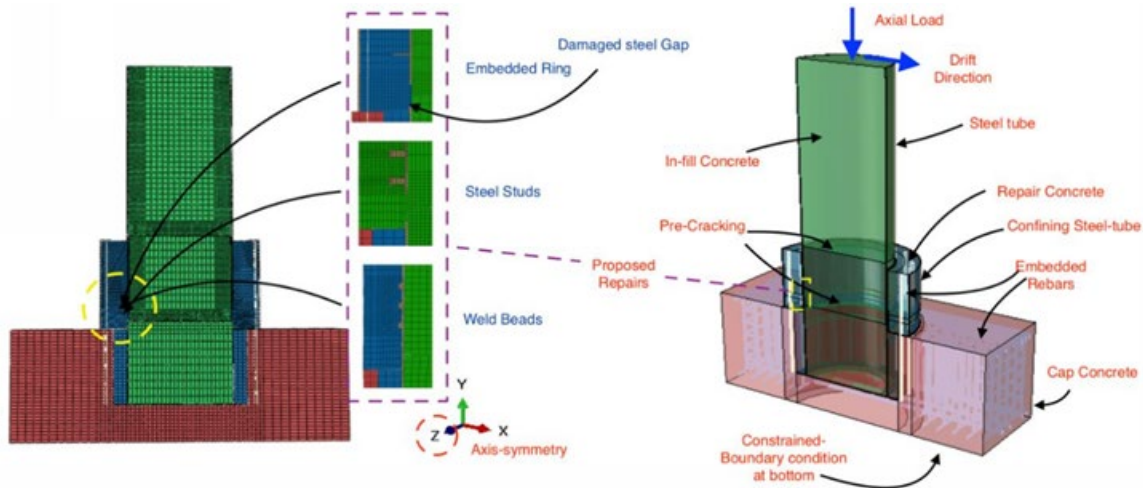


**Figure 142. Finite Element Model for Repair Methods**

The results from the analysis indicated that all of the repair methods are effective in restoring the column's original stiffness and strength. The welded bead repair is the most effective. The top four analysis results were: two embedded rings having a width of  $x4$  the pipe thickness (ER-2x4t), four shear studs equally spaced (SS-x4), three welded beads equally spaced (WB-x3), and three welded beads with a thicker pedestal confinement tube (WB-x3-1). The graphical results of the described methods are shown in Figure 143 and Figure 144 while Figure 145 depicts the various repair methods that exhibited the highest results.

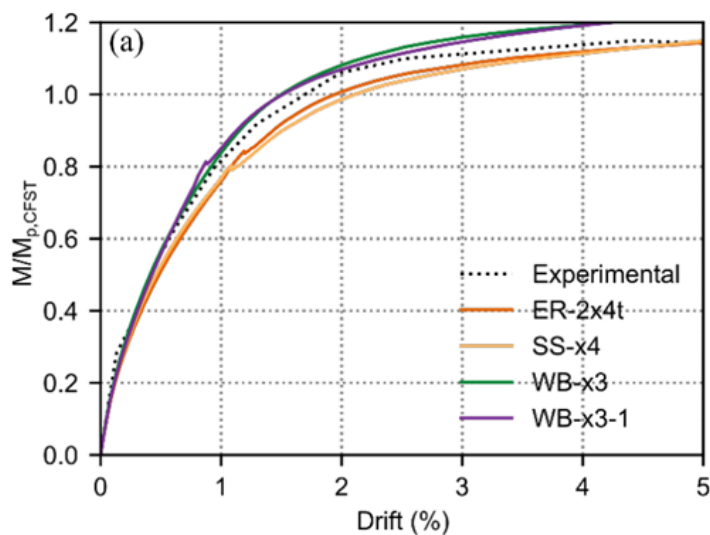


**Figure 143. Moment vs. Drift for Repair Methods**

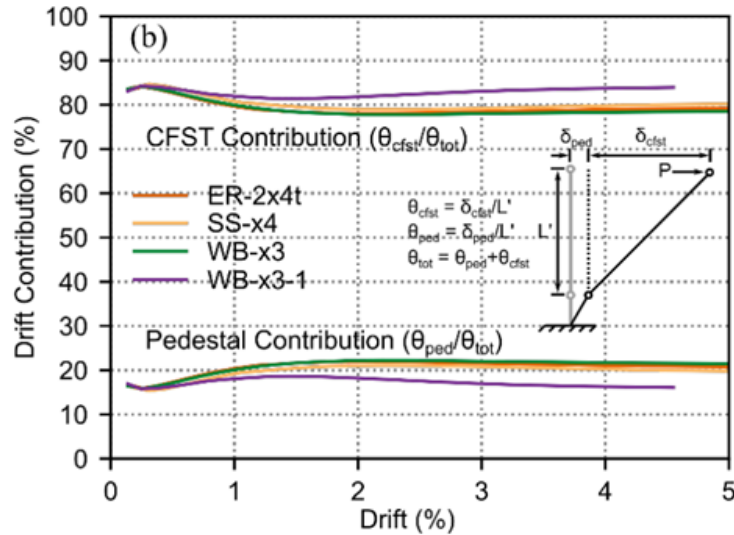


Figure 144. Pedestal Rotation for Repair Methods

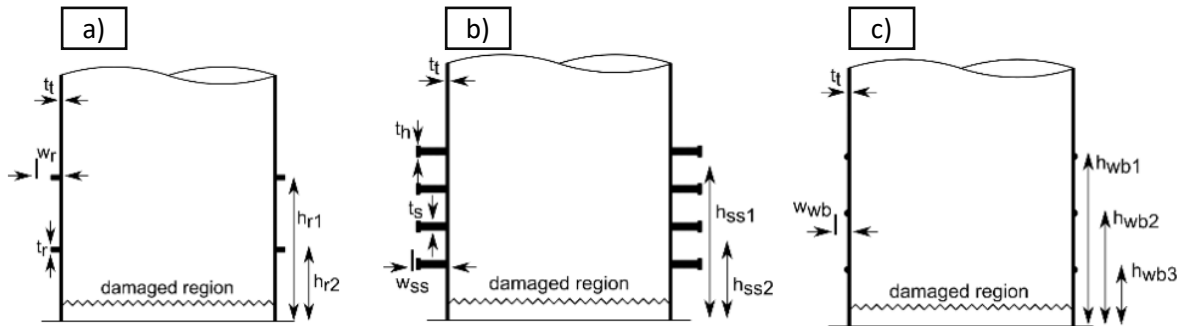
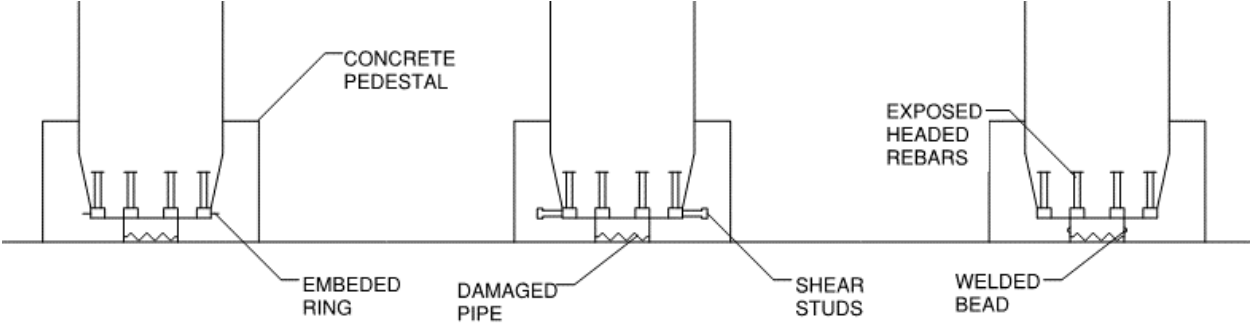


Figure 145. Repair Methods with the Highest Results, a) ER-2x4t, b) SS-x4, c) wb-x3 and wb-x3-1

Some of the repair methods proposed by Bumstead (2019) could be applied to the precast column connection investigated in this report with some adjustments. Figure 146 presents a proposed repair methodology for the pipe connection based on existing literature. A concrete pedestal is cast around the base of the precast column. This repair methodology aims to push the plastic hinge further up the column and essentially transform the column behavior to a cast-in-place column. The plastic hinge is expected to form on top of the pedestal during a future earthquake. The diameter of the pedestal should be 1.5 times the diameter of the precast column. The height of the pedestal should be extended up until the termination point of the HSS member inside the column as shown in Figure 146. The longitudinal rebars of the pedestal are epoxied or grouted to the drilled holes in the foundation. A combination of an embedded annular ring at the base and epoxied studs around the circumference of the column are used to connect the precast column to the pedestal.

To secure the threaded bars to the column and the pedestal rebars to the footing, the column and footing should be scanned to locate the existing rebar, so the drill does not damage any rebar. The embedded ring should be welded to the exposed headed rebars instead of the HSS member because of the difficulty

of welding in a confined area. An alternative to welding the embedded ring to the column after a seismic event is to weld the embedded ring before the precast column is poured. The embedded ring will not provide any support to the column until after the column has been damaged and a pedestal is poured. Testing should be carried out to validate the proposed repair methodologies in Figure 146.



**Figure 146. Proposed Repair Method for the ITD Precast Pier: a) Embedded Ring, b) Shear Stud, c) Weld Bead**

The use of a concrete jacket in order to push the plastic hinge zone at the top of the jacket could be one of the most practical approaches to repair the piers after an earthquake. Recently Mission Bridge in Canada was seismically retrofitted using this methodology (Figure 147). The jacket can be made of normal concrete, Ultra-High-performance concrete (UHPC) or structural steel. Similar to concrete jacketing for the cast-in-place piers, Figure 148 shows a proposed repair method that uses concrete jacketing for the precast pier. This would turn the precast pier to an equivalent cast-in-place column, but with shorter height. The proposed repair using concrete jacketing has to be experimentally tested to investigate its adequacy in restoring stiffness and strength to the precast pier.



**Figure 147. Mission Bridge, BC, Canada**

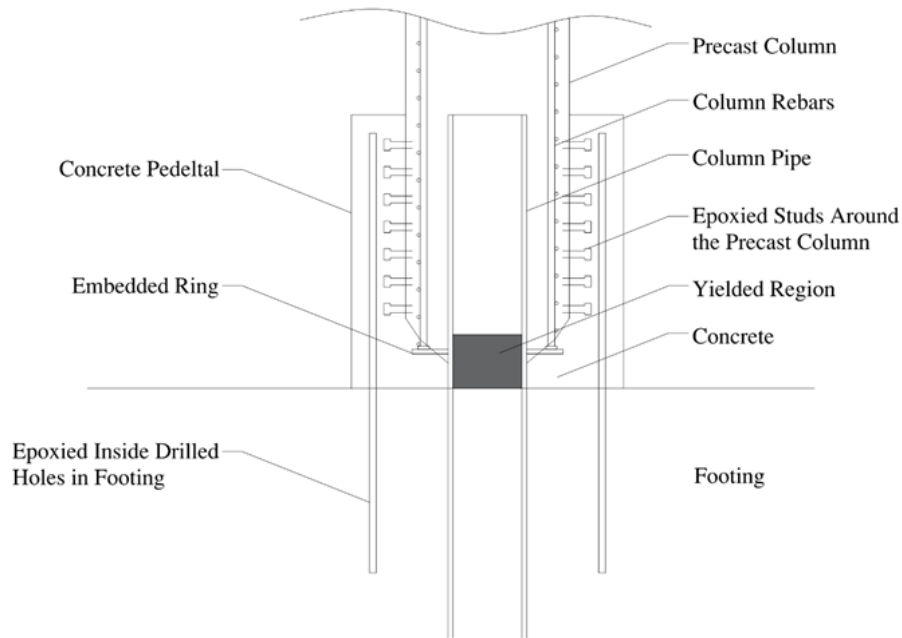


**Figure 148. Proposed Concrete Jacketing Repair Method for Precast Column Connection**

## Summary

The flexural analysis of the pier can be conducted similar to CFSTs. Some design considerations and recommendations for construction/assembly are proposed. A series of interaction diagrams were created using the WSDOT Bridge Design Manual. The interaction diagrams show the moment capacity increasing as the HSS member diameter and wall thickness increase. The interaction diagrams do not account for an axial load but can be used as an effective tool in sizing the HSS/pipe to match a certain cast-in-place capacity. Some limitations of the precast column were presented with respect to the capacity of the connection, precasting technology, and the weight of the precast element. It should not be used in areas with highly corrosive environments until further data/information is available on the performance of unbonded length and elastomeric bearings. Other areas it should not be used include places where the plastic hinging goes under the water, where plastic hinging cannot be inspected easily, and the places with liquifiable soil until further research is available in soil-structure interaction of the system. It is also recommended to avoid in places where Quality Assurance/Quality Control (QA/QC) cannot be maintained. Several potential repair methods using an embedded ring, welded beads, and concrete jacketing were discussed. The proposed repair methods should be experimentally tested to verify their effectiveness in restoring stiffness and strength to the precast pier. Some post-earthquake inspection and indication of damage to the HSS/pipe was also discussed.

## 7. Conclusions

Both the cast-in-place and precast columns were designed with nearly the same materials properties, flexural capacity, overall shape, and dimensions. The only material that varied was the HSS member. The cast-in-place cantilever column was determined to have a moment capacity of 165 kip-ft compared to the precast column connection which had a moment capacity of 143 kip-ft. Although the cast-in-place column was designed to have a larger moment capacity, its overall seismic performance was lower compared to the precast column.

The precast cantilever column endured more drift cycles (16 cycles) compared to the 13 cycles that the cast-in-place column endured. The maximum displacement of the cast-in-place column during the testing procedure was 7.7 in. which corresponded to a 9.9% drift. The maximum load applied to the cast-in-place column during the testing procedure was 37.8 kip which corresponded to a 245.7 kip-ft moment capacity. The maximum displacement of the precast column during the testing procedure was 9.6 in. which corresponded to a 12.3% drift. This is 20% higher compared to the cast-in-place benchmark. The maximum load applied to the precast column during the testing procedure was 41.2 kip which corresponded to a 267.8 kip-ft moment capacity. This was 9% higher compared to the cast-in-place benchmark. The precast column also dissipated more energy 1025 kJ (756,001 ft-lb) compared to 456 kJ (336,328 ft-lb) for the cast-in-place column which was just below half of what the precast column dissipated. The residual drift for both columns were similar.

Based on the results above, several conclusions can be made when comparing a precast cantilever column and cast-in-place column having identical overall dimensions and moment capacities.

- The precast column pipe connection offers ABC advantages as well as better tolerances and performance compared to other connections.
- During a seismic event, the precast column absorbs more of the seismic energy. The precast column can absorb more energy because there is more steel located at the column to footing interface as a result of the HSS pipe which makes the connection more energy dissipative and ductile.
- The precast column has better confinement and shear resistance.
- The precast column connection will maintain its structural integrity during a major seismic event. This is evident because the precast column was able to endure more of the cyclic loads during the testing procedure.
- Based on the observations during each of the testing procedures, the precast column does not get damaged during smaller seismic events due to lower initial stiffness and flexibility to accommodate small displacements at the top. This provides better performance for the serviceability of the bridge. Testing showed that cracks appeared on the cast-in-place column after the first cycle (0.16 in. of displacement or 0.2% drift) compared to the third cycle (0.47 in. of displacement or 0.6% drift) for the precast column.

- Overall, the precast column performs better during a seismic event compared to the cast-in-place column.
- It is possible to repair the precast column using traditional methodologies such as concrete jacketing after an earthquake

With the CIP and precast bent piers having been designed identical, in both dimensional and performance capacities, the two are easily compared. The two systems performed similar in nature, with the precast bent pier showing less overall damage than that of the CIP bent pier. The precast bent pier also achieved a higher moment capacity of 498 kip-ft., than that of the CIP bent pier, having achieved 468 kip-ft. The precast bent pier withstood a total of 24 complete loading cycles, culminating in a final ultimate drift ratio of 9.15%. The CIP bent pier failed far short of the precast achievement, having withstood a total of 15 loading cycles, resulting in an ultimate drift ratio of 4.94%. The two specimens exhibited similar ultimate capacities at similar drift ratios during the experiment. The precast bent pier achieved a maximum force of 71.4 kip at a drift ratio of 2.69%. While the CIP bent pier achieved a maximum force of 66 kip at a drift ratio of 2.46%. Similarly, the precast bent pier dissipated a much higher amount of energy than that of the CIP bent pier, as it endured more loading cycles. The total dissipated energy of the precast and CIP bent pier was 2,125 kJ (1,567,320 ft-lb) and 342 kJ (252,246 ft-lb). The precast bent pier had however dissipated more energy at the fifteenth cycle than that of the CIP bent pier, having dissipated a total of 466 kJ (343,704 ft-lb) to that point.

From the experimental investigation and comparison of the bent specimens made in the research presented, here several conclusions can be made.

- Compared to an equivalent cast-in-place pier, the precast pier with the proposed pipe connection achieved higher strength and ductility.
- The precast bent withstood small displacement without suffering hairline cracking due to the presence of the elastomeric bearing.
- The precast bent displayed better confinement through reduced cracking observed throughout the experimental program.
- The precast bent displayed far more resilience during the loading as it withstood an additional 9 loading cycles than that of the CIP bent.
- The resilience of the precast bent is demonstrated by the cumulative energy dissipation levels it was capable of achieving during testing.
- Buckling and tearing of the HSS pipe is observed during large drift ratios to be the failure mechanism of the proposed precast connection.
- The precast pier demonstrates a reduced stiffness as it approaches ultimate capacity than that of the CIP bent.

- The precast bent also exhibited a higher yield displacement of 1.13% drift ratio compared to the 0.5% drift exhibited by the CIP bent.
- The precast bent displayed more energy dissipation at the point of failure for the CIP bent as once the precast bent had achieved ultimate capacity it displayed far less degradation than that of the CIP bent pier, constituting its ability to withstand additional cycles.
- The precast bent with the proposed precast connection proved capable of successfully emulating the CIP bent under similar quasi-static loading.

The analytical modeling in this report is aimed to provide a practical tool for bridge engineers when considering new connection details. Analytical models were created for the CIP column and precast column with proposed pipe connection using the Open System for Earthquake Engineering Simulation (OpenSees) software. To predict the experimental results, low-cycle fatigue data were included in the OpenSees model. Results show good agreement between the analytical and experimental data. Similarly, analytical models were created for the CIP bent pier and precast bent pier with proposed pipe connection using OpenSees software. The results showed good agreement between the analytical and experimental data. It was difficult to capture shear deformation and Bauschinger effects for the precast bent pier after 6% drift ratio.

As far as parametric studies are concerned, some limited nonlinear static (pushover) and nonlinear dynamic (time-history analysis) were run on an actual bridge model to compare the global seismic response (e.g., formation of plastic hinges, ductility, strength, force-displacement response etc.) for both cast-in-place and precast models. Results showed that the precast pier emulates the cast-in-place behavior closely under nonlinear static and dynamic loads.

Based on the experimental program, flexural analysis, interaction diagrams, design and detailing considerations, construction/assembly technology, limitations, inspection, potential post-earthquake repairs, were presented. Most of these guidelines are following existing cast-in-place and precast technologies for a wider adoption of the proposed ITD connection.

## Future Research Work

The following topics are recommended for future research:

- Refining the embedment length of the HSS using experimental pull-out tests and analytical Finite Element modeling. In this report, two embedment lengths were calculated to determine an appropriate length. The two calculations were from the WSDOT LRFD Bridge Manual (WSDOT 2019) and Integral Abutment for Steel Bridges (Wasserman and Walker 1996). Additional research should be conducted to not only verify the methods, but also to close the gap between the two existing methods.
- Quantifying the appropriate gap between the column and footing pipes that is optimized for construction tolerance and structural performance.

- Experimental and analytical work to quantify the accurate unbonded length of the pipe. More information is needed on this topic to understand the effects of the unbonded length of a pipe embedded in concrete. Leaving an unbonded length is not a common practice and needs to be understood to clarify its use in CFST.
- The durability aspects of the pier with an unbonded length in the plastic hinge zone should be investigated.
- The proposed repair methods should be validated experimentally. The literature regarding CFST is a good resource, but they are based on analytical work only.
- Bi-directional quasi-static cyclic, shake table testing, and consideration of soil-structure interaction for the proposed pipe connection will provide valuable data about its performance for a wider application and various seismic hazard/ground motion type.

## Cited Works

- AASHTO. (2020). *AASHTO LRFD Bridge Design Specifications*. American Association of State Highway and Transportation Officials, 9th Edition.
- AASHTO. (2011). *AASHTO LRFD Seismic Bridge Design*. American Association of State Highway and Transportation Officials, 2nd Edition.
- AASHTO M 251. (2015). *AASHTO Standard Specification for Plain and Laminated Elastomeric Bridge Bearings*. American Association of State Highway and Transportation Officials, 2015 Edition.
- ACI Committee 374. (2013). *Guide for testing reinforced concrete structural elements under slowly applied simulated seismic loads (ACI 374.2R-13)*. American Concrete Institute, Farmington Hills, MI.
- AISC Committee. (2010). *Steel Construction Manual American Institute of Steel Construction*. Chicago, Ill
- Al-Kaseasbeh, Q., and Mamaghani, I. H. P. (2019). "Performance of Thin-Walled Steel Tubular Circular Columns with Graded Thickness under Bidirectional Cyclic Loading." *ASCE Structures Congress 2019*.
- Ameli, M. J., Brown, D. N., Parks, J. E., and Pantelides, C. P. (2016). "Seismic column-to-footing connections using grouted splice sleeves." *ACI Structural Journal*.
- ASCE. (2017). "Infrastructure Report Card." ASCE's Infrastructure Report Card, <<https://www.infrastructurereportcard.org/cat-item/bridges/>> (Jan. 8, 2020)
- ASCE. (2018). *Report Card for Idaho's Infrastructure*." ASCE's Infrastructure Report Card, <<https://www.infrastructurereportcard.org/cat-item/bridges/>> (Jan. 8, 2020)
- Brown, J. and S. K. Kunnath (2000). *Low-cycle Fatigue Behavior of Longitudinal Reinforcement of Reinforced Concrete Bridge Columns*. Report No. MCEER 00-0007. University at Buffalo, The State University of New York.
- Bumstead, J., Korat, J., and Stephens, M. T. (2019). "Repair Strategies for Earthquake-Damaged CFST Bridge Columns." *ASCE Structures Congress 2019*, 154–164.
- Chapel Steel. (2018). *Structural, Carbon & HSLA Steel Plate*. <<https://www.chapelsteel.com/a709-grade50-grade-345.html>> (Feb. 22, 2020).
- Caltrans. (2013). *Seismic Design Criteria-Version 1.7*. Caltrans. California Department of Transportation, Sacramento, CA
- Chopra, Anil K. (2017). *Dynamics of Structures: Theory and Applications to Earthquake Engineering*. Pearson Education Limited.
- Collins, M. P., and Mitchell, D. (1991). *Prestressed Concrete Structures*. Prentice-Hall. Englewood Cliffs, NJ.
- Ebrahimpour, A., B. E. Earles, S. Maskey, M. Tangarife, and A. D. Sorensen (2016). *Seismic performance of columns with grouted couplers in Idaho accelerated bridge construction applications*. Report No. FHWA-ID-16-246. Idaho Transp. Department, Boise, ID.
- Galvis, F., and Correal, J. F. (2017). "Characterization of the seismic behavior of a column-foundation connection for accelerated bridge construction."

- Haber, Z. B., M. S. Saiidi, and D. H. Sanders (2013). *Precast Column-Footing Connections for Accelerated Bridge Construction in Seismic Zones*. Report No. CCEER 13-08. Department of Civil Engineering, University of Nevada, Reno, NV.
- Hawileh, R., A. Rahmen, and H. Tabatabai (2010). "Evaluation of the Low-cycle Fatigue Life in ASTM A706 and A615 grade 60 Steel Reinforcing Bars," *Journal of Materials in Civil Engineering*, V. 22(1), pp. 65-76.
- Kim, C. S., Lim, W. Y., Park, H. G., and Oh, J. K. (2016). "Cyclic loading test for cast-in-place concrete-filled hollow precast concrete columns." *ACI Structural Journal*.
- Marsh, L. P. (2018). "Seismic Design and Accelerated Bridge Construction (ABC)." <<http://onlinepubs.trb.org/onlinepubs/webinars/180711.pdf>>. (Jan. 10, 2020)
- Marsh, M. L. et al. (2011). *Application of Accelerated Bridge Construction Connections in Moderate-to-High Seismic Regions*.
- Mashal, M., and Palermo, A. (2019a). "Low-damage seismic design for accelerated bridge construction." *Journal of Bridge Engineering*.
- Mashal, M., and Palermo, A. (2019b). "Emulative seismic resistant technology for Accelerated Bridge Construction." *Soil Dynamics and Earthquake Engineering*, Elsevier Ltd, 124(December 2018), 197–211.
- Mashal, M., White, S., and Palermo, A. (2016). "Quasi-static Cyclic Testing of Emulative Cast-in-place Connections for Accelerated Bridge Construction in Seismic Regions." *Bulletin of the New Zealand Society for Earthquake Engineering*, 49(3).
- Maskey, S. (2017). "Low-cycle Fatigue Behavior of Reinforcing Steel in Idaho Bridge Columns During Earthquakes." M.S. thesis, Dept. of Civil and Environmental Engineering, Idaho State Univ.
- McCormac, J.C., and Brown, R.H. (2014) *Design of Reinforced Concrete*. Wiley, Hoboken, NJ
- Mehraein, M., and Saiidi, M. S. (2016). *Seismic Performance of Bridge Column-Pile-Shaft Pin Connections for Application in Accelerated Bridge Construction*. Reno, NV.
- Open System for Earthquake Engineering Simulation (OpenSees) [Computer software]. Univ. of California, Berkeley, Berkeley, CA. <<http://opensees.berkeley.edu/OpenSees/user/index.php>> (October 21, 2019).
- Ou, Y. C., Alrasyid, H., Haber, Z. B., and Lee, H. J. (2015). "Cyclic behavior of precast high-strength reinforced concrete columns." *ACI Structural Journal*.
- Pampanin, S. et al. (2010). *PRESSS Technology Design Handbook*. NZCS, Auckland N.Z.
- PEER. (2020). "Ground Motion Database." PEER Ground Motion Database, University of California, Berkeley <<http://ngawest2.berkeley.edu>>
- Priestley, M. J. N., Calvi, G. M., and Kowalsky, M. J. (2007). *Displacement-Based Seismic Design of Structures*. *Earthquake Spectra*, IUSS Press.
- Tazarv, M., and Saiidi, M. S. (2015a). *Design and Construction of Precast Bent Caps with Pocket Connections for High Seismic Regions*. Reno, NV.

- Tazarv, M., and Saiidi, M. S. (2015b). *Design and Construction of Bridge Columns Incorporating Mechanical Bar Splices in Plastic Hinge Zones*. Reno, NV.
- U.S. Department of Transportation/Federal Highway Administration. (2019). "Accelerated Bridge Construction." <<https://www.fhwa.dot.gov/bridge/abc/>> (Jan. 8, 2020).
- Vielma, J. C., and Mulder, M. M. (2017). "Procedure for Assessing the Displacement Ductility Based on Seismic Collapse Threshold and Dissipated Energy Balance." *16th World Conference on Earthquake Engineering*, (January).
- Wasserman, E. P., and Walker, J. H. (1996). *Integral Abutments for Steel Bridges*. American Iron and Steel Institute, Chicago, Ill
- Wehbe, N. I., M. S. Saiidi, and D. H. Sanders (1999). "Seismic Performance of Rectangular Bridge Columns with Moderate Confinement," *ACI Structural Journal*. 96(2), pp. 248-258.
- WSDOT. (2019). "*Bridge Design Manual (LRFD)*." Engineering and Regional Operations Bridge and Structures Office
- Zaghi, A. E., and Saiidi, M. S. (2010). *Seismic Design of Pipe-Pin Connections in Concrete Bridges*. Reno, NV.
- Zollman, C. C., Depman, F., Nagle, J., and Hollander, E. F. (1992). "Building and Rebuilding of Philadelphia's Walnut Lane Memorial Bridge." *PCI Journal*, 37(4), 66–82.

## Appendices

# Appendix A. [Design Calculations of the Column Specimen]

## A.1 Cast-In-Place Column Calculations

Circular Column Dimensions		Compression strain = -0.003	Key Values
Column Diameter =	18 in	Tensile strain = 0.002	Input Values
Cover =	1.5 in	$f_y =$	60 ksi
Sturup Spacing =	3	$f_c =$	4 ksi
Long. Bar # =	6	$E_s =$	29000 ksi
Total bars =	12	$\beta_1 =$	0.85 (see pg 68)
$D_{core} =$	13.5 in	$\phi =$	0.75 (Figure 3.5 pg. 72)

For equivalent rectangular Column (Figure 10.9)

$$B = A_g / (.8D) = 17.67$$

$$H = .8 * D = 14.40$$

$$H_s = D_s * 2/3 = 9.00$$

$$A'_s = 2.65$$

$$Cover = 2.70$$

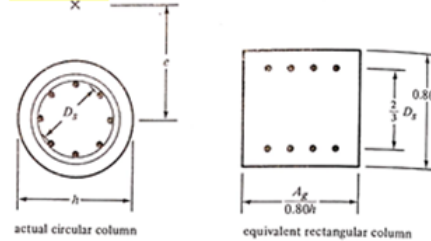


FIGURE 10.9 Replacing a circular column with an equivalent rectangular one.

Determine values of  $y$  and of the steel stains

$y$  = distance from extreme compression fiber to neutral axis

$\epsilon'_s$  = strain in compression reinforcement

$\epsilon_s$  = strain in tension reinforcement

$$y = 0.003 / (0.003 + 0.002) * 14.4 = 8.64 \text{ in.}$$

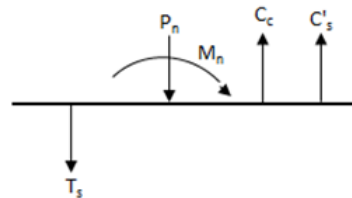
$$\epsilon'_s = ((8.64 - 2.7) / 8.64) * 0.003 = 0.00206 > 0.002 \text{ Yields}$$

$$\epsilon_s = ((14.4 - 8.64 - 2.7) / (14.4 - 8.64)) * 0.002 = 0.00106 < 0.002 \text{ Does Not Yield}$$

$a = \beta_1 * y = 0.85 * 8.64 = 7.34 \text{ in.}$	$a$ = depth of equivalent stress block
$C_c = \beta_1 * a * B * f_c = -441.25 \text{ kips}$	$C_c$ = total compression in the concrete
$C'_s = f_y * A'_s - \beta_1 * A'_s * f_c = -150.03 \text{ kips}$	$C'_s$ = total compression in the compression steel
$T_s = \epsilon_s * E * A'_s = 81.68 \text{ kips}$	$T_s$ = total tension in the tensile steel

$$P_n = 509.60 \text{ kips}$$

$$F_e * P_n = 382.20 \text{ kips}$$



$M_n = 2599.40 \text{ kip-in.} = 216.62 \text{ kip-ft.}$	Column height = 78.00 in.
$\phi * M_n = 1949.55 \text{ kip-in.} = 162.46 \text{ kip-ft.}$	$V_u = 24.99 \text{ kip}$

## A.2 Precast Column Calculations

Key Values

Input Values

HSS8.625X0.625

Pipe Connection		$f_y =$	42 ksi	AISC Table 2-4 pg 2-48
Pipe Diameter =	8.625 in.	$f_u =$	58 ksi	AISC Table 2-4 pg 2-48
Pipe Thickness =	0.581 in.	$f_c =$	4 ksi	
Concrete Diameter =	7.463 in.	$E_s =$	29000 ksi	

$$D/t = 14.85 < \text{Good} \quad 103.57$$

$$A_s = 14.68 \text{ in}^2$$

$$A_c = 43.74 \text{ in}^2$$

$$y = 0 \text{ in.} \quad \text{Distance to the neutral axis}$$

WSDOT CH7

Compressive resistance of a member without consideration of flexure

$$P_o = 782.9 \text{ kips} = 0.95f_c A_c + F_{y,st} A_{st} \quad 7.10.2-5$$

Radius to the center of the steel tube

$$r_m = 4.02 \text{ in.} = r - t/2 \quad 7.10.2-9$$

Angle used to define c

$$\theta = 0.00 \text{ degrees} = \sin^{-1}(y/r_m) \quad 7.10.2-8$$

One half the chord length of the tube in compression

$$c = 3.73 \text{ in.} = r_m \cos \theta \quad 7.10.2-7$$

Nominal moment resistance as a function of the parameter y

$$M_n(y) = 1710.58 \text{ kip-in.} = (c(r_m^2 - y^2) - c^3/3) * 0.95f_c + 4ct(r_m^2/r_m)F_y \quad 7.10.2-6$$

$$= 142.5 \text{ kip-ft.}$$

$$\text{Column height} = 78.00 \text{ in.}$$

$$V_u = 21.93 \text{ kip}$$

## Appendix B. [Design Calculations of the Bent Specimen]

### B.1 Cast-In-Place Bent Calculations

Circular Column Dimensions

Diameter = 14 in  
 Cover = 1.5 in  
 Stirrup = 3  
 Long. Bar # = 6  
 Total bars = 7  
 Ds = 9.5 in

Compression strain = -0.003

Tensile strain = 0.002  
 fy = 60 ksi  
 fc = 4 ksi  
 Es = 29000 ksi  
 B1 = 0.85 (see pg 68)

For equivalent rectangular Column (Figure 10.9)

$B = A_g / (.8D) = 13.74$   
 $H = .8 * D = 11.20$   
 $H_s = D_s * 2/3 = 6.33$   
 $A's = 1.55$   
 Cover = 2.43

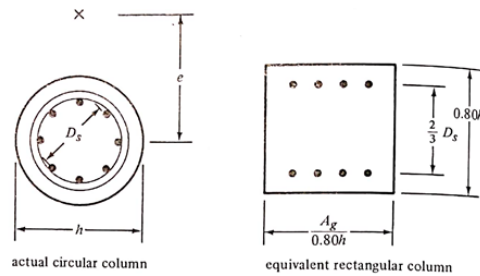


FIGURE 10.9 Replacing a circular column with an equivalent rectangular one.

Determine values of y and of the steel strains

$$y = 0.003 / (0.003 + 0.002) * 11.2 = 6.72 \text{ in.}$$

$$e's = ((6.72 - 2.43) / 6.72) * 0.003 = 0.00191 < 0.00207$$

Compression Steel Does Not Yield

$$e_s = ((11.2 - 6.72 - 2.43) / (11.2 - 6.72)) * 0.002 = 0.00091 < 0.00207$$

Tension Steel Does Not Yield

$$a = B1 * c = 0.85 * 6.72 = 5.71 \text{ in.}$$

$$C_c = B1 * a * B * f_c = -266.93 \text{ k} \quad F_e = 0.75$$

$$C's = f_y * A's - B1 * A's * f_c = -87.52 \text{ k}$$

$$T_s = e_s * E * A's = 40.97 \text{ k}$$

$$\text{Column height} = 6.48 \text{ ft}$$

## B.2 Precast Bent Calculations

Pipe Connection  $f_y = 42$  ksi AISC Table 2-4 pg 2-48

Pipe Diameter = 6 in.  $f_u = 58$  ksi AISC Table 2-4 pg 2-48

Pipe Thickness = 0.465 in.  $f_c = 8$  ksi

Concrete Diameter = 5.07 in.  $E_s = 29000$  ksi

$D/t = 12.90322581 < \text{Good}$  103.57

$A_s = 8.09$  in<sup>2</sup>

$A_c = 20.19$  in<sup>2</sup>

Determine y value by changing the following values:

Applied axial load (P) = 50.0 kips  $T_s = 355.02$  kips  $P + T_s = 405.0225634$  kips

$A_{st} = 8.453$  in<sup>2</sup>  $C_c = 143.38$  kips  $C_c + C_s = 405.0225634$  kips

$A_{cc} = 18.866$  in<sup>2</sup>  $C_s = 261.64$  kips 0 kips \*\* Set this value equal to zero using solver.

$A_{sc} = 6.230$  in<sup>2</sup>

Determine y value by using the solver

Summing the moments about the c.g.c of the column:

$y = 0.0$  in.  $M = 32.81250014$  kip-in.

\*\* Set this value equal to zero using solver.

# Appendix C. [Grout Product Data Sheet]



## PRODUCT DATA SHEET

# SikaGrout®-328

High performance, precision, grout with extended working time

### PRODUCT DESCRIPTION

SikaGrout®-328 is a non-shrink, non-metallic, cementitious precision grout powered by ViscoCrete technology. This grout provides extended working time and exceptional physical performance at fluid consistency. A structural, precision grout, SikaGrout®-328 can be placed from fluid to dry pack.

### USES

- Where exceptional one day and ultimate compressive strengths are required.
- Applications requiring a pumpable grout.
- Non-shrink grouting of machinery and equipment, base plates sole plates, precast panels, beams, columns and curtain walls.
- Applications where a non-shrink grout is needed for maximum effective bearing area to transfer optimum load.

- For underwater application in conjunction with Sikament® 100 SC. Consult Technical Service for dosage information. Independent test data is available however on site testing is recommended to confirm performance under actual field conditions.
- For grouting rebar, bolts, dowels and pins, etc.

### CHARACTERISTICS / ADVANTAGES

- Multiple fluidity with one material
- Reaches 10,000 psi in dry pack consistency
- Outstanding performance in fluid state
- Extended working time
- Excellent fluidity - sufficient time for placement
- Contains premium quality quartz aggregate
- Hardens free of segregation
- Non-metallic, will not stain or rust
- Shows positive expansion

### APPROVALS / STANDARDS

- Meets ASTM-C 1107 (Grade B & C)
- SikaGrout®-328 is USDA certifiable

### PRODUCT INFORMATION

<b>Packaging</b>	50 lb (22.7 kg) bag
<b>Appearance / Color</b>	Gray powder
<b>Shelf Life</b>	9 months from date of production if stored properly in original, unopened and undamaged sealed packaging
<b>Storage Conditions</b>	Store dry at 40–95 °F (4–35 °C) Protect from moisture. If damp, discard material

### TECHNICAL INFORMATION

Product Data Sheet  
SikaGrout®-328  
July 2018, Version 01.01  
020201010010000081

1 / 4

Compressive Strength	(ASTM C-109)	Dry Pack	Plastic	Flowable	Fluid
	73 °F (23 °C) 50 % R.H.				
1 day		5,000 psi (34.4 MPa)	4,500 psi (31 MPa)	4,000 psi (27.6 MPa)	3,500 psi (24.1 MPa)
3 day		8,000 psi (55.2 MPa)	6,500 psi (44.8 MPa)	6,000 psi (41.4 MPa)	5,500 psi (37.9 MPa)
14 day		9,200 psi (63.4 MPa)	7,000 psi (48.3 MPa)	6,700 psi (46.2 MPa)	6,500 psi (44.8 MPa)
28 day		10,000 psi (69 MPa)	8,200 psi (56.5 MPa)	8,000 psi (55.2 MPa)	7,500 psi (51.7 MPa)
Flexural Strength			<b>Fluid</b>		(ASTM C-293)
	3 day		1,100 psi (7.6 MPa)		73 °F (23 °C)
	7 day		1,200 psi (8.6 MPa)		50 % R.H.
	28 day		1,300 psi (9 MPa)		
Splitting Tensile Strength			<b>Fluid</b>		(ASTM C-496)
	3 day		350 psi (2.4 MPa)		73 °F (23 °C)
	7 day		400 psi (2.8 MPa)		50 % R.H.
	28 day		650 psi (4.5 MPa)		
Shear Strength			<b>Fluid</b>		(ASTM C-882 modified*)
	3 day		950 psi (6.6 MPa)		
	7 day		1,750 psi (12.1 MPa)		
	28 day		2,000 psi (13.8 MPa)		
*Mortar scrubbed into substrate at 73 °F (23 °C) and 50 % R.H.					
Freeze-Thaw Stability	300 Cycles		99 %		(ASTM C-666)

## APPLICATION INFORMATION

Mixing Ratio	Dry Pack	Plastic	Flowable	Fluid	
	5.5–6.0 pts (2.6–2.8 L)	6.5–7.0 pts (3.1–3.3 L)	7.0–7.5 pts (3.3–3.5 L)	8.0–8.5 pts (3.8–4 L)	
Coverage	0.44 ft <sup>3</sup> (0.01 m <sup>3</sup> ) per bag at hfluid consistency (Coverage figures do not include allowance for surface profile and porosity or material waste)				
Layer Thickness	<b>Min.</b>		<b>Max.</b>		
	1/2" (12.7 mm)		6" (152.4 mm)		
For application thicknesses of 6" or greater, consult Sika's Technical Service Department.					
Flowability	<b>Dry Pack</b>	<b>Plastic<sup>1</sup></b>	<b>Flowable<sup>1</sup></b>	<b>Fluid<sup>2</sup></b>	
	10–25 %	100–125 %	124–145 %	20–60 sec	
<sup>1</sup> ASTM C-1437					
<sup>2</sup> ASTM C-939					
Product Temperature	65–75 °F (18–24 °C)				
Ambient Air Temperature	> 45 °F (7 °C)				
Substrate Temperature	> 45 °F (7 °C)				
Set Time		<b>Dry Pack</b>	<b>Plastic</b>	<b>Flowable</b>	<b>Fluid</b>
	Initial	< 15 min	> 2 hr	> 3 hr	> 4 hr
	Final	< 2 hr	< 6 hr	< 7 hr	< 8 hr

Product Data Sheet  
SikaGrout®-328  
July 2018, Version 01.01  
020201010010000081



## SURFACE PREPARATION

- Surface must be clean and sound. Remove all deteriorated concrete, dirt, oil, grease, and other bond-inhibiting materials from the area to be repaired.
- Anchor bolts to be grouted must be de-greased with suitable solvent.
- Concrete must be sound and roughened to promote mechanical adhesion.
- To ensure optimum repair results, the effectiveness of decontamination and preparation should be assessed by a pull-off test.
- Substrate should be Saturated Surface Dry (SSD) with clean water prior to application. No standing water should remain during application.

## FORMING

- For pourable grout, construct forms to retain grout without leakage.
- Forms should be lined or coated with bond-breaker for easy removal.
- Forms should be sufficiently high to accommodate head of grout.
- Where grout-tight form is difficult to achieve, use SikaGrout®-328 in dry pack consistency.

## MIXING

- Pour the water in the recommended proportion into a suitable mixing container.
- DO NOT OVER WATER!
- Ambient and material temperature should be as close as possible to 70 °F. If higher, use cold water; if colder, use warm water.
- While mixing slowly, add the powder to the water.
- Mix thoroughly for at least 5 minutes with low speed (400-600 rpm) using a Sika mixing paddle or a jiffy paddle to avoid entraining too much air and until homogenous with no lumps.

## EXTENSION WITH AGGREGATES

- For deeper applications (plastic and flowable consistency only), 25 lbs. of 3/8" (9.5 mm) coarse aggregate can be added.
- The aggregate must be non-reactive (reference ASTM C-1260, C-227 and C-289), clean, well graded, saturated surface dry, have low absorption and high density, and comply with ASTM C-33 size number 8 per Table 2.
- Variances in aggregate may result in different strengths.
- Add pea gravel after the water and SikaGrout®-328.

## APPLICATION

- Within 60 minutes after mixing, place grout into forms in normal manner to avoid air entrapment.
- Vibrate, pump, or ram grout as necessary to achieve flow or compaction.

- SikaGrout®-328 must be confined leaving minimum exposed surface.
- After grout has achieved final set, remove forms, trim or shape exposed grout shoulders to designed profile.
- SikaGrout®-328 is an excellent grout for pumping, even at high flow. For pump recommendations, contact Technical Service.

## CURING TREATMENT

- Wet cure for a minimum of 3 days or apply a curing compound which complies with ASTM C-309 on exposed surfaces.

## LIMITATIONS

- Do not use as a patching or overlay mortar or in unconfined areas.
- As with all cement based materials, avoid contact with aluminum to prevent adverse chemical reaction and possible product failure. Insulate potential areas of contact by coating aluminum bars, rails, posts etc. with an appropriate epoxy such as Sikadur 32 Hi-Mod.

## BASIS OF PRODUCT DATA

Results may differ based upon statistical variations depending upon mixing methods and equipment, temperature, application methods, test methods, actual site conditions and curing conditions.

## OTHER RESTRICTIONS

See Legal Disclaimer.

## ENVIRONMENTAL, HEALTH AND SAFETY

For further information and advice regarding transportation, handling, storage and disposal of chemical products, user should refer to the actual Safety Data Sheets containing physical, environmental, toxicological and other safety related data. User must read the current actual Safety Data Sheets before using any products. In case of an emergency, call CHEMTREC at 1-800-424-9300, International 703-527-3887.

Product Data Sheet  
SikaGrout®-328  
July 2018, Version 01.01  
020201010010000081

3 / 4

BUILDING TRUST



**DIRECTIVE 2004/42/CE - LIMITATION OF EMISSIONS OF VOC**

0 g/l

(EPA method 24)

**LEGAL DISCLAIMER**

- **KEEP CONTAINER TIGHTLY CLOSED**
- **KEEP OUT OF REACH OF CHILDREN**
- **NOT FOR INTERNAL CONSUMPTION**
- **FOR INDUSTRIAL USE ONLY**
- **FOR PROFESSIONAL USE ONLY**

Prior to each use of any product of Sika Corporation, its subsidiaries or affiliates ("SIKA"), the user must always read and follow the warnings and instructions on the product's most current product label, Product Data Sheet and Safety Data Sheet which are available at [usa.sika.com](http://usa.sika.com) or by calling SIKA's Technical Service Department at 1-800-933-7452. Nothing contained in any SIKA literature or materials relieves the user of the obligation to read and follow the warnings and instructions for each SIKA product as set forth in the current product label, Product Data Sheet and Safety Data Sheet prior to use of the SIKA product.

SIKA warrants this product for one year from date of installation to be free from manufacturing defects and to meet the technical properties on the current Product Data Sheet if used as directed within the product's shelf life. User determines suitability of product for intended use and assumes all risks. User's and/or buyer's sole remedy shall be limited to the purchase price or replacement of this product exclusive of any labor costs.

**NO OTHER WARRANTIES EXPRESS OR IMPLIED SHALL APPLY INCLUDING ANY WARRANTY OF MERCHANTABILITY OR FITNESS FOR A PARTICULAR PURPOSE. SIKA SHALL NOT BE LIABLE UNDER ANY LEGAL THEORY FOR SPECIAL OR CONSEQUENTIAL DAMAGES. SIKA SHALL NOT BE RESPONSIBLE FOR THE USE OF THIS PRODUCT IN A MANNER TO INFRINGE ON ANY PATENT OR ANY OTHER INTELLECTUAL PROPERTY RIGHTS HELD BY OTHERS.**

Sale of SIKA products are subject to the Terms and Conditions of Sale which are available at <https://usa.sika.com/en/group/SikaCorp/termsandconditions.html> or by calling 1-800-933-7452.

**Sika Corporation**  
201 Polito Avenue  
Lyndhurst, NJ 07071  
Phone: +1-800-933-7452  
Fax: +1-201-933-6225  
[usa.sika.com](http://usa.sika.com)

**Sika Mexicana S.A. de C.V.**  
Carretera Libre Celaya Km. 8.5  
Fracc. Industrial Balvanera  
Corregidora, Queretaro  
C.P. 76920  
Phone: 52 442 2385800  
Fax: 52 442 2250537



**Product Data Sheet**  
SikaGrout®-328  
July 2018, Version 01.01  
020201010010000081

4 / 4

SikaGrout-328-en-US-(07-2018)-1-1.pdf

**BUILDING TRUST**



## Appendix D. [Interaction Diagrams and Tables for the Precast Column]

Screenshots of table calculations for various pipe connections and thicknesses follows. To view accessible tables displaying these calculations, please contact the research group in the Disaster Response Complex at Idaho State University (208-282-2902), or the Idaho Transportation Department Research Program (research@itd.idaho.gov).

### D.1 HSS Pipe Connection $f'_c = 4$ ksi

#### D.1.1 HSS thickness = 0.174 in.

Key Values	
Input Values	
$f_y =$	42 ksi AISC Table 2-4 pg 2-48
$f_u =$	58 ksi AISC Table 2-4 pg 2-48
$f'_c =$	4 ksi
$E_s =$	29000 ksi
Pipe Thickness =	0.174 in.

Pipe D (in.)	Concrete D (in.)	D/t		$A_s$ (in <sup>2</sup> )	$A_c$ (in <sup>2</sup> )	$P_o$ (kips)	$r_m$ (in.)	$\theta$ (deg.)	c (in.)	Mn(y) (kip-ft)	
20	19.65	114.94	> BAD								
18	17.65	103.45	< Good	103.57	9.74	244.72	1339.2	8.91	0.00	8.83	338.7
15	14.65	86.21	< Good	103.57	8.10	168.61	981.1	7.41	0.00	7.33	216.9
10	9.65	57.47	< Good	103.57	5.37	73.17	503.6	4.91	0.00	4.83	82.5

#### D.1.2 HSS thickness = 0.233 in.

Key Values	
Input Values	
$f_y =$	42 ksi AISC Table 2-4 pg 2-48
$f_u =$	58 ksi AISC Table 2-4 pg 2-48
$f'_c =$	4 ksi
$E_s =$	29000 ksi
Pipe Thickness =	0.233 in.

Pipe D (in.)	Concrete D (in.)	D/t		$A_s$ (in <sup>2</sup> )	$A_c$ (in <sup>2</sup> )	$P_o$ (kips)	$r_m$ (in.)	$\theta$ (deg.)	c (in.)	Mn(y) (kip-ft)	
30	29.53	128.76	> BAD								
24	23.53	103.00	< Good	103.57	17.40	434.99	2383.7	11.88	0.00	11.77	804.6
20	19.53	85.84	< Good	103.57	14.47	299.69	1746.5	9.88	0.00	9.77	515.3
15	14.53	64.38	< Good	103.57	10.81	165.91	1084.4	7.38	0.00	7.27	258.8
10	9.53	42.92	< Good	103.57	7.15	71.39	571.6	4.88	0.00	4.77	100.7

D.1.3 HSS thickness = 0.291 in.

Key Values  
Input Values

$f_y = 42$  ksi      AISC Table 2-4 pg 2-48  
 $f_u = 58$  ksi      AISC Table 2-4 pg 2-48  
 $f_c = 4$  ksi  
 $E_s = 29000$  ksi  
 Pipe Thickness = 0.291 in.

Pipe D (in.)	Concrete D (in.)	D/t		$A_s$ (in <sup>2</sup> )	$A_c$ (in <sup>2</sup> )	$P_o$ (kips)	$r_m$ (in.)	$\theta$ (deg.)	c (in.)	Mn(y) (kip-ft)	
40	39.42	137.46	> BAD								
30	29.42	103.09	< Good	103.57	27.16	679.70	3723.6	14.85	0.00	14.71	1570.8
20	19.42	68.73	< Good	103.57	18.02	296.14	1882.1	9.85	0.00	9.71	588.8
15	14.42	51.55	< Good	103.57	13.45	163.27	1185.2	7.35	0.00	7.21	299.4
10	9.42	34.36	< Good	103.57	8.88	69.66	637.5	4.85	0.00	4.71	118.1

D.1.4 HSS thickness = 0.349 in.

Key Values  
Input Values

$f_y = 42$  ksi      AISC Table 2-4 pg 2-48  
 $f_u = 58$  ksi      AISC Table 2-4 pg 2-48  
 $f_c = 4$  ksi  
 $E_s = 29000$  ksi  
 Pipe Thickness = 0.349 in.

Pipe D (in.)	Concrete D (in.)	D/t		$A_s$ (in <sup>2</sup> )	$A_c$ (in <sup>2</sup> )	$P_o$ (kips)	$r_m$ (in.)	$\theta$ (deg.)	c (in.)	Mn(y) (kip-ft)	
40	39.30	114.61	> BAD								
36	35.30	103.15	< Good	103.57	39.09	978.79	5361.1	17.83	0.00	17.65	2713.5
30	29.30	85.96	< Good	103.57	32.51	674.35	3927.9	14.83	0.00	14.65	1737.8
20	19.30	57.31	< Good	103.57	21.55	292.61	2016.8	9.83	0.00	9.65	661.5
15	14.30	42.98	< Good	103.57	16.06	160.65	1285.1	7.33	0.00	7.15	339.4
10	9.30	28.65	< Good	103.57	10.58	67.96	702.7	4.83	0.00	4.65	135.0

D.1.5 HSS thickness = 0.465 in.

Key Values  
Input Values

$f_y = 42$  ksi      AISC Table 2-4 pg 2-48  
 $f_u = 58$  ksi      AISC Table 2-4 pg 2-48  
 $f_c = 4$  ksi  
 $E_s = 29000$  ksi  
 Pipe Thickness = 0.465 in.

Pipe D (in.)	Concrete D (in.)	D/t		$A_s$ (in <sup>2</sup> )	$A_c$ (in <sup>2</sup> )	$P_o$ (kips)	$r_m$ (in.)	$\theta$ (deg.)	c (in.)	Mn(y) (kip-ft)	
50	49.07	107.53	> BAD								
48	47.07	103.23	< Good	103.57	69.44	1740.12	9529.0	23.77	0.00	23.54	6429.5
40	39.07	86.02	< Good	103.57	57.75	1198.88	6981.4	19.77	0.00	19.54	4117.6
30	29.07	64.52	< Good	103.57	43.15	663.71	4334.2	14.77	0.00	14.54	2068.0
20	19.07	43.01	< Good	103.57	28.54	285.62	2283.9	9.77	0.00	9.54	804.1
15	14.07	32.26	< Good	103.57	21.23	155.48	1482.6	7.27	0.00	7.04	417.3
10	9.07	21.51	< Good	103.57	13.93	64.61	830.5	4.77	0.00	4.54	167.7

D.1.6 HSS thickness = 0.581 in.

Key Values  
Input Values

$f_y = 42$  ksi      AISC Table 2-4 pg 2-48  
 $f_u = 58$  ksi      AISC Table 2-4 pg 2-48  
 $f_c = 4$  ksi  
 $E_s = 29000$  ksi  
 Pipe Thickness = 0.581 in.

Pipe D (in.)	Concrete D (in.)	D/t		$A_s$ (in <sup>2</sup> )	$A_c$ (in <sup>2</sup> )	$P_o$ (kips)	$r_m$ (in.)	$\theta$ (deg.)	c (in.)	Mn(y) (kip-ft)	
70	68.84	120.48	> BAD								
60	58.84	103.27	< Good	103.57	108.46	2718.98	14887.2	29.71	0.00	29.42	12554.7
50	48.84	86.06	< Good	103.57	90.20	1873.29	10907.0	24.71	0.00	24.42	8040.2
40	38.84	68.85	< Good	103.57	71.95	1184.69	7523.7	19.71	0.00	19.42	4705.7
30	28.84	51.64	< Good	103.57	53.70	653.16	4737.3	14.71	0.00	14.42	2392.8
15	13.84	25.82	< Good	103.57	26.32	150.40	1676.9	7.21	0.00	6.92	492.7
10	8.84	17.21	< Good	103.57	17.19	61.35	955.2	4.71	0.00	4.42	198.6

## D.2 HSS Pipe Connection $f'_c = 8$ ksi

### D.2.1 HSS thickness = 0.174 in.

Key Values
Input Values

$f_y =$	42 ksi	AISC Table 2-4 pg 2-48
$f_u =$	58 ksi	AISC Table 2-4 pg 2-48
$f_c =$	8 ksi	
$E_s =$	29000 ksi	
Pipe Thickness =	0.174 in.	

Pipe D (in.)	Concrete D (in.)	D/t		$A_s$ (in <sup>2</sup> )	$A_c$ (in <sup>2</sup> )	$P_o$ (kips)	$r_m$ (in.)	$\theta$ (deg.)	c (in.)	Mn(y) (kip-ft)	
20	19.65	114.94	> BAD								
18	17.65	103.45	< Good	103.57	9.74	244.72	2269.2	8.91	0.00	8.83	483.8
15	14.65	86.21	< Good	103.57	8.10	168.61	1621.8	7.41	0.00	7.33	299.9
10	9.65	57.47	< Good	103.57	5.37	73.17	781.7	4.91	0.00	4.83	106.3

### D.2.2 HSS thickness = 0.233 in.

Key Values
Input Values

$f_y =$	42 ksi	AISC Table 2-4 pg 2-48
$f_u =$	58 ksi	AISC Table 2-4 pg 2-48
$f_c =$	8 ksi	
$E_s =$	29000 ksi	
Pipe Thickness =	0.233 in.	

Pipe D (in.)	Concrete D (in.)	D/t		$A_s$ (in <sup>2</sup> )	$A_c$ (in <sup>2</sup> )	$P_o$ (kips)	$r_m$ (in.)	$\theta$ (deg.)	c (in.)	Mn(y) (kip-ft)	
30	29.53	128.76	> BAD								
24	23.53	103.00	< Good	103.57	17.40	434.99	4036.6	11.88	0.00	11.77	1148.6
20	19.53	85.84	< Good	103.57	14.47	299.69	2885.4	9.88	0.00	9.77	712.0
15	14.53	64.38	< Good	103.57	10.81	165.91	1714.9	7.38	0.00	7.27	339.9
10	9.53	42.92	< Good	103.57	7.15	71.39	842.8	4.88	0.00	4.77	123.5

D.2.3 HSS thickness = 0.291 in.

Key Values  
Input Values

$f_y = 42$  ksi      AISC Table 2-4 pg 2-48  
 $f_u = 58$  ksi      AISC Table 2-4 pg 2-48  
 $f_c = 8$  ksi  
 $E_s = 29000$  ksi  
 Pipe Thickness = 0.291 in.

Pipe D (in.)	Concrete D (in.)	D/t		$A_s$ (in <sup>2</sup> )	$A_c$ (in <sup>2</sup> )	$P_o$ (kips)	$r_m$ (in.)	$\theta$ (deg.)	c (in.)	Mn(y) (kip-ft)	
40	39.42	137.46	> BAD								
30	29.42	103.09	< Good	103.57	27.16	679.70	6306.4	14.85	0.00	14.71	2242.6
20	19.42	68.73	< Good	103.57	18.02	296.14	3007.4	9.85	0.00	9.71	782.1
15	14.42	51.55	< Good	103.57	13.45	163.27	1805.6	7.35	0.00	7.21	378.5
10	9.42	34.36	< Good	103.57	8.88	69.66	902.2	4.85	0.00	4.71	140.1

D.2.4 HSS thickness = 0.349 in.

Key Values  
Input Values

$f_y = 42$  ksi      AISC Table 2-4 pg 2-48  
 $f_u = 58$  ksi      AISC Table 2-4 pg 2-48  
 $f_c = 8$  ksi  
 $E_s = 29000$  ksi  
 Pipe Thickness = 0.349 in.

Pipe D (in.)	Concrete D (in.)	D/t		$A_s$ (in <sup>2</sup> )	$A_c$ (in <sup>2</sup> )	$P_o$ (kips)	$r_m$ (in.)	$\theta$ (deg.)	c (in.)	Mn(y) (kip-ft)	
40	39.30	114.61	> BAD								
36	35.30	103.15	< Good	103.57	39.09	978.79	9080.5	17.83	0.00	17.65	3874.4
30	29.30	85.96	< Good	103.57	32.51	674.35	6490.5	14.83	0.00	14.65	2401.8
20	19.30	57.31	< Good	103.57	21.55	292.61	3128.8	9.83	0.00	9.65	851.2
15	14.30	42.98	< Good	103.57	16.06	160.65	1895.6	7.33	0.00	7.15	416.6
10	9.30	28.65	< Good	103.57	10.58	67.96	960.9	4.83	0.00	4.65	156.3

### D.2.5 HSS thickness = 0.465 in.

Key Values
Input Values

$f_y = 42$  ksi      AISC Table 2-4 pg 2-48  
 $f_u = 58$  ksi      AISC Table 2-4 pg 2-48  
 $f_c = 8$  ksi  
 $E_s = 29000$  ksi  
 Pipe Thickness = 0.465 in.

Pipe D (in.)	Concrete D (in.)	D/t		$A_s$ (in <sup>2</sup> )	$A_c$ (in <sup>2</sup> )	$P_o$ (kips)	$r_m$ (in.)	$\theta$ (deg.)	c (in.)	Mn(y) (kip-ft)
50	49.07	107.53	> BAD							
48	47.07	103.23	< Good	103.57	69.44	1740.12	23.77	0.00	23.54	9181.5
40	39.07	86.02	< Good	103.57	57.75	1198.88	19.77	0.00	19.54	5691.4
30	29.07	64.52	< Good	103.57	43.15	663.71	14.77	0.00	14.54	2716.2
20	19.07	43.01	< Good	103.57	28.54	285.62	9.77	0.00	9.54	987.1
15	14.07	32.26	< Good	103.57	21.23	155.48	7.27	0.00	7.04	490.8
10	9.07	21.51	< Good	103.57	13.93	64.61	4.77	0.00	4.54	187.3

### D.2.6 HSS thickness = 0.581 in.

Key Values
Input Values

$f_y = 42$  ksi      AISC Table 2-4 pg 2-48  
 $f_u = 58$  ksi      AISC Table 2-4 pg 2-48  
 $f_c = 8$  ksi  
 $E_s = 29000$  ksi  
 Pipe Thickness = 0.581 in.

Pipe D (in.)	Concrete D (in.)	D/t		$A_s$ (in <sup>2</sup> )	$A_c$ (in <sup>2</sup> )	$P_o$ (kips)	$r_m$ (in.)	$\theta$ (deg.)	c (in.)	Mn(y) (kip-ft)
70	68.84	120.48	> BAD							
60	58.84	103.27	< Good	103.57	108.46	2718.98	29.71	0.00	29.42	17929.9
50	48.84	86.06	< Good	103.57	90.20	1873.29	24.71	0.00	24.42	11114.2
40	38.84	68.85	< Good	103.57	71.95	1184.69	19.71	0.00	19.42	6251.6
30	28.84	51.64	< Good	103.57	53.70	653.16	14.71	0.00	14.42	3025.7
15	13.84	25.82	< Good	103.57	26.32	150.40	7.21	0.00	6.92	562.6
10	8.84	17.21	< Good	103.57	17.19	61.35	4.71	0.00	4.42	216.8

### D.3 Cast-in-place Moment Capacities with $f'_c = 4$ ksi

**Key values**  
**Input values**  
 Circular Column Dimensions  
 Cover = 1.5 in.  
 Stump Spacing = 3 in.  
 Long Bar # = 6  
 $\phi = 0.75$  (Figure 3.5 pg. 72)  
 Compression strain = -0.003  
 Tensile strain = 0.002  
 $f_y = 60$  ksi  
 $f'_c = 4$  ksi  
 $E_s = 29000$  ksi  
 $\beta_1 = 0.85$  (see pg 68)

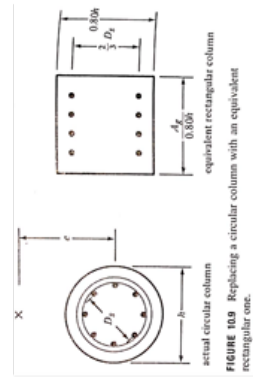


FIGURE 10.9 Replacing a circular column with an equivalent rectangular one.

Apprx. Pipe size	D (in.)	$D_{core}$ (in.)	# of bars	$\rho$	B	H	$H_s$	$A'_s$	Cover	y	$e'_s$	$\epsilon_s$	a (in.)	$C_c$ (kips)	$C'_s$ (kips)	$T_s$ (kips)	$P_n$ (kips)	$\phi M_n$ (kip-ft.)
9	18	13.5	12	2.1%	17.67	14.40	9.00	2.65	2.70	8.64	0.00206	0.00106	7.34	-441.25	-150.03	81.68	509.60	162.46
15	24	19.5	22	2.1%	23.56	19.20	13.00	4.86	3.10	11.52	0.00219	0.00119	9.79	-784.44	-275.06	168.09	891.41	410.65
21	30	25.5	33	2.1%	29.45	24.00	17.00	7.29	3.50	14.4	0.00227	0.00127	12.24	-1225.69	-412.58	268.65	1369.63	812.35
27	36	31.5	48	2.1%	35.34	28.80	21.00	10.60	3.90	17.28	0.00232	0.00132	14.69	-1765.00	-600.12	406.77	1958.34	1439.14
33	42	37.5	65	2.1%	41.23	33.60	25.00	14.36	4.30	20.16	0.00236	0.00136	17.14	-2402.36	-812.67	566.33	2648.69	2313.35
39	48	43.5	86	2.1%	47.12	38.40	29.00	19.00	4.70	23.04	0.00239	0.00139	19.58	-3137.77	-1075.22	764.67	3448.32	3512.41
45	54	49.5	110	2.1%	53.01	43.20	33.00	24.30	5.10	25.92	0.00241	0.00141	22.03	-3971.24	-1375.28	993.36	4353.16	5069.64
51	60	55.5	135	2.1%	58.90	48.00	37.00	29.82	5.50	28.8	0.00243	0.00143	24.48	-4902.77	-1687.85	1234.14	5356.48	6982.08
57	66	61.5	160	2.1%	64.80	52.80	41.00	35.34	5.90	31.68	0.00244	0.00144	26.93	-5932.35	-2000.41	1477.24	6455.52	9252.04
63	72	67.5	190	2.1%	70.69	57.60	45.00	41.97	6.30	34.56	0.00245	0.00145	29.38	-7059.99	-2375.49	1768.63	7666.84	12054.57